Experimental investigation and fracture simulation of welded steel connections

A Thesis Submitted in Fulfilment of the Requirements

for the Degree of

Doctor of Philosophy

In

Civil Engineering

By

Xiaofan Liu

[REDACTION]

Supervisor: Prof. Kim J.R. Rasmussen

Supervisor: A/Prof. Shen Yan

School of Civil Engineering

Faculty of Engineering

The University of Sydney, NSW 2006

Australia

2023

Statement of originality

This is to certify that to the best of my knowledge, the content of this thesis is my own work. This thesis has not been submitted for any degree or other purposes.

I certify that the intellectual content of this thesis is the product of my own work and that all the assistance received in preparing this thesis and sources has been acknowledged.

Signature*

Name: Xiaofan Liu

Authorship attribution statement

Chapter 3 of this thesis is published as:

Liu, X., Yan, S., Rasmussen, K.J.R. and Deierlein, G.G., 2022. Experimental investigation of the effect of Lode angle on fracture initiation of steels. *Engineering Fracture Mechanics*, 271, p.108637.
Liu, X., Yan, S., Rasmussen, K.J.R. and Deierlein, G.G., 2022. Verification of void growth-based exponential damage function for ductile crack initiation over the full range of stress triaxialities. *Engineering Fracture Mechanics*, 269, p.108571.
Contribution: Methodology, Formal analysis, Investigation, Data Curation, Writing – Original Draft.

Chapters 2 and 8 of this thesis contain materials published in:

Liu, X., Yan, S., Rasmussen, K.J.R. and Deierlein, G.G., 2022. Experimental investigation of the effect of Lode angle on fracture initiation of steels. *Engineering Fracture Mechanics*, 271, p.108637.
Liu, X., Yan, S., Rasmussen, K.J.R. and Deierlein, G.G., 2022. Verification of void growth-based exponential damage function for ductile crack initiation over the full range of stress triaxialities. *Engineering Fracture Mechanics*, 269, p.108571.
Contribution: Methodology, Formal analysis, Investigation, Data Curation, Writing – Original Draft.

In addition to the statements above, in cases where I am not the corresponding author of a published item, permission to include the published material has been granted by the corresponding author.

Xiaofan Liu

Signature:

Date: 28th February 2023

As supervisor for the candidature upon which this thesis is based, I can confirm that the authorship attribution statements above are correct.

Kim J.R. Rasmussen

Signature:

Date: 28th February 2023

Publications

The following publications by the author are based on the research delivered in this thesis:

1. Liu, X., Yan, S., Rasmussen, K.J.R. and Deierlein, G.G., 2022. Experimental investigation of the effect of Lode angle on fracture initiation of steels. *Engineering Fracture Mechanics*, 271, p.108637.
2. Liu, X., Yan, S., Rasmussen, K.J.R. and Deierlein, G.G., 2022. Verification of void growth-based exponential damage function for ductile crack initiation over the full range of stress triaxialities. *Engineering Fracture Mechanics*, 269, p.108571.

Acknowledgements

I am grateful for this challenging and memorable journey, and I would like to appreciate all the kindness and support that I received. First and foremost, I would like to express my deepest gratitude to my supervisor Prof. Kim Rasmussen. His expertise and guidance are vital for the completion of this research project. I appreciate his patience and caring throughout my PhD study, and I will always treasure the experience of working in his research team. A massive thank to Prof. Shen Yan, who has been my second supervisor. His suggestions and supervision supported me in completing the publications and this thesis. Without them, it would not have been possible to complete this study.

I would like to express my appreciation to Prof. Anna Paradowska for her suggestions on the measurement of weld residual stress and support during the experiments at ANSTO. I would like to express my gratitude to Prof. Gwénaëlle Proust for her assistance with macroetching and hardness tests. I would like to express my thanks to Prof. Gregory Deierlein for his suggestions on fracture mechanical models. I would like to thank Prof. Hao Zhang for the valuable discussions. Big thanks to the students in Rooms 360 and 101 for their friendship and generous help.

I would like to express my gratitude to Mr Garry Towell for his guidance on conducting experiments. I am grateful to all the staff in the structures laboratory, especially Mr Paul Busstra, Mr Paul Geddes, Mr Alexander Moore, Mr James Ryder, Mr Sergio Carvalho and Mr Paul Burrell. Without their support and assistance, I could not have completed these experiments.

I would like to thank my family and friends for their support and encouragement. The deepest gratitude to my parents, husband, Chuan, and best friend, Danni, for their accompany and love.

Abstract

This thesis aims to conduct an experimental and numerical investigation of the mechanical properties and fracture performance of welded steel connections. First, in order to study the fracture of structural steels, the effects of the two key parameters, stress triaxiality and Lode angle, are discussed based on the experimental data collected from the literature and the test results of two newly designed specimen types. It is observed that the void growth exponential function can accurately describe the effect of the stress triaxiality in the whole stress state, and the effect of the Lode angle can be considered using an exponential function, based on which a new fracture model is proposed and termed Lode angle modified void growth model (LMVGM). Second, the mechanical properties in the weld zone and the weld residual stresses (WRS) are measured from welded connections made of the same steel grade and weld materials under the same welding process. The mechanical properties of the weld, heat affected zone (HAZ) and base metal, including their stress-strain relationships and fracture strains under various stress states, are measured in longitudinal and transverse directions by conducting tensile tests on a series of miniature coupons extracted from butt-welded plates. The test results show that the strength and ductility of the HAZ are generally in-between those of the base metal and the weld. The magnitude and distribution of WRS of fillet welds with different weld sizes and butt welds are measured from a series of welded cruciform specimens and an end-plate connection using the neutron diffraction method. Finally, experimental investigation and numerical simulation of the fracture in welded cruciform specimens are conducted, and it is concluded that (i) material inhomogeneity in the weld zone has a significant effect on the performance of the welded connections, and (ii) ignoring the properties of the weld and HAZ will underestimate the capacity of the connection. Based on the measurement results of the mechanical properties in the weld zone, the fracture process of the cruciform specimens is simulated using the calibrated LMVGM, and the good agreement with the test results verifies the applicability of the proposed fracture model and measurement results of the weld-zone mechanical properties.

Keywords: Steel, fracture, welded connections, stress triaxiality, Lode angle parameter, miniature coupons, heat affected zone, stress-strain relationships, fracture strains, weld residual stress, welded cruciform specimens, end-plate connection, neutron diffraction method, experiments, numerical simulation.

Table of contents

List of Figures

List of Tables

Chapter 1 Introduction

1.1 Introduction

This dissertation aims to experimentally investigate and simulate the fracture in welded connections. In this thesis, first, a new fracture model is proposed to predict the fracture initiation of structural steels, based on the discussion of the effects of the two key parameters, the stress triaxiality and the Lode angle. Then the mechanical properties in the weld zone of welded connections, such as the stress-strain relationships and fracture strains, and weld residual stresses (WRS), are investigated. Tensile tests are conducted on a series of miniature coupons to measure the mechanical properties of the weld and heat affected zone (HAZ) and their results are compared with those of the base metal. The weld residual stresses of fillet welds and butt welds are measured using the neutron diffraction method. After that, tensile tests are conducted on welded cruciform specimens to investigate the effect of material inhomogeneity on the performance of welded connections. The fracture process of the cruciform specimens is simulated using the proposed fracture model calibrated by the test results of the miniature coupons extracted from the three material areas. This chapter presents an overview of the thesis. In Section 1.2, the motivation and methodology of the research are presented. In Section 1.3, the structure of the thesis is introduced.

1.2 Research motivation and methodology

Steel is a widely used material in structures due to its outstanding performance characteristics, including strength, durability and flexibility. Numerous notable steel structures have been built around the world, such as the Sydney Harbour Bridge, Beijing National Stadium and the Eiffel Tower. In the design of steel structures, the development of highly advanced analysis tools enables fully nonlinear analyses of the steel structures as a system. This system-based method is termed the direct design method (DDM) which has been permitted by most standards, such as AS4100 and AISC360-14. In the DDM, the behaviour and strength of a structure can be predicted by covering limit states in the analysis, however, fracture in welded steel connections has not been considered in DDM. In steel structures, fracture in welded connections is one of the main failure modes, which was observed in the 1994 Northridge Earthquake and the 2011 Christchurch Earthquake. Various fracture mechanics models have been proposed to predict the fracture initiation of structural steels, but the isolated effects of the two key parameters, stress triaxiality and Lode angle, have not been studied based on experimental evidence.

Meanwhile, in welded connections, the high temperature and different cooling rates during the welding process will locally change the microstructure in the weld zone, which can be divided into three material areas, viz. base metal, weld and HAZ. Materials in the three areas have different chemical compositions and/or microstructures, and correspondingly have different mechanical properties. Although numerous studies have been conducted on experimental or numerical investigations of fracture in welded steel connections, the effects of the material inhomogeneity in the weld zone have rarely been discussed, and limited studies have been carried out on the simulation of fracture in welded steel connections considering the mechanical properties of the three material areas. Therefore, it is necessary to study the fracture in welded connections to bridge this gap in DDM.

This doctoral thesis focuses on the mechanical properties and fracture performance of welded connections under monotonic tensile loading. The welded connections studied in this thesis are butt-welded plates, welded cruciform specimens and an end-plate connection, which are made of the same steel grades and weld materials under the same welding process. First, the effects of the stress triaxiality and the Lode angle on the fracture of structural steels are discussed under various stress states based on experimental results collected from the literature and the test results of two newly designed specimen types. Considering the effects of these two key parameters, a new fracture model is then proposed to predict the fracture initiation of steel.

Second, in welded connections, the high temperature and different cooling rates during the welding process will cause locally different microstructures, inhomogeneous properties and residual stresses in the weld zone, which can be divided into three material areas, base metal, weld and HAZ. The stress-strain relationships and fracture strains of the weld and HAZ are measured in both longitudinal and transverse directions through tensile tests on a series of miniature coupons extracted from the butt-welded plates, and their results are compared with those of the base metal. The magnitude and distribution of weld residual stresses of fillet welds and butt welds in longitudinal, transverse and normal directions are measured from a series of welded cruciform specimens and an end-plate connection using the neutron diffraction strain scanner Kowari at the Australian Nuclear Science and Technology Organization (ANSTO).

Finally, tensile tests are conducted on welded cruciform specimens, and three finite element models are developed for each specimen type by assuming the stress-strain relationships of the weld and HAZ are the same as the base metal (FEM-B), adopting the properties of the weld (FEM-BW) or adopting the properties of both the weld and HAZ (FEM-BWH). The simulated

results are compared with the test results to discuss the effect of the material inhomogeneity in the weld zone on the performance of the welded connections. The fracture process of the cruciform specimens is simulated by considering the local properties of the base metal, weld and HAZ using the proposed fracture model calibrated by the test results of the miniature coupons. Therefore, based on the test data and discussion provided by the experimental and numerical studies, the mechanical properties and fracture performance of welded connections are comprehensively studied.

1.3 Structure of the thesis

This thesis is written in eight chapters:

In Chapter 1, an overview of the thesis topic is provided.

In Chapter 2, an extensive literature review is conducted about the fracture prediction models, measurement of stress-strain relationships and fracture strains of weld and HAZ, measurement of weld residual stresses, and experimental studies and numerical simulation of fracture in welded connections.

In Chapter 3, the effects of the stress triaxiality and the Lode angle on fracture strains of structural steels are discussed under various stress states based on the experimental data collected from the literature and two newly designed specimens. A new fracture model, termed the Lode angle Modified Void Growth Model (LMVGM) is proposed by predicting the fracture strains as a function of the two key parameters.

In Chapter 4, a series of miniature flat plate coupons are designed and extracted from the base metal, weld and HAZ in the weld zone of butt-welded plates. The stress-strain relationships of the weld and HAZ are measured for both longitudinal and transverse directions and are compared with those of the base metal.

In Chapter 5, the fracture strains of the weld and HAZ under various stress states are measured using miniature coupons for both longitudinal and transverse directions and are compared with those of the base metal. The fracture loci of the three material areas in the whole stress state regime are then predicted using the fracture model LMVGM calibrated by the test results of the miniature coupons.

In Chapter 6, the distribution and magnitude of residual stresses generated by fillet welds and butt welds in welded cruciform specimens and an end-plate connection are measured using the neutron diffraction method. Based on the measurement results, the effect of weld size and weld

types on the residual stress patterns of welded connections made by the same materials under the same welding conditions is discussed.

In Chapter 7, tensile tests are carried out on a series of welded cruciform specimens, and finite element models are developed to discuss the effects of the inhomogeneity of mechanical properties in the weld zone. The fracture process of the welded cruciform specimens is then simulated using the fracture model LMVGM calibrated by the fracture strains of the three material areas measured from the miniature tests.

In Chapter 8, the thesis conclusions are summarized and the suggestions for further research are provided.

Chapter 2 Literature review

2.1 Introduction

This chapter introduced the present understanding of the fracture prediction models, the measurement methods of mechanical properties in the weld zone and the weld residual stresses, and the fracture investigation of welded steel connections. Section 2.2 introduced previous studies about fracture prediction models. The fracture strains of structural steels were highly affected by the stress triaxiality and the Lode angle, which were used to characterize the stress states for various loading conditions. Various widely used fracture mechanics models were then introduced. Different specimen types were tested in previous studies for the investigation of the fracture under different stress states, and a summary of existing fracture specimen types was presented.

In welded connections, the steel components are connected by the heating, melting and fusing of weld materials. During this welding process, the high temperature locally changes the microstructure around the weld, and the weld zone always includes, from the centreline of the weld outward, a weld area, a HAZ area, and an unaffected base metal (BM) area. Materials in the three areas have different chemical compositions or microstructures, and correspondingly have different mechanical properties. The mechanical properties of the weld and HAZ, including their stress-strain relationships and fracture strains, and weld residual stresses, will have a significant effect on the performance of welded connections. However, these properties have not been fully considered in the fracture analysis of welded connections. To summarize the measurement methods and recent results, Section 2.3 briefly introduced previous research on the weld-zone mechanical properties and WRS. Numerous experiments were carried out on welded connections to study their strength and failure mode under monotonic tensile loading, and some fracture models were used to simulate the fracture process of connections. In Section 2.4, an overview of previous investigations on experiments and numerical simulations of fracture in welded connections was provided. Section 2.5 summarizes the whole chapter.

2.2 Fracture mechanics models

2.2.1 Characterization of stress states

A series of parameters are defined to characterize the stress states for various specimen types under loading conditions. Letting σ_1, σ_2 and σ_3 denote the three principal stresses, the first

invariant of the stress tensor, I_1, and the second and third invariants of the stress deviator tensor, J_2 and J_3, are given respectively as:

$$I_1 = \sigma_1+\sigma_2+\sigma_3=3\sigma_m \tag{2-1}$$

$$J_2 = \frac{1}{6}\left[(\sigma_1-\sigma_2)^2+(\sigma_2-\sigma_3)^2+(\sigma_1-\sigma_3)^2\right] \tag{2-2}$$

$$J_3 = (\sigma_1-\sigma_m)(\sigma_2-\sigma_m)(\sigma_3-\sigma_m) \tag{2-3}$$

where $\sigma_m = (\sigma_1+\sigma_2+\sigma_3)/3$ is the hydrostatic stress. The von Mises stress $\bar{\sigma}$ is defined as a function of J_2 as follows:

$$\bar{\sigma}=\sqrt{3J_2}\,. \tag{2-4}$$

The stress state of a material point can be characterized by the stress triaxiality T and Lode angle parameter ξ, defined in terms of the normalised first invariant of the stress tensor, I_1, and the normalized third invariant of the stress deviator tensor, J_3, respectively:

$$T = \frac{I_1}{3\bar{\sigma}} \tag{2-5}$$

$$\xi = \frac{27J_3}{2\bar{\sigma}^3} \tag{2-6}$$

The Lode angle parameter ξ is related to the associated Lode angle θ as follows,

$$\xi=\cos(3\theta)\,. \tag{2-7}$$

Note that θ ranges between 0 and $\pi/3$, and hence the range of ξ is between -1 and 1. Two other related parameters, which are sometimes adopted to describe the Lode angle dependence, are normalized Lode angle $\bar{\theta}$ and the Lode parameter L, which are defined as follows,

$$\bar{\theta}=1-\frac{6\theta}{\pi} \tag{2-8}$$

$$L=\frac{2\sigma_2-\sigma_1-\sigma_3}{\sigma_1-\sigma_3}=\frac{\sigma_2-\sigma_{1|3}}{\tau}\,. \tag{2-9}$$

In Eq. (2-9), $\tau=(\sigma_1-\sigma_3)/2$ and $\sigma_{1|3}=(\sigma_1+\sigma_3)/2$ are the maximum shear stress and the normal stress on the same plane, respectively. The Lode angle parameter ξ is closely related to the normalized Lode angle $\bar{\theta}$ and Lode parameter L as follows,

$$\xi = \cos\left[\frac{\pi}{2}(1-\bar{\theta})\right] \tag{2-10}$$

$$\xi = \frac{L(L-3)(L+3)}{(L^2+3)^{3/2}} \tag{2-11}$$

.

In the space of stress triaxiality and Lode angle parameter, as shown in Fig. 2-1, the main distinguishing stress states are located in different quadrants. The values of Lode angle parameter for several common stress states are as follows: (1) tensile axisymmetric stress state, with σ_2 equal to σ_3, corresponds to ξ=1; (2) compressive axisymmetric stress state, with σ_1 equal to σ_2, corresponds to ξ=-1; and (3) plane strain, with $\sigma_2 = (\sigma_1 + \sigma_3)/2$, corresponds to ξ=0. For instance, the axisymmetric tensile (i.e. $T > 0$, $\xi = 1$), equi-biaxial tensile (i.e. $T > 0$, $\xi = -1$), axisymmetric compressive (i.e. $T < 0$, $\xi = -1$) and equi-biaxial compressive (i.e. $T < 0$, $\xi = 1$) stress states are located in the first, second, third and fourth quadrants, respectively. The plane stress state (dashed line in Fig. 2-1) crosses all four quadrants, under which T and ξ are related by the following expression

$$\xi = -\frac{27}{2}T(T^2 - \frac{1}{3}) \text{ .} \tag{2-12}$$

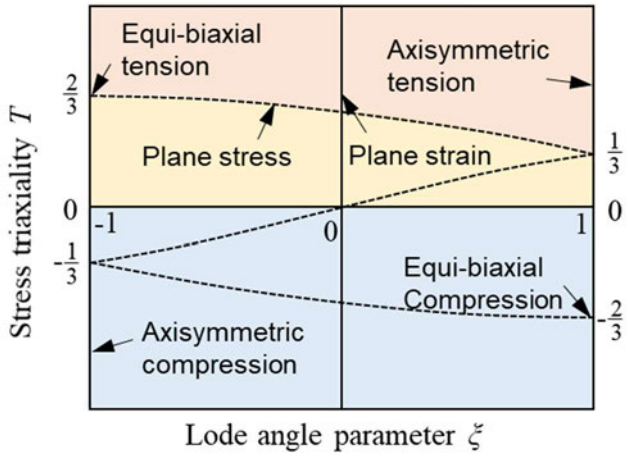

Figure 2-1. Stress states plotted on the plane of stress triaxiality versus Lode angle parameter.

In Fig. 2-1, the stress states in the top shaded region, above the plane stress state, are considered as high stress triaxiality. Medium stress triaxiality refers to a stress state in which the stress triaxiality is non-negative but not sufficiently high to make all three principal stresses positive (tensile). The medium stress triaxiality states fall in the yellow shaded region between the top segment of the plane stress state and the abscissa (the axis of the Lode angle parameter). Pure shear and combined shear and tension stress states are typical examples of medium stress triaxiality states. Low stress triaxiality refers to a negative stress triaxiality state in the blue

shaded region below the abscissa, which can be achieved by combined shear and compression and three-dimensional compression.

Since the values of the stress triaxiality and Lode angle parameter normally vary during plastic deformation, their equivalent average values are employed in the fracture analysis to reflect the loading history. The average values of stress triaxiality T_{avg} and Lode angle parameter ξ_{avg} over the loading history are calculated as:

$$T_{\text{avg}} = \frac{1}{\varepsilon_{\text{f}}} \int_0^{\varepsilon_{\text{f}}} T d\varepsilon_{\text{p}} \tag{2-13}$$

$$\xi_{\text{avg}} = \frac{1}{\varepsilon_{\text{f}}} \int_0^{\varepsilon_{\text{f}}} \xi d\varepsilon_{\text{p}} \tag{2-14}$$

where ε_{f} and ε_{p} are the fracture strain and equivalent plastic strain, respectively. The stress and strain tensors needed to calculate T, ξ and ε_{p} can be obtained from finite-element analyses.

2.2.2 Fracture models considering the effect of stress triaxiality

Over the last four decades, a substantial body of research has been conducted to understand the underlying mechanisms governing the ductile fracture of metals including the prediction of fracture initiation as a function of local plastic strain and multi-axial stresses. Microscopically, ductile metals fracture due to the nucleation, growth and coalescence of microvoids [1], based on which a variety of fracture mechanics models have been proposed to predict the fracture initiation.

Rice and Tracy [2] studied the effect of the stress triaxiality, defined as the ratio of the hydrostatic stress to the von Mises stress, on the growth rate of a spherical void in an infinite axisymmetric continuum. They concluded that the growth rate of a spherical void with a radius of R_{v} in a rigid-plastic continuum relates to the plastic strain rate $d\varepsilon_{\text{p}}$ and the stress triaxiality T through the following,

$$\frac{dR_{\text{v}}}{R_{\text{v}}} = 0.283 d\varepsilon_{\text{p}} e^{1.5T}. \tag{2-15}$$

It is generally acknowledged that when subjected to high stress triaxiality, ductile metals fracture when the microscopic voids grow to a critical size, causing coalescence of voids [2]. Hence, following Eq. (2-15), the fracture initiation strain ε_{f} is assumed to be inversely proportional to void growth rate, and thus decreases exponentially as the stress triaxiality increases, i.e.,

$$\varepsilon_{\mathrm{f}} = a \cdot e^{-bT} \tag{2-16}$$

where a and b are free parameters. Herein, Eq. (2-16) is the so-called void growth-based exponential function, i.e., VGEF. Since Eq. (2-15) was first proposed, several fracture initiation models have been developed with forms similar to Eq. (2-16).

Hancock et al. [3] added the strain at which the microscopic voids nucleate to the right-hand side of Eq. (2-16), and assigned a value of 1.5 to parameter b to be consistent with Eq. (2-15), thereby expressing the fracture strain as:

$$\varepsilon_{\mathrm{f}} = \varepsilon_{\mathrm{n}} + a \cdot e^{-1.5T} \tag{2-17}$$

where ε_{n} is the void nucleation strain, which Hancock et al. [3] found to be about 0.2. Following this form, Johnson and Cook [4] proposed the more general expression for the fracture strain:

$$\varepsilon_{\mathrm{f}} = c + a \cdot e^{-bT}. \tag{2-18}$$

Another prominent model, termed the Void Growth Model (VGM) [5], is expressed as follows,

$$D = \eta \int e^{\lambda T} d\varepsilon_p \tag{2-19}$$

where η and λ are two free parameters and fracture occurs when D=1. The VGM is essentially the integral form of the VGEF.

VGEF is the foundation of the fracture initiation models described above, along with other similar models that have been presented in the literature. The validity of the VGEF has generally been established for regions of moderate to high stress triaxiality based on cylindrical notched bar tests and is further substantiated by microscopic images of the dimpled fracture surface. A remaining challenge, which is addressed by the tests describe below, is to further valid the VGEF for low stress triaxiality regimes where the microscopic voids grow more slowly with plastic strain.

2.2.3 Fracture models considering the effects of stress triaxiality and Lode angle

Recent numerical [6] and experimental [7] studies have shown that stress triaxiality by itself is insufficient for determining the fracture strain, especially for low triaxiality stress states. Zhang et al. [6] performed numerical three-dimensional analyses of a spherical void contained within a cubic cell under various stress states. The results showed that the effect of Lode angle cannot be ignored, and that the effect increases as the stress triaxiality decreases. Barsoum et al. [7] designed and tested a series of double notched tube specimens. The fractography of the fracture surfaces revealed (1) that the fracture mode at low stress triaxiality is characterised by internal

void shearing, as compared to the internal void necking mode occurring at high stress triaxiality, and (2) that the Lode angle plays a significant role in the transition between the fracture modes.

Following these initial studies, the effect of the Lode angle has been a field of active research, and several fracture models have been proposed to incorporate the Lode angle effect [8-15]. In the phenomenological fracture models proposed in [8-9], the Lode angle effect was empirically considered along with the stress triaxiality, while recently numerical methods were employed [10-11] to evaluate the effect of the Lode angle on the growth and change of the shape of voids.

Accordingly, some VGEF-based fracture initiation models have been modified to incorporate the effect of the Lode angle. Xue et al. [8] assumed that the most and least favourable conditions for fracture are the axisymmetric (ξ=1) and plane strain (ξ=0) stress states, respectively. Therefore, by using two VGEFs to describe the fracture criteria corresponding to these two stress states, the Xue-Wierzbicki model is expressed as:

$$\varepsilon_{\mathrm{f}} = C_1 e^{-C_2 T} - (C_1 e^{-C_2 T} - C_3 e^{-C_4 T})(1 - \xi^{1/n})^n \tag{2-20}$$

in which C_1, C_2, C_3 and C_4 are free parameters. Xue et al. [8] assumed an even integer for $1/n$, such that Eq. (2-20) implies a symmetric fracture locus with respect to ξ.

Bai et al. [9] suggested that in addition to the ξ=1 and ξ=0 stress states, the ξ=-1 stress state should also be a limiting case in the fracture locus. After introducing another VGEF for the ξ=-1 stress state, the Bai-Wierzbicki model takes the following form:

$$\varepsilon_{\mathrm{f}} = \left[\frac{1}{2}(D_1 e^{-D_2 T} + D_5 e^{-D_6 T}) - D_3 e^{-D_4 T}\right]\bar{\theta}^2 + \frac{1}{2}(D_1 e^{-D_2 T} - D_5 e^{-D_6 T})\bar{\theta} + D_3 e^{-D_4 T} \tag{2-21}$$

where D_1 to D_6 are free parameters and $\bar{\theta}$ is a modified form of the Lode angle parameter, related to ξ by the expression ξ=sin($\bar{\theta}\cdot\pi/2$).

Smith et al. [14-15] proposed a Stress-Weighted Ductile Fracture Model (SWDFM) based on Rice and Tracey's void growth theory [2] and observations from finite element plasticity simulations of void growth as well as the fractographic analyses of fracture surfaces. The SWDFM is expressed as,

$$D = C_{\mathrm{SWDFM}} \times \int_{\varepsilon_{\mathrm{p}}} \left[\exp(1.3T) - \left(\frac{1}{\beta_{\mathrm{SWDFM}}}\right)\exp(-1.3T)\right] \cdot \exp\left[k_{\mathrm{SWDFM}}\left(|\xi| - 1\right)\right] d\varepsilon_{\mathrm{p}} \tag{2-22}$$

where C_{SWDFM}, β_{SWDFM} and k_{SWDFM} are free parameters.

In addition to fracture models using VGEF to describe the stress triaxiality effect, other fracture initiation models have been proposed , which describe the effect of stress triaxiality using other functional forms [16-20] or simply neglect the stress triaxiality effect for stress states with low stress triaxiality [21]. Lou and Huh [16-17] analysed the damage accumulation induced by nucleation, growth, and shear coalescence of voids and developed a shear-controlled ductile fracture model (LHM) with the stress triaxiality and Lode parameter as variables in the form of,

$$D=\frac{1}{C_3}\int\left(\frac{2}{\sqrt{L^2+3}}\right)^{C_1}\left(\frac{\langle 1+3T\rangle}{2}\right)^{C_2} d\varepsilon_p \quad \text{with} \quad \langle x\rangle=\begin{cases} x, & \text{when } x\geq 0 \\ 0, & \text{when } x<0 \end{cases} \tag{2-23}$$

where L is the Lode parameter, which is related to the Lode angle parameter ξ through Eq. (2-11), and C_1 to C_3 are free parameters.

Despite numerous fracture models considering the effect of Lode angle, its effect on fracture strains is still not fully understood. These fracture models are primarily based on numerical observations. Moreover, in most of the experimental studies, the effect of the Lode angle was generally not isolated, since the analyses are based on experimental results of specimens featuring both different Lode angles and different stress triaxialities. Therefore, it is necessary to conduct experimental investigation of the Lode angle effect using the test results of specimens under stress states with identical stress triaxiality to eliminate the stress triaxiality effect.

2.2.4 Specimen types for fracture tests

To evaluate the fracture strain of ductile metals under varying stress states, experiments have previously been conducted on various types of specimens for different stress states [10,14,22-23]. The most common specimen types for fracture analysis are smooth and notched round bars [10], as shown in Fig. 2-2(a). These specimens generally generate a tensile axisymmetric stress state with high T and ξ=1 in the first quadrant in Fig. 2-1. Bridgman [24] tested smooth round bars under longitudinal tensile loading in a high-pressure chamber, where the circumferential pressure generated the equi-biaxial compression stress states with medium or low stress triaxiality states with ξ=1 in the fourth quadrant in Fig. 2-1.

Another widely used specimen type is grooved plates [25], as shown in Fig. 2-2(b), which represents the plane strain stress state with high T and ξ=0 in the first quadrant in Fig. 2-1. Note that there is a lack of test data set that covers the continuous range of stress triaxiality from low to high stress triaxiality regimes with ξ=0. One exception is the double notched specimens in

[26], which generate stress states with stress triaxiality ranging between -0.24 and 0.64, but the stress triaxiality of 0.64 is apparently not high enough for the effect of high stress triaxiality to be reflected. Inclined notched specimens [27], as shown in Fig. 2-2(c), are also tested under longitudinal loading at both ends for stress states in the first quadrant in Fig. 2-1. By changing the inclining angle from 0 to 90 degree, the loading condition in the central area changes from pure shear, combined tension and shear, to uniaxial tension and the stress states with positive T and ξ ranging from 0 to 1 can be generated. The equi-biaxial tension state with positive T and ξ = -1 in the second quadrant in Fig. 2-1 can be tested using the disk specimen [28], punch specimen [29], and Nakajima specimen [30], as shown in Fig. 2-2(d). For the stress states in the third quadrant in Fig. 2-1, Bai et al. [27] conducted compression tests on short cylindrical specimens and large diameter round bars with notches in the middle, as shown in Fig. 2-2(e), to generate the compressive axisymmetric stress state.

It is noticed that there are limited specimen types available for stress states with constant stress triaxiality. One of the rare exceptions is the study by Smith et al. [14], where a series of rectangular notched specimens were designed to generate a series of stress states with the Lode angle parameter (ξ) ranging from 0 to 1, while the stress triaxiality (T) was approximately constant, equal to about 1.1, as shown in Fig. 2-2(f). While these tests provide valuable experimental data to isolate the effect of the Lode angle, they only cover a narrow range of stress states, i.e. $T \approx 1.1$ and $0 \leq \xi \leq 1.0$. Therefore, additional data are required to evaluate the Lode angle effect over a wider space of stress states, particularly the range of moderate stress triaxialities where the Lode angle effect is more pronounced [6].

To provide experimental data for the stress states with limited data available, two new specimen types were designed and introduced in Sections 3.2.1 and 3.3.1. Together with results collected from the literature, the effects of stress triaxiality and Lode angle are investigated and a new fracture model is proposed in Section 3.4.

(a) Smooth and notched round bars [10]

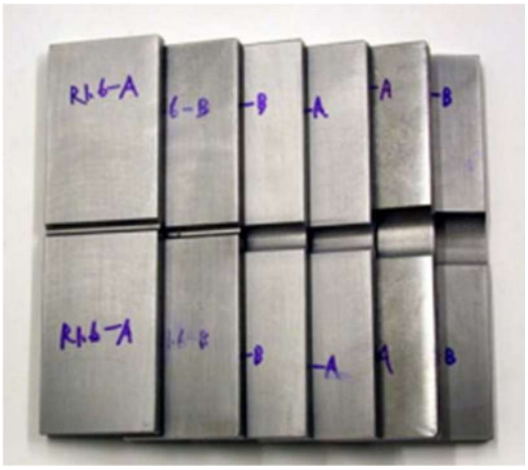

(b) Grooved plates [25]

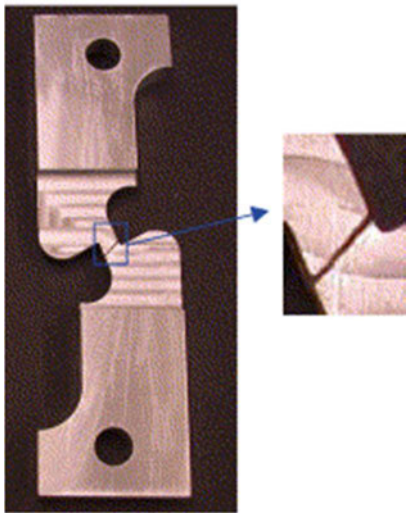

(c) Inclined notched specimen [27]

(d) Disk specimen [28]

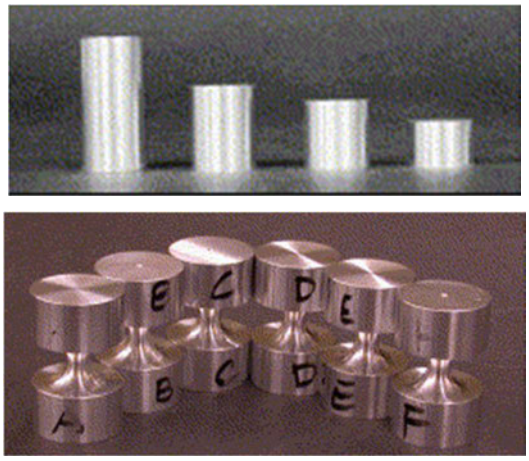

(e) Compression cylindrical specimens [27]

(f) Rectangular notched specimen [14]

Figure 2-2. Widely used specimen types for fracture under various stress states.

2.3 Measurement of weld-zone mechanical properties and WRS

2.3.1 Characterization of weld zone

Welding is one of the most common methods in civil engineering for connecting steel components for its high manufacturing speed, flexibility and reliability with low costs [31]. However, welding is a complex metallurgical process. In a welded connection, the steel components are connected by melting and fusing of the weld material and a portion of base metal. During this process, the high temperature and different cooling rates lead to locally different microstructures, inhomogeneous properties and residual stresses in the weld zone, which can then be divided into three material areas, base metal, weld and heat affected zone (HAZ). To investigate the heterogeneous properties in the weld zone, the first step is to characterize the areas of weld, HAZ and base metal. In previous research [32-34], microstructure observation and hardness tests are common methods to determine the shapes and distributions of weld and HAZ.

To identify the weld, HAZ and base metal by observing the microstructure in the weld zone, specimens are normally cut perpendicular to the weld, and the cross-sections are subsequently polished and chemically etched. The fusion line and the line between HAZ and base metal can then be observed, as shown in Fig. 2-3 [35]. The distinct features in the weld zone become visible, including geometries of weld and HAZ, and multiple weld passes. Fig. 2-4 presents the SEM images of the microstructure of the base metal, weld and HAZ in a welded steel connection [33]. The base metal consists of martensite and ferrite dual phases (Fig. 2.4(a)), while weld mainly exhibits martensite (Fig. 2.4(b)). It is observed that the microstructure in HAZ is inconsistent, and this material area can be divided into two parts: HAZ near weld that mainly consists of martensite (Fig. 2.4(c)), and HAZ near base metal where is dual phases of martensite and ferrite (Fig. 2.4(d)). The difference of microstructure in the weld zone can be explained by different peak heating temperatures and cooling rates during the welding process [36]. The weld is heated to melting at the highest peak temperature and then is cooled down at the highest cooling rate, which forms a full martensite microstructure in the weld. In the HAZ, the material is partially heated to melting with a lower peak temperature followed by rapid cooling, which forms the martensite microstructure in the part near the weld and remains the dual phases in the part near the base metal. In the case of welding with multiple running passes, the weld zone experiences several cycles of heating and cooling, which will lead to a more complex microstructural distribution and property distribution, especially in the HAZ.

In addition to the discussion of the microstructure in the weld zone, Fig. 2-5 shows a grid of Vickers indents across the weld zone and the corresponding hardness map of a butt weld [37]. The highest hardness is observed in the weld because of the martensite microstructure, which has higher hardness and strength than the ferrite microstructure. As discussed, different parts in the HAZ experience different heat treatments during the heating and cooling cycles, resulting in various microstructures, which lead to inconsistent hardness distributions in the HAZ. The material heterogeneity of the weld zone is further verified by this hardness map, and therefore, it is necessary to determine and consider the inhomogeneous mechanical properties in the weld zone for accurate understanding and simulation of welded connections.

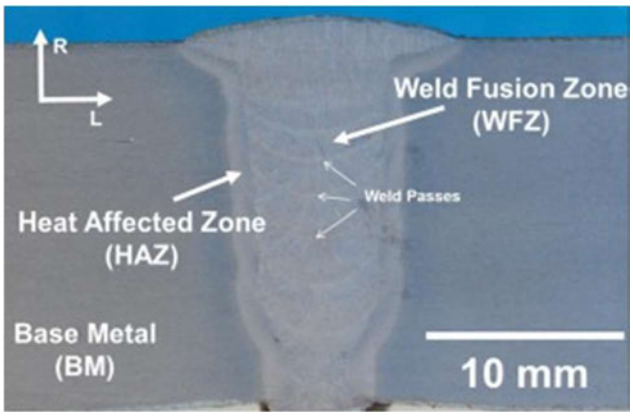

Figure 2-3. Macroetched image of a butt weld [35].

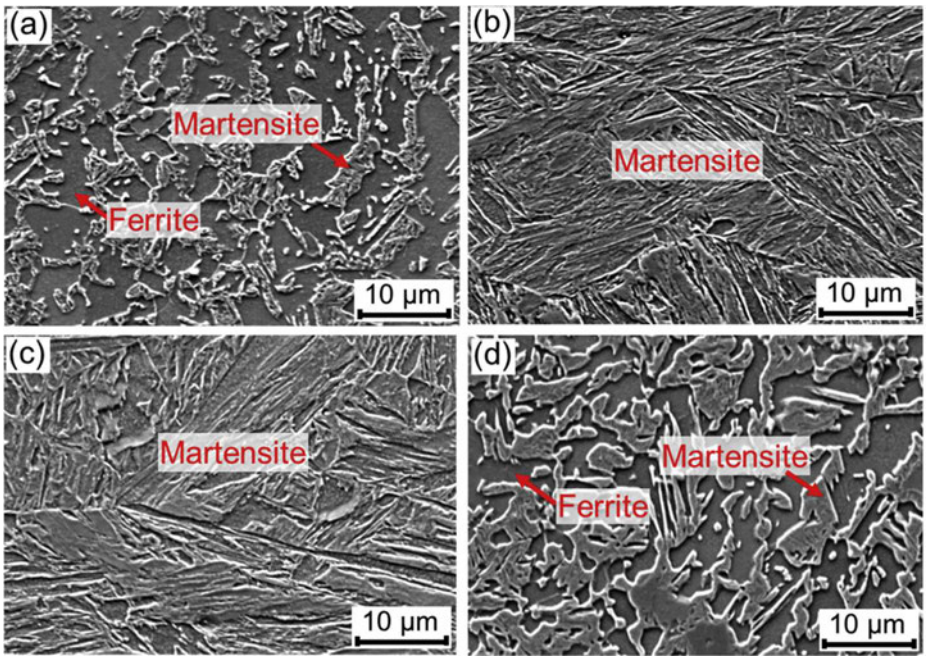

Figure 2-4. Microstructure of (a) base metal; (b) weld; (c) HAZ near weld; (d) HAZ near base metal [33].

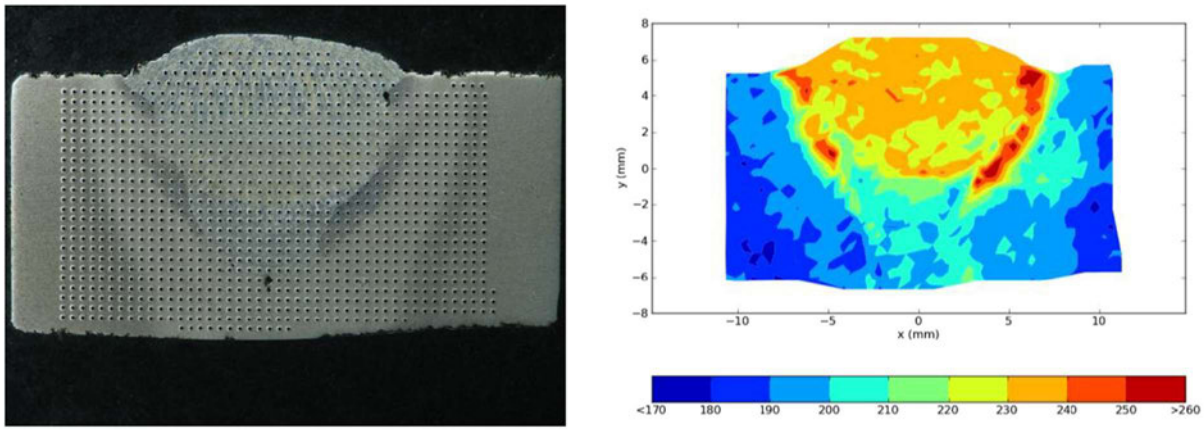

Figure 2-5. Vickers hardness map of a butt weld [37].

2.3.2 Stress-strain relationships of weld and HAZ

Through tests of coupons, the strengths and stress-strain curves of metals (i.e.,) can be easily obtained. The conventional method to obtain the properties of the weld zone in welded connections is to conduct tensile tests on standard specimens [38-39]. As shown in Fig. 2-6, the standard specimens are extracted from the weld or HAZ of welded connections, but conventional coupons are in the scale of the centimetre, which is obviously too large for the tests of HAZ, the width of which is normally around 2 to 5 mm [31]. Therefore, it is difficult to ensure the parallel part of the coupon consists of only the material in the HAZ and get reliable properties of the HAZ. In addition, for many practical welded connections with small or awkwardly located welds, it is not possible to extract standard specimens from weld or HAZ, and the alternative method is to test the specimen extracted from a standard butt-welded plate using the same weld and base metal. However, the obtained properties may not be transferable to the practical connections since the effects of different connection geometries and different heat treatments during the welding process are ignored.

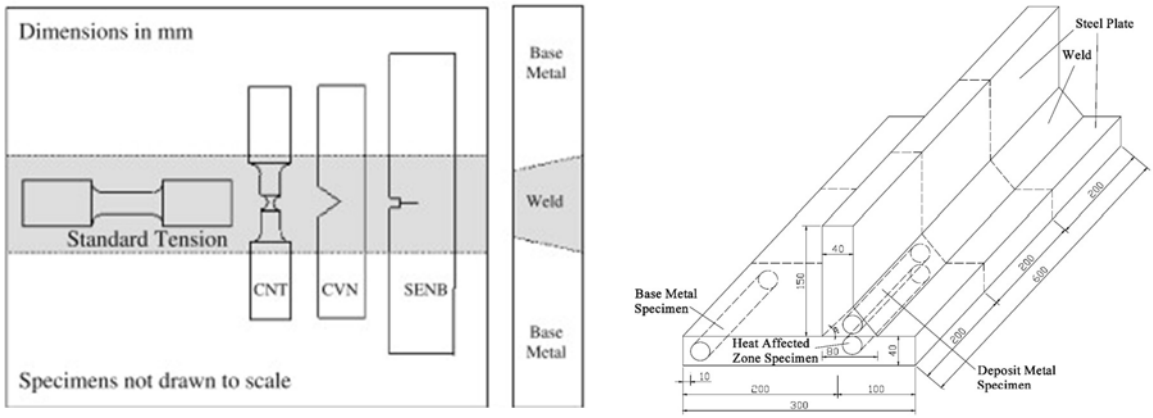

(a) Extraction from a welded plate [38] (b) Extraction from a T-connection [39]

Figure 2-6. Tests on standard specimens.

Recently, three other methods have been used to identify the local properties of weld and HAZ: 1) Perform the Vickers hardness test and then compute the material yield stress and tensile strength through empirical hardness-strength correlation functions [36, 40-43]. Pavlina et al. [40] collected the hardness values and yield and tensile stresses for over 150 steel grades covering a wide range of compositions and microstructures and determined the correlation of the yield and ultimate stresses to the hardness values using regression analysis, as shown in Fig. 2-7. Pham et al. [42] conducted nanoindentation across the weld zone to estimate the mechanical properties of the weld, base metal and HAZ, as shown in Fig. 2-8 and it is concluded that the weld has the highest elastic modulus and hardness and the base metal has the lowest values, while the properties in the HAZ gradually decrease from the weld part to the base metal part. Among these investigation methods, the hardness-strength correlation method has a relatively simple test process, but its accuracy highly depends on the precision of the correlation functions, which also change between materials.

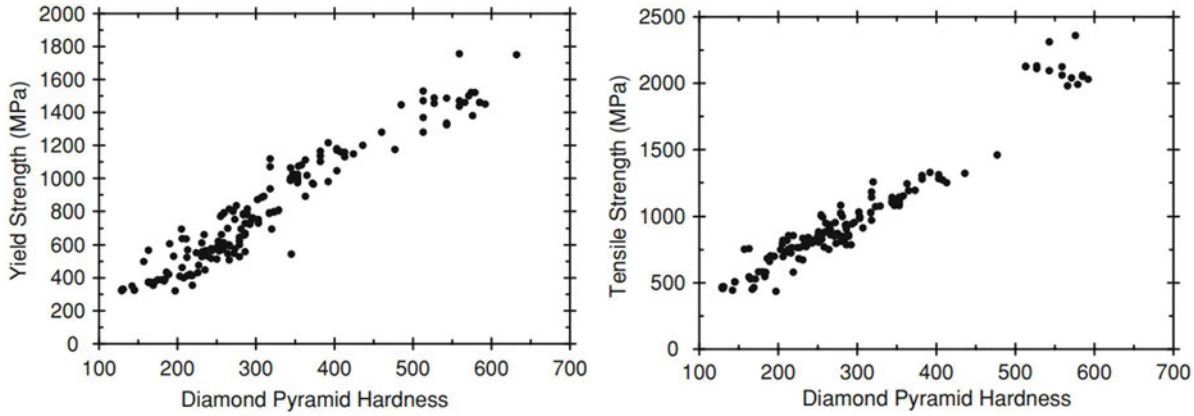

(a) Plot of yield stress and hardness (b) Plot of tensile stress and hardness

Figure 2-7. Linear correlation between strength and hardness [40].

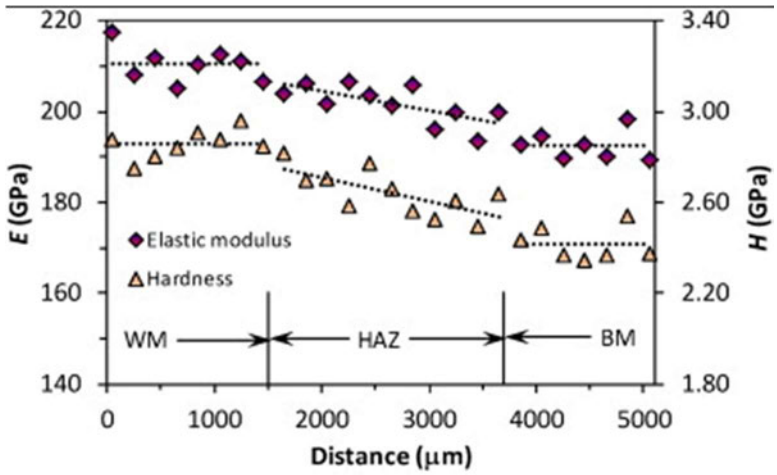

Figure 2-8. Distribution of elastic modulus and hardness across the weld zone [42].

2) Extract miniature coupons with the cross-sectional dimension of the millimetre from the weld and HAZ, and perform tests on the miniature coupons [33, 44-49]. Due to the small and irregular shapes of weld and HAZ, miniature coupons are designed and extracted from the three material areas to directly measure their material properties, as shown in Fig. 2-9. To support these miniature coupons, a pair of grippers need to be made and fixed in a special test frame with the digital image correlation (DIC) system to measure the local deformation within a small gauge length, as shown in Fig. 2-10. Among all the measurement methods, the greatest advantage of the miniature tensile test method is that the properties of weld and HAZ can be directly obtained, but the manufacture of miniature coupons is difficult, and special testing frames are required resulting in a complex fabrication and testing process.

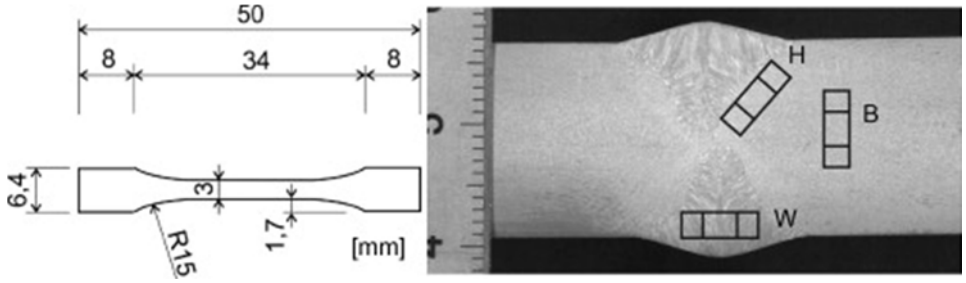

Figure 2-9. Geometry and dimensions of miniature tensile test specimen [48].

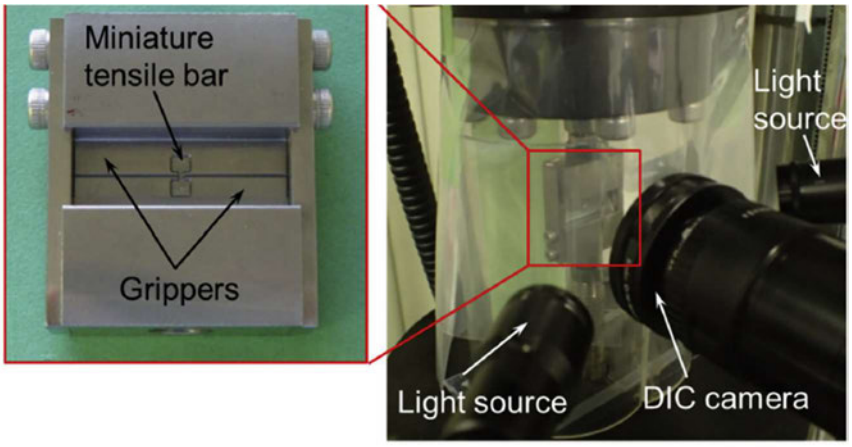

Figure 2-10. Test frame for miniature tensile tests [33].

3) With the help of the DIC system, the material properties can be measured based on the strain distribution in the welded area [50-55]. Reynolds and Duvall [50] first introduced the method of determining the properties of the weld, HAZ and base metal using DIC. In this method, tensile tests are conducted on transverse weld samples, as shown in Fig. 2-11, and the strain fields over the loading process are captured by DIC, as shown in Fig. 2-12. After calculating the local stress using the iso-stress assumption [50] or using the virtual field method [51], the stress-strain relationships of the three material areas can be obtained. In this method, the

difference in properties between the longitudinal and transverse directions is ignored. Since only the surface strain can be obtained using DIC, it is assumed that the strain distribution is the same through the thickness, so this method is less accurate for bulk material.

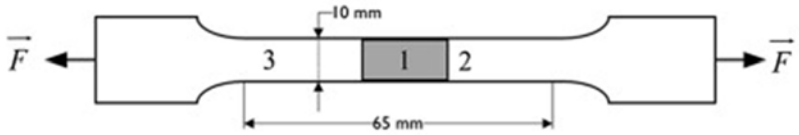

Figure 2-11. A transverse weld sample (1-weld, 2-HAZ, 3-base metal) [52].

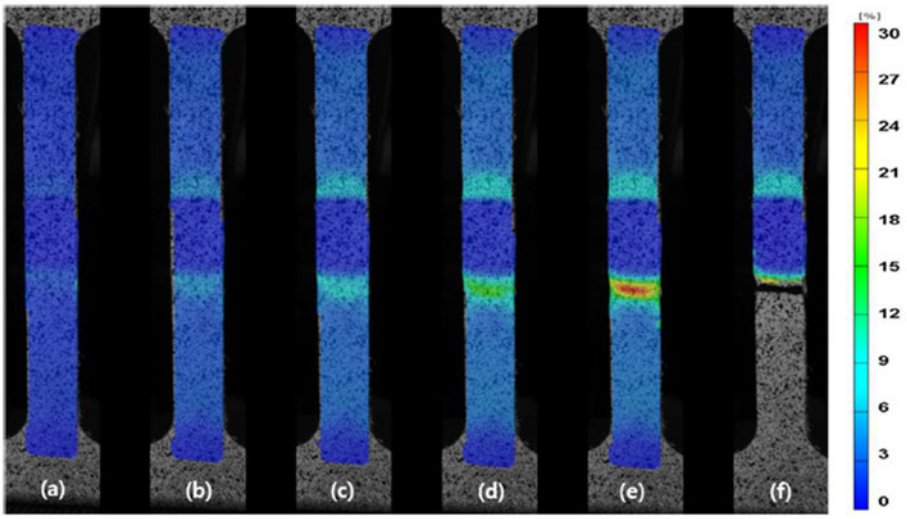

Figure 2-12. Strain maps measured by DIC during the loading process [53].

2.3.3 Fracture strains of weld and HAZ

A great number of coupon tests have also been conducted to evaluate the fracture strains of base metal, weld and HAZ materials. Similar to the measurement of stress-strain relationships over the weld zone, the conventional method is conducting tensile tests on normal-size specimens [38-39, 56-57]. As introduced in Section 2.2.4, the fracture strain of a ductile metal is notably affected by the stress state the material is subjected to, so the coupons are designed with various geometries to generate different stress states, e.g., notched round bars for axisymmetric tri-axial tension states and grooved plates for plane strain tri-axial tension states, as shown in Fig. 2-13. However, as stated in Section 2.3.2, the normal-size coupons are always too large for the weld and HAZ areas, and it is difficult to extract normal-size coupons from practical weld connections. In addition, the difference in properties between the longitudinal and transverse directions cannot be determined using normal-size specimens.

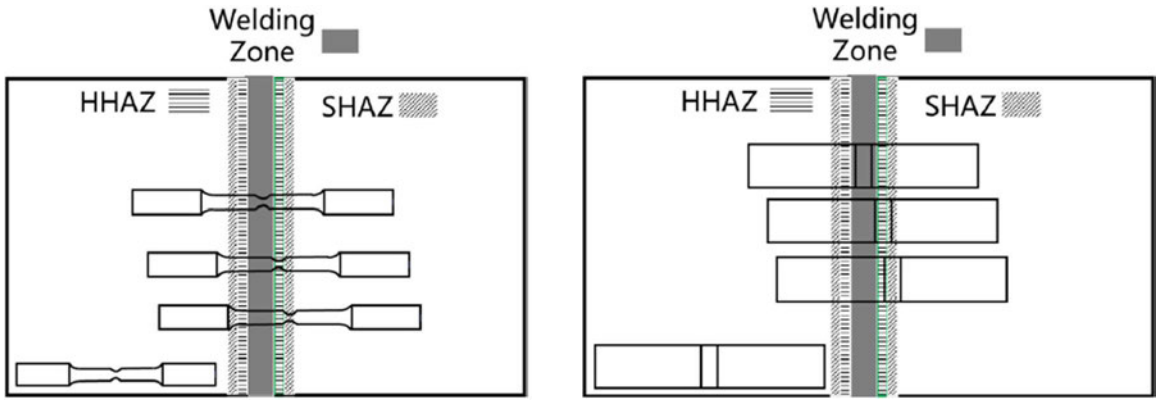

(a) Notched round bars (b) Grooved plates

Figure 2-13. Normal size specimens for fracture strains of weld, HAZ and base metal [57].

Tests on specially designed miniature coupons for various stress states are thus preferred to investigate the fracture strains of small-scale materials. Mae et al. [58] tested mini-notched and unnotched bars and mini-flat butterfly coupons to characterise the fracture properties of a cast aluminium alloy, as shown in Fig. 2-14. Gorji et al. [59] conducted experiments on aluminium alloy 6016-T4 using miniature uniaxial tension coupons, notched tension coupons, central hole coupons and smiley shear coupons, as shown in Fig. 2-15. Miniature coupon tests for various stress states were also conducted on welded connections. Pandya et al. [60] developed a micro-tensile testing technique to characterise the fracture strains of weld and HAZ materials in a resistance spot weld of dual-phase steel sheets, as shown in Fig. 2-16. Despite the many methods and studies summarised above, limited experimental data is available for structural steel weld and HAZ materials, and the differences in the fracture strains between the longitudinal and transverse directions are hardly discussed.

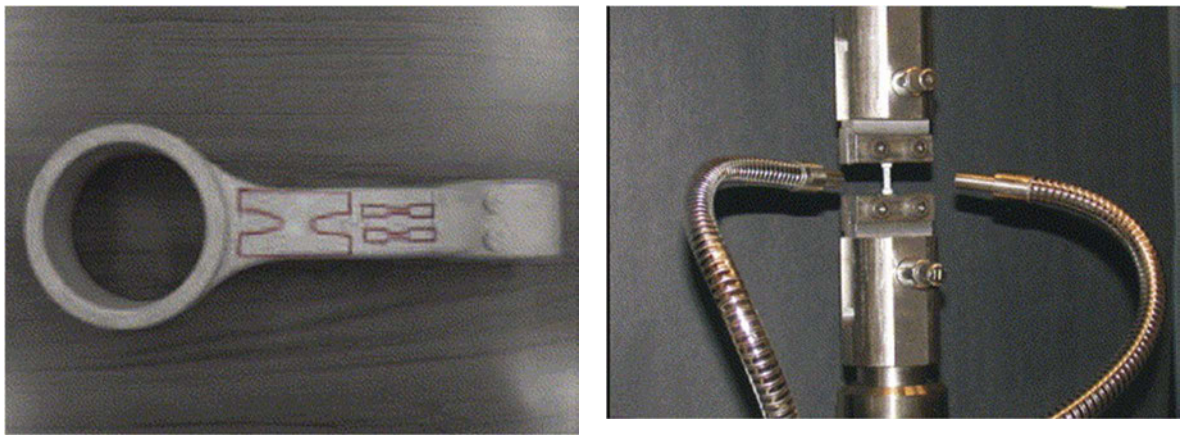

(a) Specimen preparation (b) Test setup for miniature round bars

Figure 2-14. Miniature coupon tests on a cast aluminium component [58].

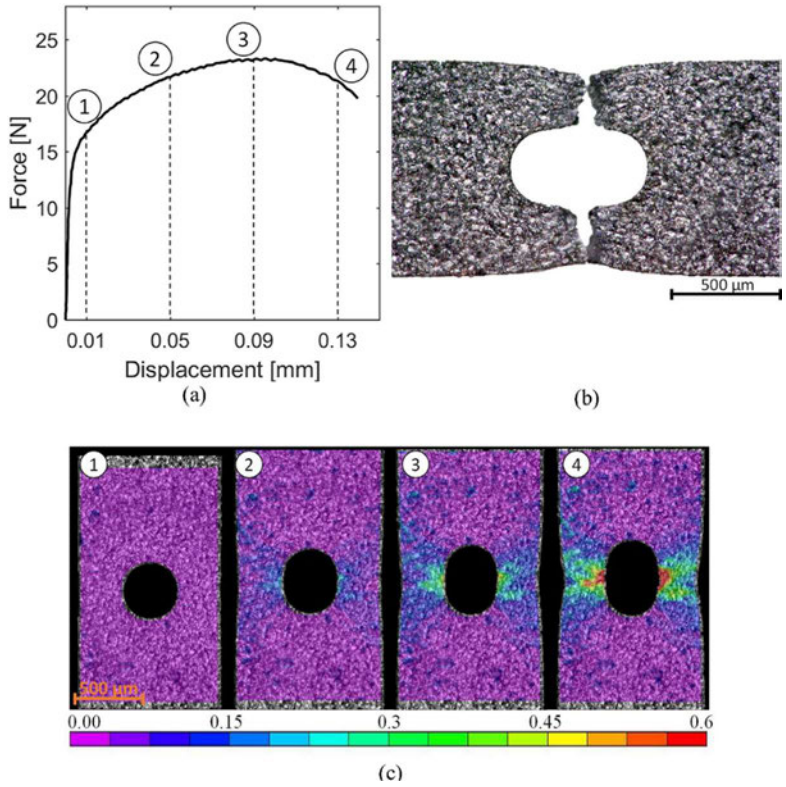

Figure 2-15. Experimental results of miniature central hole coupons: (a) Force-displacement curve, (b) top view of fracture specimen, (c) evolution of the surface strain field [59].

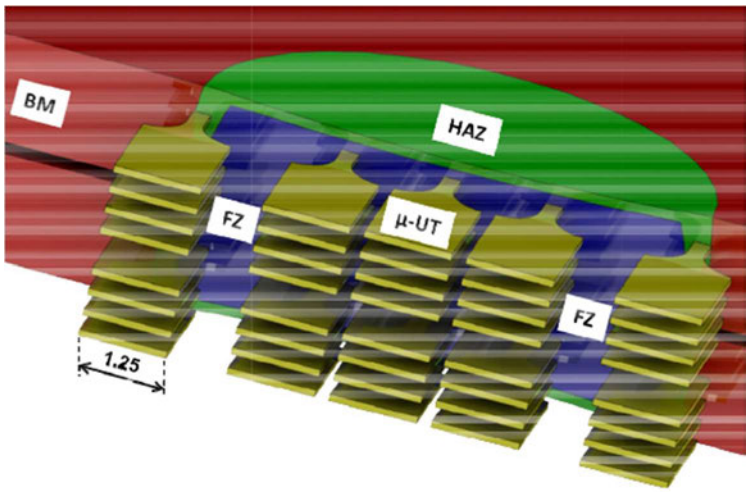

Figure 2-16. Location of miniature tensile coupons extracted from the weld and HAZ [60].

2.3.4 Weld residual stresses

Weld residual stresses are the internal stresses in a welded connection which are in equilibrium with the surroundings [61-62]. The heating and cooling in the welding process lead to a non-uniform temperature distribution and differential contractions within the weld zone, and residual stresses are formed by the constraint of the weld contraction by the surrounding base metal when the weld solidifies [63]. For a single-pass butt weld, the typical distributions of the

residual stresses in the longitudinal and transverse directions are shown in Fig. 2-17. Residual stresses can overlap or offset the service-induced stresses and then be detrimental or beneficial. Therefore, it is necessary to conduct experimental measurements to quantitatively investigate the magnitude and distribution of weld residual stresses.

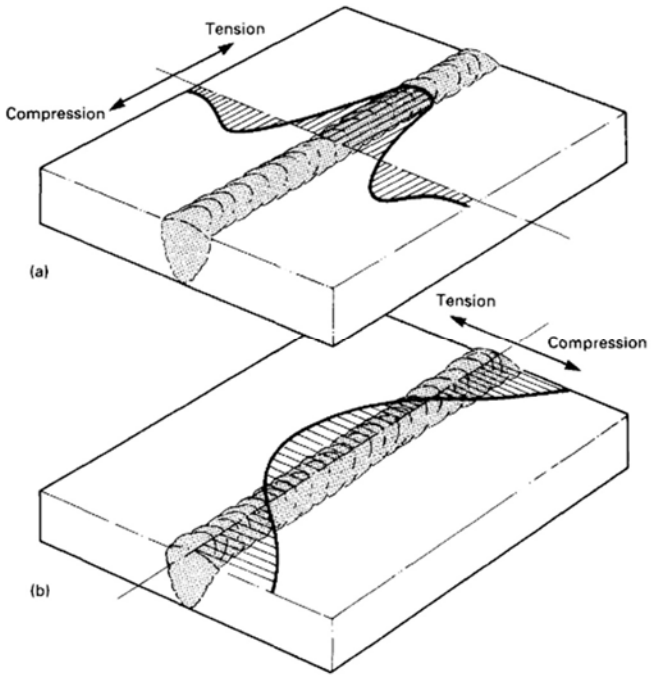

Figure 2-17. Distribution of residual stresses (a) longitudinal; (b) transverse [64].

Various measurement methods have been used to evaluate the weld residual stresses, including destructive methods [61, 65], such as slitting [66-68] and hole drilling [69-73], and non-destructive methods, such as X-ray diffraction [75-77] and neutron diffraction [78-81]. The slitting method is a mechanical relaxation technique and is well suited for through thickness measurement [67], in which a planar slit is cut from the component and the residual stress is calculated from the deformation near the slit due to stress release, as shown in Fig. 2-18(a). Hole drilling method is another destructive method, in which the residual stress is determined based on the redistributed strain field formed by drilling a hole through the centre of a strain gauge rosette, as shown in Fig. 2-18(b). In these destructive methods, the accuracy of the measurement highly depends on the gauge volume, which is the size of the cut strip, and the relatively large gauge volume leads to a coarse stress gradient [74], as shown in Fig. 2-19. In the non-destructive methods such as diffraction techniques, the lattice spacing is used as the gauge volume, which can provide more information and increase the measurement accuracy. The X-ray diffraction method [75-77] is suitable for surface measurement, in which normal stress is normally assumed to be zero, and the in-plane residual stresses are determined by

measuring lattice spacing under various angles [61]. Compared to X-ray diffraction, the neutron diffraction method has a similar measurement technology but with better penetration because neutrons interact with nuclei while X-ray interacts with electrons [63]. Therefore, the neutron diffraction method is outstanding in providing high-resolution results in small gauge volumes and under various thicknesses, and it has been widely used to investigate the magnitude and distribution of weld residual stresses in three directions [78-81].

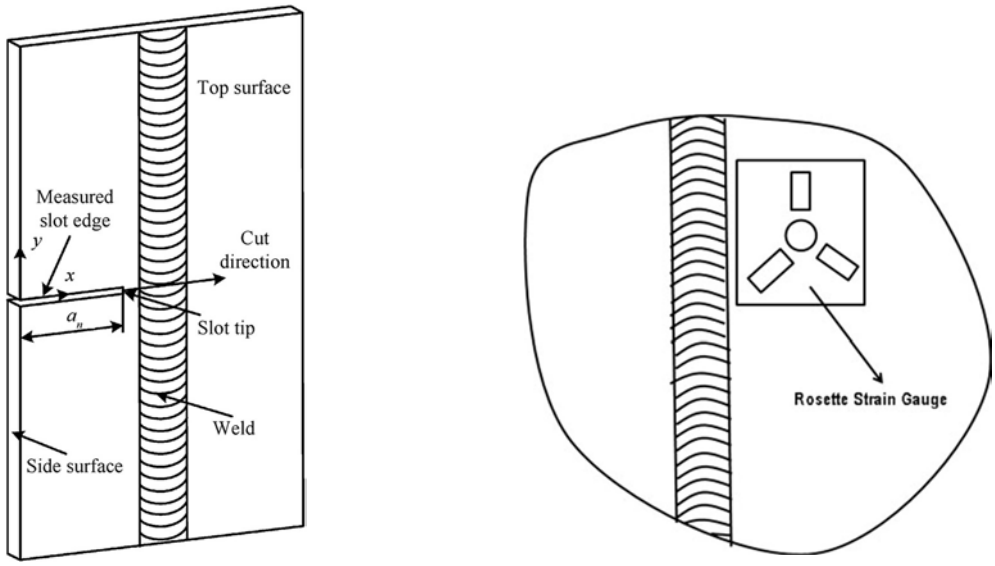

(a) Slitting method [68] (b) Hole-drilling method [70]

Figure 2-18. Destructive methods of residual stress measurement.

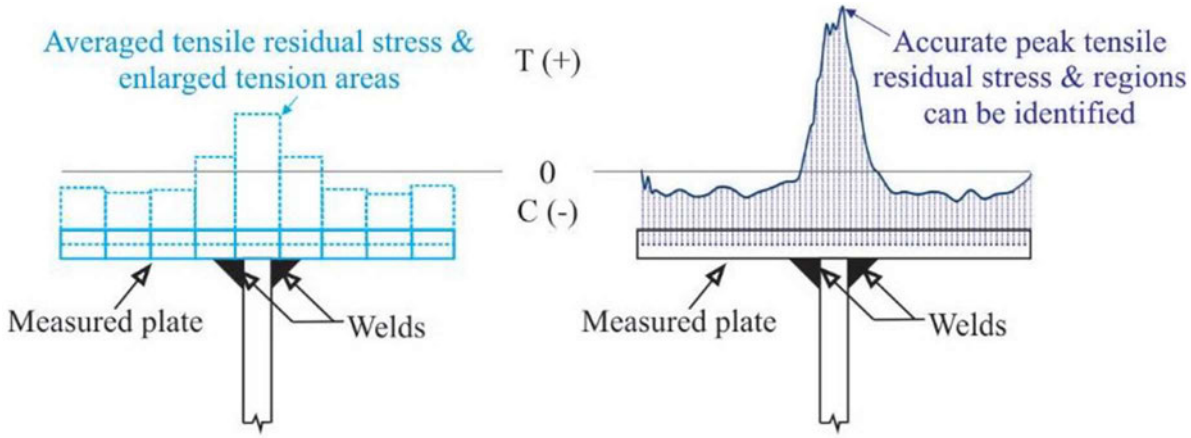

(a) Destructive method (b) Non-destructive methods

Figure 2-19. Comparison between destructive and non-destructive methods [74].

2.4 Investigation of fracture in welded connections

2.4.1 Experimental investigation

Fracture of welded connections is one of the primary failure modes in steel structures, and numerous experimental investigations have been carried out on simple specimens or large-

scale welded connections to study their failure mode and fracture behaviour. The photos of fractured simple specimens, such as T-stubs [82-83], local welded specimens [84], lap-welded specimens [85], and welded cruciform specimens [86-87], and the photos of fractured large-scale welded connections, such as welded CHS-RHS joints [90], square column and H-beam joints [91], RHS-to-RHS T-connections [92], and end-plate connections [93], are summarized in Figs. 2-20 and 2-21, respectively. It is observed that fracture always occurs in the weld area or HAZ area within the weld zone of the weld connection with large-scale plastic deformation, and it is indicated that the determination of the weld-zone mechanical properties is critical to the investigation of the fracture performance of welded connections.

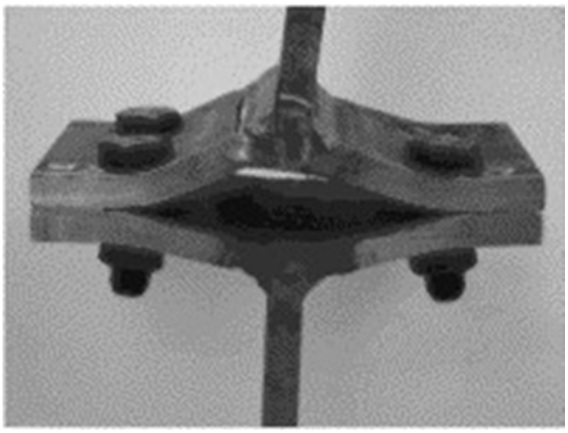

(a) T-stub [82]

(b) Local welded connection [84]

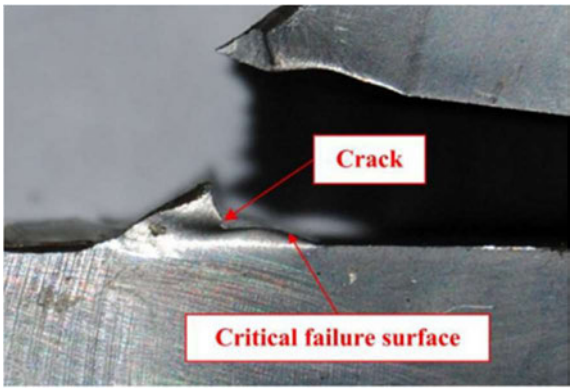

(c) Lap-welded specimen [85]

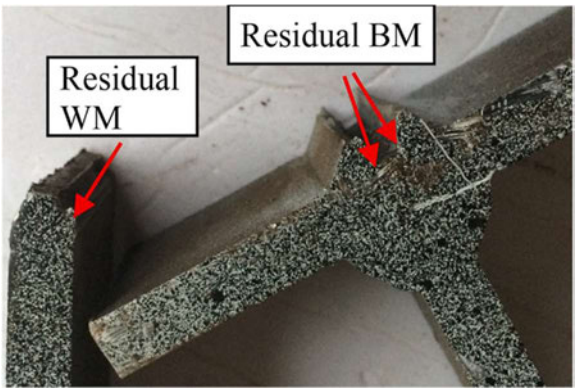

(d) Welded cruciform specimen [87]

Figure 2-20. Tests of fracture in simple welded specimens.

(a) Welded CHS-RHS joint [90]

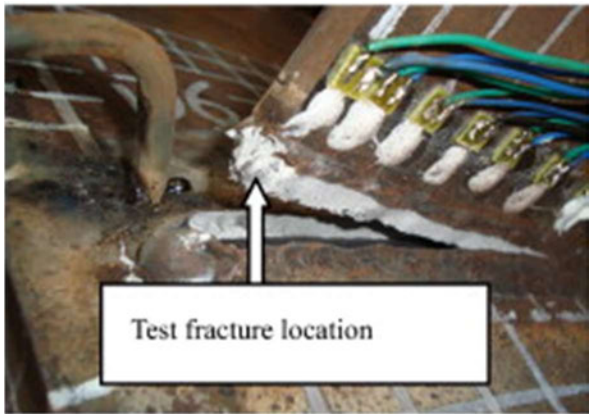

(b) Square column and H-beam joint [91]

(c) RHS-to-RHS T-connections [92]

(d) End-plate connections [93]

(e) H-section connections [94]

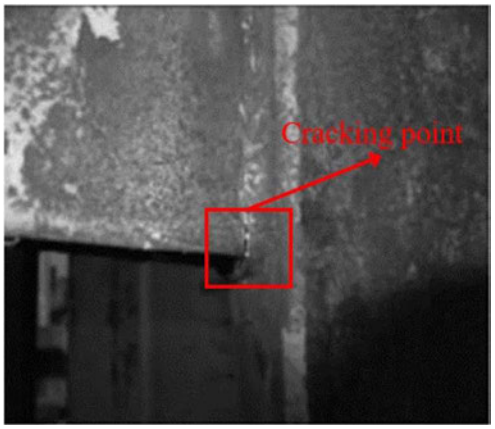

(f) Square tube connections [95]

Figure 2-21. Tests of fracture in large-scale welded connections.

2.4.2 Numerical investigation

Various fracture prediction models were adopted to simulate the fracture initiation of welded connections, including the CTOD method [98], the J-integral method [97], VGM [91], SMCS [99] and the Hosford-Coulomb model [94]. As explained in Section 2.3, the mechanical properties in the weld zone are inhomogeneous, but in the analysis or finite-element (FE)

simulations of welded connections, the properties of the weld and HAZ are normally assumed to be the same as those of the base metal [84, 88, 94, 96-97]. This simplified assumption is due to the lack of experimental data related to mechanical properties of the weld and HAZ areas and may lead to inaccurate prediction of the performance of welded connections.

Recent studies have started to measure the mechanical properties of the weld and include them in the numerical simulation of welded connections. Shi et al. [85] conducted tensile tests on a series of lap-welded joints, and it was observed that the fracture always initiated from the weld root and propagated through the weld area. Coupon tests were carried out on rectangular specimens and smooth and notched round bars extracted from the weld, as shown in Fig. 2-22(a), to obtain the fracture strains and calibrate the fracture parameters of VGM and Stress Modified Critical Strain Model (SMCS). The fracture strains of two weld materials (ER55-G and ER55-D2) were compared, and it was concluded that the weld material with higher yield stress (ER55-D2) showed lower ductility. The fracture process of lap-welded joints was simulated, as shown in Fig. 2-22(b), and predicted using the two fracture models, and VGM provided better predictive results.

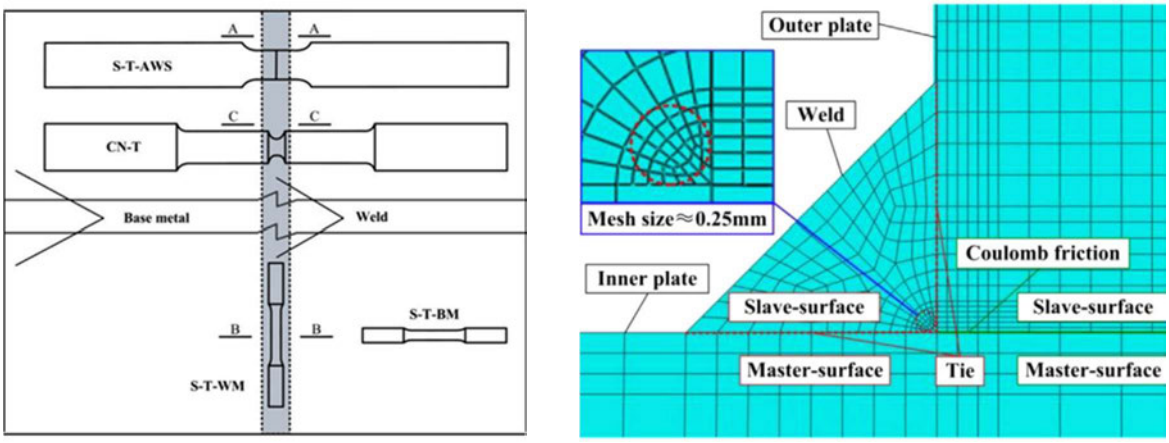

(a) Coupons for various stress states (b) Distribution of weld and base metal

Figure 2-22. Fracture simulation of lap- welded connections [85].

Ran et al. [89] conducted tensile tests on lap-welded connections and cruciform welded connections, and it was observed that fracture occurs in the weld zone for both specimen types and the fracture was more likely to be located near the fusion line in the cruciform specimens. To determine the fracture strains of the weld and base metal, the smooth and notched round bars and rectangular notched specimens were extracted from a butt-welded plate, as shown in Fig. 2-23(a), and it was found that weld has lower fracture ductility than the base metal. Finite element modes were established for welded connections using the properties of the weld and

base metal obtained from the coupon tests, where the weld zone was extended 0.5 mm into the base metal and its shape was simplified as rectangular, as shown in Fig. 2-23(b). The fracture process of the welded connection was simulated using the Bai-Wierzbicki model which considered the effects of both stress triaxiality and Lode angle.

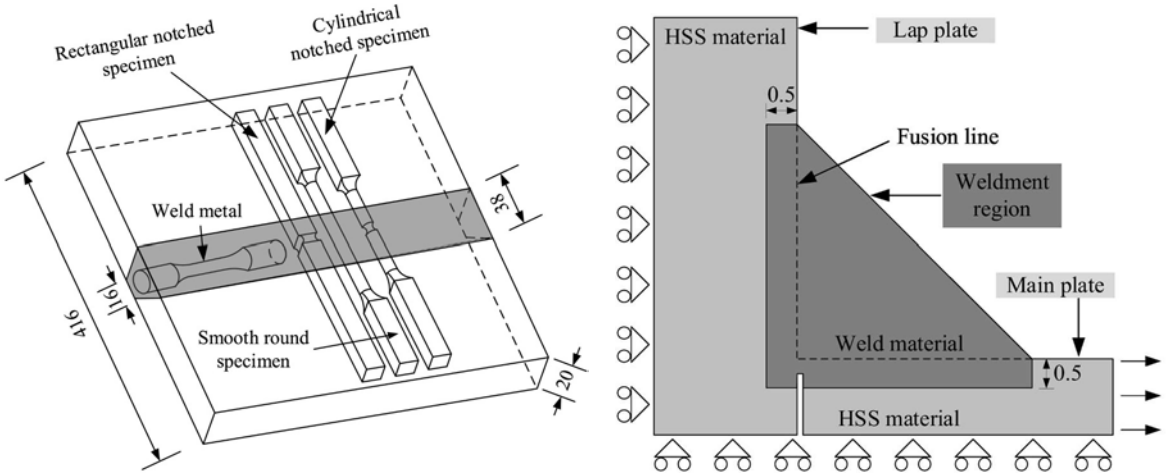

(a) Coupons for various stress states (b) Distribution of weld and base metal

Figure 2-23. Fracture simulation of welded cruciform connections [89].

In these recent research results, although the mechanical properties of the weld area were measured and included in the numerical simulation of welded connections, the mechanical properties of the HAZ area were ignored. In addition, the difference in properties of the weld zone between longitudinal and transverse directions was not considered in the fracture analyses. Therefore, to achieve an overall understanding of the performance of welded connections, it is necessary to conduct a detailed investigation of the mechanical properties of the three material areas in the weld zone in both longitudinal and transverse directions and to include these measurement results in the fracture simulation of welded connections.

2.5 Summary

This chapter introduced previous investigations about the fracture prediction models, the mechanical properties in the weld zone, the weld residual stress and fracture investigation of welded steel connections. As summarized in Section 2.2, experimental and numerical analyses have determined that the stress triaxiality and the Lode angle are the key factors for the fracture of structural steels. Various fracture models have been proposed and used to predict fracture initiation by considering the effects of stress triaxiality and Lode angle. In terms of the stress triaxiality effect, the void growth-based exponential function is the foundation of many models and has been widely used to describe the effect of the stress triaxiality, but its applicability to stress states with low stress triaxiality has rarely been discussed. The Lode angle effect has

been considered in many fracture models based on numerical observations, but its isolated effect has not been investigated using experimental methods. Therefore, it is necessary to discuss the effects of the stress triaxiality and the Lode angle for the whole stress states based on experimental evidence.

Due to locally different microstructures and inhomogeneous properties, the weld zone can be divided into three material areas, the base metal, weld and HAZ. Section 2.3 introduced methods of measuring the mechanical properties of the weld and HAZ, including their stress-strain relationships and fracture strains under various stress states, and weld residual stresses. Among the methods of determining their mechanical properties, the test of miniature coupons is the only method to directly measure the properties of the three material areas in both the longitudinal and transverse directions. Although the mechanical properties of the weld and HAZ have been measured by some previous studies, limited experimental data is available for the weld and HAZ materials used in steel structures, and the difference in the properties between longitudinal and transverse directions has rarely been discussed. Measurement methods of the weld residual stresses were introduced, and the neutron diffraction method is outstanding in providing high-resolution results in small gauge volumes and under various thicknesses. Section 2.4 introduced previous experimental investigation and numerical simulation of fracture in welded connections. It is observed that fracture always occurred in weld zone, and it is indicated that determining the weld-zone mechanical properties is critical for fracture investigation of welded connections. Although the mechanical properties of the weld area have been included in some studies, the properties of the HAZ area were always ignored, and the difference in properties of the weld zone between the longitudinal and transverse directions has hardly been discussed. Therefore, it is necessary to conduct a detailed investigation of the weld-zone mechanical properties and discuss their effects on the performance of the welded connections.

Chapter 3 A new fracture model considering the effects of stress triaxiality and Lode angle

3.1 Introduction

In this chapter, the effects of the stress triaxiality and the Lode angle on fracture strains of structural steels are discussed under a wide range of stress states. Considering that fracture strains are affected by these two parameters, test results with constant values of stress triaxiality or Lode angle parameter were collected from the literature to discuss the isolated effect of each parameter. Two specimen types were designed for stress states with limited test data available, including plane strain specimens for stress states with the Lode angle parameter being 0 and rectangular notched specimens for stress states with stress triaxiality being 0.6.

In Section 3.2, the effect of the stress triaxiality on fracture strains of steels is discussed. In available fracture initiation models, the void growth-based exponential function (VGEF) was widely used to describe the effect of stress triaxiality. Its validity has largely been demonstrated for loading conditions with high stress triaxiality, but it has rarely been validated for situations with medium to low stress triaxialities. To fill this knowledge gap, the dependence of fracture strains on the stress triaxiality over the entire stress triaxiality regime was investigated based on test data collected from published literature and the newly designed plane strain specimens.

In Section 3.3, the effect of the Lode angle is investigated based on experimental data. As mentioned in Section 2, the Lode angle has a significant effect on fracture, but existing studies of the effect of the Lode angle were primarily based on numerical observation. This section aims to discuss the effect of the Lode angle on the fracture strain of steels based on the fracture strains obtained from both the literature and newly designed rectangular notched specimens. It was observed that the influence of the Lode angle could be modelled by an exponential function of the Lode angle parameter.

In Section 3.4, having evaluated the effect of the Lode angle, a new fracture model termed the Lode angle Modified Void Growth Model (LMVGM) is proposed, which can be used to predict the fracture strains of steels as a function of stress triaxiality T and Lode angle parameter, ξ. Section 3.5 summarizes the whole chapter.

3.2 The effect of stress triaxiality

3.2.1 Tests on plane strain specimens

3.2.1.1 Specimen design

The flat grooved specimen (Fig.2-2(b)) and inclined notched specimen (Fig.2-2(c)) with an inclining angle of 0-degree have been widely adopted to generate ξ=0 stress states in the high and medium stress triaxiality regimes, respectively. By combining the features of these two specimen types, a new plane strain specimen type was designed, as shown in Fig. 3-1, to investigate the ε_f -T dependency at more closely spaced stress triaxiality values between 0 and 1.0. To generate the plane strain stress state, the Plane Strain (PS) specimen was designed with the thickness much larger than the in-plane dimension of the central region where the plastic deformation localized.

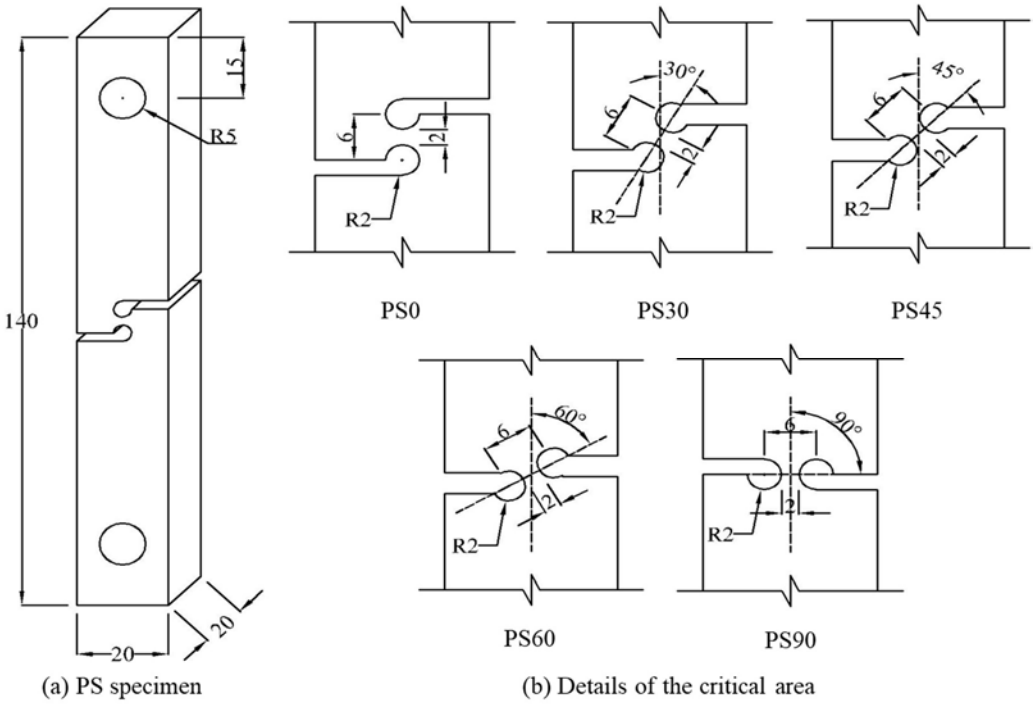

Figure 3-1. Geometry of Plane Strain (PS) specimens.

Similar to the inclined notched specimens, the inclining angle of the central region is changed to generate different stress triaxiality at the central region. As shown in Fig. 3-1, Specimens PS0, PS30, PS45, PS60 and PS90 features inclining angles of 0°, 30°, 45°, 60° and 90° in the centre region, respectively. Ideally, the central region of Specimens PS0 is subjected to pure shear. However, for high ductility materials, the inclining angle of the central region may increase as the specimen deforms and rotates, leading to a stress triaxiality slightly higher than 0. The central region of Specimen PS90 is subjected to a high stress triaxiality, the value of

which depends on the radius of the two cylindrical holes forming the central region. For specimens with inclining angles between 0° and 90°, the central region is subjected to a stress triaxiality between those of the PS0 and PS90 specimens.

3.2.1.2 Stress-strain relationship

Two standard Smooth Round Bar (SRB) coupons, SRB1 and SRB2, were extracted from a 20 mm thick plate of steel grade AS350 [100], the same plate from which the PS specimens were extracted. The SRB geometries are shown in Fig. 3-2, and the coupons were tested in accordance with AS 1391 [101]. The specimen deformations were measured over the 25 mm gauge length using an extensometer located at the centre of the specimen. The loading strain rate was less than 0.006/min before initial yielding, while after yielding the strain rate was increased to about 0.05/min. To obtain the static load-deformation curves, stress relaxation was accommodated by pausing the straining for 100s at numerous intervals during the loading process [102]. Fig. 3-3(a) shows an example of converting the original quasi-static curve with stress relaxation to the static load-deformation curve and Fig. 3-3(b) shows the static load-deformation curves for the two specimens.

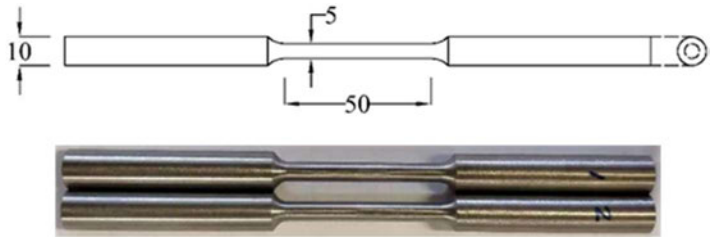

Figure 3-2. Smooth round bars.

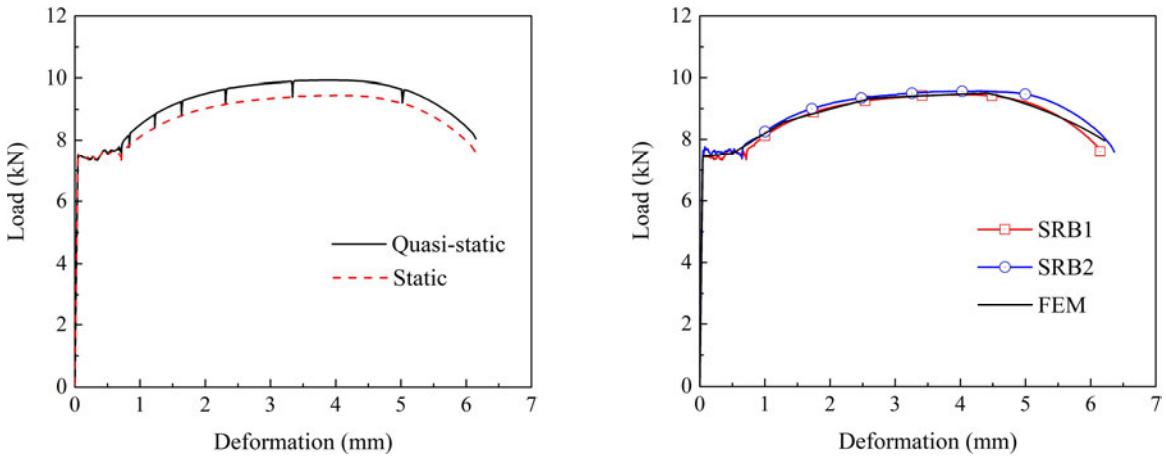

(a) A quasi-static curve with stress relaxation (b) Static load-deformation curves

Figure 3-3. Load-deformation curves of smooth round bars.

The average static values of elastic modulus, yield stress and tensile strength are 206 GPa, 379 MPa and 483 MPa, respectively, and the mechanical properties are summarised in Table 3-1. Prior to the commencement of necking, the true stress and strain (i.e., σ_{true} and ε_{true}) were calculated using the following equations from the engineering stress and strain (i.e., σ_{eng} and ε_{eng}):

$$\varepsilon_{true} = \ln(1 + \varepsilon_{eng}) \tag{3-1}$$

$$\sigma_{true} = \sigma_{nom}\left(1 + \varepsilon_{eng}\right). \tag{3-2}$$

A linear post-necking true stress-strain relationship was assumed, as pre [103], and several trial-and-error finite element analyses were performed, the results of which were compared with the coupon test results to determine the appropriate post-necking strain hardening modulus, as shown in Fig. 3-3(b). The stress-strain curve obtained is shown in Fig. 3-4.

Table 3-1. Mechanical properties (static).

Specimen	Elastic modulus E (GPa)	Yield stress σ_y (MPa)	Tensile strength σ_u (MPa)
SRB1	202	378	480
SRB2	210	380	487
Average	206	379	483

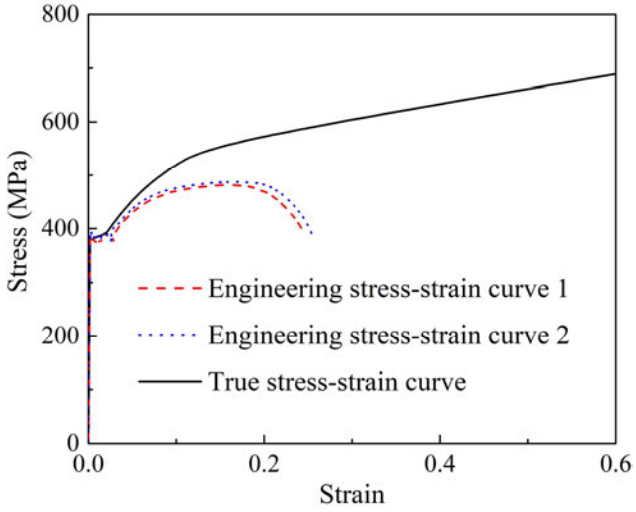

Figure 3-4. True stress-plastic strain curve.

3.2.1.3 Experimental investigation

For each of the five types of plane strain (PS) tensile coupons shown in Fig. 3-1, three replicated tests were performed, as shown in Fig. 3-5. The initial thickness, t_{ini}, and the initial width of the central region, w_{ini}, were measured for each specimen, as summarised in Table 3-2. The

deformation of the specimen was also measured using the 25mm gauge length extensometer. The loading rates were adjusted (between 0.1 mm/min and 0.3 mm/min) for the strain rate being about 0.01/min before initial yielding and 0.1/min after yielding commenced. The technique of stress relaxation was also adopted to obtain the static response of the specimens. For all specimens, the plastic deformation was highly localized at the central region, and fracture occurred in this region, as shown in Fig. 3-5(b). As mentioned in Section 3.2.1.1, although designed to generate a pure shear stress state, the PS0 specimen experienced a combined shear and tension stress state at the later loading stage due to the deformation and rotation of the central region. Hence, in addition to the PS specimens, three nominally identical Inclined Notched specimen with an inclining angle of 0-degree (IN0) were also tested, as shown in Fig. 3-6, to provide additional data for the pure shear condition.

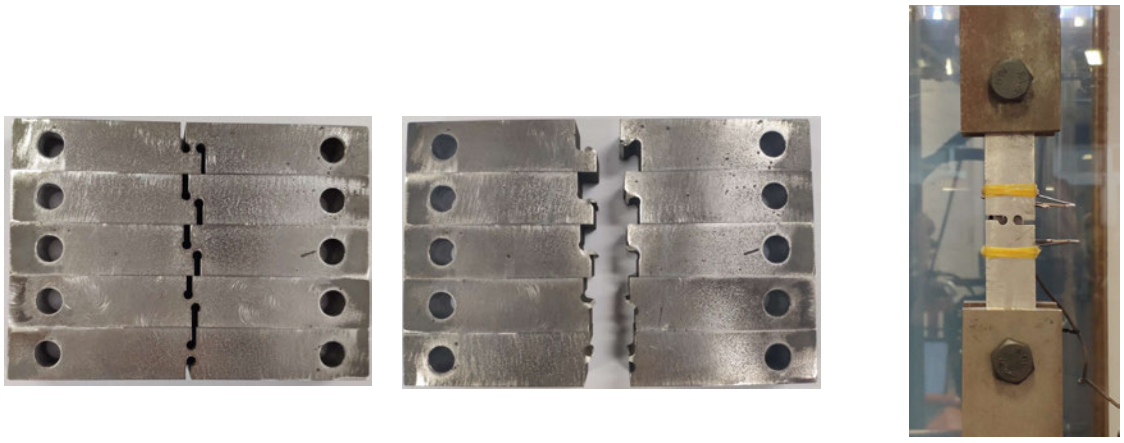

(a) Unfractured specimens (b) Fractured specimens (c) Test setup

Figure 3-5. Plane strain (PS) specimens.

Table 3-2. Dimensions and fracture deformations of PS and IN0 specimens.

Specimen	t_{ini} (mm)	w_{ini} (mm)	D_f (mm)	Specimen	t_{ini} (mm)	w_{ini} (mm)	D_f (mm)
IN0-1	4.00	4.07	3.92	PS45-1	19.69	2.04	1.94
IN0-2	4.00	4.06	3.69	PS45-2	19.68	2.03	2.09
IN0-3	4.01	4.06	3.89	PS45-3	19.73	2.03	2.07
IN0-Avg	4.00	4.06	3.83	PS45-Avg	19.70	2.03	2.00
PS0-1	19.71	2.05	3.21	PS60-1	19.73	2.07	1.19
PS0-2	19.72	2.07	3.31	PS60-2	19.72	2.06	1.18
PS0-3	19.72	2.07	3.27	PS60-3	19.72	2.06	1.11
PS0-Avg	19.72	2.06	3.26	PS60-Avg	19.72	2.06	1.16

PS30-1	19.70	2.07	2.70	PS90-1	19.70	2.05	0.31
PS30-2	19.69	2.08	2.53	PS90-2	19.72	2.01	0.30
PS30-3	19.77	2.08	2.52	PS90-3	19.70	2.02	0.28
PS30-Avg	19.72	2.08	2.58	PS90-Avg	19.71	2.03	0.30

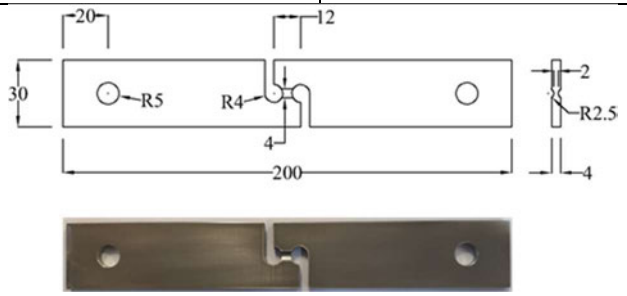

Figure 3-6. Inclined notch specimen (IN0).

The load-deformation curves of the IN0 and PS specimens are shown in Fig. 3-7. The fracture plane developed almost instantaneously without an obvious fracture propagation process, so only a very short degradation stage was experienced before complete fracture and a steep drop in load. For all specimens, the deformations corresponding to the complete fracture (D_f), as measured by the extensometer over the 25 mm gauge length, are summarised in Table 3-2. The PS specimens with smaller inclining angles sustained larger deformations than those with larger angles.

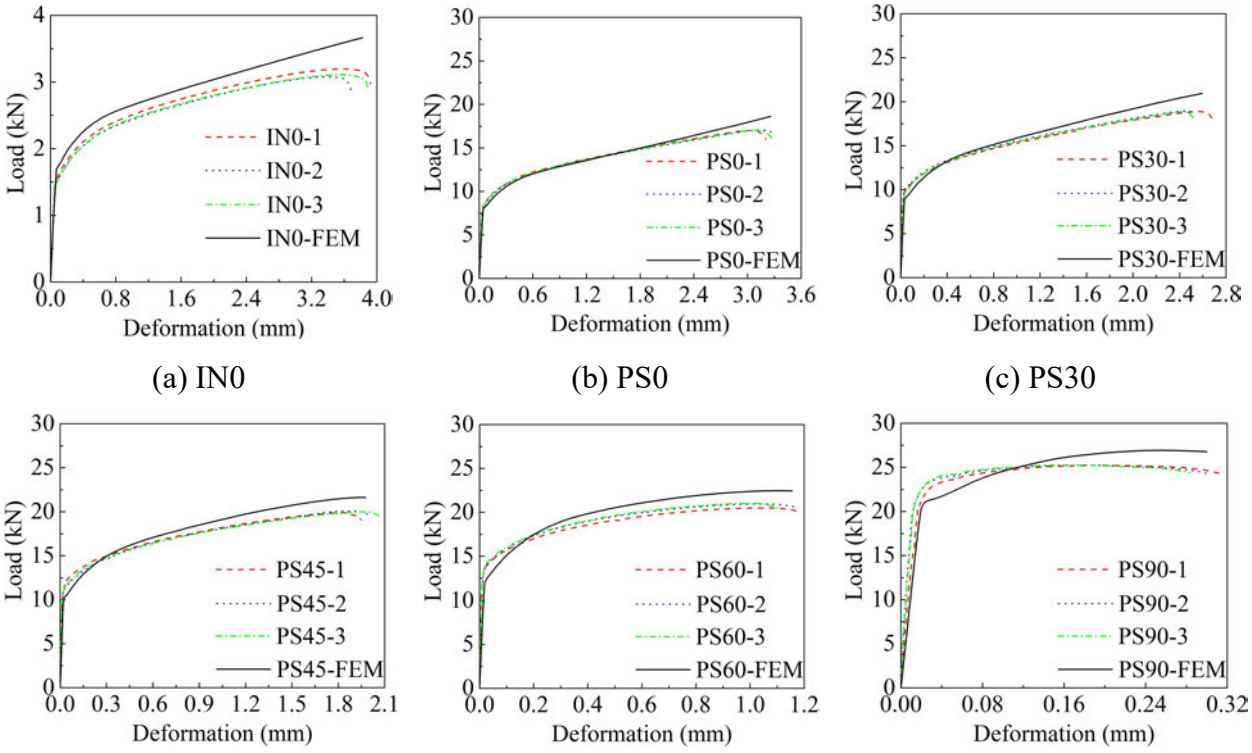

(a) IN0 (b) PS0 (c) PS30

(d) PS45 (e) PS60 (f) PS90

Figure 3-7. Load-deformation curves of IN0 and PS specimens.

3.2.1.4 Numerical simulation

Complementary numerical simulations of the specimen tests were performed using the commercial finite element (FE) software ABAQUS to determine the stress and strain states in the central region of the specimens. Four-node plane strain elements with reduced integration (CPE4R) and eight-node linear solid elements with reduced integration (C3D8R) were used to model the plane strain specimens and the inclined notch specimen, respectively, with element sizes of approximately 0.2mm in the central region of the specimens. Boundary and displacement loading conditions in the FE simulations matched those of the experiments. The FE model geometries are based on measured average dimensions, as shown in Table 3-2, and the material properties are based on those shown in Table 3-1 and Fig. 3-4.

To verify the plane strain assumption and the accuracy of the FE simulations using the 2D CPE4R plane strain elements, FE models were also run using 3D eight-node solid elements (C3D8R), and the simulation results for the PS60 specimen were compared in Fig. 3-8. Utilizing symmetry, only half of the specimen was modelled using C3D8R elements. As observed in the Fig. 3-8, the two models agreed well in terms of both von Mises stress distribution and load-deformation curve, therefore confirming the accuracy of the plane strain assumption. For the elements in the central zone, the average Lode angle parameter over the loading history was calculated from the 3D model, as per Eq. (2-14), and it ranged from 0.007 to 0.011 (close to 0), which further confirms that the plane strain state in the specimens.

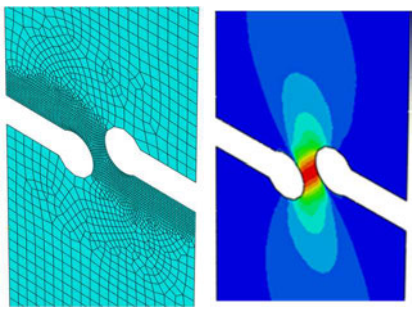

(a) Numerical model and von-Mises contours of model using plane strain elements

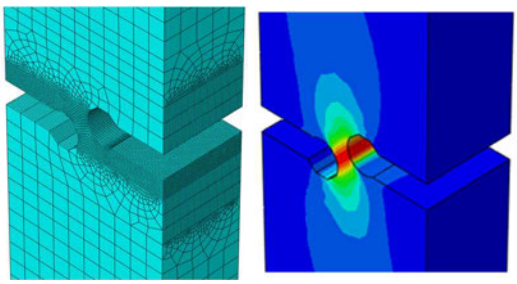

(b) Numerical model and von-Mises contours of model using solid elements

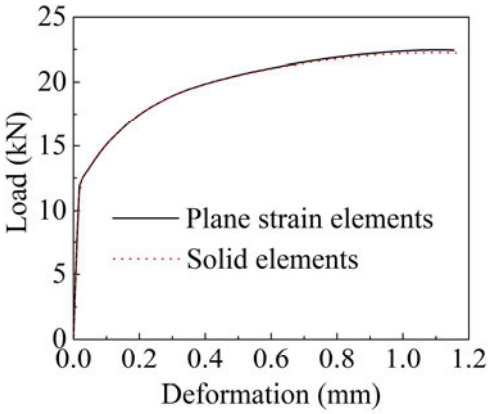

(c) Load-deformation curves

Figure 3-8. Comparison of models for the PS60 specimen using (2D) plane strain elements and (3D) solid elements.

The load-deformation curves from the tests and simulations are compared in Fig. 3-7, and the surface deformations and strains of Specimen PS60 are compared in Fig. 3-9. As shown in these figures, both the overall load-deformation response and the localized deformations in the centre region are accurately captured by the FE simulations. Accordingly, the FE models are assumed to accurately simulate the localized stresses and strains during the loading process.

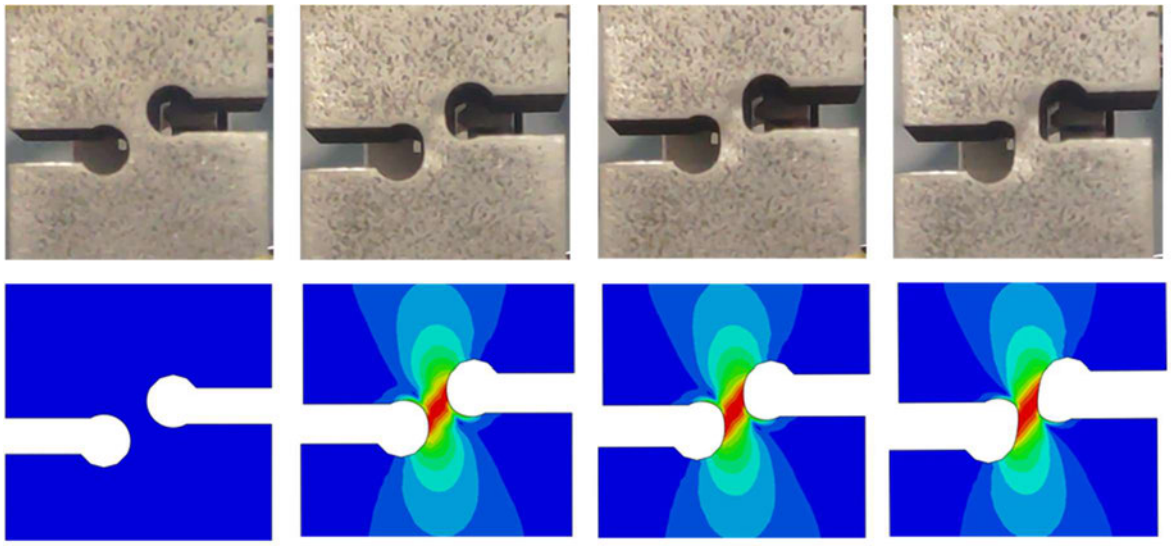

Note: 1. ΔL is the elongation of gauge length, measured by extensometer.
2. FE results in the bottom are presented in the form of contours plots of equivalent plastic strain.

Figure 3-9. Deformation of PS60 specimen over the loading history.

Since complete fracture of the PS specimens occurred rapidly, it was difficult to determine the fracture initiation location directly from the experimental observation. Through detailed measurements of the specimens after complete fracture, the angle of the fracture plane was

found for each specimen. Assuming the fracture plane went through the centre of the specimen, the point on the edge of the fracture plane could then be determined. Based on the average stress triaxialities (T_{avg}), Lode parameters (ξ_{avg}) and equivalent plastic strains (ε_{eq}), which are summarised in Table 3-3, at the instant of fracture, all of the PS specimens had almost identical stress states but notably different equivalent plastic strains at the edges. This suggests that fracture did not initiate from the edges as otherwise the equivalent plastic strains at the edges would have been nearly identical for all specimens. As the equivalent plastic strain at the centre of the fracture plane was always higher than or similar to that of all the other points on the fracture plane, fracture is assumed to initiate at the centre of the PS specimens. This is consistent to observations reported for similar types of specimens, including butterfly specimens [23], inclined notched specimens [27] and double-notched specimens [26].

Table 3-3. Stress indices and plastic strains at centre and edge of fractured sections.

Specimens	Center			Edge		
	T_{avg}	ξ_{avg}	ε_{eq}	T_{avg}	ξ_{avg}	ε_{eq}
PS0	0.161	0.001	0.973	0.553	0.006	0.497
PS30	0.265	0.006	0.748	0.574	0.010	0.568
PS45	0.396	0.004	0.744	0.577	0.004	0.647
PS60	0.531	0.005	0.615	0.597	0.004	0.626
PS90	0.923	0.013	0.247	0.629	0.011	0.196

Using the average stress indices (T_{avg}, ξ_{avg}) and the equivalent plastic strains (ε_{eq}) at the point of failure, the critical VGEF fracture strain ($\varepsilon_{f\text{-}VEGF}$) was calculated using Eq. (2-16). Referring to Eq. (2-16), the two free parameters, a and b, were calibrated using the test results in Table 3-4 using a least square regression to minimize the error between the calculated ($\varepsilon_{f\text{-}VEGF}$) and measured ($\varepsilon_{f\text{-}test}$) values of the fracture strain, where the measured fracture strain was assumed to be the value of plastic strain (ε_{eq}) in the FE simulation at the applied displacement when the specimen fractured. The results shown in Table 3-4 demonstrate the following trend: the larger the inclining angle, the higher the stress triaxiality at the fracture initiation location, and the lower the fracture strain. The relative percentile error (RE) between the calculated and measured fracture strains is then calculate as follows:

$$\mathrm{RE} = \frac{\varepsilon_{f\text{-}VGEF} - \varepsilon_{f\text{-}test}}{\varepsilon_{f\text{-}test}} \times 100\% . \tag{3-3}$$

Subsequently, the root mean squared relative error (RMSRE) of the prediction for the entire set of data is calculated as follows to evaluate the overall accuracy of the VGEF model:

$$\mathrm{RMSRE} = \sqrt{\frac{\sum_{i=1}^{N} \mathrm{RE}_i^2}{N}} \tag{3-4}$$

where N is the number of tests in the group. As shown in Table 3-4, for this set of tests the maximum RE is 21.0% and the RMSRE is 11.2%. Together with additional test results collected from the literature, the data summarised in Table 3-4 will be used to validate the VGEF in the following section.

Table 3-4. Experimental data and fracture prediction for AS350 steel.

Specimen	T_{avg}	ξ_{avg}	$\varepsilon_{f\text{-test}}$	$\varepsilon_{f\text{-VGEF}}$	RE	RMSRE
IN0	0.010	0.062	1.239	1.231	-0.62%	11.21%
PS0	0.160	0.001	0.973	0.975	0.19%	
PS30	0.265	0.006	0.748	0.829	10.86%	
PS45	0.396	0.004	0.744	0.677	-8.96%	
PS60	0.531	0.005	0.615	0.549	-10.56%	
PS90	0.923	0.013	0.247	0.299	21.00%	

3.2.2 Discussion of the effect of stress triaxiality

3.2.2.1 Stress states with ξ=0

In the high stress triaxiality regime, stress states with ξ=0 have $\sigma_2=(\sigma_1+\sigma_3)/2$ where the three principal stresses σ_1, σ_2, σ_3 are all positive. This is a tensile plane strain stress state, which can be generated by tensile flat grooved specimens. In addition, the newly designed PS specimens provide results for low, medium and high stress triaxiality with ξ=0. Besides these specimens, three other specimen types were used to evaluate the ξ=0 stress states, including: (1) the inclined notched specimens with an inclining angle of 0°, which generate low stress triaxiality; (2) the double notched specimens which generate high or medium stress triaxiality when loaded in tension and low stress triaxiality when loaded in compression; and (3) the rectangular notched specimens, which generate high stress triaxiality states.

In addition to the data of AS350 steel presented in Section 3.2.1, four sets of data were collected for steel grades AISI 1045 [26], A572 [14], Q460 [105] and Q690 [104]. The Young's modulus and yield stress of the materials are listed in Columns 3 and 4 of Table 3-5, respectively. In the publications, it was stated that the tests were conducted under very slow loading rates, so the

experimental results were deemed quasi-static. The average stress triaxialities T_{avg}, average Lode angle parameter ξ_{avg} and fracture strain $\varepsilon_{f\text{-}test}$ were obtained from the literature and summarized in Table 3-6. Column 4 of Table 3-6 shows the designation of the coupons, where letters "GP-R" refers to a grooved plate with a groove radius of R in mm; "FP" refers to a flat plate specimen which can be construed as an equivalent groove plate specimen with a groove radius of infinity; "DN- φ" refers to a double notch specimen with an inclining angle of φ in degrees; "RN" refers to a rectangular notched specimen; and "IN" refers to an inclined notched specimen.

The VGEF parameters (a and b coefficients from Eq. (2-16)) shown in Table 3-5 were obtained through regression analyses to minimize the error between the calculated and measured fracture strains for all of the experimental data within each group, similar to the procedure described previously for the tests summarized in Table 3-4. Similarly, the last two columns of Table 3-6 list the RE for each test and the RMSRE for each material group. The data of Q460 present stress states with high stress triaxiality and illustrate that the VGEF has an excellent accuracy for high stress triaxiality states with ξ=0, with both RMSREs smaller than 3%. The data of the remaining materials present stress states over the full range of stress triaxialities. In general, the comparisons reveal better agreement (lower REs and RMSREs) for the tests and test groups with higher stress triaxialities, although overall the VGEF is shown to provide reliable prediction results with reasonable accuracy.

Table 3-5. Basic properties of materials and fracture parameters of VGEF.

No.	Material	E	σ_y	VGEF		$VGEF_{Tension}$	
		(MPa)	(MPa)	a	b	$a_{Tension}$	$b_{Tension}$
1	AISI 1045	—	333	0.45	2.46	—	—
2	A572	196000	353	2.35	1.19	1.64	0.84
3	AS350	206000	379	1.25	1.55	—	—
4	Q460	222800	430	2.57	1.30	—	—
5	Q690	216000	745	1.37	0.55	0.99	0.18

Table 3-6. Experimental data and fracture prediction for different materials.

No.	Material	No.	Specimen	Tavg	ξavg	$\varepsilon_{f\text{-test}}$	$\varepsilon_{f\text{-VGEF}}$	RE	RMSRE
1	AISI 1045	1.1	DN-φ=110	0.640	0	0.155	0.101	-34.61%	21.38%
		1.2	DN-φ=100	0.461	0	0.173	0.144	-16.95%	
		1.3	DN-φ=90	0.335	0	0.213	0.196	-7.80%	
		1.4	DN-φ=80	0.061	0	0.302	0.383	27.06%	
		1.5	DN-φ=60	-0.242	0	0.829	0.808	-2.65%	
2	A572	2.1	GP-R=1.19	1.280	0	0.530	0.515	-2.80%	6.18%
		2.2	GP-R=1.59	1.080	0	0.710	0.653	-8.01%	
		2.3	RN	1.050	0	0.670	0.676	1.01%	
		2.4	GP-R=3.18	0.920	0	0.730	0.789	8.17%	
		2.5	IN-φ=0	0.140	0	1.860	1.992	7.10%	
		2.6	IN-φ=0	0.130	0	2.150	2.015	-6.23%	
4	Q460	4.1	GP-R=1	1.204	0	0.524	0.537	2.58%	2.83%
		4.2	GP-R=3	0.884	0	0.846	0.814	-3.67%	
		4.3	GP-R=10	0.755	0	0.945	0.963	1.98%	
5	Q690	5.1	GP-R=5	0.962	0	0.826	0.809	-2.07%	1.73%
		5.2	GP-R=15	0.845	0	0.844	0.862	2.17%	
		5.3	IN-φ=0	0.007	0	1.364	1.363	-0.10%	

Note: Test data and VGEF predictions of AS350 are shown in Table 3-4 and are not repeated here.

Comparisons between the predicted VGEF fracture loci and the test results, plotted as a function of stress triaxiality and fracture strain, are shown in Fig. 3-10. For each material, the experimental data largely follow an exponential curve over the entire stress triaxiality range. For practical applications, it is substantially easier to machine and test high stress triaxiality coupons, (GP specimens in the case of ξ=0), as compared to the medium and low stress triaxiality coupons. Accordingly, the dashed curves for A572 and Q690 steel in Fig. 3-10(b) and Fig. 3-10(e) were calculated using only high stress triaxiality data to determine the a and b parameters defining the $VGEF_{Tension,}$ as shown in Table 3-5. An obvious deviation is observed between the calibrated curves and the experimental data at low stress triaxiality, indicating that data from specimens representing both high and low stress triaxialities are required to accurately calibrate the VGEF parameters for the medium to low stress triaxiality range.

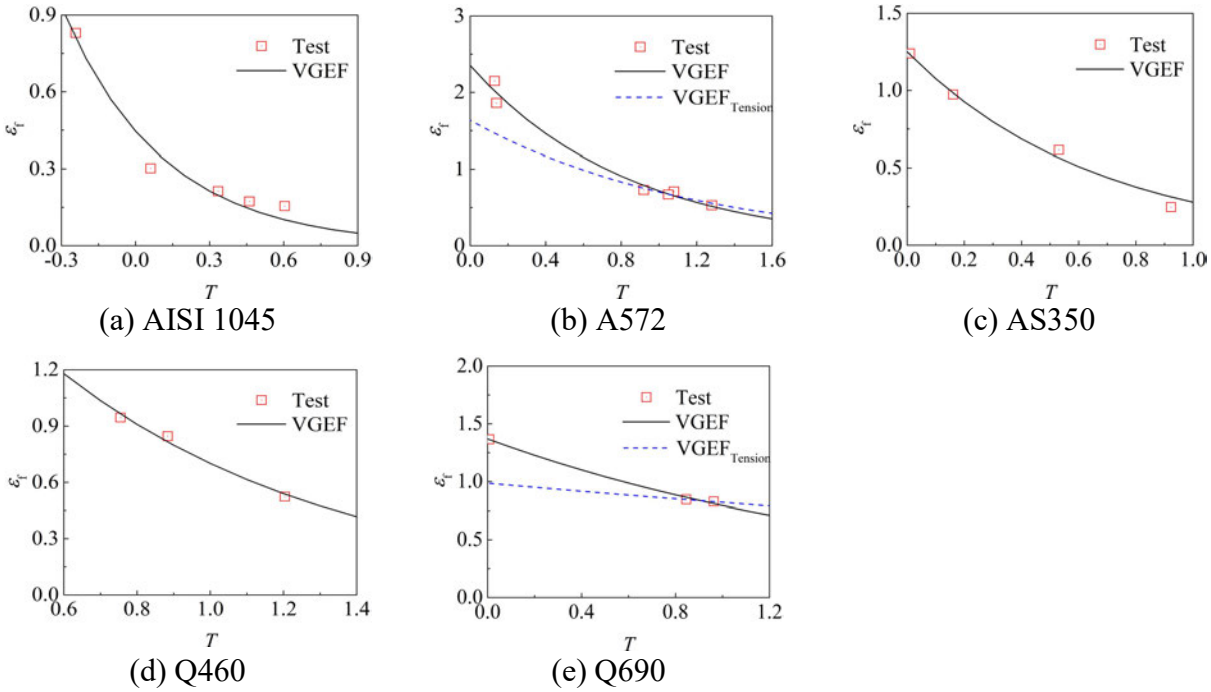

(a) AISI 1045 (b) A572 (c) AS350

(d) Q460 (e) Q690

Figure 3-10. Predicted fracture loci for stress states with ξ =0 and various stress triaxialities.

3.2.2.2 Stress states with ξ=1

In the high stress triaxiality regime, stress states with ξ=1 have $\sigma_1>\sigma_2=\sigma_3>0$, which is an axisymmetric tension stress state. Tensile smooth round bars and the notched round bars are commonly used to generate these stress states. For the stress states with high stress triaxiality, four sets of data were collected for steel grades Q460 [105], Q690 [104], AISI 1045 [106] and AISI 316L [107]. In contrast, data of tests that cover a broader range of stress triaxialities were collected from Bridgman [24], who conducted a series of experiments, in which smooth round bars were pulled longitudinally in a high-pressure chamber. Due to the circumferential pressure, the specimens were subjected to medium or low stress triaxiality states with ξ=1. For each material tested, an additional smooth round bar coupon, with high stress triaxiality and ξ=1, was tested under normal atmospheric pressure. The basic properties of the test materials used to evaluate cases with ξ=1 are summarized in Table 3-7.

Table 3-7. Basic properties of materials and fracture parameters of VGEF.

No.	Material	E	σ_y	σ_{max}	Hollomon hardening		VGEF	
		(MPa)	(MPa)	(MPa)	K	n	a	b
1	Q460	222800	430	—	—	—	3.81	1.57
2	Q690	216000	745	—	—	—	8.25	3.04
3	AISI 1045	—	—	—	1147.60	0.23	3.26	2.19

4	AISI 316L	—	—	—	1358.30	0.36	4.22	1.66
5	Steel-1	—	689.50	890.49	—	—	2.08	1.87
6	Steel-2	—	896.35	1043.14	—	—	2.23	2.39
7	Steel-3	—	1034.25	1331.49	—	—	1.79	3.89
8	Steel-4	—	1034.25	1458.71	—	—	0.94	4.47
9	Steel-5	—	772.24	1060.11	—	—	1.85	1.06
10	Steel-7	—	965.30	1314.53	—	—	2.62	1.87
11	Steel-8	—	965.30	1289.09	—	—	2.21	1.62

As Bridgman [24] did provide information about the local stress triaxiality T_{avg} and fracture strain $\varepsilon_{f\text{-}test}$ for his tests, the $\varepsilon_{f\text{-}test} - T_{avg}$ dependency, T_{avg}, and $\varepsilon_{f\text{-}test}$ have been calculated in the present investigation. Ideally, the detailed stress triaxiality and strain history of the tests would be determined through a FE simulation, in a similar manner as reported previously for the IN0 and PS tests. However, Ref. [24] did not report the necessary material and specimen response data to calibrate the FE model. Rather, the available data were limited to: the axial stresses at initial yielding (σ_y), necking (σ_{max}), and fracture (σ_f), the test chamber pressure P, the neck aspect ratio a/R (i.e. ratio of the radius of curvature at the neck to the cross-sectional radius of the neck) measured after specimen fracture, and the reduction in the specimen area A_0/A. Therefore, the approximation method proposed in [14] is herein adopted to estimate the stress triaxialities and equivalent plastic strains at yield, necking, and fracture, which are then used to calculate the average stress triaxiality over the loading history. For the first point, corresponding to initial yielding, the stress triaxiality and equivalent plastic strain are calculated, respectively, as:

$$T = \frac{1}{3} - \frac{P}{\sigma_y} \tag{3-5}$$

$$\varepsilon_{p\_ys} = 0. \tag{3-6}$$

For the second point, corresponding to necking initiation, the stress triaxiality and equivalent plastic strain are calculated, respectively, as:

$$T = \frac{1}{3} - \frac{P}{\sigma_{max}} \tag{3-7}$$

$$\varepsilon_{p\_ni} = 0.2\,. \tag{3-8}$$

For the third point, corresponding to complete fracture, the stress triaxiality and equivalent plastic strain are calculated, respectively, as [24]:

$$T = -\frac{P}{\sigma_{\mathrm{f}}} + \frac{1}{3} + \ln(1 + \frac{a}{R}) \tag{3-9}$$

$$\varepsilon_{\mathrm{p\_cf}} = \ln\frac{A_0}{A}. \tag{3-10}$$

Using these equations, the average values of the stress triaxiality, Lode angle parameter, and fracture strain are calculated for Bridgeman's tests and summarized in Table 3-8. These tests had stress triaxialities varying from about -0.5 to about 0.5, covering the high, medium and low stress triaxiality regimes.

Table 3-8. Experimental data and fracture prediction for different materials.

No.	Material	No.	Specimen	P (psi)	T_{avg}	ξ_{avg}	$\varepsilon_{\mathrm{f\text{-}test}}$	$\varepsilon_{\mathrm{f\text{-}VGEF}}$	RE	RMSRE
1	Q460	1.1	NRB-R=1.5	—	1.330	1	0.542	0.470	-13.25%	7.82%
		1.2	NRB-R=3.125	—	1.029	1	0.739	0.755	2.17%	
		1.3	NRB-R=6.25	—	0.835	1	0.951	1.024	7.74%	
		1.4	SRB	—	0.566	1	1.599	1.564	-2.13%	
2	Q690	2.1	NRB-R=5	—	1.206	1	0.185	0.211	14.42%	9.09%
		2.2	NRB-R=10	—	1.050	1	0.362	0.339	-6.33%	
		2.3	SRB	—	0.642	1	1.170	1.171	0.15%	
3	AISI 1045	3.1	NRB-R=1.2	—	1.209	1	0.328	0.228	-30.21%	17.83%
		3.2	NRB-R=2.5	—	0.944	1	0.415	0.409	-1.29%	
		3.3	NRB-R=5	—	0.731	1	0.551	0.653	18.67%	
		3.4	SRB	—	0.465	1	1.209	1.172	-2.99%	
4	AISI 316L	4.1	NRB-R=1.2	—	0.990	1	0.830	0.818	-1.42%	0.91%
		4.2	NRB-R=2.5	—	0.820	1	1.080	1.084	0.41%	
		4.3	NRB-R=5	—	0.700	1	1.310	1.323	0.99%	
		4.4	SRB	—	0.520	1	1.790	1.783	-0.38%	
5	Steel-1	5.1	1-5	Atmos.	0.450	1	0.91	0.893	-1.82%	1.27%
		5.2	1-3	40000	0.223	1	1.35	1.366	1.23%	
		5.3	1-10	140000	-0.198	1	3.01	3.007	-0.08%	
6	Steel-2	6.1	2-4	Atmos.	0.429	1	0.77	0.797	3.59%	3.75%
		6.2	2-7	54000	0.193	1	1.34	1.401	4.55%	
		6.3	2-6	117000	-0.020	1	2.45	2.337	-4.61%	
		6.4	2-2	188000	-0.200	1	3.55	3.593	1.22%	

7	Steel-3	7.1	3-1	Atmos.	0.375	1	0.46	0.416	-9.58%	6.96%
		7.2	3-8	26000	0.258	1	0.61	0.654	7.34%	
		7.3	3-5	96000	0.066	1	1.39	1.382	-0.57%	
8	Steel-4	8.1	4-1	Atmos.	0.336	1	0.23	0.208	-9.58%	8.19%
		8.2	4-6	28000	0.219	1	0.40	0.351	-12.14%	
		8.3	4-4	112000	-0.033	1	1.03	1.085	5.36%	
		8.4	4-3	200000	-0.189	1	2.20	2.182	-0.79%	
9	Steel-5	9.1	5-1	Atmos.	0.462	1	1.12	1.131	0.99%	0.71%
		9.2	5-2	83000	0.057	1	1.75	1.737	-0.74%	
		9.3	5-5	227000	-0.453	1	2.98	2.983	0.11%	
10	Steel-7	10.1	7-1	Atmos.	0.476	1	1.10	1.077	-2.08%	2.61%
		10.2	7-2	115000	0.069	1	2.22	2.304	3.82%	
		10.3	7-3	155000	-0.002	1	2.71	2.633	-2.84%	
		10.4	7-4b	189000	-0.068	1	2.97	2.981	0.36%	
11	Steel-8	11.1	8-1	Atmos.	0.475	1	1.09	1.025	-5.82%	21.48%
		11.2	8-2	88000	0.167	1	2.00	1.684	-15.40%	
		11.3	8-4	158000	-0.103	1	2.51	2.608	3.93%	
		11.4	8-5	Atmos.	0.431	1	0.79	1.100	38.15%	

Table 3-8 summarizes the specimen properties, stress states, measured fracture strains, and calculated VGEF fracture strains, along with the RE and RMSRE error statistics for each material group. The specimen designations in Column 4 of Table 3-8 are defined as follows: "NRB-R" refers to notched round bar with a circumferential notch radius R in mm; and "SRB" refers to a smooth round bar which represents an NRB with a notch radius of infinity; and for Bridgman's tests, the first and second numbers show the material type and specimen number, respectively. The two VGEF parameters calibrated for each material are listed in Table 3-7. Referring to Table 3-8, the generally low values of RE and RMSRE confirm the accuracy of the VGEF for ξ =1 over the full range of stress triaxiality. Additionally, the comparison between the tests and VGEF-predicted results in Fig. 3-11 further illustrates that the VGEF reliably captures the ε_f - T dependency.

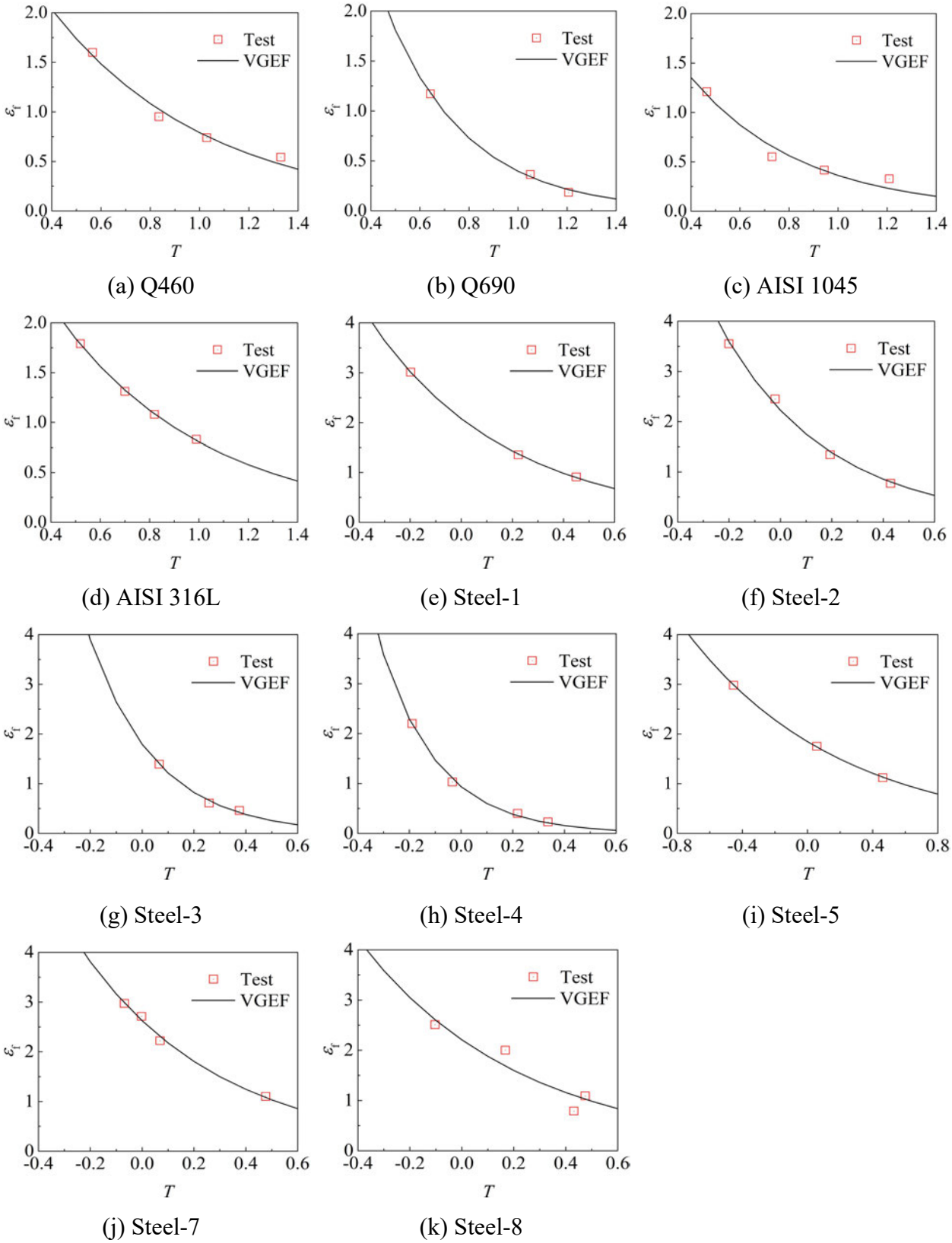

(a) Q460 (b) Q690 (c) AISI 1045

(d) AISI 316L (e) Steel-1 (f) Steel-2

(g) Steel-3 (h) Steel-4 (i) Steel-5

(j) Steel-7 (k) Steel-8

Figure 3-11. The predicted fracture locus for stress states with ξ=1 and low stress triaxialities.

3.2.2.3 Stress states with ξ=-1

In the high stress triaxiality regime, stress states with ξ =-1 have $\sigma_1=\sigma_2>\sigma_3>0$. Notable tests included in this regime include the disk punch tests by Bai and Wierzbicki [28], punch tests by

Qin and Beese [29], and Nakajima specimen tests by Gu et al. [30]. These tests exhibited equal-biaxial tension (ξ=-1 and $T \approx 0.66$), while stress states with ξ=-1 and other positive T values were not achieved. Similarly, in the medium stress triaxiality regime, stress states with ξ=-1 have $\sigma_1=\sigma_2>0>\sigma_3$, which is also difficult to achieve with coupon tests, and no data was found covering this stress state.

In the low stress triaxiality regime, stress states with ξ=-1 can be investigated using compression cylinder tests. Structural steels have good compressive ductility and require very high plastic strains to fracture under compression, which is difficult to achieve prior to the specimen failing by buckling. Bao and Wierzbicki [22] conducted a series of compression cylinder tests on 2024-T351 aluminium alloy, which is relatively more brittle than structural steels to interrogate this space. The compression cylinders featured stress triaxialities ranging from T = -0.224 to -0.278, and the VGEF was shown to be accurate for this range. However, this stress triaxiality range is too narrow to conclude the validity of VEGF in the negative stress triaxiality regime.

To investigate the dependence of fracture strain on T for ξ=-1, at least three stress states with the same ξ=-1 are needed to establish the relationship between fracture strain and T. However, only two stress states with ξ=-1 were often reported in the past, i.e., equal-biaxial tension (ξ=-1 and $T \approx 0.66$) and uni-axial compression (ξ=-1 and $T \approx$ -0.33). Furthermore, these two stress states were seldomly studied for the same material. The equal-biaxial tension stress state was predominantly used for sheet metal while the uni-axial compression for bulk metal. Hence, a need remains for additional tests with more stress triaxiality values in order to conclusively deem the VGEF valid for all ξ=-1 stress states.

3.3 The effect of Lode angle

3.3.1 Tests on rectangular notched specimens

3.3.1.1 Specimen design

A series of Rectangular Notched (RN) specimens was designed and tested to obtain data of fracture strains under stress states with different Lode angle parameters but almost identical moderate stress triaxiality. As shown in Fig. 3-12(a), the RN specimen is shaped as a square bar with a flat groove on each side, producing a small rectangular prism with fillets at the central region of the specimen. The RN specimen is similar to one designed by Smith et al. [14] (referred to as the Smith RN specimen or SRN specimen), shown in Fig. 3-12(b). However, the flat grooves of the RN specimen induce relatively low stress triaxiality, as compared to the

high stress triaxiality induced by the circular notches of the SRN specimens. The parametric study in [14] showed that when the area of the SRN net section is held constant, the aspect ratio (ratio of nominal width t_1 to depth t_2) of the cross-section has a strong influence on the Lode angle parameter at the centre of the specimen, where fracture initiates, and a relatively minor effect on the stress triaxiality. Therefore, to generate identical stress triaxiality but different Lode angle parameters in the RN specimens, the central regions of the RN specimens were designed to have identical net section area but different aspect ratios. Five types of RN specimens were tested, whose nominal width t_1, depth t_2 and area A_{RN} are summarized in Table 3-9.

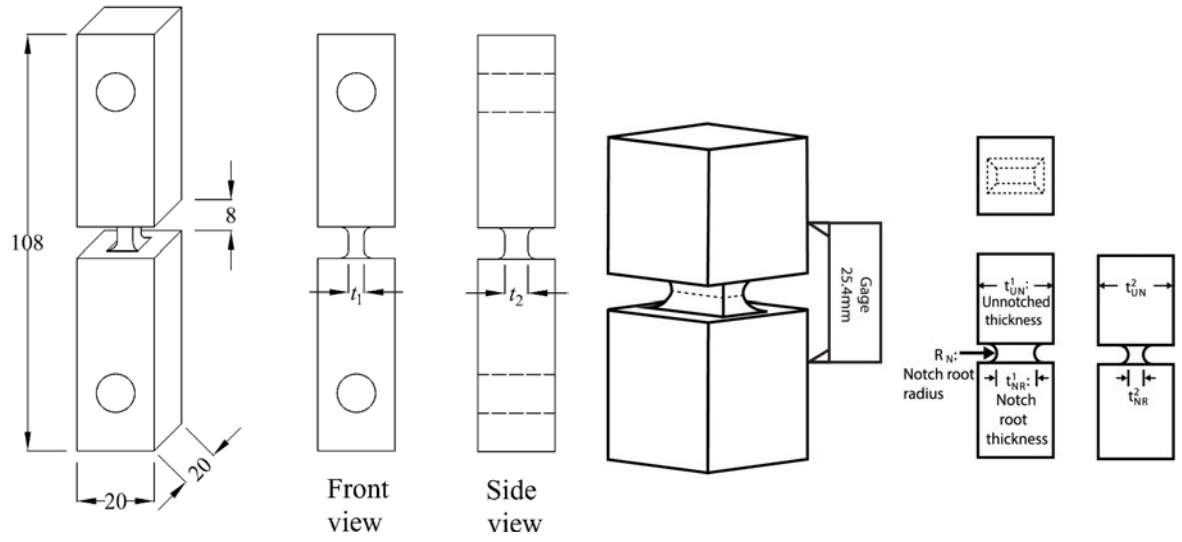

(a) RN specimen (b) SRN specimen [14]

Figure 3-12. Geometry of RN and SRN specimens.

Table 3-9. Dimensions and fracture deformations of RN specimens (AS350 steel).

Test	t_1 (mm)	t_2 (mm)	A_{RN} (mm^2)	$t_{1\text{-test}}$ (mm)	$t_{2\text{-test}}$ (mm)	D_f (mm)
RN-1	4	6	24	3.99	6.03	1.95
RN-2	3	8	24	2.98	7.99	1.83
RN-3	2.4	10	24	2.42	10.01	1.68
RN-4	2	12	24	2.02	11.99	1.46
RN-5	1.5	16	24	1.53	16.02	1.31

3.3.1.2 Experimental investigation

All rectangular notched specimens were extracted from the 20mm thick plate of steel grade AS350 described in Section 3.2.1.2. The mechanical properties of the material are summarized in Table 3-4 and the true stress-strain curve is shown in Fig. 3-1. For each of the five RN

specimen geometries listed in Table 3-9, two nominally identical tests were performed, and the average values of the measured notch dimensions ($t_{1\text{-test}}$, $t_{2\text{-test}}$) are reported. The specimens were loaded using a Criterion 50kN machine, as shown in Fig. 3-13(c), with the loading rate set to 0.1 mm/min. The elongation of the middle portion of the specimen was measured using a 25mm gauge length extensometer. Stress relaxation was accommodated by pausing each test for 100s at regular intervals during the loading process to obtain static load-deformation curves. The resulting load-deformation curves for all RN specimens are plotted in Fig. 3-14.

Plastic deformations in the specimens were highly localized at the grooved portion, where necking subsequently occurred at the mid-height of this portion, denoted by the peak load on the load-deformation curve. The load then gradually dropped until fracture initiated at the center of the necked cross-section, leading to a sudden change of stiffness. Therefore, the point on the load-deformation curve corresponding to the sudden change of stiffness was regarded as the point where fracture initiated, identified by the square and circle points in Fig. 3-14. The deformations D_f corresponding to the fracture initiation points were averaged and are summarized in Table 3-9, where one can see that the RN specimens with larger aspect ratios exhibited larger values of D_f. Eventually, the fracture propagated through the entire cross-section, marking the complete failure of the specimens, as shown in Fig. 3-13(b).

(a) Unfractured specimens (b) Fractured specimens (c) Test setup

Figure 3-13. Rectangular notched specimens.

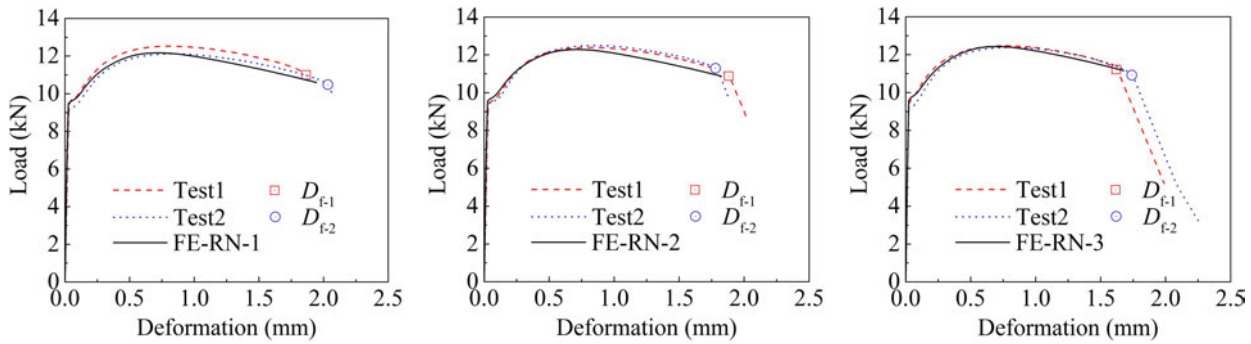

(a) RN-1 (b) RN-2 (c) RN-3

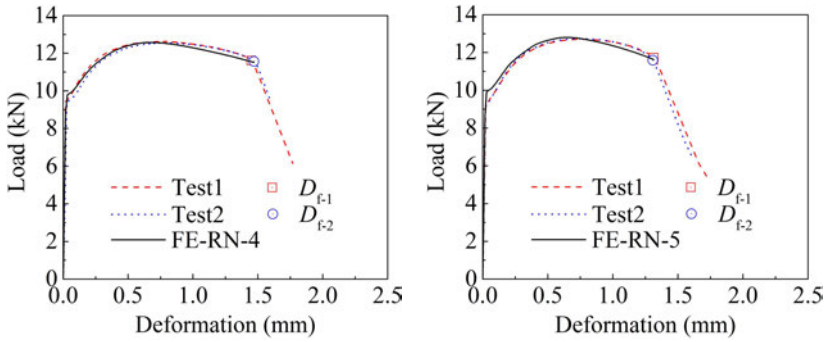

(d) RN-4 (e) RN-5

Figure 3-14. Load-deformation curves for RN specimens.

3.3.1.3 Numerical simulation

In order to determine the stress and strain fields at the fracture initiation point and to calculate the histories of the stress state parameters (T and ξ) and plastic strain (ε_p), a three-dimensional Finite Element (FE) model was developed for each RN specimen using ABAQUS. Utilizing symmetry, half of the specimen was modeled using eight-node linear solid elements with reduced integration (C3D8R). The boundary conditions and applied displacements were chosen in accordance with the assumed half-model symmetry and the experimental loading procedure. The material was modelled by isotropic von-Mises plasticity with the same strain hardening stress-strain relationship as the true stress-strain curve shown in Fig. 3-1.

Finite element models with mesh sizes ranging from 0.1 mm to 1 mm in the grooved region were established for the RN-1 specimen, as shown in Fig. 3-15. The corresponding load-deformation curves and strain (at the centre of the specimen)-deformation curves are compared in Fig. 3-16, from which it can be observed that progressively lower load curves and higher strain curves are obtained as the mesh is refined. In general, the difference between the curves becomes insignificant when the mesh size is smaller than 0.5 mm, and the curves can be considered to have converged to a stable state when the mesh size is 0.2 mm, or less. Hence, a mesh size of approximately 0.2 mm (resulting in about 8 to 20 elements across the smallest dimension of the notch) was adopted for the grooved region of the specimen to provide a sufficiently accurate mesh density in the fracture initiation region.

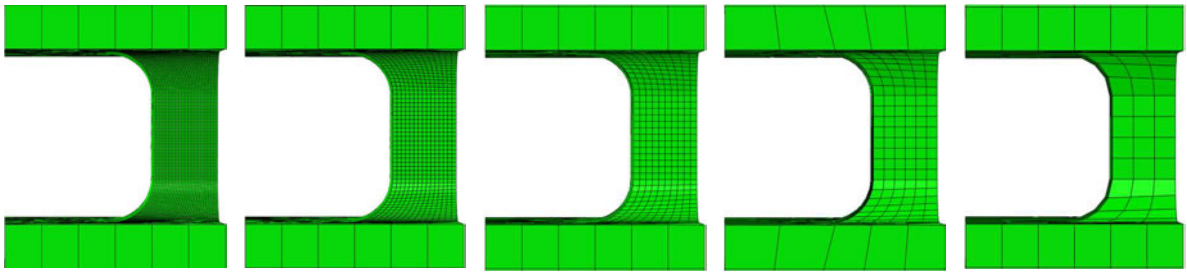

(a) 0.1 mm (b) 0.2 mm (c) 0.3 mm (d) 0.5 mm (e) 1 mm

Figure 3-15. Finite element models of RN-1 specimen with varying mesh sizes.

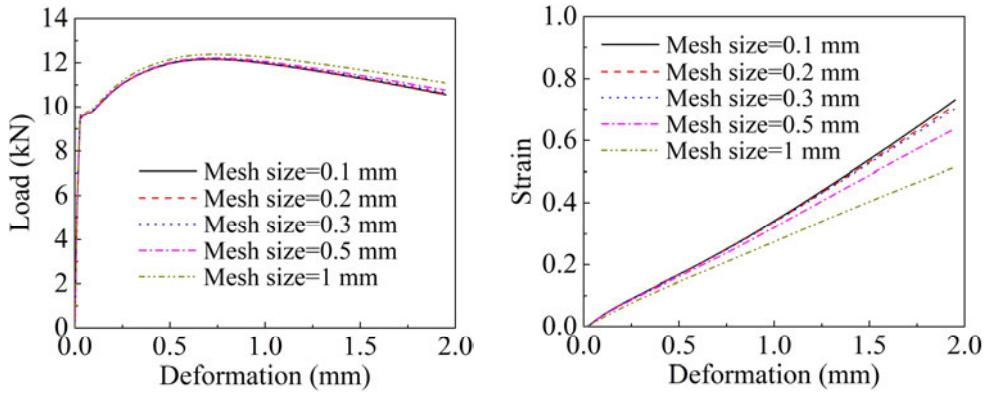

(a) Load-deformation curves (b) Strain-deformation curves

Figure 3-16. FE curves of RN-1 specimen modelled with varying mesh sizes.

As shown in Fig. 3-14 the load-deformation curves from the FE simulations compared well with the experimental results for all RN specimens. Shown in Fig. 3-17 is a comparison of the deformed geometry of test specimen RN-5 and its FE counterpart in the grooved portion where plasticity localized. On the right-hand side of Fig. 3-17, the simulated von Mises stresses are overlaid on the deformed geometry. The results shown in Fig. 3-14 and Fig. 3-17 verify that the FE models can accurately capture the full-range behaviour, substantiating the calculated stress triaxiality, Lode angle parameter and plastic strains for each specimen.

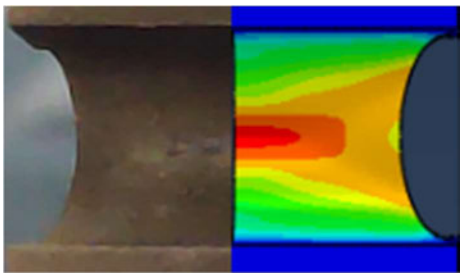

Figure 3-17. Plastic deformation of RN-5 specimen at longitudinal deformation over the gauge length before fracture; left half experiment, right half FE.

As illustrated previously in Fig. 3-1, the true stress-strain relationship for the FE simulations was calibrated to data from standard axisymmetric tensile coupons. As shown in Fig. 3-14,

when used in conjunction with the von-Mises yielding criterion, this plasticity model accurately simulates the load-deformation curves of the RN specimens, even though the stress triaxialities and Lode angle parameters in the RN specimens are different from those of the axisymmetric tensile coupons. This implies that the flow stress of the material in these specimens (i.e., AS 350 grade steel) is insensitive to both the hydrostatic stress and the Lode angle. Therefore, notwithstanding that the yield surface (i.e. flow stress) may, in general, be affected by the stress state the material [9], in this study, the effect of the stress state on the flow stress is small enough to allow the use of a large strain plasticity model with the classical von-Mises yielding criterion.

For each specimen, the fracture strain ε_f is defined as the equivalent plastic strain at the fracture initiation location when fracture initiated at the measured deformation D_f. Specifically, for each specimen, the stress and strain fields were calculated from the FE model, and the plastic strain ε_p, average stress triaxiality T_{avg}, and Lode angle parameter ξ_{avg}, were calculated until the instant of fracture initiation, as identified from Fig. 3-14 using Eqs. (2-13) and (2-14), respectively, and ε_f was obtained as ε_p at the same instant. In the positive stress triaxiality regime, it is widely accepted that under stress states with identical Lode angle parameter, the fracture strain reduces as the stress triaxiality increases for many steel grades. According to the numerical simulations, for all RN specimens the centre of the necked cross-section had the highest stress triaxiality as well as the largest equivalent plastic strain. Hence, while the fracture initiation location and propagation were not visibly observable during the tests, it is assumed that fracture initiated from the centre of the necked cross section and, accordingly, the fracture strain was determined from that location. As summarized in Table 3-10, up to the strain at failure, ε_f, the average stress triaxiality T_{avg} was about 0.6 for all RN specimens while the average Lode angle parameter ξ_{avg} varied from 0.1 to 0.9. Hence, the variation in fracture strains is assumed to depend on the Lode angle parameter at the constant value of triaxiality, where the RN specimens with larger aspect ratio exhibited higher Lode angle parameters and lower fracture strains. Shown also in Table 3-10 are the relative percentile error (RE) of using an exponential function, i.e., Eq. (3-11) in Section 3.3.2, to describe the dependence of the fracture strain on the Lode angle parameter observed in the tests and the root mean square of the REs (RMSRE). RE and RMSRE are defined as per Eqs. (3-3) and (3-4), respectively.

Table 3-10. Experimental results and fracture prediction for RN specimens (AS350 steel).

Specimen	T_{avg}	ξ_{avg}	$\varepsilon_{f\text{-test}}$	$\varepsilon_{f\text{-pred}}$	RE	RMSRE
RN-1	0.569	0.950	0.712	0.711	-0.1%	2.3%
RN-2	0.574	0.771	0.733	0.723	-0.9%	
RN-3	0.595	0.557	0.755	0.743	-1.6%	
RN-4	0.610	0.365	0.728	0.759	4.2%	
RN-5	0.641	0.112	0.796	0.780	-2.0%	

3.3.2 Discussion of the effect of Lode angle

The SRN specimens in [14] are similar to the RN specimens in that both tests obtained values of fracture strain under constant values of stress triaxiality but different positive Lode angle parameters, thereby enabling the effect of Lode angle on the fracture strain to be investigated. The key difference between the two series is that the stress triaxialities in the SRN and RN specimens are different, about 1.1 and 0.6 respectively.

Seven SRN specimens made from steel grade A357 were tested in [14]. The fracture strain of each specimen and the corresponding effective stress triaxiality and Lode angle parameters are summarized in Table 3-11. The resulting dependence of the fracture strain on the Lode angle parameters obtained from the RN and SRN tests are plotted in Figs. 3-18(a) and 3-18(b). From Tables 3-10 and 3-11 and Fig. 3-18, it is clearly observed that for the range of Lode angle parameter investigated, the fracture strain decreases as the Lode angle parameter increases, and the dependence can be characterized by an exponential function, i.e.:

$$\varepsilon_f = c_1 \cdot e^{c_2 \cdot \xi} \tag{3-11}$$

where c_1 and c_2 are free parameters.

Table 3-11. Experimental results and fracture prediction for SRN specimens for A572.

Specimen	T_{avg}	ξ_{avg}	$\varepsilon_{f\text{-test}}$	$\varepsilon_{f\text{-pred}}$	RE	RMSRE
SRN-1	1.14	1	0.39	0.36	-7.6%	9.5%
SRN-2	1.15	0.85	0.43	0.39	-8.5%	
SRN-3	1.12	0.82	0.37	0.40	8.3%	
SRN-4	1.15	0.64	0.48	0.44	-7.2%	
SRN-5	1.09	0.48	0.42	0.49	16.6%	
SRN-6	1.09	0.30	0.51	0.54	6.8%	
SRN-7	1.05	0.08	0.67	0.62	-7.5%	

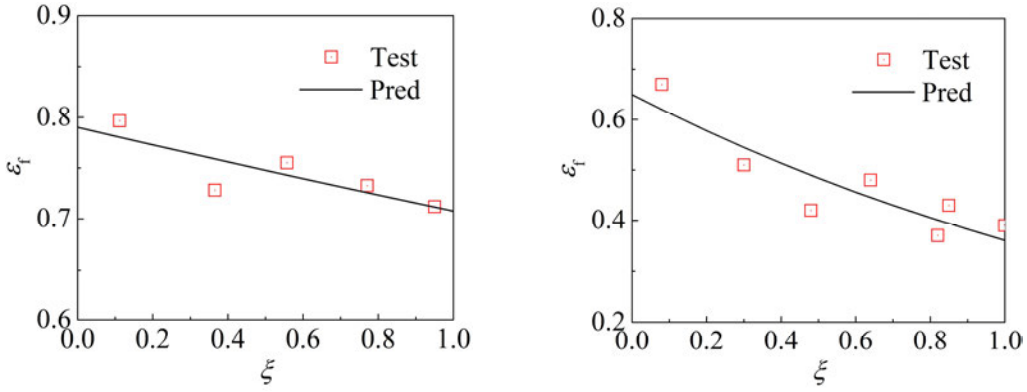

(a) AS350 (T=0.6) (b) A572 (T=1.1)

Figure 3-18. The test results and predicted fracture locus.

Using the fracture strains of the RN and SRN specimens, the values of c_1 and c_2 were calibrated using least square regression to be 0.79 and -0.11 for AS350 steel at the triaxiality T = 0.6, respectively, and 0.65 and -0.59 for A572 steel at the triaxiality T = 1.1, respectively. Using Eq. (3-11) and the calibrated parameters, the fracture strain corresponding to the RN and SRN specimens can be predicted and are summarised in Tables 3-10 and 3-11, respectively. The fracture strain calculated by Eq. (3-11), using the fitted parameters, are plotted and compared to the test results in Fig. 3-18. Considering the scatter in the experimental results, the comparison indicates that Eq. (3-11) presents a good estimation of the dependence of fracture strain on the Lode angle parameter in both medium and high triaxiality ranges.

The accuracy of Eq. (3-11) is further evaluated by comparing the test results $\varepsilon_{f\text{-test}}$ and the predicted strains $\varepsilon_{f\text{-pred}}$ by calculating RE for each specimen type using Eq. (3-3), and the overall accuracy of Eq. (3-11) for each material is quantified by calculating RMSRE of the prediction using Eq. (3-4). For the RN specimens made from AS350 steel, the absolute values of RE are all less than 5%, and the RMSRE is 2.3%, as shown in Table 3-10. For SRN specimens made from A572 steel, with the exception of one test, the absolute values of RE are less than 9%, and the RMSRE is 9.5%, as shown in Table 3-11.

The above comparisons have confirmed the accuracy of Eq. (3-11) for describing the dependence of fracture strains on the Lode angle parameter, but only in the first quadrant of the T-ξ stress space. The main reasons for having focused on this quadrant are, firstly, fracture in steel structures primarily occurs in tension or tension-dominated stress states, i.e. $T > 0$, and secondly, experimental data in the second quadrant of the T-ξ stress space are sparse. Stress states falling in the second quadrant are difficult to achieve using coupon tests because they typically involve bi-axial tension loading, which requires a complex loading set-up. However,

in practice, fracture may occur in this quadrant. A simple example would be a plane stress state with equal bi-axial tension, i.e. $\sigma_1 = \sigma_2 > 0$, $\sigma_3 = 0$. This stress state, corresponding to $T = 2/3$ and $\xi = -1$, is found in 3D beam-column connections and is very common for metal sheets.

To evaluate the effect of Lode angle in the negative Lode angle parameter range, notably for stress states in the second quadrant of the T-ξ stress space, experimental data were collected from the literature covering stress states with the Lode angle parameter ranging from -1 to 1. Four sets were collected for steel grades DP600 [29], TRIP 690 [28], DP980 [30] and 22MnB5 [108], whose material properties are summarized in Table 3-12. The test data for the stress state with $\xi = -1$ were generated under equi-biaxial tension state by punch tests using the punch specimen [29], disk specimen [28] and Nakajima specimen [30]. While punch tests may produce less well-defined stress states than those produced by dog-bone and butterfly specimens, they provide a practical way to interrogate the $\xi = -1$ stress state. Table 3-13 shows the average stress triaxiality T_{avg}, average Lode angle parameter ξ_{avg} and fracture strain $\varepsilon_{f\text{-}test}$ of each test for each material. Note that the original sources of the DP600, TRIP 690 and DP980 steel test data used $\bar{\theta}_{avg}$ to characterize the stress states, and the source for 22MnB5 steel used L_{avg}. The values of $\bar{\theta}_{avg}$ and L_{avg} were converted to ξ_{avg} using Eqs. (2-10) and (2-11), respectively.

Table 3-12. Material properties of steels.

Material	Yield stress (MPa)	Hardening parameters		
		A (MPa)	K (MPa)	n
DP600	—	1004	694	0.16
TRIP 690	446.4	—	—	—
DP980	—	1386	848	0.075
22MnB5	1108.7	—	—	—

Table 3-13. Experimental data for different steels.

No.	Material	No.	No.	Specimen	T_{avg}	ξ_{avg}	$\bar{\theta}_{avg}$	L_{avg}	$\varepsilon_{f\text{-}test}$	a	b
1	DP600	1-1	1-1-1	Punch	0.66	-1.00	-1.00	1.00	0.74	—	—
		1-2	1-2-1	Butterfly-β=90	0.58	0.00	0.00	0.00	0.37	0.75	1.22
			1-2-2	Butterfly-β=0	0	0.02	0.01	-0.01	0.75		
					(0.66)	(0.00)	—	—	(0.34)		

		1-3	1-3-1	Butterfly-β=70	0.47	0.74	0.53	-0.49	0.30	0.69	1.77
			1-3-2	Butterfly-β=30	0.17	0.68	0.48	-0.44	0.51		
					(0.66)	(0.70)	—	—	(0.21)		
		1-x	1-x-1	Central hole	0.33	1.00	0.96	-0.95	0.61	—	—
			1-x-2	Notched plate-R=6	0.51	0.60	0.41	-0.38	0.32		
			1-x-3	Notched plate-R=10	0.47	0.75	0.54	-0.50	0.32		
			1-x-4	Notched plate-R=20	0.42	0.90	0.72	-0.69	0.32		
2	TRIP 690	2-1	2-1-1	Disk	0.67	-0.99	-0.92	0.91	0.95	—	—
		2-2	2-2-1	Butterfly-1	0.58	0.00	0.00	0.00	0.46	0.65	0.59
			2-2-2	Butterfly-2	0.00	0.00	0.00	0.00	0.65		
					(0.67)	(0.00)	—	—	(0.44)		
		2-3	2-3-1	Dog-bone	0.38	1.00	1.00	-1.00	0.75	1.32	1.5
					(0.67)	(1.00)	—	—	(0.48)		
		2-x	2-x-1	Flat	0.47	0.70	0.50	-0.46	0.39	—	—
3	DP980	3-1	3-1-1	Nakajima	0.66	-1.00	-0.96	0.95	0.65	—	—
		3-2	3-2-1	V-bending	0.54	0.15	0.10	-0.09	0.53	0.90	0.98
			3-2-1	Notched plate-R=5	0.62	0.18	0.11	-0.10	0.49		
					(0.66)	(0.17)	—	—	(0.47)		
		3-3	3-3-1	Central hole	0.34	0.99	0.93	-0.92	0.57	0.95	1.5
					(0.66)	(0.99)	—	—	(0.35)		
		3-x	3-x-1	Notched plate-R=10	0.58	0.43	0.29	-0.26	0.52	—	—
			3-x-2	Notched plate-R=20	0.53	0.65	0.45	-0.42	0.56		
			3-x-3	In-plane shear	0.01	0.05	0.04	-0.03	0.75		
			3-x-4	Out-of-plane shear	0.05	0.00	0.00	0.00	0.57		
4	22MnB5	4-1	4-1-1	Equi-biaxial	0.63	-1.00	—	0.97	0.38	—	—
		4-2	4-2-1	Notched plate-R=5	0.69	0.09	—	-0.05	0.52	0.85	0.71
			4-2-2	In-plane shear	0.02	0.08	—	-0.04	0.85		
					(0.63)	(0.08)	—	—	(0.54)		
		4-3	4-3-1	Central hole	0.48	0.98	—	-0.85	0.69	1.42	1.5
					(0.63)	(0.98)	—	—	(0.55)		

Notes: 1. The values of T_{avg} and ξ_{avg} are obtained from the literature as the reported integrated values, as per Eqs. (2-13) and (2-14). 2. Fracture strains in brackets are calculated using VGEF.

As summarized in Table 3-13, the four sets of tests included various types of coupons, which generated a variety of stress states. The only stress state with a negative Lode angle parameter is the plane stress state with $\xi = -1$. To account for differences in stress triaxiality between the tests, the triaxiality of the specimen with $\xi \approx -1$ is taken as the reference for each material, and the fracture strains representing $\xi \approx 0$ and $\xi \approx 1$ are adjusted if their stress triaxialities differ from the reference value. This adjustment allows the Lode angle parameter dependency to be analysed across constant values of stress triaxiality.

As discussed in Section 3.2, the Void Growth-based Exponential Function (VGEF) with free parameters a and b is validated to describe the effect of stress triaxiality in the whole stress state. Hence, for a given steel alloy, as long as there are test results of specimens representing two triaxialities, Eq. (2-16) can be calibrated, and the fracture strain can be normalized to have the reference triaxiality. To demonstrate the adjustment for differing stress triaxialities, consider the DP600 steel. As shown in Table 3-13, specimen No. 1-1-1 has $\xi = -1$, so its stress triaxiality, $T = 0.66$, is taken as the reference stress triaxiality. Using the test results for specimens Nos. (1-2-1, 1-2-2) and (1-3-1, 1-3-2), the values of a and b were calculated using Eq. (2-16) for stress states with $\xi = 0$ and $\xi = 0.7$, respectively. The calibrated VGEFs were then employed to calculate the fracture strains for $T = 0.66$ with $\xi = 0$ and $\xi = 0.7$, shown in brackets in Table 3-13. These fracture strains with identical triaxiality ($T = 0.66$) and various Lode angle parameters were subsequently plotted in Fig. 3-19(a) to show the $\varepsilon_f - \xi$ relationship. Figs. 3-19(b), 3-19(c) and 3-19(d) show the results for the other three materials obtained using the same process. The values of a and b for various steel grades and triaxiality levels are summarized in the last two columns in Table 3-13. Note that for the TRIP 690, DP980 and 22MnB5 steels, only one test was available for $\xi \approx 1$. Hence, for these three materials, the value of b for stress state with $\xi \approx 1$ was assumed to be 1.5, according to Rice and Tracey's theory [2], and the value of a was calculated based on the available test result using Eq. (2-16). Results for the these and other specimens with different triaxialities are also presented in Table 3-13 for use in Section 3.4 to validate the proposed fracture model.

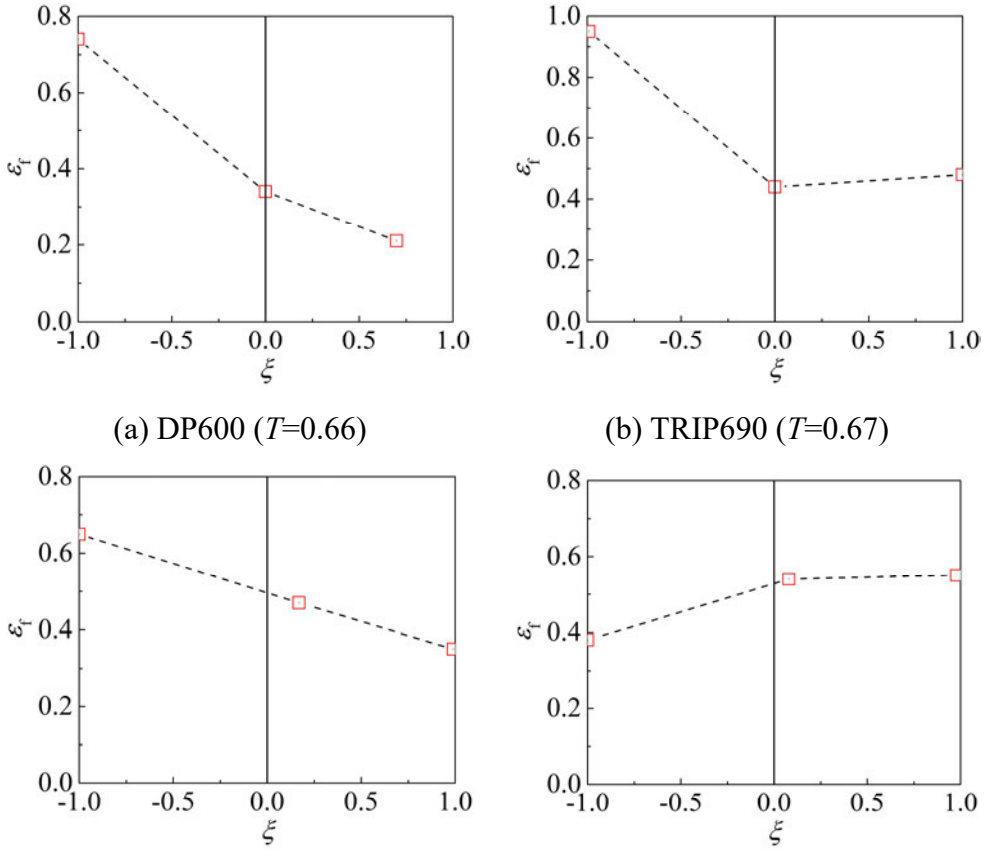

(a) DP600 (T=0.66) (b) TRIP690 (T=0.67)

(c) DP980 (T=0.66) (d) 22MnB5 (T=0.63)

Figure 3-19. Effect of Lode angle parameter.

Three observations can be made from Fig. 3-19. First, the effect of Lode angle parameter on fracture strain is asymmetric with respect to ξ=0. This contradicts the assumption made in many fracture models [8-9, 14], where the fracture response is assumed to be symmetric about ξ=0. Second, for the high strength 22MnB5 steel, the fracture strain increases slightly with increasing Lode angle parameter, while it decreases for the others. The microscopic mechanisms behind this inconsistency are not yet understood, implying that the effect of Lode angle parameter for a particular steel should be determined by testing, since trends from tests of similar steels (e.g. steels of similar strength and other properties) are not necessarily transferable. Thirdly, irrespective of whether the fracture strain increases or decreases with the Lode angle parameter, the dependence of the fracture strain can be estimated by an exponential curve. Hence, Eq. (3-11) can be extended to the negative Lode angle parameter range. (Note that functions other than the exponential function could be used to fit the trend of the fracture strain for varying Lode angle parameters. However, the exponential function has a practical advantage of allowing the effects of Lode angle parameter and triaxiality to be combined in a simple expression for the fracture criterion, as discussed further in Section 3.4).

3.3.3 Influence of stress triaxiality and yield stress on the Lode angle effect

Previous numerical studies of the Lode angle [6, 109] suggest that its effect on the fracture strain depends on the level of stress triaxiality and yield stress. However, this finding has not been systematically established by a broad range of experimental evidence. The RN and SRN results, presented in Sections 3.3.1 and 3.3.2, provide some evidence on the Lode angle effect for two steel grades with discrete values of stress triaxiality, i.e., $T \approx 0.65$ and $T \approx 1.1$. Additional experimental data were obtained from other published sources that extend this study for specimens with a range of stress triaxialities and ξ=1 or ξ=0.

Notched round bars with varying notch radii are routinely used to quantify the relationship between triaxiality T and fracture under axisymmetric tension stress with a constant Lode angle parameter. Such tests are routinely used to calibrate the VGEF model, i.e., Eq. (2-16), for ξ = 1. Similarly, grooved plate specimens with varying groove radii and pure shear specimens have been used to calibrate the VGEF for stress states with ξ = 0. Taken together, data from these previous tests with varying T and ξ = 1 or ξ = 0 can be used to further establish the relationship between Lode angle parameter and fracture strains under different stress triaxialities for various steels.

Experimental data are collected from the literature for steel grades A572 [14], AISI 1045 [106], Q460 [105] and Q690 [104]. The average stress triaxialities T_{avg}, average Lode angle parameter ξ_{avg} and fracture strains $\varepsilon_{f\text{-}test}$ of each test are listed in Table 3-14. Note that, the tests of Q460 and Q690 steels reported the stress states in terms of $\bar{\theta}_{avg}$ values, which are converted to ξ_{avg} using Eq. (2-10). For each steel, the two free parameters in Eq. (2-16), a and b, were calibrated for stress states with ξ = 1 and ξ = 0, using the corresponding data and a least square regression. These data are summarized in Table 3-14, along with results of additional tests with the other values of Lode angle parameter that will be used in Section 6 to validate the proposed fracture model.

Table 3-14. Experimental data for stress state with positive values of ξ.

No.	Material	No.	Specimen	T_{avg}	ξ_{avg}	$\bar{\theta}_{avg}$	L_{avg}	$\varepsilon_{f\text{-}test}$	a	b
1	A572	1-1-1	Rectangular notched-1	1.14	1	—	-1	0.39	2.01	1.44
		1-1-2	Notched round bar	1.57	1	—	-1	0.21		
		1-0-1	Grooved plate-1	0.92	0	—	0	0.73	2.34	1.18
		1-0-2	Grooved plate-2	1.08	0	—	0	0.71		
		1-0-3	Grooved plate-3	1.28	0	—	0	0.53		

		1-0-4	Inclined notched-5	0.14	0.09	—	-0.05	1.86		
		1-0-5	Inclined notched-6	0.13	0.05	—	-0.03	2.15		
		1-0-6	Rectangular notched-7	1.05	0.08	—	-0.05	0.67		
		1-x-1	Rectangular notched-2	1.15	0.85	—	-0.61	0.43		
		1-x-2	Rectangular notched-3	1.12	0.82	—	-0.57	0.37		
		1-x-3	Rectangular notched-4	1.15	0.64	—	-0.41	0.48		
		1-x-4	Rectangular notched-5	1.09	0.48	—	-0.29	0.42		
		1-x-5	Rectangular notched-6	1.09	0.30	—	-0.18	0.51		
		1-x-6	Inclined notched-1	0.54	0.85	—	-0.61	0.93		
		1-x-7	Inclined notched-2	0.48	0.62	—	-0.39	1.30		
		1-x-8	Inclined notched-3	0.45	0.58	—	-0.36	1.14		
		1-x-9	Inclined notched-4	0.34	0.27	—	-0.16	1.68		
2	AISI 1045	2-1-1	Smooth round bar	0.47	1	—	-1	1.21	3.25	2.19
		2-1-2	Notched round bar-R=5mm	0.73	1	—	-1	0.55		
		2-1-3	Notched round bar-R=2.5mm	0.94	1	—	-1	0.42		
		2-1-4	Notched round bar-R=1.2mm	1.21	1	—	-1	0.33		
		2-0-1	Torsion	0.02	0	—	0	1.34	1.36	1.13
		2-0-2	Tension-κ	0.67	0	—	0	0.64		
		2-x-1	Compression cylinder	-0.49	-0.68	—	0.45	1.50		
		2-x-2	Combination-κ=0.5	0.08	0.36	—	-0.22	1.13		
		2-x-3	Combination-κ=1	0.15	0.61	—	-0.38	1.11		
3	Q460	3-1-1	Smooth round bar	0.57	1	1	1	1.60	3.81	1.57
		3-1-2	Notched round bar-R=6.25mm	0.88	1	1	1	0.95		
		3-1-3	Notched round bar-R=3.125mm	1.03	1	1	1	0.74		
		3-1-4	Notched round bar-R=1.5mm	1.33	1	1	1	0.54		
		3-0-1	Grooved plate-R=10mm	0.76	0	0	0	0.95	2.57	1.30
		3-0-2	Grooved plate-R=3mm	0.84	0	0	0	0.85		
		3-0-3	Grooved plate-R=1mm	1.20	0	0	0	0.52		
		3-x-1	Pure shear flat plate	0.11	0.32	0.21	-0.19	1.46		
		3-x-2	Tensile shear flat plate	0.43	0.90	0.71	-0.68	1.26		
4	Q690	4-1-1	Smooth round bar	0.64	1	1	-1	1.17	8.25	3.03
		4-1-2	Notched round bar-2	1.05	1	1	-1	0.36		
		4-1-3	Notched round bar-1	1.21	1	1	-1	0.19		

4-0-1	Pure shear	0.01	0	0	0	1.36	1.36	0.54
4-0-2	Grooved plate-2	0.85	0	0	0	0.84		
4-0-3	Grooved plate-1	0.96	0	0	0	0.83		

Note: The values of T_{avg} and ξ_{avg} are obtained from the literature as the reported integrated values, as per Eqs. (2-13) and (2-14).

Data from the notched round bars, grooved plate, and pure shear specimens are plotted in Fig. 3-20 along with the calibrated VGEFs for Lode angle parameter stress states of $\xi = 1$ and $\xi = 0$. The close agreement between the VGEF and measured fracture strains confirms the accuracy of VGEF in capturing the effect of stress triaxiality for the four steel grades and two Lode angle parameters.

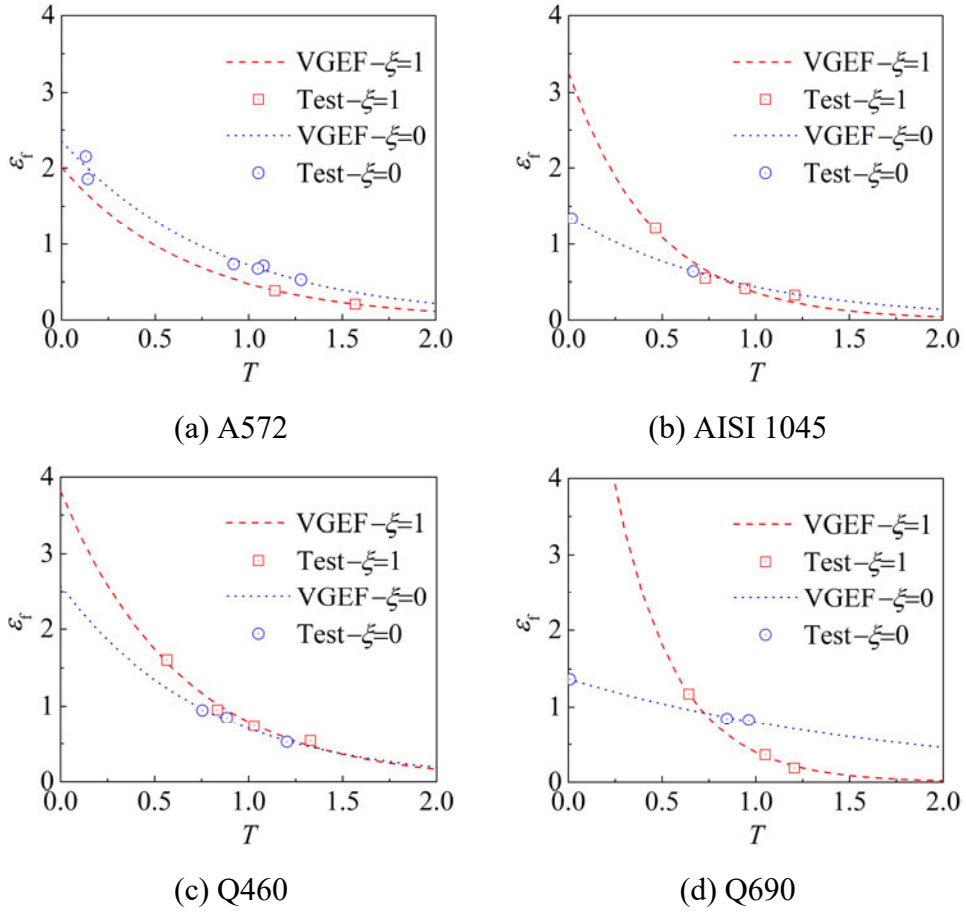

(a) A572 (b) AISI 1045

(c) Q460 (d) Q690

Figure 3-20. Experimental and predicted fracture strains.

The parameter $K(T)$, calculated according to the following equation is proposed to relate the Lode angle parameter to the fracture strain at different stress triaxialities,

$$K(T) = \frac{\varepsilon_f^{\xi=1}(T) - \varepsilon_f^{\xi=0}(T)}{1-0} = \varepsilon_f^{\xi=1}(T) - \varepsilon_f^{\xi=0}(T) = a_1 \cdot e^{-b_1 T} - a_0 \cdot e^{-b_0 T} \tag{3-12}$$

where a_1 and b_1 are the two parameters defined in Eq. (2-16) for $\xi = 1$, and a_0 and b_0 are the two parameters in the same equation for $\xi = 0$.

As illustrated in Fig. 3-21, $K(T)$ is the slope, relative to the T-ξ plane, of the straight line connecting two corresponding points with identical T. The solid black line in Fig. 3-21 highlights the connection between two measured data points with T=0.9 for Q460 steel. A value (slope) of $K(T)$ equal to zero implies a negligible effect of Lode angle on the fracture strain, while a large (absolute) value of $K(T)$ indicates a significant Lode angle effect. For each steel alloy considered in this section, $K(T)$-values were calculated for T in the range between 0 and 2. Table 3-15 summarises the $K(T)$-values for representative stress triaxialities.

It is noted from Table 3-14 that for each material, two tests shared approximately identical values of triaxiality T while one had a Lode angle parameter of $\xi = 1$ and the other $\xi = 0$. These test pairs included Nos. 1-1-1 and 1-0-2 for A572 steel, Nos. 2-1-2 and 2-0-2 for AISI 1045 steel, Nos. 3-1-2 and 3-0-2 for Q460 steel, and Nos. 4-1-2 and 4-0-3 for Q690 steel. Therefore, $K(T)$ can also be directly calculated using these test results simply as $\varepsilon_f^{\xi=1}(T) - \varepsilon_f^{\xi=0}(T)$. In Table 3-15, these experimentally calculated values are shown in brackets. The values are very close to the values calculated by Eq. (3-12) based on the VGEF, further confirming the accuracy of the VGEF and Eq. (3-12).

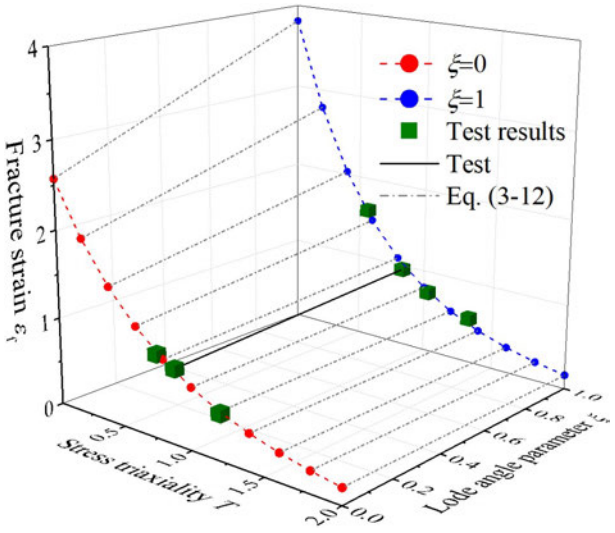

Figure 3-21. Experimental and predicted fracture strains for Q460.

Table 3-15. $K(T)$ for T ranging from 0 to 2.

T	0	0.1 to 0.6	0.7	0.8	0.9	1.0	1.1	1.2 to 1.9	2.0
A572	-0.34	-0.34 to -0.31	-0.29	-0.27	-0.25	-0.24	-0.22 (-0.30)	-0.21 to -0.12	-0.11
AISI 1045	1.89	1.40 to 0.18	0.08 (-0.09)	0.01	-0.03	-0.07	-0.10	-0.11 to -0.11	-0.10
Q460	1.24	1.00 to 0.30	0.23	0.17	0.13 (0.11)	0.09	0.06	0.04 to -0.03	-0.03
Q690	6.88	4.79 to 0.35	0.05	-0.15	-0.30	-0.40 (-0.46)	-0.46	-0.50 to -0.46	-0.44

Note: Values in brackets are calculated using test results in Table 3-14.

The calibrated values of $K(T)$ versus T are plotted in Fig. 3-22 for the four steels. The points representing the $K(T)$-values calculated by Eq. (3-12) using the test results are also plotted in the figure, highlighting that the calibration is anchored to experimental data for triaxialities between 0.65 and 1.1. The non-zero values of $K(T)$ confirm that the Lode angle has a significant influence on the fracture strains of the steels, however, the differences between the various curves indicate that the Lode angle effect varies with stress triaxiality and type of steel. A few specific observations are as follows:

1) The absolute value of K decreases sharply with increasing stress triaxiality until reaching a value of approximately zero, indicating a less important influence of the Lode angle at high triaxialities. This observation is consistent with the well-acknowledged theory that stress triaxiality is the primary driving force causing fracture in the high triaxiality region.
2) In the low triaxiality range, the value of K increases with increasing yield stress. This can most likely be related to the different microscopic behaviour of the steels caused by different crystalline structures and inclusions, e.g. resulting from different chemical compositions and different thermal or mechanical processes used to produce the steel; a topic requiring further investigation at the microscopic level.
3) The $K(T)$-curve for A572 steel is negative over the entire range of stress triaxiality, which is different from the trends of the other three steels. This variability $K(T)$ between the steels is consistent with data shown previously in Figs. 3-18 and 3-19, where the fracture strain at $\xi = 1$ can be either larger or smaller than that at $\xi = 0$, depending on the alloy. This finding reiterates the result that the fracture properties

of seemingly similar steels are not necessarily similar.

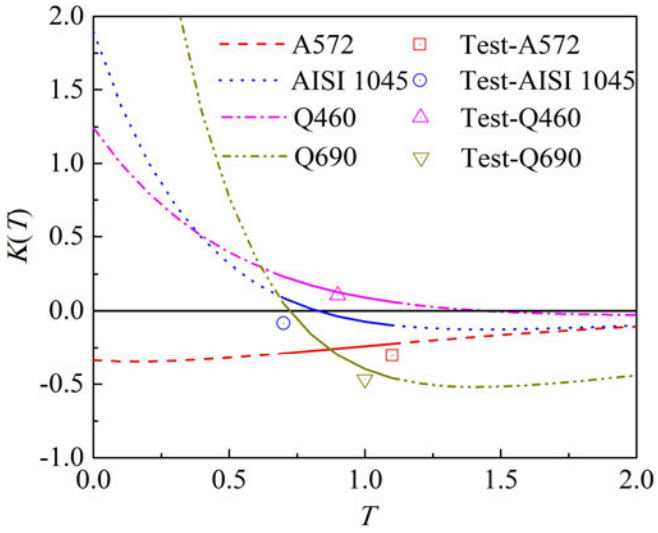

Figure 3-22. Slope $K(T)$ of fracture surface for increasing Lode angle parameter ξ as function of triaxiality T.

3.4 Lode angle modified void growth model

Based on the data presented in Section 3.3, it is concluded that the relationship between the Lode angle parameter and fracture strain can be described using an exponential function, i.e. Eq. (3-12). Therefore, by combining this equation and the Void Growth-based Exponential Function (VGEF), i.e. Eq. (2-16), which has been shown to be capable of describing the effect of stress triaxiality in Section 3.2, a new fracture model, termed the Lode angle Modified Void Growth Model (LMVGM), is proposed as follows,

$$\varepsilon_{\mathrm{f}} = \alpha \cdot e^{-\beta \cdot T + \gamma \cdot \xi} \tag{3-13}$$

where α, β and γ are free parameters. Average values of stress triaxiality T_{avg} and Lode angle parameter ξ_{avg}, as defined in Eqs. (2-13) and (2-14) respectively, would ordinarily be used for T and ξ in Eq. (3-13) when the stress state changes during loading. An alternative way of accommodating variations in T and ξ during the loading history is to integrate the damage index D over the plastic strain history as follows,

$$D = \int_{\varepsilon_{\mathrm{p}}} \frac{1}{\alpha} \cdot e^{\beta T - \gamma \xi} d\varepsilon_{\mathrm{p}} \tag{3-14}$$

where fracture is predicted when D reaches unity.

In the rest of this section, the LMVGM is compared to three alternative models from the literature, including VGM (Eq. (2-19)), SWDFM (Eq. (2-22)), and LHM (Eq. (2-23)). The

three fracture models are widely accepted, which have been introduced in Section 2.3 and have comparable numbers of parameters as LMVGM. In addition, for LHM According to [17], the parameters C_1 to C_3 should all be positive values, however, as demonstrated by the test data in Sections 4 and 5, the parameter C_1, which describes the effect of the Lode angle, can also be negative for certain steel grades.

It is noted that the SWDFM has a similar form to the LMVGM. However, the two models are different in the following respects. First, the SWDFM is targeted at cyclic loading, while the LMVGM is based on monotonic loading tests. Second, in the SWDFM, the effect of the stress triaxiality is described using a hyperbolic sine function (with the added term $1/\beta_{SWDFM}$), which can consider both the void growth at positive triaxiality and void shrinkage at negative triaxiality under cyclic loading. The parameter β_{SWDFM} is then used to represent the ratio between the rates of void growth and shrinkage. The hyperbolic sine function also implies the existence of a cutoff value for the stress triaxiality below which no damage occurs. The cutoff value can be zero or negative depending on the value of the parameter β_{SWDFM}. The LMVGM, on the other hand, uses the VGEF to describe the effect of stress triaxiality. Since the presence or absence of a cutoff value of stress triaxiality for various materials and stress states is still under discussion and fracture has been observed at stress triaxialities lower than -0.4 in experiments [24, 110], the VGEF, whose applicability for negative low and high triaxialities has been verified experimentally in Section 3.2, is chosen for the LMVGM. (Note that fracture under high negative stress triaxiality rarely occurs in practice, because the fracture strain under such triaxialities is substantially higher than the strain magnitudes typically developing in structural components. Hence, whether a cut-off value of triaxiality should be imposed is more an academic than practical consideration). Third, according to [14, 15], the fracture locus under cyclic loading is symmetric with respect to ξ=0 in the first and third quadrants of the T-ξ stress space, i.e. $T > 0$, $\xi > 0$ and $T < 0$, $\xi < 0$. This is the reason for the absolute value applied to the ξ variable in Eq. (2-22). This symmetry with respect to ξ in the SWDFM is in contrast to the situation studied in Section 3.3, where under monotonic loading, the fracture locus is asymmetric about ξ=0 in the first and second quadrants of the T-ξ stress space, i.e. $T > 0$, $\xi > 0$ and $T > 0$, $\xi < 0$. Therefore, in comparing how symmetry with respect to ξ is treated in the LMVGM versus SWDFM, one should recognize that they were each developed with different loading states in mind, i.e., monotonic loading in the case of LMVGM and reverse cyclic loading for SWDFM.

The experimental results collected from the literature in Tables 3-13 and 3-14 were used to compare the accuracy of the LMVGM to those of the VGM, LHM and SWDFM. Firstly, the free parameters of the fracture models are calibrated and summarized in Table 3-16. As noted previously, for the LHM, the Lode parameter L (or alternatively L_{avg}) is related to the Lode angle parameter ξ (or alternatively ξ_{avg}) using Eq. (2-11). In addition, since the test of the compressive cylinder for AISI 1045 steel has a stress triaxiality of T = -0.49 that is lower than the cutoff value in LHM (T_{cutoff} = -1/3) and SWDFM (T_{cutoff} = 0), comparisons of the AISI 1045 steel are not included for LHM and SWDFM.

Based on the calibrated parameters in Table 3-16, the predictive accuracy of each fracture model is evaluated by comparing the model prediction to the experimental data. Two indexes are used to quantify the accuracies. The first one, as compared in Fig. 3-23, is the RMSRE (Eq. (3-4)) of the predicted fracture strains for each steel type, and the second one, as compared in Fig. 3-24, is the Average Squared Error (ASE) of predicted damage $D_{\text{f-pred}}$, calculated as follows,

$$\text{ASE} = (1/N) \times \sum_{i=1}^{N} \left(1 - D_{\text{f-pred}}^{i}\right)^2 \times 100\% \tag{3-16}$$

where N is the number of tests for each material.

Table 3-16. Free parameters of fracture models.

No.	Fracture models		DP600	TRIP 690	DP980	22MnB5	A572	AISI 1045	Q460	Q690
1	LMVGM	α	0.73	0.59	0.67	0.84	2.39	1.06	1.51	1.50
		β	0.97	0.12	0.33	0.83	1.30	1.29	0.86	0.77
		γ	-0.45	-0.34	0.11	0.25	-0.33	0.38	0.23	-0.67
2	VGM	η	0.55	0.60	0.64	0.82	2.29	1.02	1.80	1.53
		λ	0.92	0.29	0.29	0.91	1.44	0.85	0.88	1.43
3	LHM	C_1	4.98	3.98	1.02	-1.07	-3.46	—	1.75	-5.88
		C_2	0.95	0.35	0.24	0.54	1.17	—	0.89	0.56
		C_3	0.68	0.80	0.65	0.55	0.81	—	1.50	0.54
4	SWDFM	C_{SWDFM}	1.50	0.80	0.87	0.94	0.55	—	0.35	0.72
		β_{SWDFM}	6	10	17	14	8	—	15	10
		k_{SWDFM}	-0.13	-0.72	-0.44	-0.13	0.28	—	-0.33	0.19

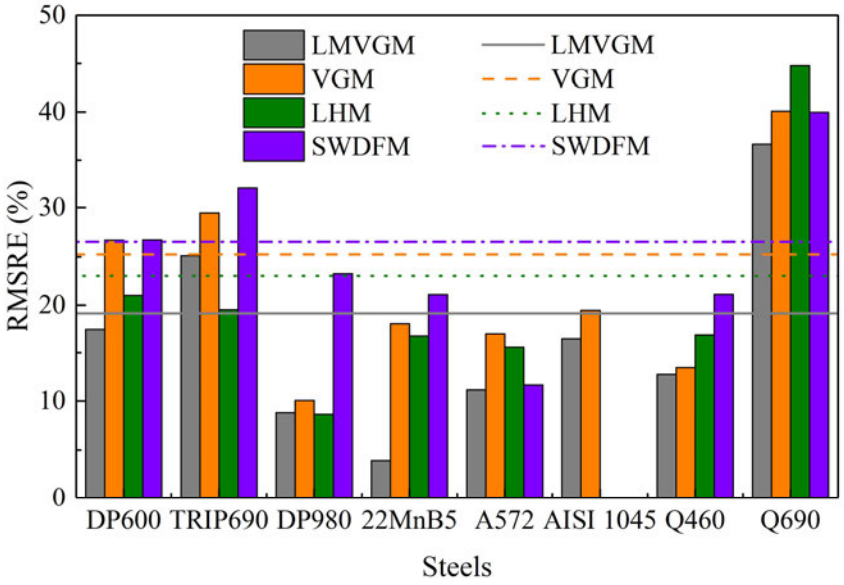

Figure 3-23. The RMSRE values of fracture models.

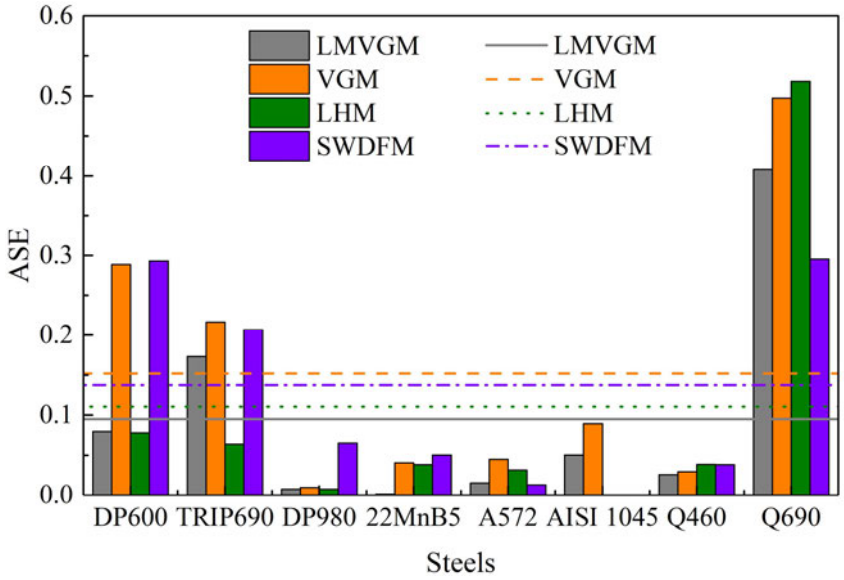

Figure 3-24. The ASE values of fracture models.

The overall RMSREs for LMVGM, VGM, LHM and SWDFM are 19.1%, 25.2%, 23.0%, and 26.5%, respectively, while the overall ASE values are 0.09, 0.15, 0.11, and 0.14. It is noted that for all four fracture models, the RMSRE and ASE values of Q690 steel are significantly higher than those of the other seven steels. Excluding the results for Q690 steel, the overall RMSREs of the other seven steels for LMVGM, VGM, LHM and SWDFM are 15.0%, 20.2%, 16.8% and 23.5%, respectively, while the overall ASE values are 0.05, 0.10, 0.04, and 0.11.

From Figs. 3-23 and 3-24, it is observed that the accuracy of the SWDFM is consistently less than the other models for the first four steel grades, which include results for tests under equi-biaxial tension. The lower accuracy is explained in part by the fact that the SWDFM was

developed for cyclic loading in the first and third quadrants of the T-ξ stress space (Fig. 2-2), whereas the equi-biaxial tension specimens interrogate the second quadrant of the T-ξ stress space. For the other four steels, the results for the SWDFM are more in line with the other models but still less accurate than the LMVGM model. Compared to the other two monotonic fracture models (VGM and LHM), the LMVGM is consistently more accurate because of the way that accounts for the Lode angle effect. Overall, the newly proposed LMVGM provides the most accurate predictions using a simple equation with only three free parameters.

3.5 Summary

This chapter investigated the effects of stress triaxiality and Lode angle on the fracture of structural steels under a wide range of stress states based on experimental evidence. A large amount of experimental data was collected from the literature, and additional series of newly designed plane strain specimens and rectangular notched specimens were tested to augment the experimental database. The discussion was carried out separately for groups of tests with identical stress triaxiality or Lode angle parameter to obtain the isolated effect of each parameter.

The validity of the void growth-based exponential function over a wide range of stress triaxialities was assessed based on the fracture strains under stress states with identical Lode angle parameter and different stress triaxialities. The VGEF showed good accuracy for high stress triaxiality states, while for stress states covering high, medium and low stress triaxialities, the average relative error of VGEF slightly increased. It is concluded that, in general, the VGEF can be adopted to accurately describe the effect of stress triaxiality over the full range of stress triaxialities. In addition, although it is difficult to perform tests in the low stress triaxiality regime, it is recommended to calibrate the VGEF parameters with some data in this region, rather than extrapolating the calibration from tests in the high stress triaxiality regime.

A thorough understanding of the Lode angle effect was developed based on analyses of experimental results. It is concluded that the Lode angle has a demonstrative effect on the fracture strain of steels, and its dependence can be captured by an exponential function for the full range of Lode angle parameters from -1 to 1. This also implied an asymmetric fracture locus with respect to the central Lode angle parameter line, $\xi = 0$. The effect of the Lode angle increased with a decreasing value of the stress triaxiality and was more pronounced for high strength steels.

Having quantified the dependence of the fracture strain on the stress triaxiality and the Lode angle parameter based on these data sets, a new fracture model called the Lode angle Modified Void Growth Model (LMVGM, see Eq. (3-13)) was proposed and validated against experimental results. The LMVGM, which included three free parameters, combined the effect of stress triaxiality T, through the Void Growth Exponential Function (VGEF), and the effect of the Lode angle parameter ξ, using an exponential function. Similar to other void growth models, the LMVGM predicted that the critical fracture strain would decrease under increasing T. On the other hand, the model and supporting test data indicated that critical fracture strain did not present a consistent trend with respect to the Lode angle parameter, ξ, i.e., the fracture strains might increase or decrease with increasing ξ, depending on the material.

Chapter 4 Stress-strain relationships of weld, HAZ and base metal

4.1 Introduction

Fracture in welded steel connections accompanying large plastic deformation is an important mode of failure in steel structures. Therefore, it is necessary to investigate and simulate the fracture in welded connections to assess the performance of the steel structures. In welded connections, the high temperature and different cooling rates during the welding process lead to locally different microstructures, inhomogeneous properties and residual stresses in the weld zone, which can be divided into three material areas, base metal, weld and heat affected zone (HAZ). To investigate the fracture in welded connections, the weld-zone mechanical properties and WRS were measured to discuss their effects on the performance of the welded connections in the following chapters. As introduced in Chapter 2, many studies have been carried out to quantitatively investigate the mechanical properties of the weld zone, but limited data is available for structural steels, and the difference in the properties between the longitudinal and transverse directions has rarely been discussed. In this chapter, the stress-strain relationships of the weld and HAZ in the weld zone of butt-welded plates were measured for both longitudinal and transverse directions and compared with those of the base metal.

In Section 4.2, the weld geometry, the materials and welding parameters of the butt-welded plates are introduced. In Section 4.3, after macroetching the cross-sections of the plates, the areas of the base metal, weld and HAZ are identified, after which hardness tests are performed for the three material areas. In Section 4.4, considering the narrow sizes and irregular shapes of the weld and HAZ in the weld zone, a series of miniature flat plate coupons are designed to measure the stress-strain relationships of the three material areas in both longitudinal and transverse directions. To support these miniature coupons, a pair of custom-built jigs were designed, and tensile tests were then conducted. In Section 4.5, the true stress-strain relationships of the base metal, weld and HAZ are obtained for both directions based on the experimental results and corresponding FE simulations. The differences in the yield stress and ultimate stress among the three material areas and between the two directions are discussed. In Section 4.6, tensile tests are carried out on normal-size specimens extracted from the base metal. Their test results are compared with those obtained from the miniature coupons to discuss the accuracy of the miniature coupon testing scheme and setup. Section 4.7 summarizes the

experimental and simulated results of the miniature flat plate coupons extracted from the three material areas in the two directions.

4.2 Materials and welding

Two butt-welded plates were made for the measurement of local properties in the weld zone, as shown in Fig. 4-1. The components were cut from 10 mm thick AS350 grade steel plates [100]. The single-V butt welds were welded on one side of the plate with a backing strip on the other side, and the joint preparation was prequalified according to [111] with the width of the root gap being 6 mm and the included angle being 30°. The longitudinal and transverse directions were defined in Fig. 4-1, where the longitudinal direction was the same as the rolling direction of the steel plate. The butt welds were made by four runs through the Gas Metal-Arc Welding (GMAW) using the welding wire of grade B-G49 [111], and the shielding gas of 18% CO_2 bal Ar. The welding voltage ranged from 23 to 26 V, the current ranged from 200 to 220 A, and the welding speed ranged from 200 to 250 mm/min, i.e. the heat input ranged from 1.10 to 1.71 kJ/mm. Weld Australia was consulted to review the Welding Procedure Specifications (WPSes) and confirmed the WPSes satisfied the requirements of the AS/NSW 1554.1:2014 SP Category [111]. Weld Australia's representative was present during the welding to ensure the welding was performed with the welding parameters within the proposed ranges.

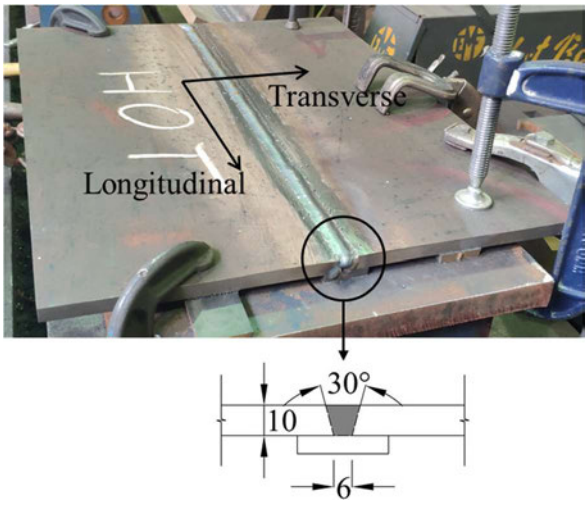

Figure 4-1. Single V groove butt weld.

4.3 Macroetching and hardness tests

Four 10 mm thick slices were cut from each welded plate, as shown in Fig. 4-2, after removing the 40 mm long parts from the edges to eliminate the run-on and run-out effects. The weld zones of the slices were cut in half, making 16 pieces in total, which were then mounted in epoxy resin. After grinding and polishing, their surfaces were etched using 4% nitric acid. The

photo of an etched surface is shown in Fig. 4-3(a). The dividing lines between the weld and HAZ and between the HAZ and the base metal were observed in the weld zone, and the three material areas were distinguished, which are highlighted with different colours in Fig. 4-3(b). It's worth noting that because it is difficult to extract miniature coupons for the HAZ subareas with tiny widths, the HAZ area studied in this project was considered a single area without subdivisions.

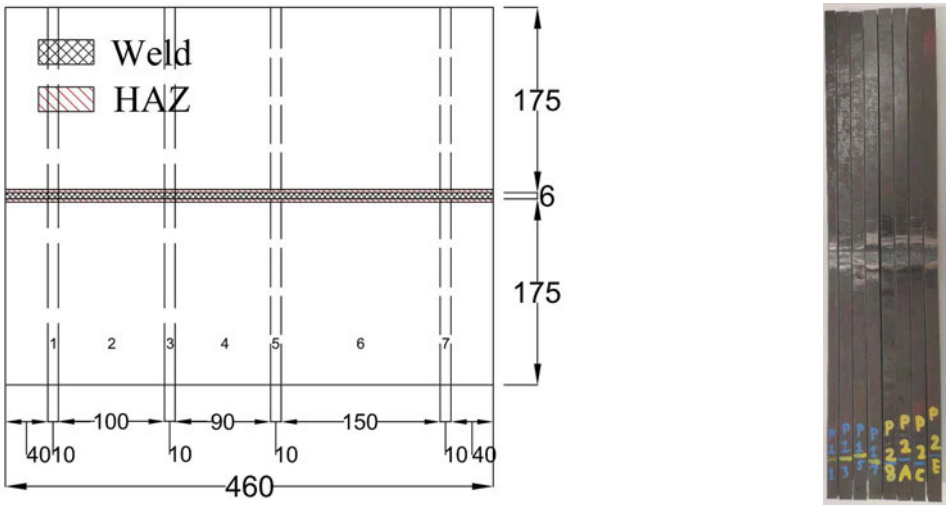

(a) Segmentation drawing of a welded plate (b) Photo of slices

Figure 4-2. Slices cut from welded plates.

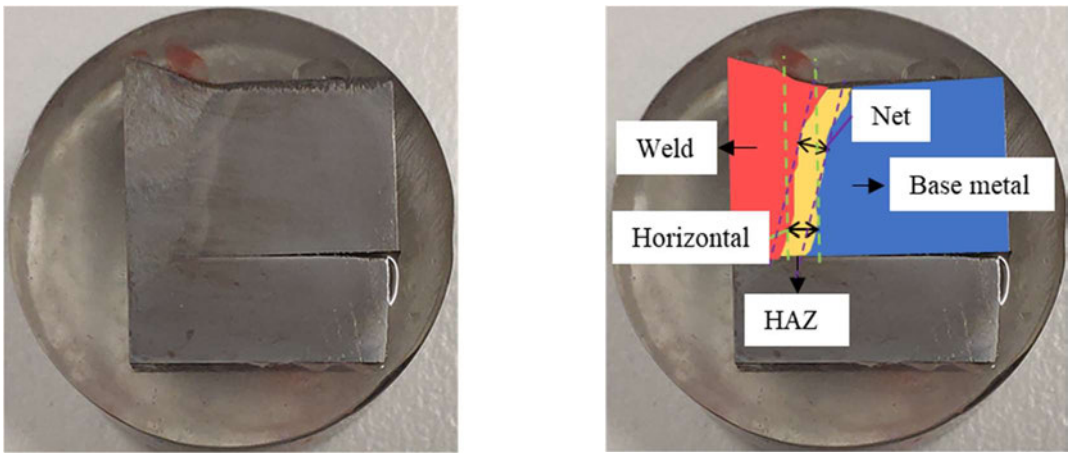

(a) Etched surface (b) Etched surface with colour-filled areas

Figure 4-3. Photo of etched surface.

The width of the HAZ was measured as the distance between the two dividing lines at different distances from the top surface of the plate along two directions. In this study, both the horizontal distance and the nominal net distance in the direction perpendicular to the V groove (i.e., the direction with a 15° slope) were measured as shown in Fig. 4-3(b), representing the horizontal width and net width of the HAZ, respectively. For each macro-etched piece, the

horizontal width and net width were measured from six positions at different distances from the top surface of the plate, making a total of 96 measurements for both the horizontal and net width, as shown in Fig. 4-4. The majority of the measurements ranged from 1.5 mm to 3.0 mm, with the average values being 2.23 mm and 2.08 mm for the horizontal and net width, respectively. It was observed that the measured results of the horizontal width were slightly more discrete than those of the net width.

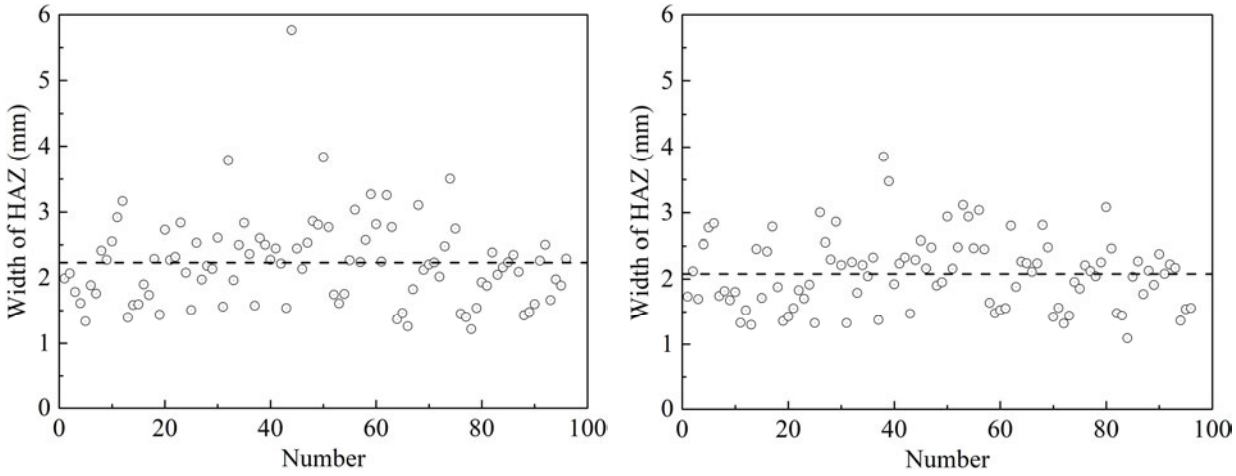

(a) Horizontal width (b) Net width

Figure 4-4. Width of HAZ.

The Vickers hardness was measured on the surfaces of two pieces cut from one slice using the DuraScan machine. Measurements were conducted at 18 locations, six in the weld area, six in the HAZ area and the rest six in the unaffected base metal area. The three locations in each material area were randomly selected, and the distance between each location was large enough that they did not interact with each other. The test result of the Vickers hardness for one location in the base metal area is shown in Fig. 4-5. Under the load of 4.9 N (0.5 kg), the average indentation sizes were 77.15 μm, 71.29 μm and 67.32 μm, and the average HV0.5 values were computed as 155.5, 182.7 and 205.3, for the base metal, HAZ and weld, respectively, as shown in Fig. 4-6. The comparison among the results of the three material areas showed that the weld had the highest hardness while the base metal was the softest.

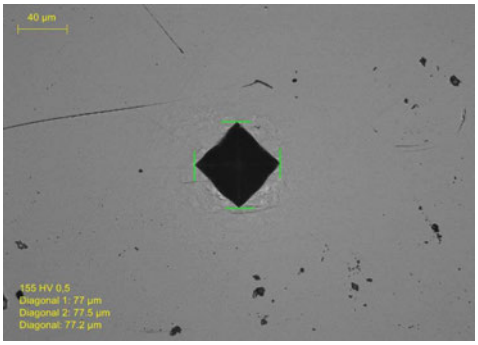

Figure 4-5. Measurement of hardness for one location in the base metal area.

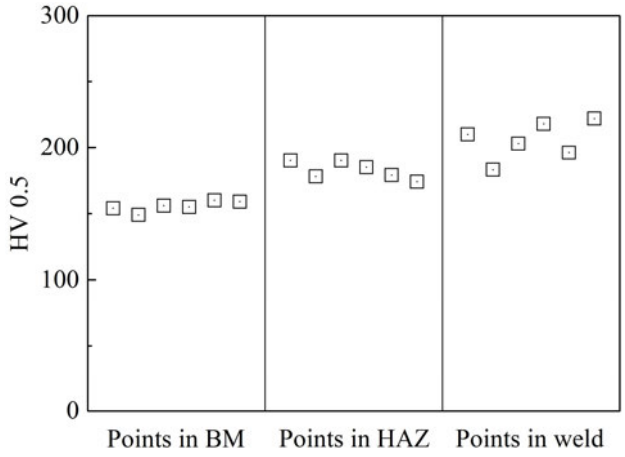

Figure 4-6. Hardness values of the base metal (BM), HAZ and weld.

4.4 Tensile coupon tests

4.4.1 Specimen design

Miniature flat plate (FP) coupons were designed to determine the stress-strain relationships of the three material areas in the weld zone of the butt-welded plates. The dimensions of the cross-section of the parallel part in these miniature FP coupons were in the range of 1 mm to 2.5 mm, and their geometries are shown in Fig. 4-7. The miniature coupons were extracted from the three material areas in the weld zone, which were identified according to the macroetching results. In order to discuss the difference in the properties between the two directions, the miniature coupons were extracted along the longitudinal and transverse directions. Fig. 4-8 demonstrates the locations and directions of the coupon extraction, where the letter "BM" refers to the base metal, "FP" to the flat plate coupons, and "L" and "T" to the longitudinal and transverse directions, respectively.

The miniature longitudinal flat plate coupons (i.e., FPL), as shown in Fig. 4-7(a), were proportionally scaled down from standard coupons [101]. The gauge length of the standard coupons was equal to $L_0 = 5.65\sqrt{A_0}$, where A_0 was the size of the cross-section of the parallel

part. Hence, the FPL coupons with a cross-section of 2.5 mm × 1 mm had a gauge length of 9.0 mm and the parallel length of 11.4 mm. As the miniature transverse flat plate (i.e., FPT) coupons crossed through the narrow areas of the weld and HAZ, the FPT coupons were designed with the parallel part being only 3 mm long and gauge length being 2 mm to ensure that an FPT coupon contained only one material area within its gauge length, as shown in Fig. 4-7(b).

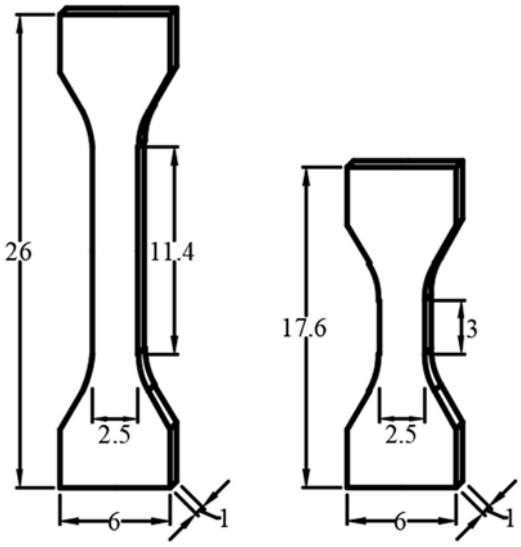

(a) FPL (b) FPT

Figure 4-7. Geometry and dimension of miniature FP coupons (mm).

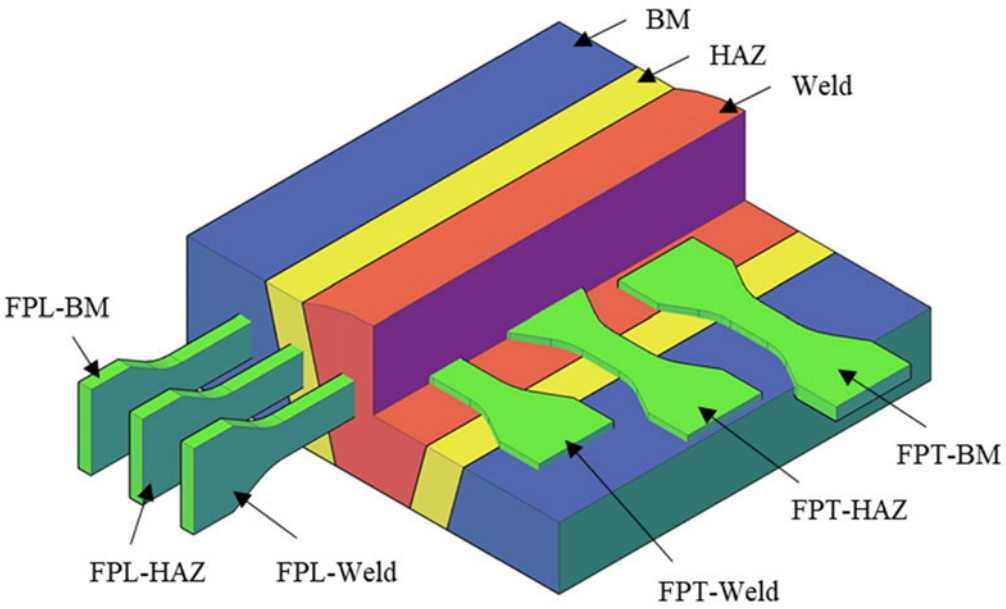

Figure 4-8. Location and direction of flat plat specimens extracted from the butt-welded plate.

4.4.2 Test setup

The uniaxial tensile tests were carried out on the miniature coupons using a 300 kN MTS Sintech testing machine, as shown in Fig. 4-9. Considering that the fracture load of the miniature FP coupons was much lower than the capacity of the testing machine, the test frame was equipped with a 300 kg load cell. Due to its small size, the miniature coupon can easily be altered or destroyed by the bending strains caused by small misalignments when performing tension tests. Therefore, the test frame was equipped with a pair of custom-built jigs consistent with the coupon dimensions to support the miniature coupons. Because the parallel part of the miniature FP coupons was only 11.4 mm, the space between the two grips could not accommodate an ordinary extensometer. Therefore, the relative displacement between the upper and lower grips was measured using an extensometer with a gauge length of 25 mm, and the deformation of the miniature coupons was directly measured using the DIC system.

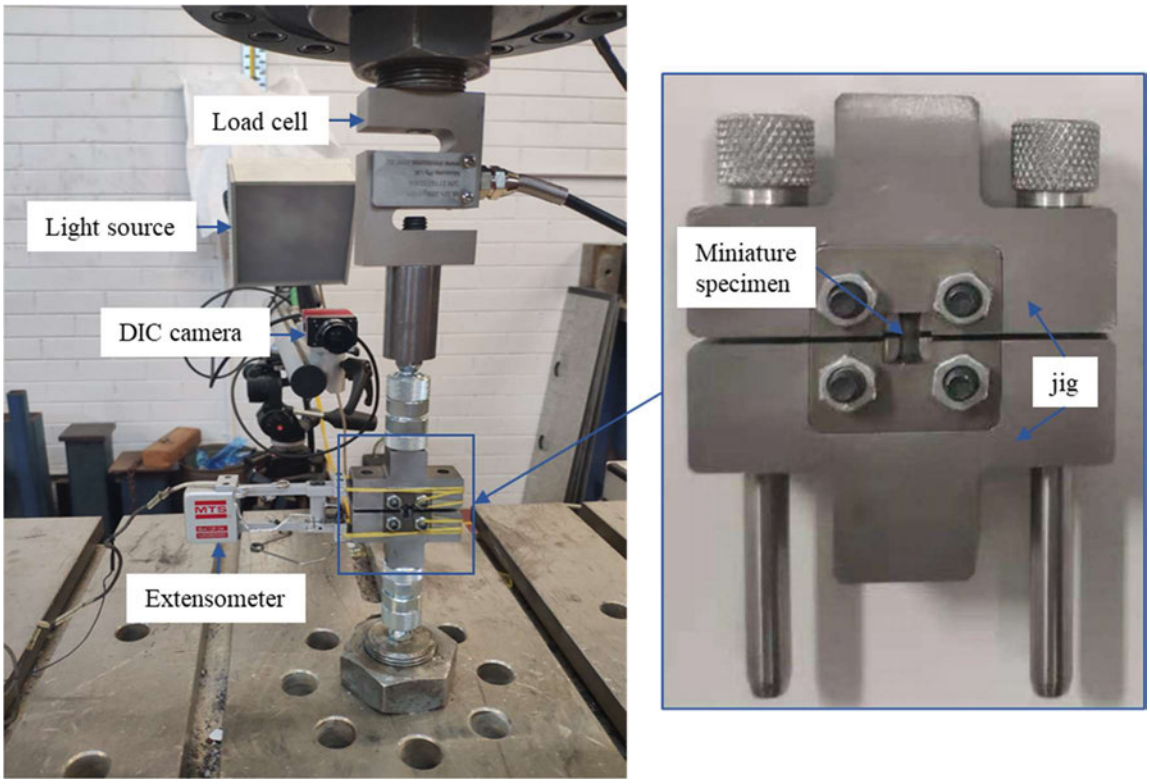

Figure 4-9. Test setup of miniature FP specimens.

The design of the test jig is shown in Fig. 4-10. The jig included two grips, each with an open slot for easy fixing of the miniature coupon and ensuring alignment of the specimen in the grips. The open slots were in the shape of the end of the miniature coupon, including the transition curves and part of the parallel length. A pair of interchangeable spacers were used to accommodate the miniature coupons with different thicknesses and fixed by a bolted top cover

from each side of the grip. At the end of each grip, a universal joint was used to connect the grip to the support and the crosshead of the testing machine. Therefore, the axiality of the miniature coupon in the grips was ensured with no bending moment applied to it caused by possible misalignments. Two guides were used to facilitate the installation of the miniature coupon into the grips, as well as the installation of the grips to the testing machine. The guides were removed before the commencement of the test to avoid the possible friction effect.

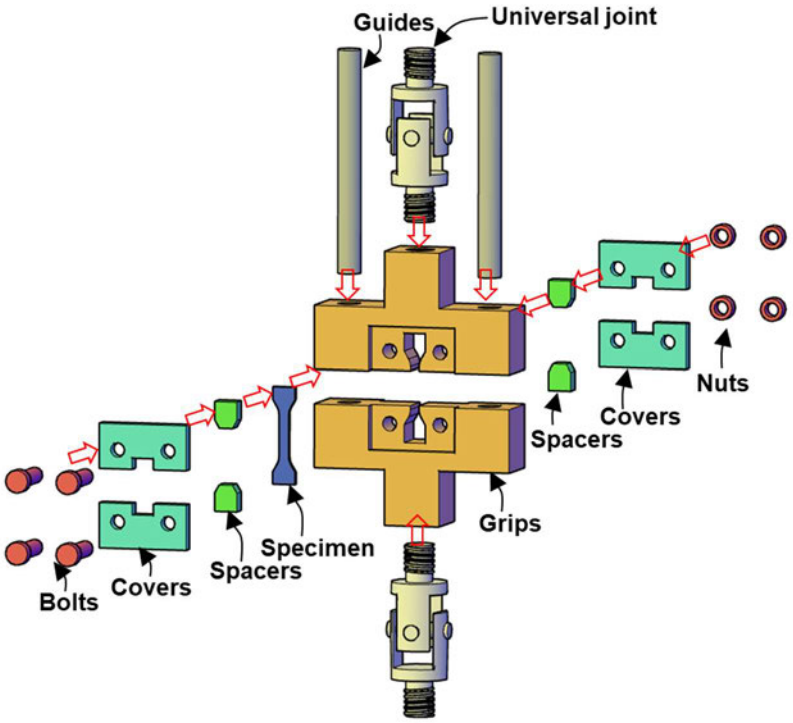

Figure 4-10. Design of custom-built jigs.

The DIC system was used to measure the deformation of the miniature coupon due to its small size. Before using the DIC to evaluate the coupon deformation from the captured camera images, the projection parameters of the system were required to be calibrated using a calibration target. To make sure the DIC system was well calibrated, the values of the relative displacement between the upper and lower grips measured by the extensometer and the DIC system were compared. Using the DIC system, one point on the upper grip and another point on the lower grip captured by DIC camera were set as reference points and the distance along the loading direction between the two points were measured during the loading process. The deformation between the upper and lower grips measured by DIC system was then calculated. The load-deformation curves measured by the two methods for the test on an FPL coupon extracted from the base metal were plotted in Fig. 4-11. It is shown that the measurements of the deformation using the extensometer and the DIC system agreed well with each other, and

it is proved that the DIC system was well calibrated, and its results were reliable. Therefore, the deformations of the miniature coupons could be directly measured using the calibrated DIC system. The gauge length (i.e., L_0) of the DIC measurement was set as 9 mm for miniature FPL coupons, while the gauge length of miniature FPT coupons was set as 2 mm. The DIC camera was set to take photos every second to obtain the images of the miniature coupon during the loading process. To obtain the static load-deformation curves, the loading was controlled at a low speed of 0.5 mm/min and paused two or three times for 100s to allow stress relaxation. The static load-deformation curves were then obtained following the same method adopted in Chapter 3.

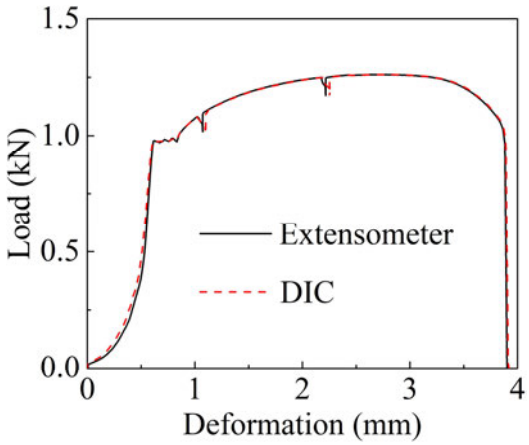

Figure 4-11. Load-deformation curves measured by extensometer and DIC.

4.5 Measurement of stress-strain relationships

4.5.1 Experiment results

As observed during the loading process and in Fig. 4-12, the plastic deformation was highly localised at the parallel part of the coupon where fracture finally occurred. Six replicated tests were conducted for each material area in each direction, leading to 36 tests in total. The load-deformation curves of the FPL and FPT coupons are presented in Figs. 4-13 to 4-15. The test curves of the miniature FP coupons reached a maximum load when necking commenced and were truncated at the fracture initiation point, where a steep drop occurred. The discreteness of the fracture deformation of FPL coupons may be caused by a slight deviation existing in the manufacturing process of the material and the tiny coupon size.

The maximum load, P_{max}, the deformation at which fracture occurred, D_f, and the percentage elongation corresponding to the fracture initiation, $\delta_f = D_f / L_0$, are summarized for the three material areas in Tables 4-1 to 4-3. Note that the δ_f values were not comparable between the FPLs and FPTs as they adopted different L_0. The following observations were made:

1) For both the longitudinal and transverse directions, the curves of the base metal were nearly identical, while those of the weld and HAZ showed large variations in terms of both the onset of yielding and post-yielding response. The large scatter indicated that the material properties of the weld and HAZ were relatively less homogeneous than those of the base metal, resulting from the steep temperature gradient near the fusion line.
2) The average maximum loads of the base metal, weld and HAZ were 1.16 kN, 1.43 kN and 1.37 kN for the longitudinal direction, and 1.13 kN, 1.45 kN and 1.30 kN for the transverse direction, respectively. The maximum loads of the HAZ were higher than those of the base metal but lower than those of the weld in both directions, and the maximum loads of the three material areas in the weld zone were similar between the two directions.
3) The average percentage elongations of base metal, weld and HAZ were 0.29, 0.24 and 0.20 for the longitudinal direction, and 0.58, 0.42 and 0.38 for the transverse direction, respectively. The comparison of percentage elongations showed that the base metal showed the best ductility in both directions, while the HAZ material showed the worst.

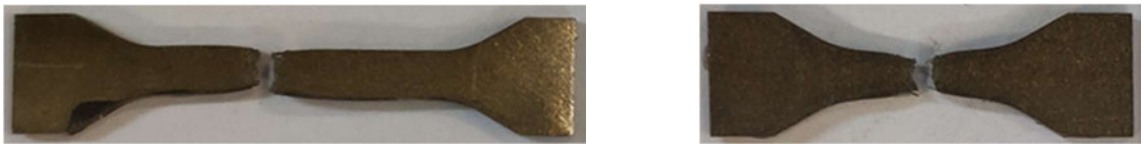

(a) FPL (b) FPT

Figure 4-12. Fractured miniature flat plates for base metal.

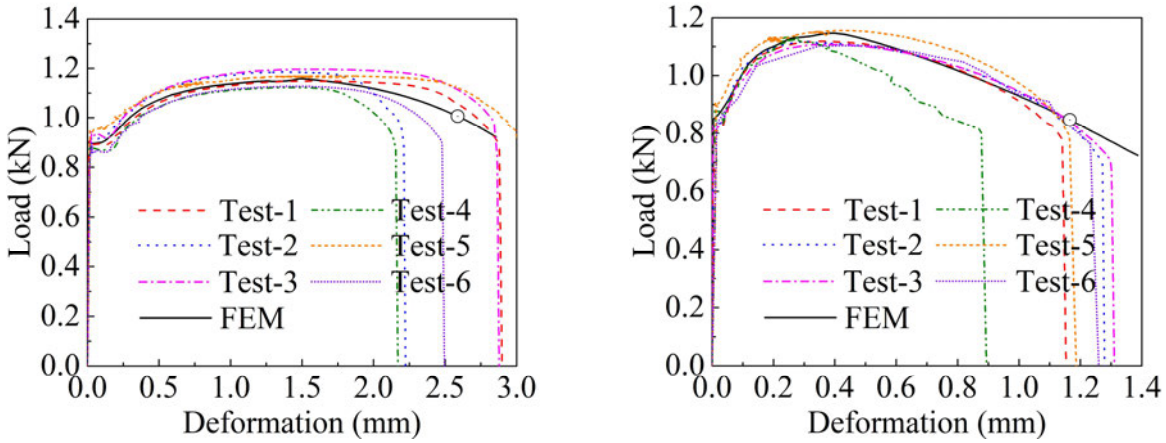

(a) Longitudinal (b) Transverse

Figure 4-13. Load-deformation curves of base metal.

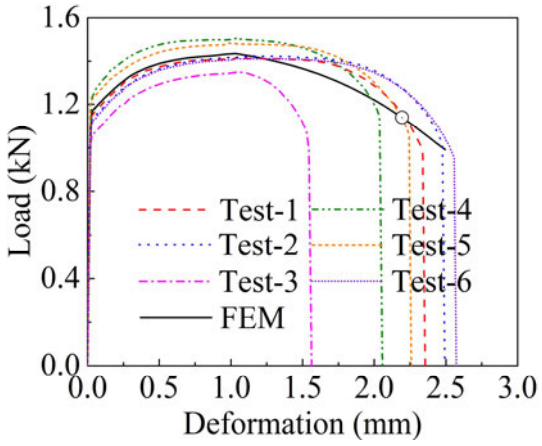

(a) Longitudinal

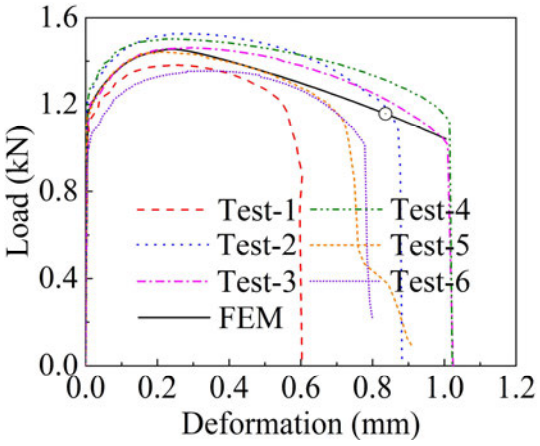

(b) Transverse

Figure 4-14. Load-deformation curves of weld.

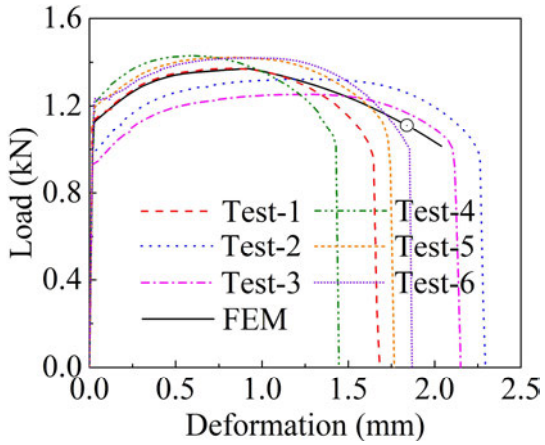

(a) Longitudinal

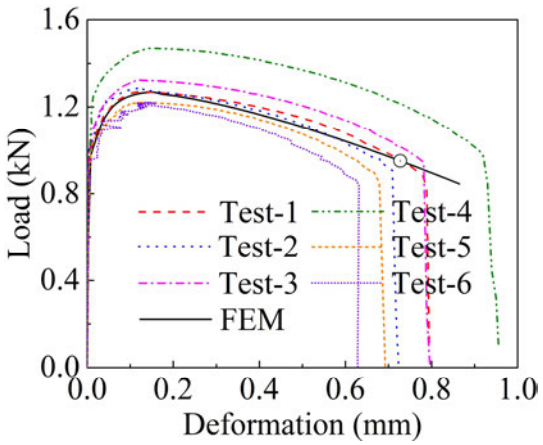

(b) Transverse

Figure 4-15. Load-deformation curves of HAZ.

Table 4-1. Maximum load, fracture deformation and percentage elongation of the base metal.

	FPL			FPT		
	P_{max} (kN)	D_f (mm)	δ_f	P_{max} (kN)	D_f (mm)	δ_f
Test-1	1.15	2.88	0.32	1.12	1.14	0.57
Test-2	1.19	2.20	0.24	1.12	1.27	0.64
Test-3	1.20	2.84	0.32	1.11	1.30	0.65
Test-4	1.12	2.16	0.24	1.14	0.88	0.44
Test-5	1.17	3.06	0.34	1.16	1.16	0.58
Test-6	1.13	2.48	0.28	1.10	1.23	0.62
Avg	1.16	2.60	0.29	1.13	1.16	0.58

Table 4-2. Maximum load, fracture deformation and percentage elongation of the weld.

	FPL			FPT		
	P_{max} (kN)	D_f (mm)	δ_f	P_{max} (kN)	D_f (mm)	δ_f
Test-1	1.42	2.34	0.26	1.38	0.58	0.29
Test-2	1.43	2.46	0.27	1.53	0.87	0.44
Test-3	1.35	1.53	0.17	1.46	1.01	0.51
Test-4	1.51	2.04	0.23	1.50	1.01	0.51
Test-5	1.49	2.24	0.25	1.45	0.72	0.36
Test-6	1.42	2.56	0.28	1.35	0.78	0.39
Avg	1.43	2.19	0.24	1.45	0.83	0.42

Table 4-3. Maximum load, fracture deformation and percentage elongation of the HAZ.

	FPL			FPT		
	P_{max} (kN)	D_f (mm)	δ_f	P_{max} (kN)	D_f (mm)	δ_f
Test-1	1.37	1.63	0.18	1.27	0.78	0.39
Test-2	1.32	2.26	0.25	1.29	0.71	0.36
Test-3	1.25	2.10	0.23	1.32	0.78	0.39
Test-4	1.43	1.41	0.16	1.47	0.92	0.46
Test-5	1.42	1.71	0.19	1.22	0.67	0.34
Test-6	1.42	1.85	0.21	1.22	0.63	0.32
Avg	1.37	1.83	0.20	1.30	0.75	0.38

4.5.2 Stress-strain relationships

As summarized in Tables 4-4 to 4-6, the engineering yield stress, σ_y, and tensile strength, σ_u, were calculated for the three material areas from each test. The average yield stresses of base metal, weld and HAZ were 357.3 MPa, 463.9 MPa and 447.9 MPa for the longitudinal direction, and 336.9 MPa, 460.1 MPa and 382.8 MPa for the transverse direction, respectively. The comparison shows that in both directions, the yield stress of the HAZ was higher than that of the base metal but lower than that of the weld, which was consistent with the results of the hardness tests. In addition, for the base metal and HAZ, the yield stresses in the longitudinal direction were higher than their transverse counterparts, while the strength of the weld was observed to be nearly independent of the direction.

Table 4-4. Yield stresses and ultimate stresses of the base metal (MPa).

	Longitudinal		Transverse	
	σ_y	σ_u	σ_y	σ_u
Test-1	360.4	465.7	330.7	458.4
Test-2	360.9	471.9	327.6	446.5
Test-3	362.4	474.0	321.7	439.5
Test-4	349.9	466.7	348.8	455.7
Test-5	362.9	449.8	357.9	462.6
Test-6	347.0	452.3	335.8	445.9
Avg	357.3	460.1	336.9	451.4

Table 4-5. Yield stresses and ultimate stresses of the weld (MPa).

	Longitudinal		Transverse	
	σ_y	σ_u	σ_y	σ_u
Test-1	460.6	566.7	443.9	553.6
Test-2	456.0	570.2	499.1	611.1
Test-3	424.3	539.7	472.1	585.3
Test-4	499.4	602.5	464.7	601.9
Test-5	494.2	594.0	446.5	578.1
Test-6	449.1	565.4	434.2	542.0
Avg	463.9	573.1	460.1	578.7

Table 4-6. Yield stresses and ultimate stresses of the HAZ (MPa).

	Longitudinal		Transverse	
	σ_y	σ_u	σ_y	σ_u
Test-1	456.4	548.6	351.9	509.1
Test-2	394.6	529.1	392.3	514.7
Test-3	378.4	501.5	382.8	529.7
Test-4	481.7	571.9	438.9	587.9
Test-5	485.6	568.8	364.5	488.3
Test-6	490.9	567.8	366.2	488.4
Avg	447.9	548.0	382.8	519.7

The stress-strain relationships of the base metal, weld and HAZ were calculated for each test following the same data processing method introduced in Section 3.2.1. The true stress σ_{true} and true strain ε_{true} before necking commencement were calculated from the engineering stress σ_{eng} and engineering strain ε_{eng} using Eqs. (3-1) and (3-2). The post-necking true stress-strain relationship was assumed to be linear [103], and the strain hardening modulus was determined by trial-and-error finite element analyses. The calculated true stress-strain relationships for all miniature FP coupons are plotted in Figs. 4-16 to 4-18. It is observed that for both longitudinal and transverse directions, the stress-strain relationships of the base metal showed less variability than those of the weld and HAZ, which was consistent with the load-deformation curves. The true stress-strain relationship of each material area in each direction was then obtained by averaging the curves of the corresponding coupons, as plotted in Fig. 4-19.

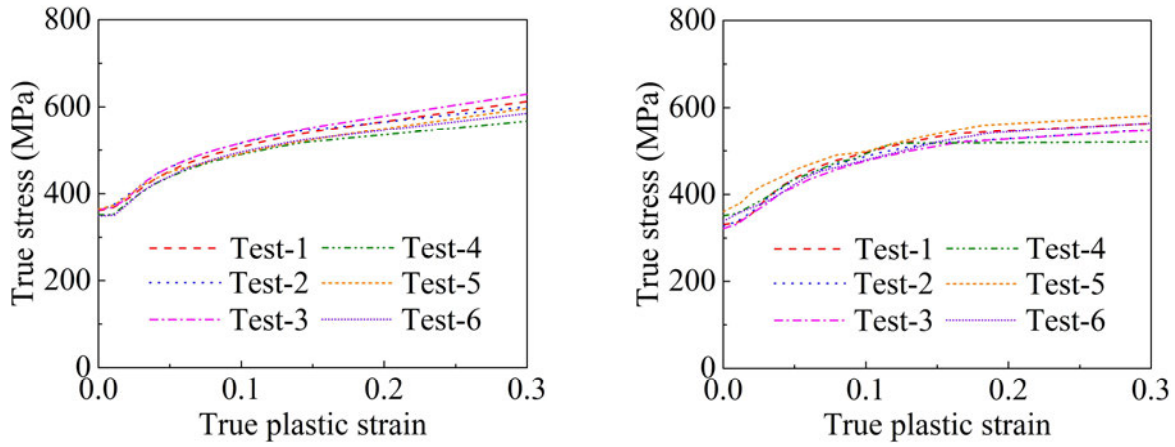

(a) Longitudinal (b) Transverse

Figure 4-16. Stress-strain curves of the base metal.

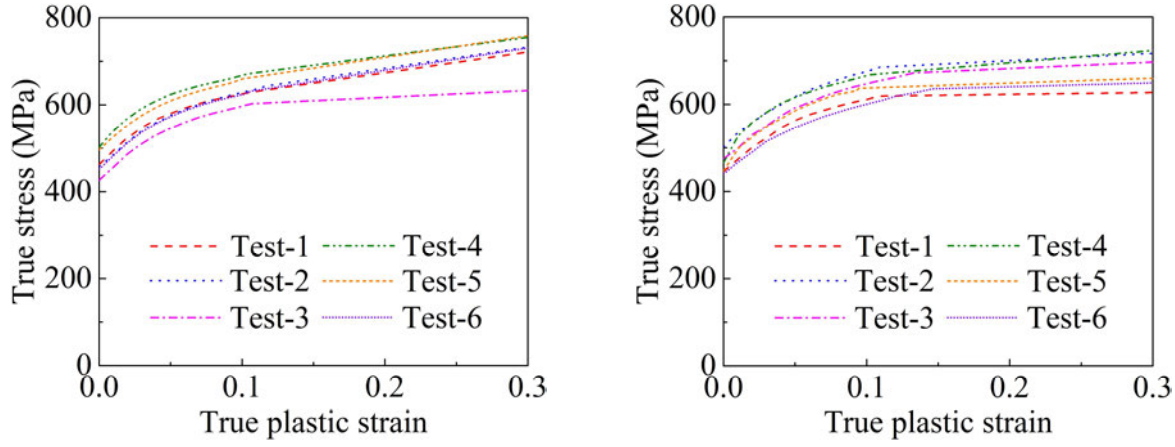

(a) Longitudinal (b) Transverse

Figure 4-17. Stress-strain curves of the weld.

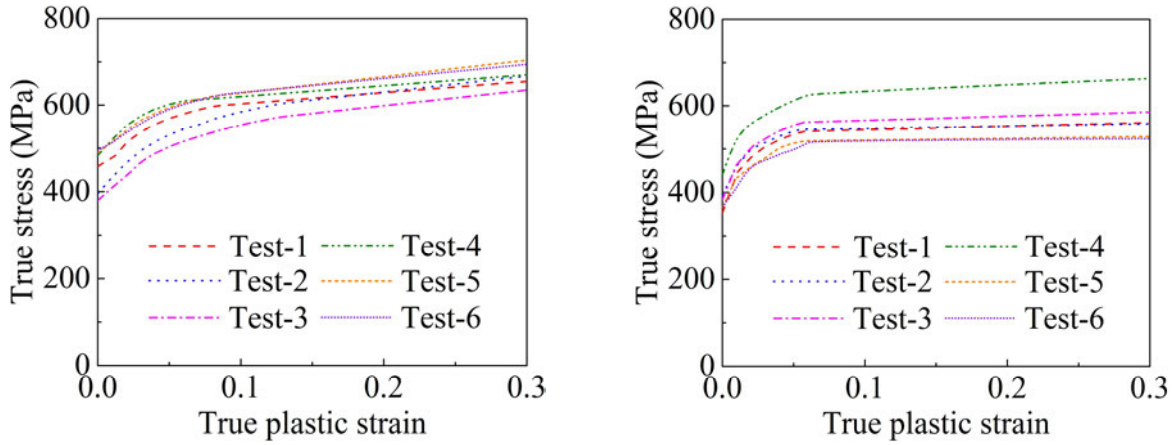

(a) Longitudinal (b) Transverse

Figure 4-18. Stress-strain curves of the HAZ.

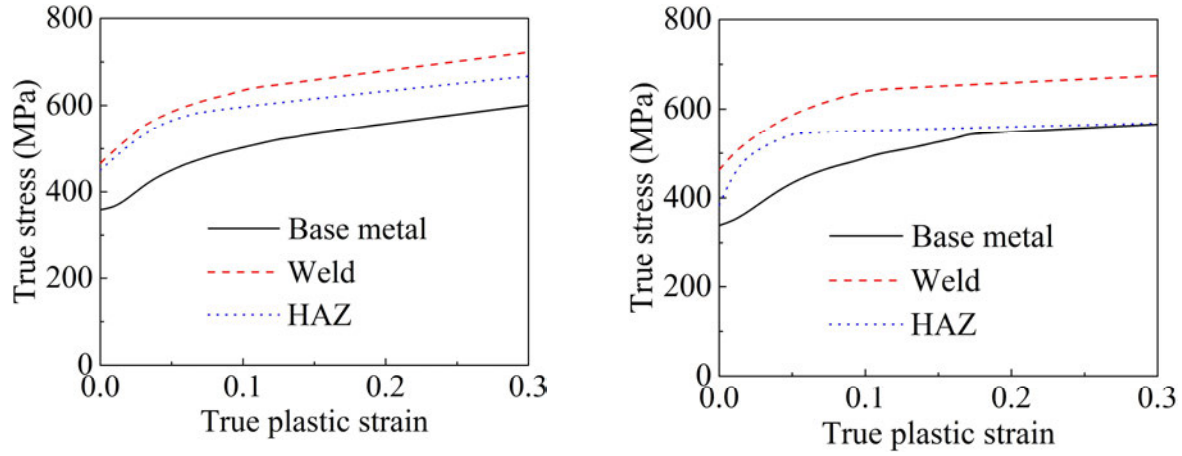

(a) Longitudinal (b) Transverse

Figure 4-19. Average stress-strain curves of the three material areas.

The tensile tests on the miniature FP coupons were numerically reproduced using the commercial FE software ABAQUS. The FE models for the FPL and FPT coupons extracted from the base metal are shown in Fig. 4-20. The materials were modelled as isotropic von Mises plasticity using the true stress-strain curves shown in Fig. 4-19. The eight-node linear solid elements with reduced integration (C3D8R) were used, with the element sizes being 0.2 mm in the parallel part, as shown in Fig. 4-20(a). The von Mises stress contours of the deformed FE models under the fracture deformation D_f are shown in Fig. 4-20(b). It is observed that the models experienced large plastic deformation before the fracture initiates, and the von Mises stress and plastic deformation were localized in the parallel part of the miniature coupon, which was consistent with the fractured specimens shown in Fig. 4-12.

The load-deformation curves obtained from the FE simulations are compared with the test curves in Figs. 4-13 to 4-15, and it is shown that the simulated results agreed well with the test

results. Note that in the FE models, the fracture phenomena were not simulated, and, therefore, the FE curves did not drop due to the onset of fracture and continued to develop into a very large deformation. The point corresponding to the average fracture deformation listed in Tables 4-1 to 4-3 was plotted on each FE curve in Figs. 4-13 to 4-15. The comparison of the results in Figs. 4-13 to 4-15 and Fig. 4-20(b) verified that both the von Mises stress distribution and the load-deformation curve of the miniature flat plates were closely simulated by the FE models. Therefore, it is confirmed that the FE models could accurately capture the behaviour of miniature coupons during the loading process. The FE models were then used to calculate the stress triaxiality, Lode angle parameter and plastic strain for each material area in both directions, as described in Section 5.3.

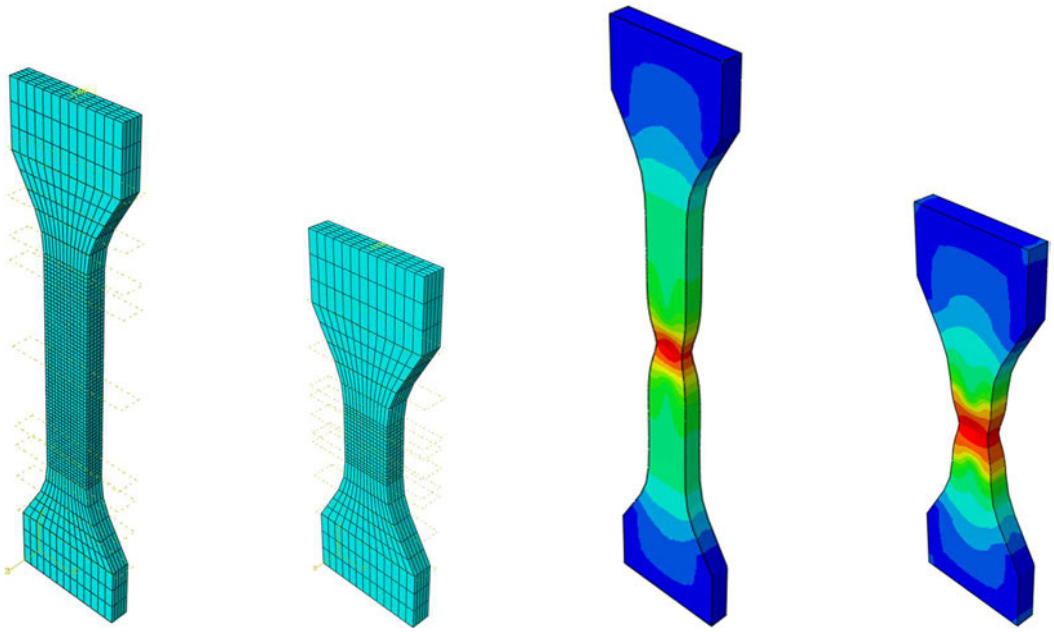

(a) Undeformed models (b) Deformed models

Figure 4-20. Numerical simulation of FPLs and FPTs of the base metal.

4.6 Tests on standard specimens

Normal-size standard specimens were extracted from the base metal in both longitudinal and transverse directions, i.e., FP-standard, and tensile tests were conducted on these specimens to verify the accuracy of the miniature coupon testing scheme and setup. As shown in Fig. 4-21, the width and thickness of the cross-section in the parallel part of the FP-standard specimens were 12.5 mm and 5 mm, respectively, which were five times those of the miniature flat plate coupons.

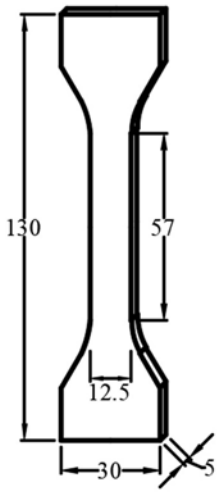

Figure 4-21. Design of FP-standard specimens (mm).

The test setup for the FP-standard specimens is shown in Fig. 4-22(a). The tensile tests were carried out in the 300 kN MTS Sintech testing machine, and the deformation of the FP-standard specimens was measured using an extensometer located in the middle of the parallel length over a gauge length of 25 mm. Two replicated tests were conducted on FP-standard specimens cut along each direction, and photos of the fractured specimens are shown in Fig. 4-22(b). It is observed that similar to the miniature flat plate coupons, the standard specimens experienced highly localised plastic deformation during the loading process and achieved final failure by the fracture at the parallel part. The elastic modulus of the base metal was measured using strain gauges attached at both surfaces of the standard specimen, as shown in Fig. 4-22(a), and the average elastic modulus was 193.32 GPa.

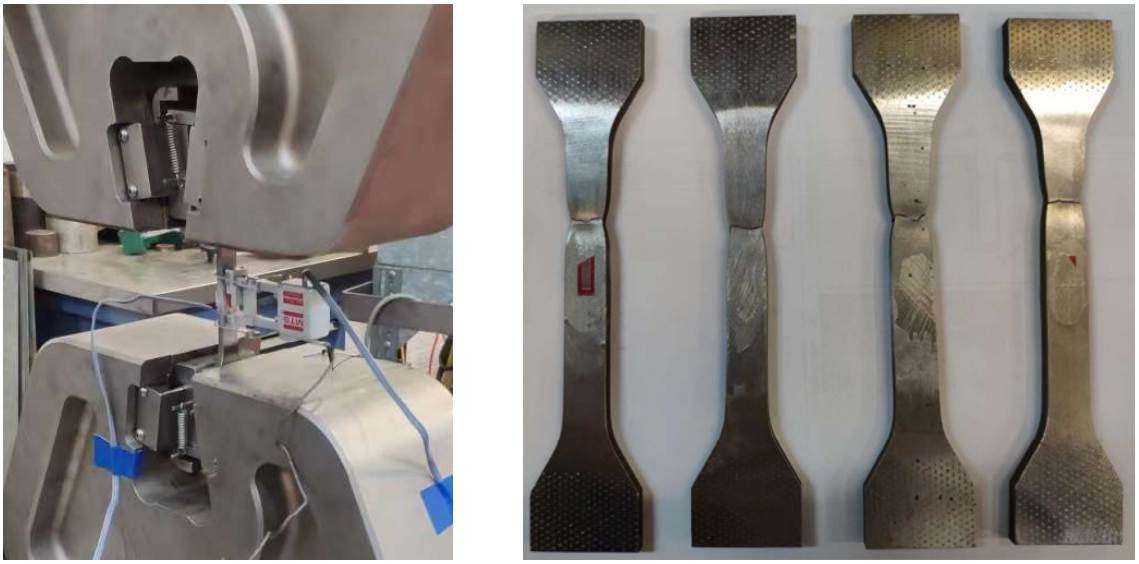

(a) Test setup (b) Photos of fractured specimens

Figure 4-22. Test and simulation of FP-standard specimens.

The load-deformation curves for the longitudinal and transverse directions are plotted in Fig. 4-23. The results of the replicated tests were almost identical, and the fracture deformation of standard specimens in the transverse direction was smaller than that in the longitudinal direction, which was consistent with the conclusions of the miniature FP coupons that the base metal presented better ductility in the transverse direction. Based on the load-deformation curves, the engineering stress-strain curves of the miniature flat plates and standard specimens extracted from the longitudinal direction were compared, as shown in Fig. 4-24, where letters "M" and "S" refer to the miniature and standard specimens, respectively. The miniature and standard specimens produced very similar curves prior to the tensile strength, which corresponded to the commencement of necking. In the post-necking range, the engineering strains of the standard specimens were slightly larger than those of the miniature coupons because the deformation of the FP-standard specimens was measured over the 25 mm gauge length, which was shorter than the proportional gauge length (i.e., $L_0 = 5.65\sqrt{A_0} = 44.7$ mm). If the gauge length was taken as 44.7 mm, the engineering stress-strain curves obtained from the miniature and standard specimens would agree well with each other over the full deformation range.

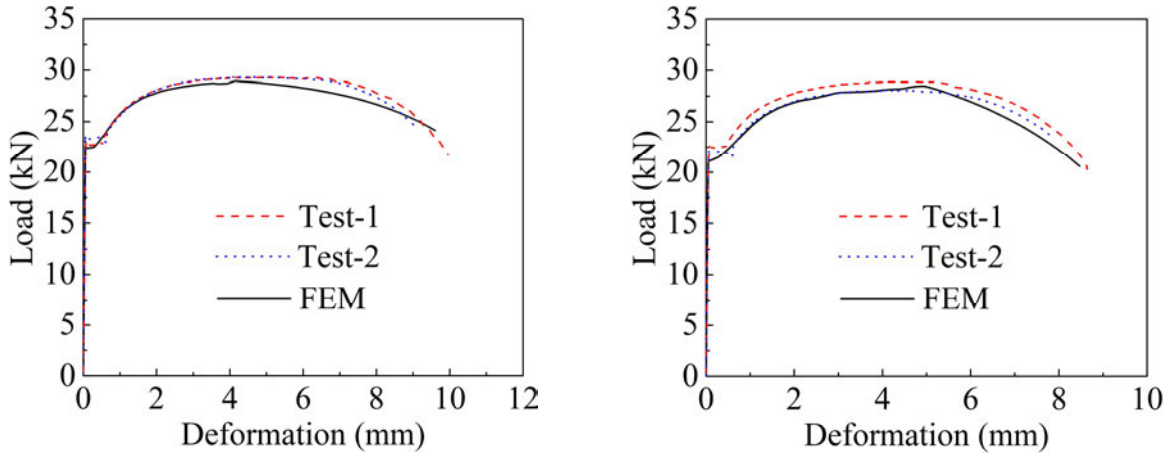

(a) Longitudinal (b) Transverse

Figure 4-23. Load-deformation curves of FP-standard specimens.

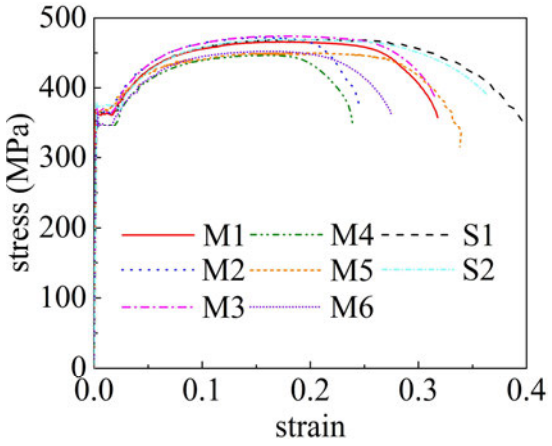

Figure 4-24. Engineering stress-strain curves for base metal in the longitudinal direction.

The tests of the standard specimens were modelled in ABAQUS, using the true stress-strain relationship of the base metal obtained from the miniature FP coupons, i.e., the solid black line in Fig. 4-19. As shown in Fig. 4-25, one-eight of the standard specimen was modelled due to the geometric symmetry, using C3D8R element with element sizes of approximately 0.2 mm in the critical area. The stress concentration and plastic deformation localized in the parallel part of the deformed FE model, which was consistent with the photo of the fractured specimens in Fig. 4-22(b) and the simulation results of the miniature FP coupons in Fig. 4-20(b). The simulated load-deformation curves are compared with the test curves in Fig. 4-23, which shows a good agreement. Therefore, it is confirmed that the tests of miniature coupons and conventional normal-size coupons provide consistent results. Thus, the accuracy of the miniature testing scheme is verified.

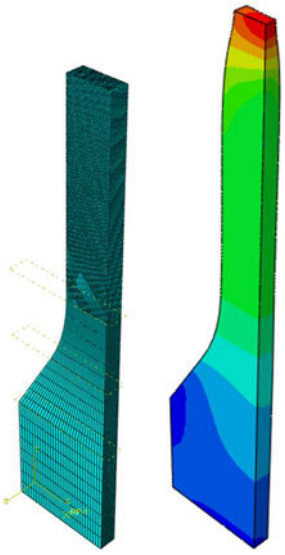

Figure 4-25. Numerical model of FP-standard specimens.

4.7 Summary

In this chapter, the stress-strain relationships of the weld and HAZ were measured for both longitudinal and transverse directions and compared with those of the base metal by conducting tensile tests on the miniature coupons extracted from the butt-welded plates. After macroetching the cross-sections of the plates, the three material areas in the weld zone were observed, and the horizontal and net widths of HAZ were measured, whose average values were 2.23 mm and 2.08 mm, respectively. The Vickers hardness was measured for the three material areas, and the results showed that the weld had the highest hardness while the base metal was the softest.

A series of miniature flat plate coupons were designed and extracted from the base metal, weld and HAZ along both the longitudinal and transverse directions. The test frame was equipped for the miniature tests with a 300 kg load cell and a custom-built jig, and the deformation of the miniature coupons was measured using the DIC system. Six replicated tests were conducted for each material area in each direction, and the comparison of the test results showed that the material properties of the weld and HAZ showed great variability than those of the base metal. The maximum loads of the HAZ were higher than those of the base metal but lower than those of the weld in both directions. The comparison of percentage elongations of miniature FP coupons indicated that the base metal showed the best ductility in both directions, while the HAZ material showed the worst.

The average engineering yield stresses of the base metal, weld and HAZ were 357.3 MPa, 463.9 MPa and 447.9 MPa for the longitudinal direction, and 336.9 MPa, 460.1 MPa and 382.8 MPa for the transverse direction, respectively. It was shown that in both directions, the yield stress of the HAZ was higher than that of the base metal but lower than that of the weld, which was consistent with the results of the hardness tests. In addition, for the base metal and HAZ, the yield stresses in the longitudinal direction were higher than their transverse counterparts, while the strength of the weld was observed to be nearly independent of the direction. The true stress-strain relationships of all the miniature FP coupons were calculated, and the true stress-strain relationship of each material area in each direction was then obtained by averaging the curves of the corresponding coupons.

Tensile tests were also conducted on the standard specimens extracted from the base metal in both longitudinal and transverse directions to assess the accuracy of the miniature coupon testing scheme and setup. The engineering stress-strain relationships of the standard specimens

were compared with those of miniature FP coupons, and the obtained good agreement confirmed that the tests of miniature coupons and normal-size coupons provide consistent results. The tests of the standard specimens were modelled using the true stress-strain relationship of the base metal obtained from the miniature FP coupons, and the simulated load-deformation curves agreed well with the test curves, thus verifing the accuracy of the miniature testing scheme.

Note that the conclusions are limited to the tested AS350 grade steel and accompanying weld, laid using grade B-G49 welding wire using the documented welding process.

Chapter 5 Fracture strains of weld, HAZ and base metal

5.1 Introduction

Numerous experiments have shown that under monotonic loading, fracture of welded connections can occur in the weld, HAZ or base metal, and many fracture models have been adopted to predict the fracture initiation and propagation in welded connections. However, the inhomogeneity of the mechanical properties within the weld zone, such as stress-strain relationships and fracture strains, was ignored in previous studies of the fracture in welded connections. Therefore, it is necessary to consider the mechanical properties of the base metal, weld and HAZ and discuss the effect of the material heterogeneity within the weld zone on the fracture performance of welded connections. In this chapter, the fracture strains of the weld and HAZ under various stress states are measured using miniature coupons for both longitudinal and transverse directions and compared with those of the base metal.

In Section 5.2, miniature notched round bars (NRB) and miniature grooved plates (GP) are designed for the axisymmetric tri-axial tension states and plane strain tri-axial tension states to fit the small areas of the weld and HAZ. Tensile tests were carried out on these miniature coupons extracted from the three material areas of the butt-welded plates along the two directions. The experimental results, such as the load-deformation curves and the fracture deformations, are summarized and compared among the three material areas. In Section 5.3, fracture strains of the miniature FP coupons, miniature NRB coupons and miniature GP coupons are obtained based on the test results and parallel FE simulations. The differences in the fracture strains among the three material areas and between the two directions are discussed. The fracture strains are then used to calibrate the free parameters of the fracture model LMVGM for the three material areas. The calibrated LMVGM is used to predict the fracture loci in the whole stress state regime, the difference in which is discussed among the base metal, weld and HAZ materials and also between the longitudinal and transverse directions. Section 5.4 summarizes the whole chapter.

5.2 Tests on miniature notched round bars and grooved plates

5.2.1 Specimen design

Miniature notched round bars and grooved plates were designed to obtain the fracture strains of the three material areas within the weld zone for the tensile axisymmetric stress state with high T and ξ=1 and the plane strain stress state with high T and ξ=0. The miniature NRB

coupons and GP coupons were made from the 10mm thick butt-welded plates described in Section 4.2. Similar to the miniature FP coupons in Section 4.4, the miniature NRB coupons and GP coupons were extracted from the weld, HAZ and base metal based on the macroetching results in Fig. 4-3. However, distinct from the miniature FP coupons for which the parallel part of the FPT coupons was designed to be shorter than the FPL coupons, the geometries of the miniature NRB coupons and GP coupons were the same in the longitudinal and transverse directions, as shown in Fig. 5-1. This is because the miniature NRB coupons and GP coupons had notched shapes at the parallel part where the stress and deformation concentrations occurred. The nominal dimensions of the smallest cross-sections of these miniature coupons were 1.5 mm and 1 mm, and since the size of the notched part was smaller than the size of the weld and HAZ, it can be guaranteed that the critical area of these miniature coupons extracted along both the longitudinal and transverse directions only covered one material area of the weld zone. Three replicated specimens were made for each material area in each direction, and the actual dimensions of the specimens were measured using callipers or digital image processing for dimensions which were too small for the callipers. Table 5-1 summarises the key dimensions, including the diameter of the smallest cross-section of the miniature NRB coupons and the width of the miniature GP coupons.

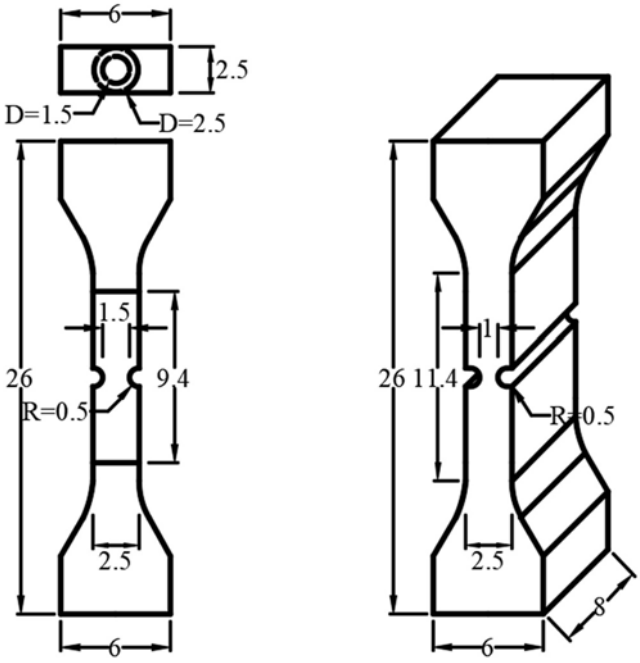

(a) NRB (b) GP

Figure 5-1. Geometry and Dimensions of miniature NRBs and GPs (mm).

Table 5-1. Measured dimensions of smallest cross-sections of the NRBs and GPs (mm).

	Longitudinal		Transverse	
	NRB	GP	NRB	GP
Base metal-1	1.51	1.16	1.55	1.10
Base metal-2	1.56	1.27	1.59	1.03
Base metal-3	1.50	1.18	1.56	1.25
Base metal-avg	1.52	1.20	1.56	1.12
Weld-1	1.53	1.18	1.55	1.20
Weld-2	1.55	1.10	1.53	1.20
Weld-3	1.54	1.15	1.48	1.19
Weld-avg	1.54	1.14	1.52	1.19
HAZ-1	1.51	1.16	1.52	1.07
HAZ-2	1.54	1.13	1.51	1.05
HAZ-3	1.53	1.24	1.56	0.97
HAZ-avg	1.52	1.17	1.53	1.03

5.2.2 Test setup

The uniaxial tensile tests of the miniature coupons were carried out on the 300 kN MTS Sintech testing machine. The test setup of miniature NRB coupons was the same as that of the miniature FP coupons, as shown in Fig. 5-2(a), while since the maximum loads of the miniature GP coupons were higher than those of the miniature FP coupons and NRB coupons, a 5000 kg load cell was equipped for the miniature GP coupons instead of the 300 kg load cell, as shown in Fig. 5-2(b). The shape of the ends of the miniature NRB coupons and GP coupons was designed to be the same as that of the miniature FP coupons, as shown in Figs. 4-7 and 5-1. Therefore, these miniature coupons could fit in the same custom-built test jig. The nominal thicknesses of the miniature NRB coupons and GP coupons were 2.5 mm and 8 mm, respectively, which were thicker than that of the miniature FP coupons, and two pairs of interchangeable spacers were then made to accommodate their thickness. The gauge lengths (i.e., L_0) of miniature NRB coupons and GP coupons were set to be the same as that of the miniature FPL coupons, i.e. 9 mm.

The test process of miniature NRB coupons and GP coupons was similar to that of the miniature FP coupons. The loading was controlled at a low speed of 0.1-0.5 mm/min, depending on the deformability of the coupon, and paused two or three times for 100s to obtain the static load-deformation curves. The deformation of the miniature coupons was measured using the DIC

system, which was calibrated by comparing the load-deformation curves measured using the 25 mm extensometer and the DIC system.

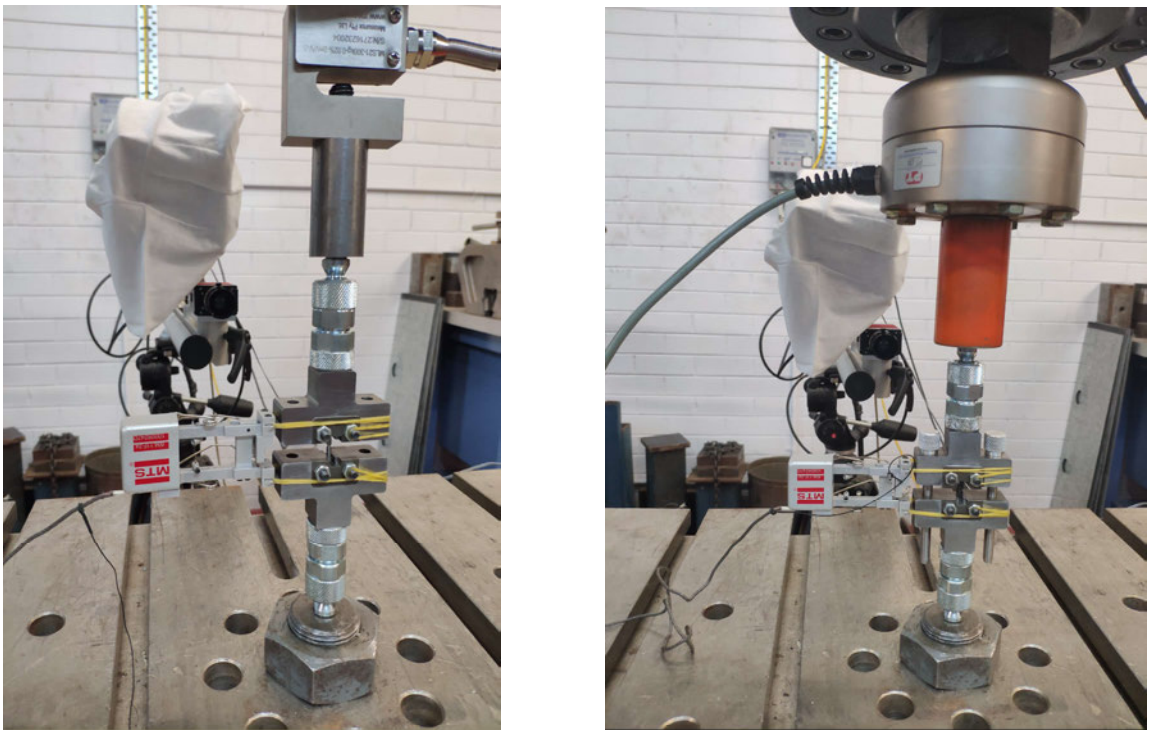

(a) Miniature NRB (b) Miniature GP

Figure 5-2. Test setup for miniature NRB and GP specimens.

5.2.3 Experimental results

During the loading process of the miniature NRB coupons and GP coupons, the plastic deformation developed and localized in the notched parts where the final fracture also occurred, as shown in Fig. 5-3. The load-deformation curves of the miniature NRB coupons are plotted for the weld, HAZ and base metal in the longitudinal and transverse directions in Figs. 5-4 to 5-7, while Figs. 5-7 to 5-9 show the load-deformation curves of the miniature GP coupons. Similar to the results of miniature FP coupons, all test curves dropped instantly when the fracture occurred. The maximum load, P_{max}, and the deformation under which fracture occurred, D_f, are summarized for the three material areas in Tables 5-2 to 5-4. Different from the miniature FP coupons, the values of the fracture deformation are comparable between the specimens extracted from the longitudinal and transverse directions as their gauge length L_0 was set to be the same. The following observations were made from the test results:

1) In the longitudinal direction, the average maximum loads of the base metal, weld and HAZ were 1.35 kN, 1.61 kN and 1.45 kN for miniature NRB coupons, and 6.29 kN, 7.61 kN and 6.65 kN for miniature GP coupons, respectively. In the transverse

direction, the average maximum loads of the base metal, weld and HAZ were 1.27 kN, 1.56 kN and 1.48 kN for miniature NRB coupons, and 6.20 kN, 7.61 kN and 5.83 kN for miniature GP coupons, respectively.

2) The comparison of the loads between the HAZ and base metal showed that the maximum loads of the HAZ were always higher than those of the base metal but lower than those of the weld, except for coupon GP-L. The comparison between the two directions showed that the maximum loads of the three material areas were always higher in the longitudinal direction, except for NRB of the HAZ. The exceptions are attributed to the measured dimensions that were slightly different from the nominal dimensions.
3) In the longitudinal direction, the average fracture deformations of the base metal, weld and HAZ were 0.20 mm, 0.33 mm and 0.17 mm for miniature NRB coupons, and 0.30 mm, 0.26 mm and 0.22 mm for miniature GP coupons, respectively. In the transverse direction, the average fracture deformations of the base metal, weld and HAZ were 0.49 mm, 0.36 mm and 0.43 mm for miniature NRB coupons, and 0.42 mm, 0.30 mm and 0.32 mm for miniature GP coupons, respectively.
4) The average fracture deformations of the base metal and HAZ were always larger in the longitudinal direction than those in the transverse direction, with the ratio of fracture deformations in the two directions (averaged between miniature NRB coupons and GP coupons) being 1.93 and 1.99 for the base metal and HAZ, respectively. This demonstrated the anisotropy of the properties of the base metal and HAZ.
5) By contrast, the properties of the weld seemed to be more isotropic, with the ratio of fracture deformations in the two directions (averaged between miniature NRB coupons and GP coupons) being only 1.12. The isotropy of the material properties of the weld was also demonstrated by the similar percentage elongation of miniature FP coupons, yield stress and tensile strength in the two directions, as shown in Tables 4-2 and 4-5. This is not surprising as the weld area was not subjected to the same rolling effects as the base metal, which also affected the properties of the HAZ.
6) The average fracture deformation of the HAZ was always lower than that of the base metal. This demonstrated that the thermal cycles applied to the base metal near the weld, which turned the base metal to the HAZ, degraded the deformability of the base metal.
7) Based on the comparison of the fracture deformations of miniature NRB coupons and

GP coupons, it is concluded that the HAZ had the lowest ductility in the longitudinal direction, while the ductility of the weld was the lowest in the transverse direction. The base metal always had the highest ductility, except for NRB-L.

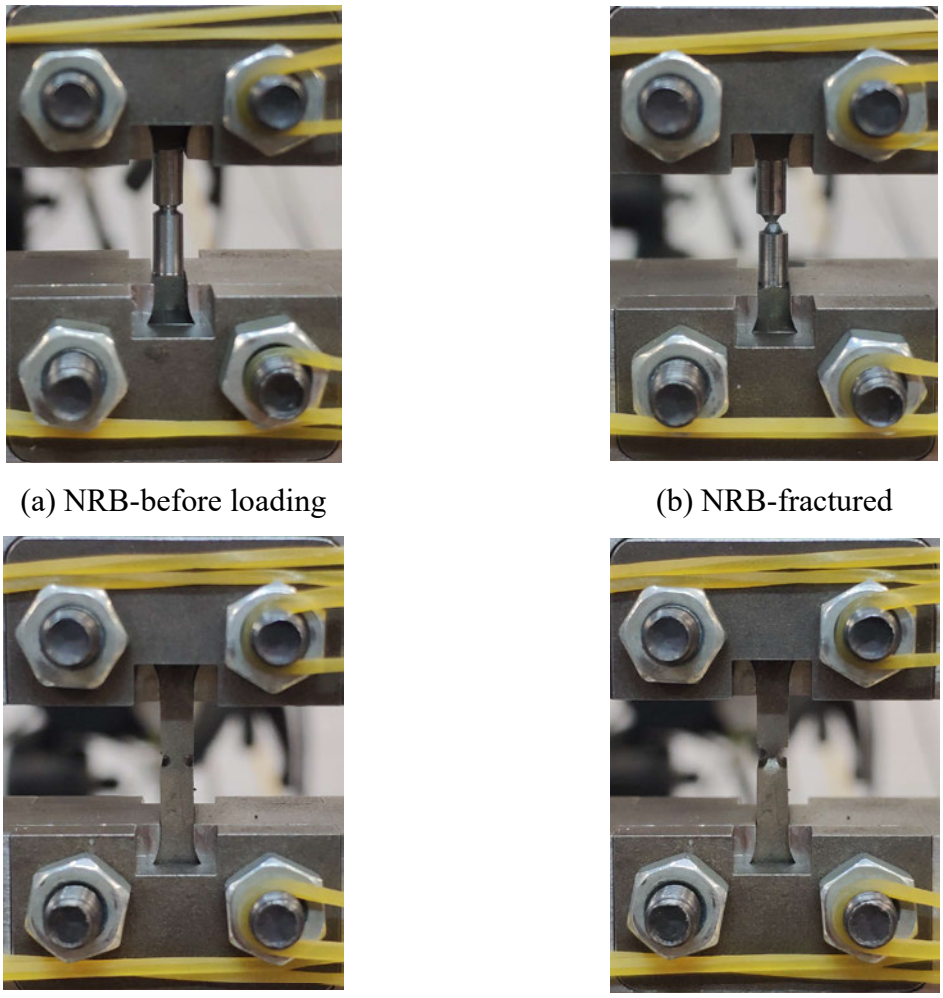

(a) NRB-before loading (b) NRB-fractured

(c) GP-before loading (d) GP-fractured

Figure 5-3. Photos of miniature NRB and GP specimens.

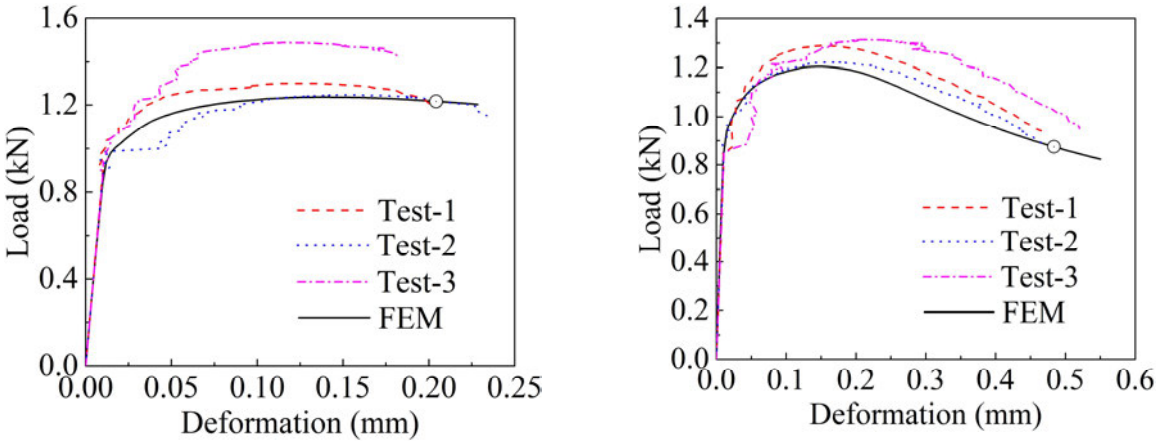

(a) Longitudinal (b) Transverse

Figure 5-4. Load-deformation curves of miniature NRB of base metal.

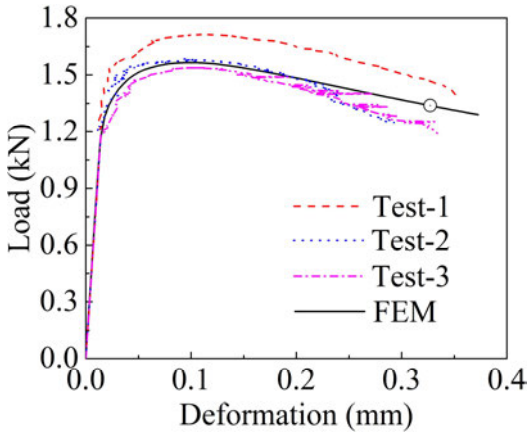

(a) Longitudinal

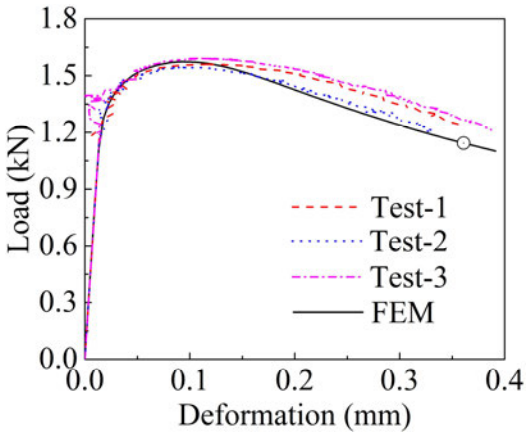

(b) Transverse

Figure 5-5. Load-deformation curves of miniature NRB of weld.

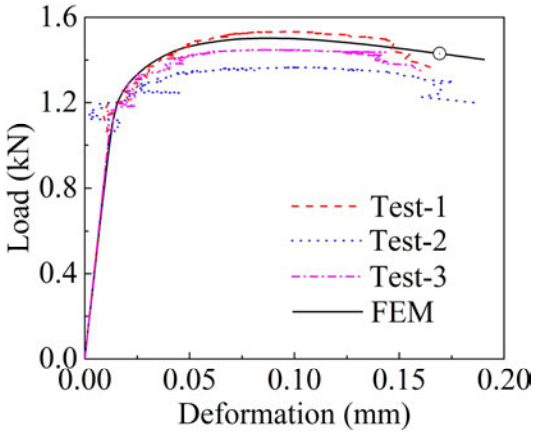

(a) Longitudinal

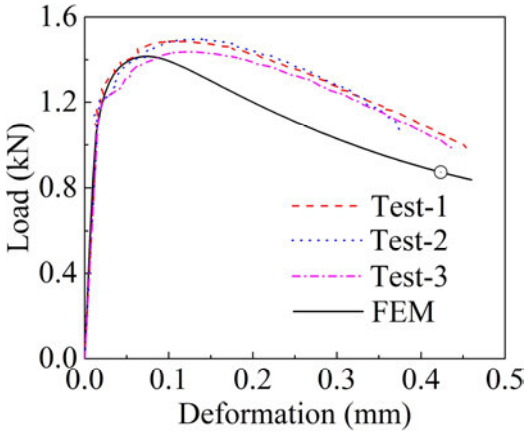

(b) Transverse

Figure 5-6. Load-deformation curves of miniature NRB of HAZ.

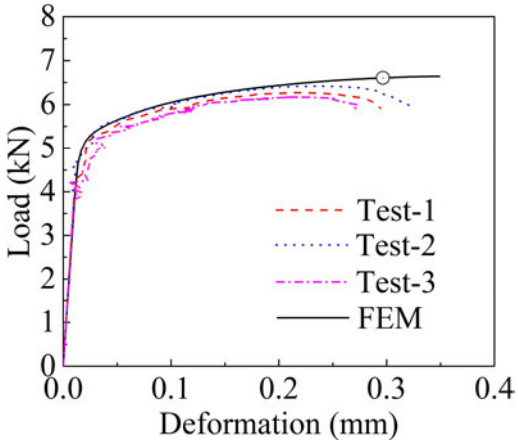

(a) Longitudinal

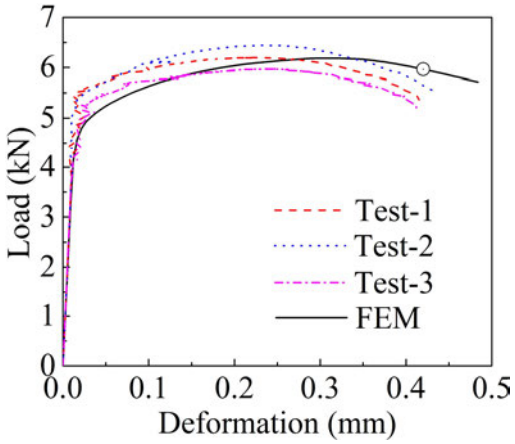

(b) Transverse

Figure 5-7. Load-deformation curves of miniature GP of base metal.

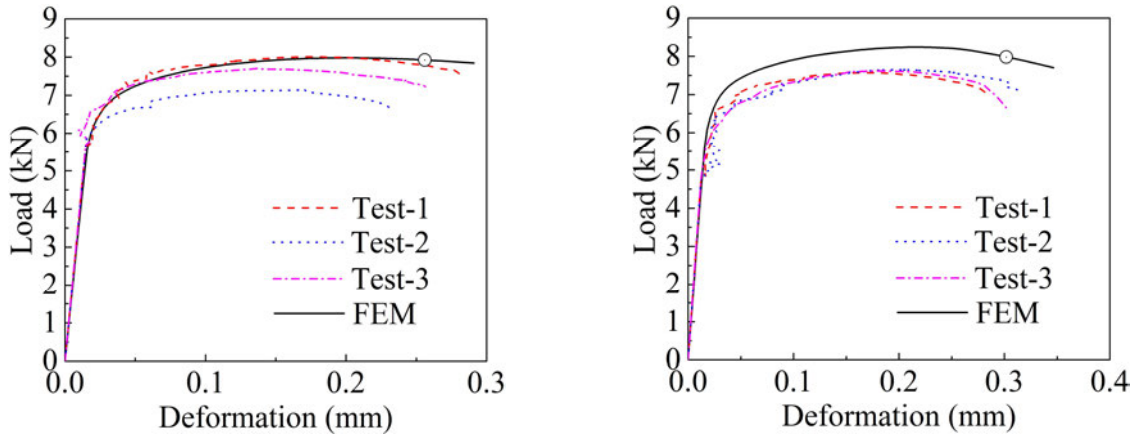

(a) Longitudinal (b) Transverse

Figure 5-8. Load-deformation curves of miniature GP of weld.

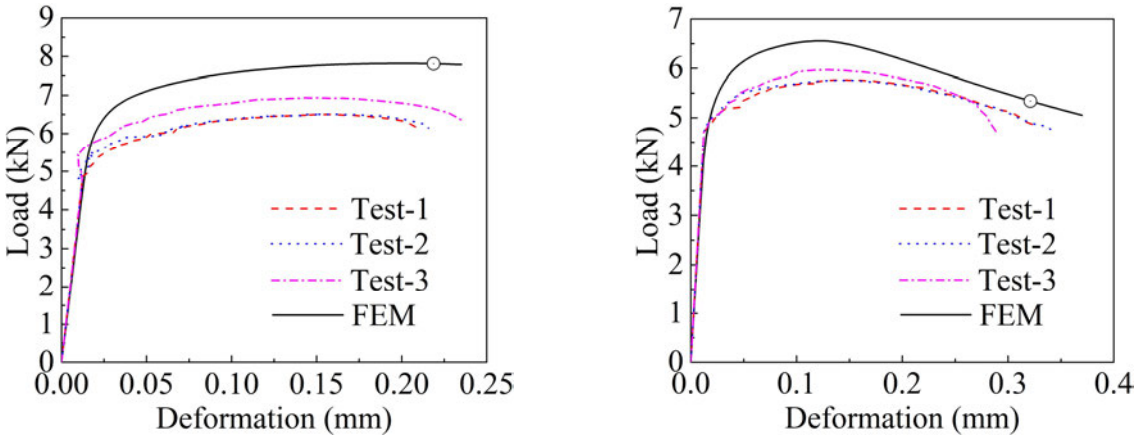

(a) Longitudinal (b) Transverse

Figure 5-9. Load-deformation curves of miniature GP of HAZ.

Table 5-2. Maximum load, fracture deformation and percentage elongation of base metal.

	NRB-L		NRB-T	
	P_{max} (kN)	D_f (mm)	P_{max} (kN)	D_f (mm)
Test-1	1.30	0.20	1.29	0.47
Test-2	1.25	0.23	1.22	0.47
Test-3	1.49	0.18	1.31	0.52
Avg	1.35	0.20	1.27	0.49
	GP-L		GP-T	
	P_{max} (kN)	D_f (mm)	P_{max} (kN)	D_f (mm)
Test-1	6.27	0.29	6.20	0.42
Test-2	6.42	0.32	6.44	0.44
Test-3	6.17	0.28	5.97	0.41
Avg	6.29	0.30	6.20	0.42

Table 5-3. Maximum load, fracture deformation and percentage elongation of weld.

	NRB-L		NRB-T	
	P_{max} (kN)	D_f (mm)	P_{max} (kN)	D_f (mm)
Test-1	1.71	0.36	1.56	0.36
Test-2	1.58	0.29	1.54	0.33
Test-3	1.53	0.33	1.59	0.39
Avg	1.61	0.33	1.56	0.36
	GP-L		GP-T	
	P_{max} (kN)	D_f (mm)	P_{max} (kN)	D_f (mm)
Test-1	8.00	0.28	7.57	0.28
Test-2	7.14	0.23	7.65	0.31
Test-3	7.70	0.26	7.62	0.30
Avg	7.61	0.26	7.61	0.30

Table 5-4. Maximum load, fracture deformation and percentage elongation of HAZ.

	NRB-L		NRB-T	
	P_{max} (kN)	D_f (mm)	P_{max} (kN)	D_f (mm)
Test-1	1.53	0.16	1.49	0.46
Test-2	1.37	0.19	1.50	0.38
Test-3	1.45	0.16	1.44	0.44
Avg	1.45	0.17	1.48	0.43
	GP-L		GP-T	
	P_{max} (kN)	D_f (mm)	P_{max} (kN)	D_f (mm)
Test-1	6.50	0.21	5.76	0.33
Test-2	6.51	0.22	5.76	0.34
Test-3	6.93	0.23	5.97	0.29
Avg	6.65	0.22	5.83	0.32

5.3 Fracture loci of weld, HAZ and base metal

5.3.1 Fracture strains under various stress states

Following the same modelling strategy described in Section 4.5.2, the tests of the miniature NRB coupons and GP coupons were simulated using ABAQUS, as shown in Fig. 5-10. The measured dimensions of the miniature coupons summarized in Table 5-1 were used for the FE models, and the true stress-strain relationships obtained from the miniature FPL coupons and

FPT coupons (i.e., Fig. 4-19) were adopted in the simulation. Similar to the miniature FP coupons, the C3D8R elements with the element sizes being 0.2 mm in the parallel part were used, as shown in Fig. 5-10(a). The von Mises stress contours of the deformed FE models under the fracture deformation D_f are shown in Fig. 5-10(b). For both miniature NRB coupons and GP coupons, the von Mises stress and plastic deformation localized in the notched parts, which was consistent with the fractured specimens shown in Fig. 5-3. The simulated load-deformation curves are compared with the experimental curves in Figs. 5-4 to 5-9. Without defining fracture propagation models in the FE analyses, the FE curves did not drop due to the onset of fracture and continued to develop into very large deformations. The points corresponding to the fracture deformations in Tables 5-2 to 5-4 are plotted on the FE curves. A good agreement between the experimental and FE curves is observed up to the fracture points. The comparison of the test and simulated results verified that both von Mises stress distribution and load-deformation curve of the miniature flat plates were accurately simulated by the FE models.

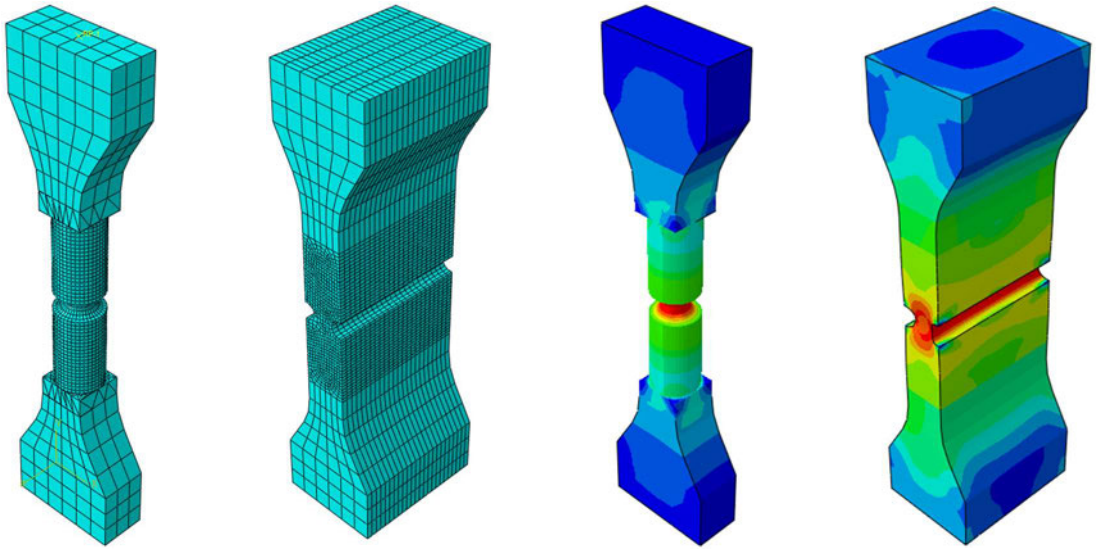

NRB GP NRB GP

(a) Undeformed specimens (b) Deformed specimens

Figure 5-10. Numerical simulation of miniature NRB and GP specimens for base metal.

The miniature FP coupons, NRB coupons and GP coupons represented different stress states, which could be characterised by the stress triaxiality, T, and Lode angle parameter, ξ, as explained in Section 2.2.1. For each coupon type, the value of fracture strain ε_f was obtained from the FE models as the plastic strain ε_p at the centre of the cross-section where fracture initiated, under the deformation corresponding to the fracture deformations summarized in Tables 4-1 to 4-3 and Tables 5-2 to 5-4. Similarly, the values of T_{avg} and ξ_{avg} represented by each coupon type were also obtained from Eqs. (2-13) and (2-14) calculated at the same

locations of the FE models using the values of the stress and strain tensors generated during the loading process. The values of ε_f, T_{avg} and ξ_{avg} of all the miniature coupons are summarized in Tables 5-5 to 5-7. The miniature FP coupons and NRB coupons exhibited stress states with ξ_{avg} values of approximately 1, and low T_{avg} values ranging from 0.40 to 0.59 and high T_{avg} values ranging from 1.04 to 1.25, respectively, while the miniature GP coupons had high T_{avg} values of 1.15 and ξ_{avg} varying from 0.04 to 0.47. In Fig. 5-11, ε_f of the base metal, weld and HAZ in the longitudinal and transverse directions are plotted relative to the T-ξ plane. As the fracture strain could be regarded as a non-dimensionalised fracture deformation, the observations made from the fracture deformations in Sections 4.5.1 and 5.2.3 also applied to the fracture strain. In addition, it is observed that, for the three material areas in both directions, ε_f generally increases with a decrease in T and an increase in ξ.

Table 5-5. Stress states and fracture strains of miniature FPs.

	Longitudinal			Transverse		
	T_{avg}	ξ_{avg}	ε_f	T_{avg}	ξ_{avg}	ε_f
Base metal	0.40	0.97	0.82	0.49	0.89	0.90
Weld	0.44	0.93	0.94	0.49	0.91	0.69
HAZ	0.44	0.94	0.80	0.59	0.77	0.78

Table 5-6. Stress states and fracture strains of miniature NRBs.

	Longitudinal			Transverse		
	T_{avg}	ξ_{avg}	ε_f	T_{avg}	ξ_{avg}	ε_f
Base metal	1.04	1.00	0.18	1.08	1.00	0.61
Weld	1.13	1.00	0.42	1.20	1.00	0.50
HAZ	1.14	1.00	0.18	1.25	1.00	0.62

Table 5-7. Stress states and fracture strains of miniature GPs.

	Longitudinal			Transverse		
	T_{avg}	ξ_{avg}	ε_f	T_{avg}	ξ_{avg}	ε_f
Base metal	1.08	0.47	0.10	1.10	0.18	0.32
Weld	1.18	0.16	0.18	1.18	0.18	0.19
HAZ	1.16	0.27	0.11	1.20	0.04	0.41

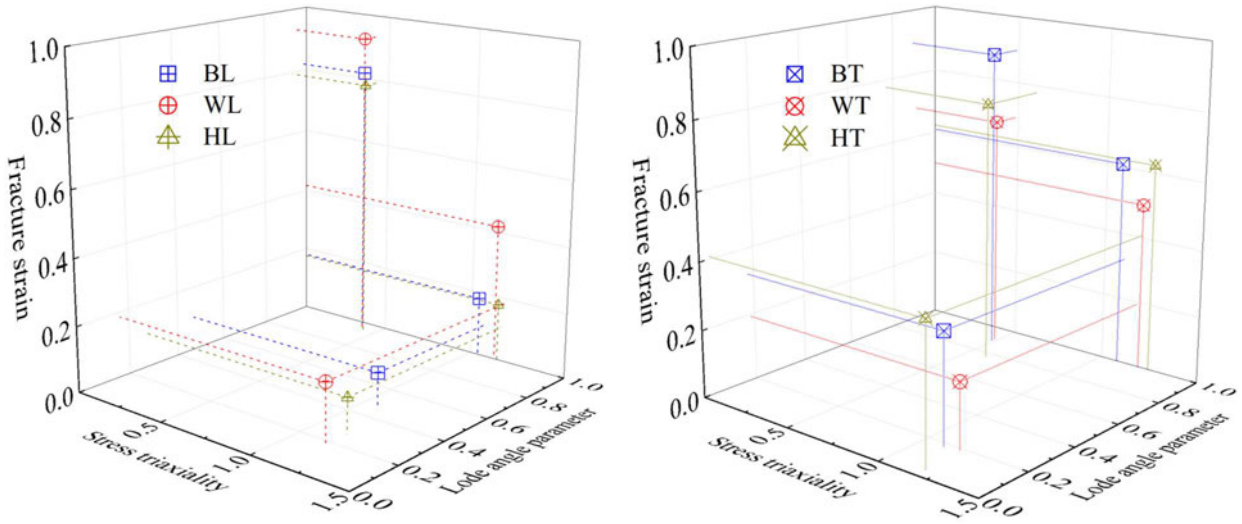

(a) Longitudinal (b) Transverse

Figure 5-11. Stress states and fracture strains of base metal, weld and HAZ.

5.3.2 Predicted fracture loci

As introduced in Chapter 3, the fracture model LMVGM was proposed based on a comprehensive body of experimental data. In the LMVGM, the effects of stress triaxiality and Lode angle were described using the void growth-based exponential function and an additional exponential term, respectively. In this section, the LMVGM was used to predict the fracture loci of the weld, HAZ and base metal in the longitudinal and transverse direction based on the experimental results of miniature coupons.

According to Eqs. (3-13) and (3-14), there are three free parameters α, β and γ in the LMVGM, which were calibrated based on the test data listed in Tables 5-5 to 5-7 and summarized in Table 5-8. Using the calibrated LMVGM model, the fracture surfaces in the space of stress triaxiality, Lode angle parameter and fracture strain are plotted in Figs. 5-12 to 5-14, where the marked points represent the test data of the miniature coupons. Fig. 5-15 presents the comparison of the test results and the predicted fracture loci for the stress states with the Lode angle parameter being 1 for base metal, weld and HAZ in the longitudinal and transverse directions. The following observations can be noted:

1) All fracture surfaces tilt towards stress states with high T and low ξ, indicating that the fracture could initiate more easily when the materials were subjected to loading conditions under these stress states.
2) The fracture strains in the longitudinal direction present larger variation over the full range of stress states than those in the transverse direction, and generally, the fracture locus of the HAZ is lower than that of the base metal but higher than that of the weld.

3) The fracture loci of the three material areas in the longitudinal direction were lower than those in the transverse direction under high stress triaxialities, while the longitudinal fracture strains increased at a steeper slope with a decreasing stress triaxiality.
4) It is indicated that generally, the ductility of HAZ was in-between those of the base metal and the weld, and the three material regions had higher longitudinal ductility under low stress triaxialities, but higher transverse ductility under high stress triaxialities.

Table 5-8. Calibrated free parameters of LMVGM.

	Longitudinal			Transverse		
	α	β	γ	α	β	γ
Base metal	0.97	2.44	0.84	0.67	0.79	0.75
Weld	0.72	1.27	0.89	0.32	0.62	1.17
HAZ	1.21	2.23	0.62	0.73	0.51	0.47

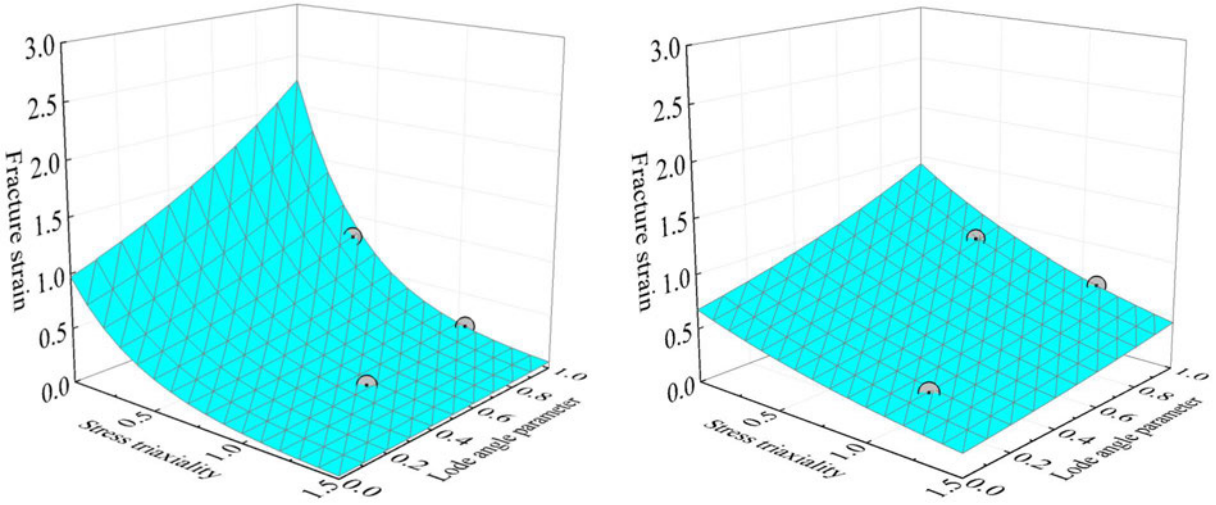

(a) Longitudinal (b) Transverse

Figure 5-12. Predicted fracture loci of base metal.

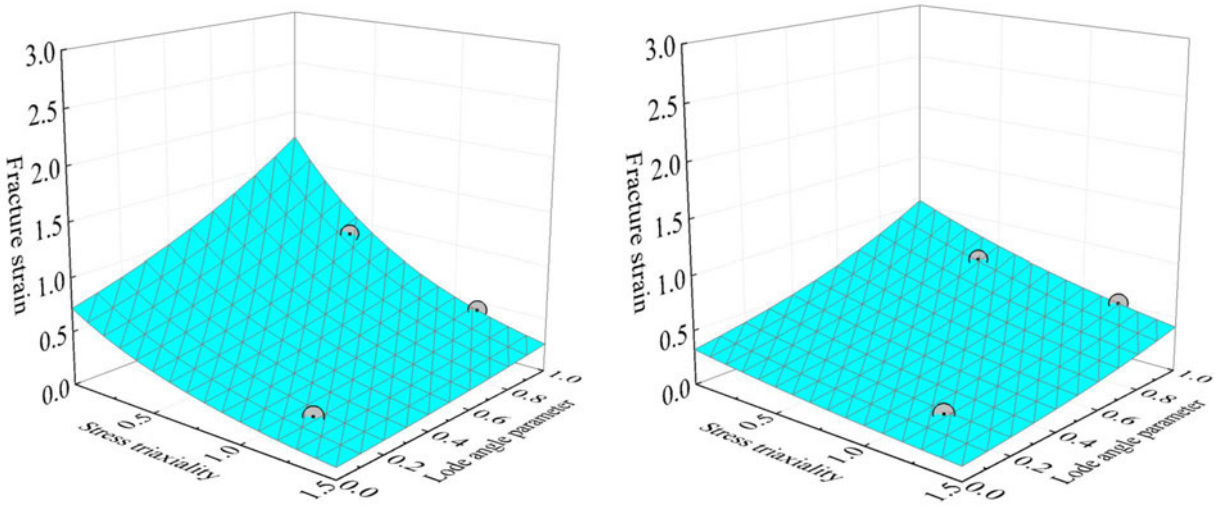

(a) Longitudinal (b) Transverse

Figure 5-13. Predicted fracture loci of weld.

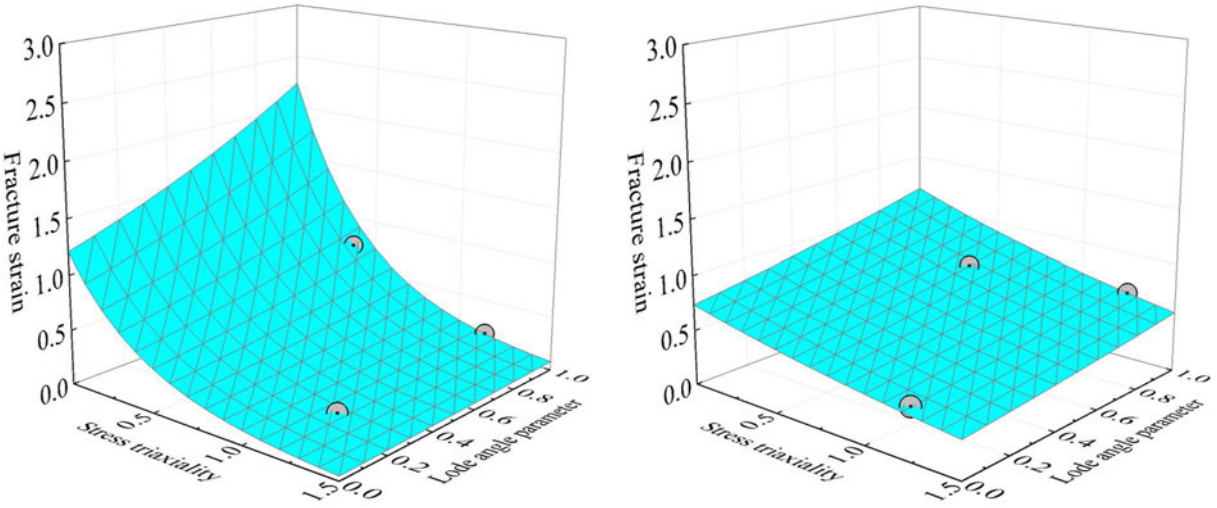

(a) Longitudinal (b) Transverse

Figure 5-14. Predicted fracture loci of HAZ.

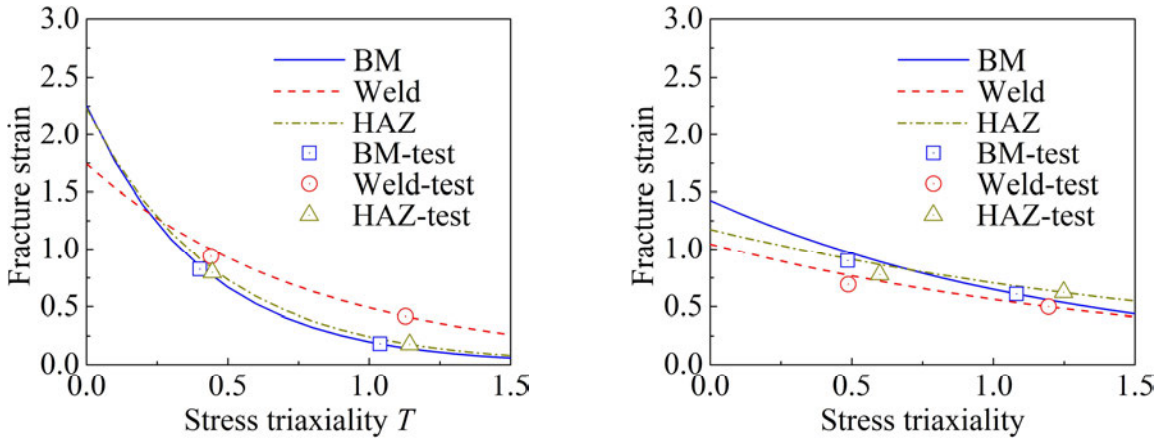

(a) Longitudinal (b) Transverse

Figure 5-15. Predicted fracture loci with Lode angle parameter being 1.

5.4 Summary

In this chapter, the fracture strains of the weld and HAZ were measured for both longitudinal and transverse directions and their values were compared with those of the base metal. A series of miniature notched round bars and grooved plates were designed and extracted from the three material areas. Tensile tests were conducted on these miniature coupons using the test frame introduced in Chapter 4. Three replicated measurements were taken for each material area in each direction and the comparison of the experimental results showed that generally, the maximum loads of the HAZ were higher than those of the base metal but lower than those of the weld, and the maximum loads of the three material areas were higher in the longitudinal direction than in the transverse direction. The properties of the weld were relatively more homogeneous in the two directions than those of the base metal and HAZ. The comparison of the fracture deformations of miniature NRB coupons and GP coupons showed that the HAZ had the lowest ductility in the longitudinal direction, while the ductility of the weld was the lowest in the transverse direction. The base metal always had the highest ductility.

Based on the experimental results and corresponding FE simulation, the average stress triaxiality, average Lode angle parameter and fracture strain of miniature FP coupons, NRB coupons and GP coupons were obtained for the weld, HAZ and base metal in both the longitudinal and transverse directions. After calibrating the free parameters using the fracture strains of the three material areas, the LMVGM fracture model was used to predict the fracture loci for the whole stress state regime. It was observed that the fracture initiation more easily occurred under stress states with high T and low ξ. Generally, the fracture locus of the HAZ was lower than that of the base metal but higher than that of the weld, and the three material areas had higher longitudinal ductility under low stress triaxialities, but higher transverse ductility under high stress triaxialities.

Note that the conclusions are limited to the tested AS350 grade steel and accompanying weld, laid using grade B-G49 welding wire using the documented welding process.

Chapter 6 Measurement of weld residual stresses

6.1 Introduction

The heating and cooling cycles that occur during the welding process cause residual stresses in welded connections, which can have a significant impact on the performance of steel components, including yielding, stability and fracture. The residual stress patterns generated by butt and fillet welds, the two most commonly used weld types, have been thoroughly studied [63, 68, 79]. However, limited studies are available to compare residual stresses generated by different weld types and weld sizes under an identical welding process using high-precision non-destructive measurement methods. Residual stresses in practical steel connections have also rarely been explored due to their complexity, although these stresses may affect their strength and stiffness. In this chapter, the distribution and magnitude of residual stresses generated by the fillet welds and butt welds in welded cruciform specimens and an end-plate connection are investigated using the neutron diffraction method to provide a better understanding of the weld residual stresses in welded connections.

As introduced in Section 2.3.4, residual stresses are normally measured through destructive methods, such as slitting or hole drilling methods, which can only provide results within relatively large gauge volumes, or the non-destructive X-ray method, which can only provide surface measurement results. Therefore, the non-destructive high-resolution neutron diffraction approach was adopted in this research to obtain the three-dimensional interior residual stresses of the welded connections, the principle of which is introduced in Section 6.2.

In Section 6.3, a series of welded cruciform specimens are designed and fabricated using 16 mm fillet welds, 12 mm fillet welds, 8 mm fillet welds, or single bevel butt welds. The residual strains of the welded cruciform specimens were measured in the longitudinal, transverse and normal directions using the neutron strain scanner Kowari at Australian Nuclear Science and Technology Organization (ANSTO). The residual stresses were calculated based on the test results and compared to discuss the effects of weld size and weld types on the residual stress patterns of welded connections made by the same materials under the same welding conditions.

In Section 6.4, a welded end-plate connection is designed by welding an I-beam to an end-plate, in which the I-beam was made by welding together three plates. The end-plate connection was fabricated using the same materials, weld geometry and weld process as the welded cruciform specimens. The magnitude and distribution of residual stresses in this practical complex steel

connection were measured and compared with those of the welded cruciform specimens to conduct a comprehensive assessment of the residual stresses in welded connections in steel structures. Section 6.5 summarizes the whole chapter.

6.2 Neutron diffraction measurements

In this study, the residual stresses of welded connections were calculated based on residual strains measured in the longitudinal, transverse and normal directions using the neutron diffraction strain scanner Kowari at ANSTO. A schematic of the Kowari test machine is shown in Fig. 6-1. In the strain scanner, the tested specimen is fixed on the 4 DOF sample positioner at various positions and directions to measure the residual strains in the longitudinal, transverse and normal directions. A neutron beam extracted from the reactor will pass through the primary slits and strike the tested specimen as the incident beam, after which the secondary slits in the detector will receive the diffracted beam. After determining the distribution of the neutron counts, the diffraction peak for each measurement point of a tested specimen is found using the software QKowari.

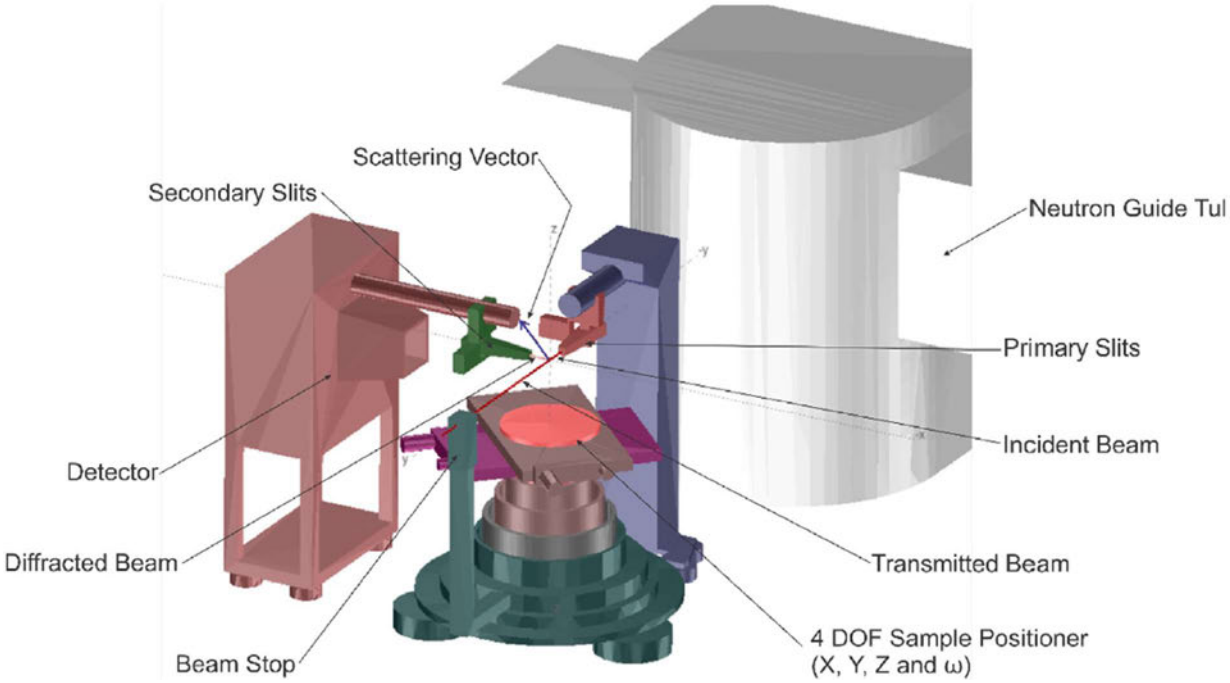

Figure 6-1. Schematic of Kowari at ANSTO [112].

In the neutron diffraction method, the residual strain can be determined by identifying the corresponding lattice deformation based on the Bragg law [63, 80], where the distance between atomic planes in the steel, lattice spacing d_{hkl}, is used as a strain gauge. When the neutron incident beam passes through the material, the diffraction can be expressed as

$$\lambda = 2d_{hkl}\sin\theta_{hkl} \tag{6-1}$$

where λ is the wavelength of the incident beam and θ_{hkl} is the diffraction angle, as shown in Fig. 6-2. Because of the tensile or compressive residual stresses, the lattice spacing will expand or contract, and the diffraction peak will shift from the stress-free state, as shown in Fig. 6-3. By comparing with the lattice spacing of a stress-free sample (d_0) under a given wavelength, the residual strain (ε_{hkl}) can be calculated by

$$\varepsilon_{hkl} = \frac{d_{hkl} - d_0}{d_0}. \tag{6-2}$$

After measuring the strains (ε_{xx}, ε_{yy}, ε_{zz}) in three orthogonal directions, the corresponding residual stresses, σ_{xx}, σ_{yy} and σ_{zz}, can be obtained according to Hooke's law

$$\sigma_{xx} = \frac{E}{(1+\nu)(1-2\nu)}\left[(1-\nu)\varepsilon_{xx} + \nu\left(\varepsilon_{yy} + \varepsilon_{zz}\right)\right] \tag{6-3}$$

$$\sigma_{yy} = \frac{E}{(1+\nu)(1-2\nu)}\left[(1-\nu)\varepsilon_{yy} + \nu\left(\varepsilon_{xx} + \varepsilon_{zz}\right)\right] \tag{6-4}$$

$$\sigma_{zz} = \frac{E}{(1+\nu)(1-2\nu)}\left[(1-\nu)\varepsilon_{zz} + \nu\left(\varepsilon_{xx} + \varepsilon_{yy}\right)\right] \tag{6-5}$$

where E is Young's modulus and v is Poisson's ratio, which are 206 GPa and 0.3 for the steel used in this study, respectively. ε_{xx}, ε_{yy} and ε_{zz} are referred to as the longitudinal, transverse and normal strains, respectively. During the testing process, experimental uncertainties, such as the uncertainty in the diffraction peak position, will affect the measurements of the residual stresses. These uncertainties in the three directions were determined [63] through

$$\Delta\sigma_{xx} = \frac{E}{1+\nu}\sqrt{\left[\left(\frac{\nu}{1-2\nu}\right)\Delta\varepsilon_{xx}^{\,2} + \left(\frac{\nu}{1-2\nu}\right)^2\left(\Delta\varepsilon_{xx}^{\,2} + \Delta\varepsilon_{yy}^{\,2} + \Delta\varepsilon_{zz}^{\,2}\right)\right]} \tag{6-6}$$

$$\Delta\sigma_{yy} = \frac{E}{1+\nu}\sqrt{\left[\left(\frac{\nu}{1-2\nu}\right)\Delta\varepsilon_{yy}^{\,2} + \left(\frac{\nu}{1-2\nu}\right)^2\left(\Delta\varepsilon_{xx}^{\,2} + \Delta\varepsilon_{yy}^{\,2} + \Delta\varepsilon_{zz}^{\,2}\right)\right]} \tag{6-7}$$

$$\Delta\sigma_{zz} = \frac{E}{1+\nu}\sqrt{\left[\left(\frac{\nu}{1-2\nu}\right)\Delta\varepsilon_{zz}^{\,2} + \left(\frac{\nu}{1-2\nu}\right)^2\left(\Delta\varepsilon_{xx}^{\,2} + \Delta\varepsilon_{yy}^{\,2} + \Delta\varepsilon_{zz}^{\,2}\right)\right]} \tag{6-8}$$

where $\Delta\varepsilon_{xx}$, $\Delta\varepsilon_{xx}$ and $\Delta\varepsilon_{xx}$ are the uncertainties in the longitudinal, transverse and normal strain components [113] and can be expressed as

$$\Delta\varepsilon_{xx} = \frac{d_{xx}}{d_0}\sqrt{\left(\frac{\Delta d_{xx}}{d_{xx}}\right)^2 + \left(\frac{\Delta d_0}{d_0}\right)^2} \tag{6-9}$$

$$\Delta\varepsilon_{yy} = \frac{d_{yy}}{d_0}\sqrt{\left(\frac{\Delta d_{yy}}{d_{yy}}\right)^2 + \left(\frac{\Delta d_0}{d_0}\right)^2} \tag{6-10}$$

$$\Delta\varepsilon_{zz} = \frac{d_{zz}}{d_0}\sqrt{\left(\frac{\Delta d_{zz}}{d_{zz}}\right)^2 + \left(\frac{\Delta d_0}{d_0}\right)^2} \; . \tag{6-11}$$

Eqs. (6-6) to (6-11) were used in the following sections to calculate the uncertainties in the residual stress calculations related to the stressed, and stress-free lattice spacing and the values of the uncertainties were then used to evaluate the reliability of the measured results.

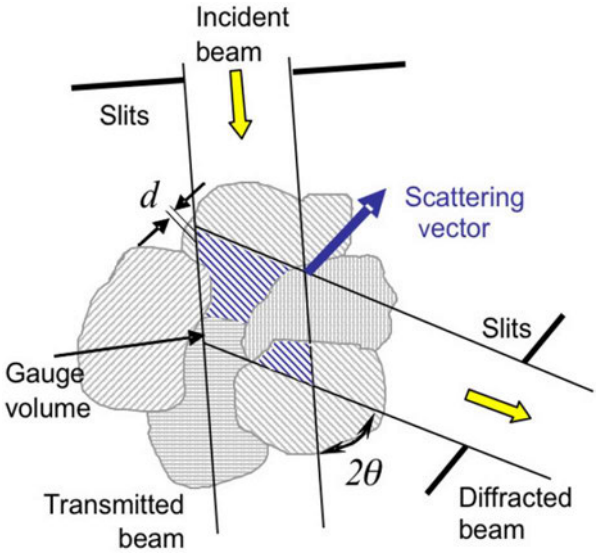

Figure 6-2. Principle of neutron diffraction technique [63].

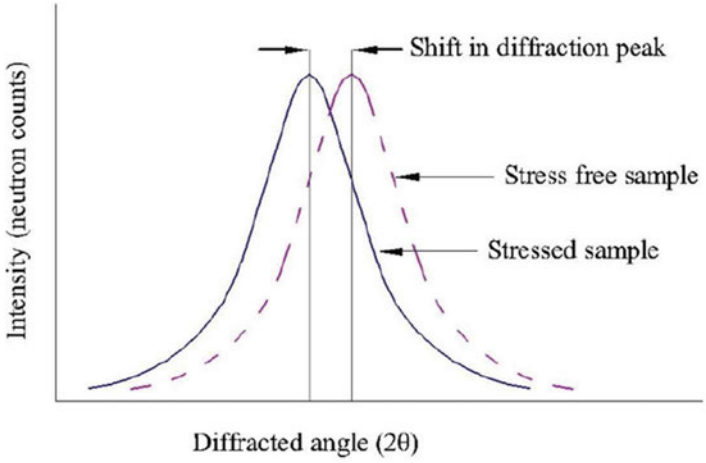

Figure 6-3. Diffraction peak shift due to residual stresses [113].

Residual stress measurement was conducted on a series of welded cruciform specimens and an end-plate connection in the following sections. The components of these welded connections were cut from the same 10 mm and 20 mm AS350 grade steel plates described in Sections 3 and 4. The specimens were welded using gas metal-arc welding (GMAW). The weld wire was of grade B-G49 [111], and the shielding gas was 18% CO_2 bal Ar. As for the butt welds in Section 4, the welding voltage ranged from 23 to 26 V, the current ranged from 200 to 220 A, and the welding speed ranged from 200 to 250 mm/min, resulting in the heat input ranging from 1.10 to 1.71 kJ/mm.

6.3 Residual stresses in welded cruciform specimens

6.3.1 Specimen design

A series of cruciform specimens were designed and fabricated, as shown in Fig. 6-4. In each specimen, the supported plates were welded perpendicularly to the supporting plate through 16 mm fillet welds by six weld passes (named F16 in Fig. 6-4(a)), 12 mm fillet welds by three weld passes (named F12 in Fig. 6-4(b)), 8 mm fillet welds by one weld pass (named F8 in Fig. 6-4(c)), or single bevel butt welds by five weld passes (named B10 in Fig. 6-4(d)). The edge preparation of B10 is prequalified based on [111], whose root gap is 10 mm and the inclining angle is 30°. The lengths of the specimens were 150 mm or 230 mm, (Figs. 6-4(a) to 6-4(c)). All plates forming the specimens were extracted from the 20 mm thick steel plate, except the 10 mm thick supported plates in the butt-welded specimen. The definition of longitudinal, transverse and normal directions is shown in Fig. 6-4(e).

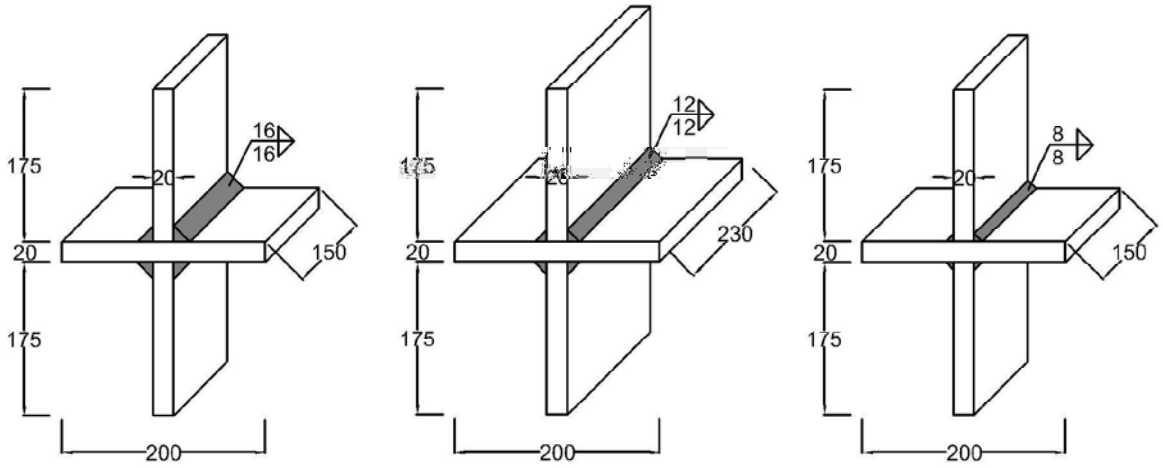

(a) F16 (b) F12 (c) F8

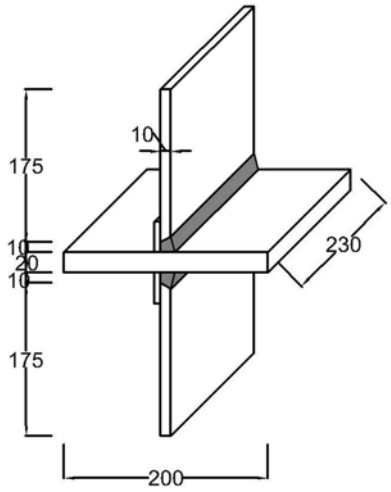

(d) B10

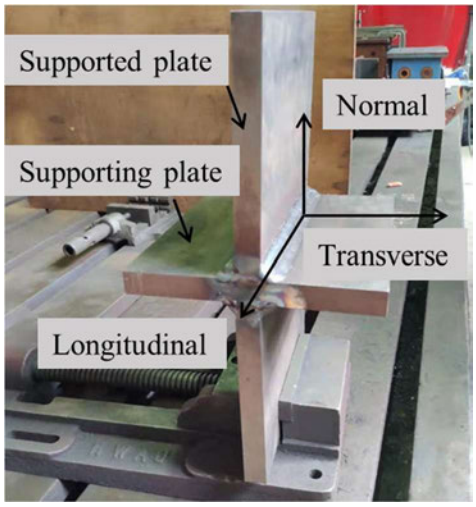

(e) Photo of a fillet-welded cruciform specimen

Figure 6-4. Design of welded cruciform specimens.

6.3.2 Test setup

For each cruciform specimen, the residual strains were measured in the three main directions at the cross-section 75 mm from the edge of the specimen. For the fillet-welded specimens, the residual strains of one fillet weld were measured along the two weld legs at the cross-section, as shown in Fig. 6-5(a), while for the butt-welded specimen, the residual strains were measured on the weld surface side along the supported plate and the supporting plate, as shown in Fig. 6-5(b). It is shown in Fig. 6-4 that the length of the branch on the supporting plate is 90 mm, which is shorter than the 175 mm branch on the supported plates. Therefore, the residual stress distribution was measured over a longer range along the weld leg on the supported plate than the supporting plate. In the neutron diffraction method, the residual stress is measured over a gauge volume, as shown in Fig. 6-2. For the measurement of the welds in the cruciform connections, the gauge volume was set as 3×3×3 mm^3 for the longitudinal direction and 3×3×20 mm^3 for the normal and transverse directions to speed up the data acquisition.

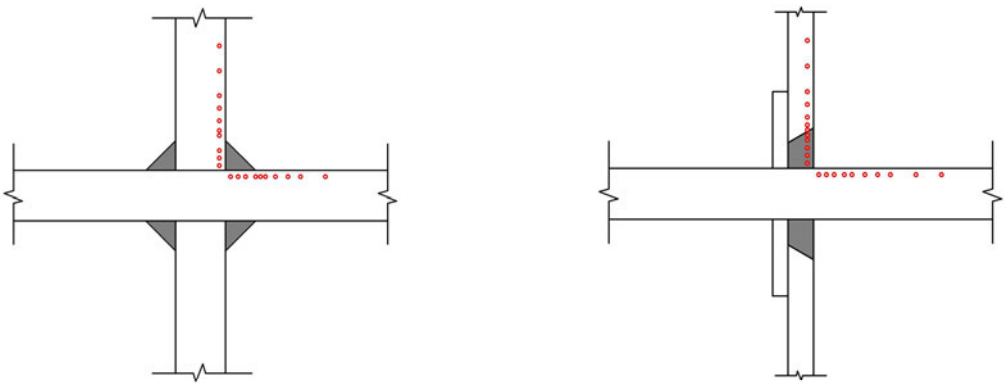

(a) Fillet-welded specimens

(b) Butt-welded specimens

Figure 6-5. Point positions of each specimen.

The interval of points in the high gradient parts was set to be 3 mm, while the measurements were carried out at the larger intervals of 5 mm or 10 mm in the low gradient parts, as shown in Fig. 6-5. All the points were measured at a depth of 2.5 mm from the surface of the plates. When measuring the residual strain, the neutrons interact with nuclei of the tested specimen and are diffracted, indicating that the more material they go through, the more counting time is required to obtain a clear diffraction peak. Therefore, the scanning time for each point was set based on its measurement position, ranging from 1 minute to more than 1 hour.

The specimen was positioned and oriented to measure the residual strains for the three directions, and the orientations of a fillet-welded specimen for the strain measurement of a point on the supported plate near the weld toe were plotted from the top view in Fig. 6-6. It is shown that the incident beam passes through the primary slit and strikes the tested specimen, and then the diffracted beam is received by the secondary slit. The direction of the measured strain is shown by the red arrows in Fig. 6-6. During the measurement, the specimen was fixed on the computer-controlled translational table, as shown in Fig. 6-7. The Kowari data analysis software was used to collect the test results, and Qkowari software was then used to process the raw data and determine the diffraction peak position for each point.

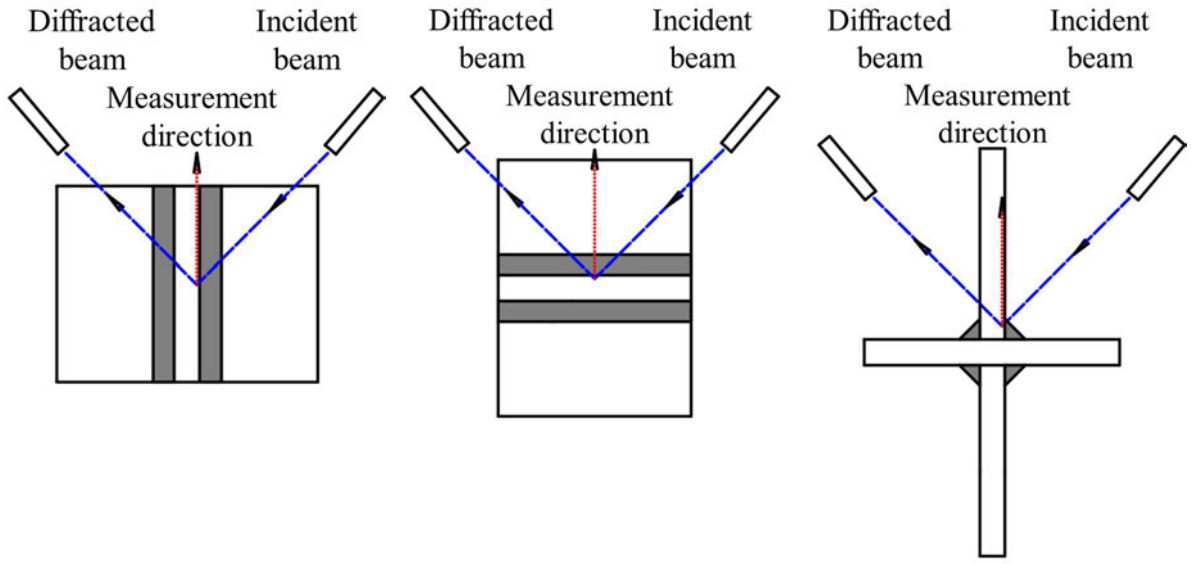

(a) Longitudinal (b) Transverse (c) Normal

Figure 6-6. Orientations plotted from the top view for the residual strain scanning of a fillet-welded specimen in the three directions.

Figure 6-7. Photo of the test setup for longitudinal residual strain measurements of a fillet-welded specimen.

6.3.3 Measurement of lattice spacing for the stress-free reference sample

As introduced in Section 6.2, for the neutron diffraction method, the residual strain is determined according to the difference in the lattice spacings between the stressed sample and the stress-free reference sample. Therefore, the lattice spacing of a stress-free reference sample is required to be measured before the residual strain measurement of the welded connections [78-79]. Considering that the welded cruciform specimens and the end-plate connection in the following section were made using the same materials and following the same welding processes, only one stress-free sample was cut from an F12 specimen, and its lattice spacings were used for all the welded connections in this study. The 40 mm long part from the edge was first removed to eliminate the run-on and run-out effects, and then a 5 mm thick slice was cut from the specimen to release its internal weld residual stresses, as shown in Fig. 6-8(a). The point positions of the reference sample were the same as those of the cruciform specimens introduced in Section 6.3.2, but the measurement was only conducted along one weld leg on the supported plate, as shown in Fig. 6-8(b).

Based on the measurement in the three directions, the lattice spacing d_0 of the stress-free sample was calculated for points with different distances from the weld root, as shown in Fig. 6-9. Since the reference sample was cut from the cruciform specimen with the weld size of 12 mm and the thickness of HAZ was assumed to be 2mm, the part from the weld root to 14 mm from the weld root was termed as the weld and HAZ areas, while points measured out of this range were within the base metal area. It is observed that the values of d_0 for points in the weld and HAZ areas were generally higher than those in the base metal area. It has been discussed in Sections 4 and 5 that the properties within the weld zone are not homogenous, and the weld,

HAZ and base metal can be considered as three different materials within the weld zone, which explains the different values of d_0 between the weld and HAZ areas and the base metal area. Therefore, the values of d_0 were divided into two groups, as shown in Fig. 6-9. The average value of the reference lattice spacing d_0 for weld and HAZ was 1.1469Å, and the average d_0 for base metal was 1.1468Å. The values of d_0 measured from the stress-free reference sample were then used in the following sections to determine the residual stresses in these welded connections.

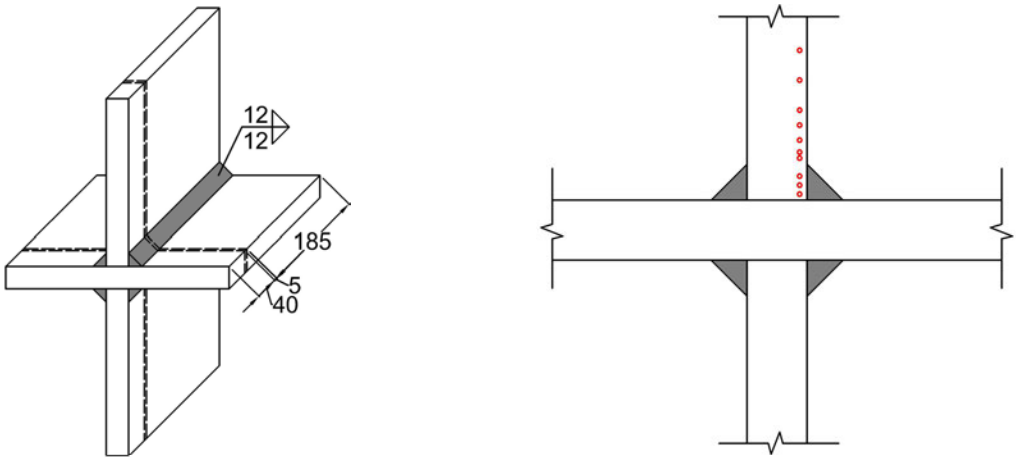

(a) A 5 mm slice cut from F12 specimen (b) Point positions

Figure 6-8. Design of the stress-free reference sample.

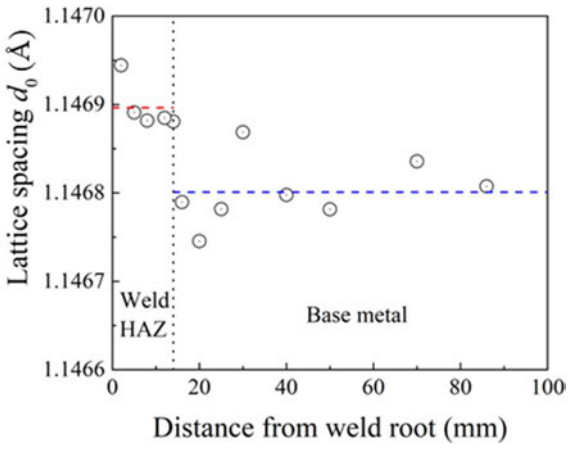

Figure 6-9. Lattice spacing in the stress-free sample.

6.3.4 Experimental results and discussion

After determining the residual strains for each specimen in the three directions, the residual stresses were calculated using Eqs. (6-3) to (6-5) and plotted in Fig. 6-10, where letters "F8-1", "F8-2", "F12-1", "F12-2", "F16-1", "F16-2", "B10-1" and "B10-2", refer to residual stresses measured for the 8 mm, 12mm or 16 mm fillet-welded or butt-welded cruciform specimen along the weld legs on the supported plate (-1) and supporting plate (-2), respectively.

The residual stresses were measured at positions from 2 mm to 86 mm from the weld root on the supported plates and from 2 mm to 40 mm from the weld root on the supporting plates.

For the fillet-welded cruciform specimens, the longitudinal residual stresses are the highest among the stresses in the three directions. The tensile longitudinal stress near the weld root decreases with increasing distance from the weld root and transforms to a compressive stress, whose absolute value decreases to zero with the increase in the distance from the weld root. Generally, the transverse stress increases slightly along the weld leg and then decreases, while the distribution of the normal stress is similar to the longitudinal stress. It is observed that for the F8 and F12 specimens, the distributions and magnitudes of residual stresses measured along the two legs agree well with each other, but the residual stresses of the F16 specimen measured on the supporting plate are slightly higher than those on the supporting plate. The distributions of the longitudinal and transverse residual stresses are consistent with the typical distributions of residual stresses shown in Fig. 2-17. As the residual stresses were measured at points with different distances from the centreline on the cross-sections perpendicular to the weld, the longitudinal stress is a set of balanced stresses, while the transverse residual stress is always positive in the measured distance range.

The magnitude and distribution of residual stresses of the butt-welded specimen are different from those of the fillet-welded specimens. The residual stress magnitudes of the B10 specimen in the three directions are generally lower than those of the fillet-welded cruciform specimens. On the supported plate, the longitudinal stress decreases with increasing distance from the weld root and then increases to about 300 MPa at a distance of 10 mm, after which the tensile stress decreases and transforms into a compressive stress. In the transverse and normal directions, the absolute values of the compressive stresses increase until the point 10 mm from the weld root and then decrease to zero with increasing distance. On the supporting plate, the distribution of the longitudinal stress is similar to those of the fillet-welded cruciform specimens, while the distributions of the transverse and normal stresses are similar to those on the supported plate of the B10 specimen.

Compared to the yield stresses of the base metal, weld and HAZ measured in Section 4.5.2, it is observed from Fig. 6-10 that the longitudinal residual stresses measured in the weld and HAZ areas are higher than the yield stresses of the materials in the weld zone. To check if the material was still in the elastic state, the von Mises stress at measurement points was calculated using Eq. (2-4) and plotted in Fig. 6-11. As shown in Fig. 6-5, most of the points measured in

the weld zone were in the HAZ area. Considering that the weld and HAZ dimensions of the cruciform specimens ranged from 8 mm to 20 mm, the yield stresses of the HAZ in the longitudinal and transverse directions were plotted in the range from the weld root to the point 20 mm from the weld root in Fig. 6-11. It is shown that although the longitudinal residual stresses reached values higher than 400 MPa, the von Mises stresses were still lower than the yield stress (447.9 MPa or 382.8 MPa) of the material. Therefore, it is verified that the materials at the measurement points were still in the elastic range.

To evaluate the reliability of the test results, the uncertainties of the measured residual stresses were calculated using Eqs. (6-6) to (6-11) and plotted in Fig. 6-12. Similar to the lattice spacing d_0 measured from the stress-free sample, the values of the lattice spacing uncertainty Δd_0 were divided into two groups and the average values of Δd_0 for the weld and HAZ areas and the base metal area were 4.4×10^{-5} Å and 4.0×10^{-5} Å, respectively. It is shown that for all the welded cruciform specimens, the values of the uncertainties were higher for the points near the weld root because the neutron beam needed to pass through more materials at these point positions. These average measurement errors of the welded cruciform specimens ranged from 13.07 MPa to 18.64 MPa, which were lower than 6% of the yield stress of the base metal. Therefore, it is verified that the measured results were reliable.

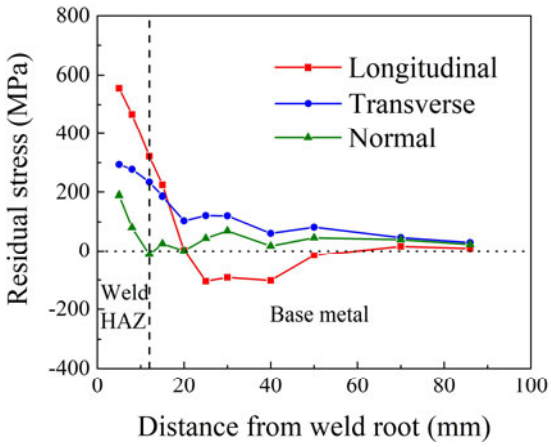

(a) F8-1 (supported plate)

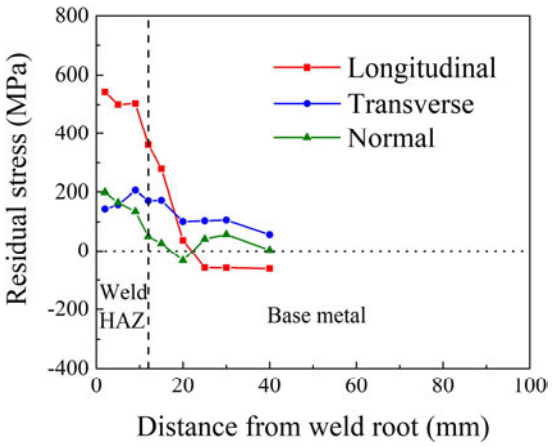

(b) F8-2 (supporting plate)

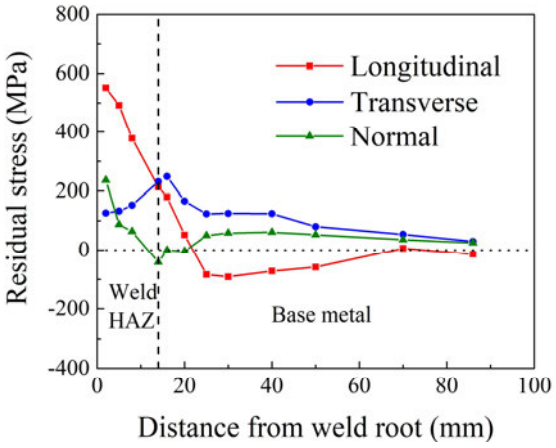

(c) F12-1 (supported plate)

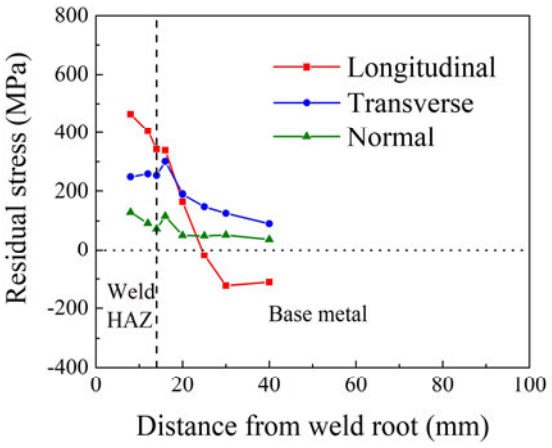

(d) F12-2 (supporting plate)

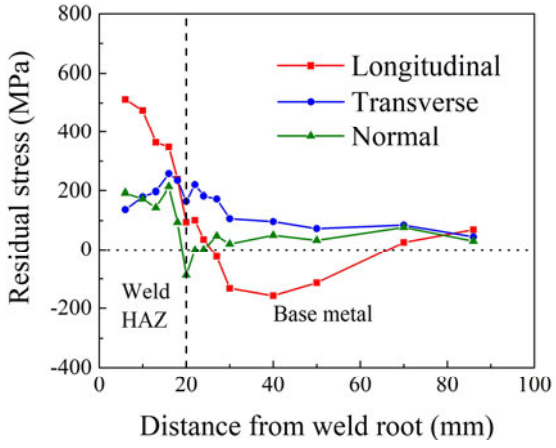

(e) F16-1 (supported plate)

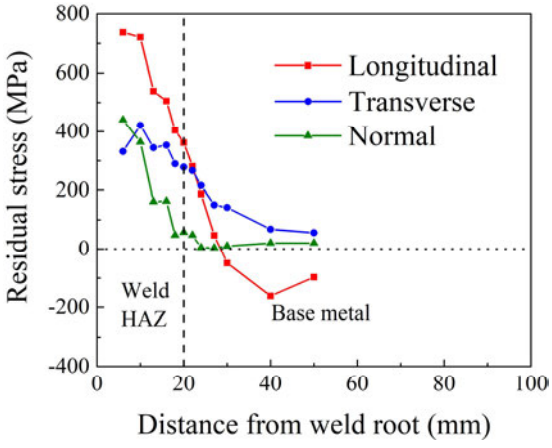

(f) F16-2 (supporting plate)

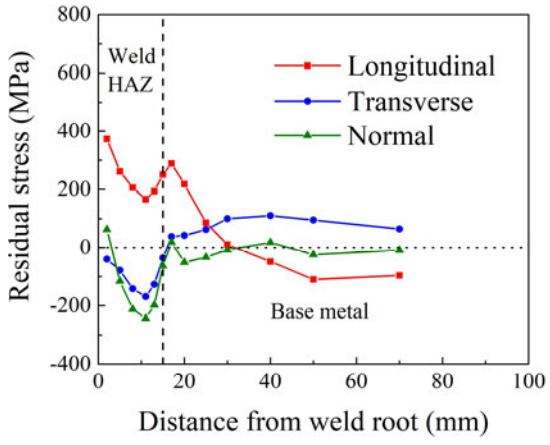

(g) B10-1 (supported plate)

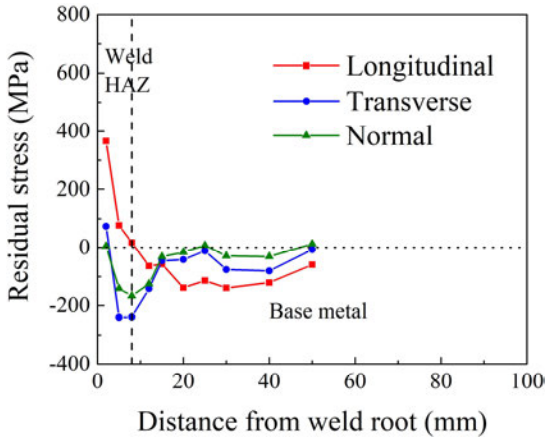

(h) B10-2 (supporting plate)

Figure 6-10. Residual stresses of points at various distances from weld root.

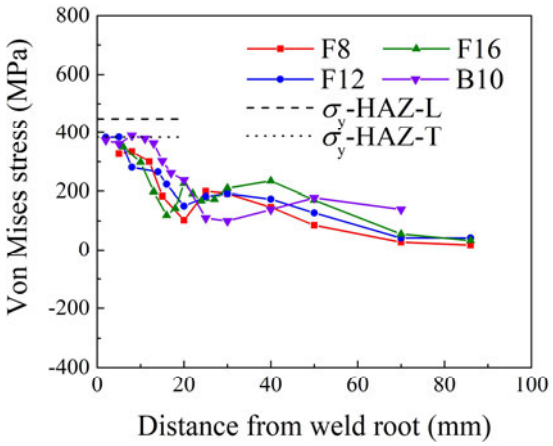

(a) Measured from supported plates

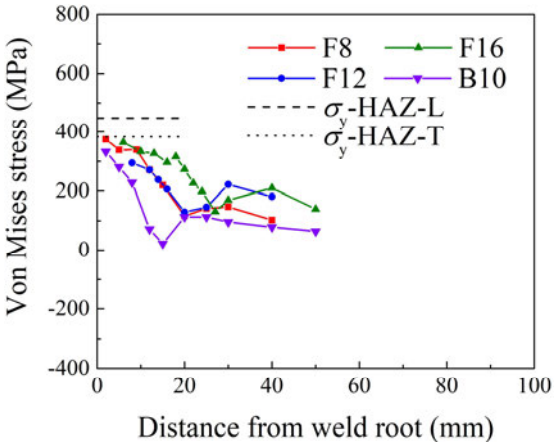

(b) Measured from supporting plates

Figure 6-11. Von Mises stresses of points at various distances from weld root.

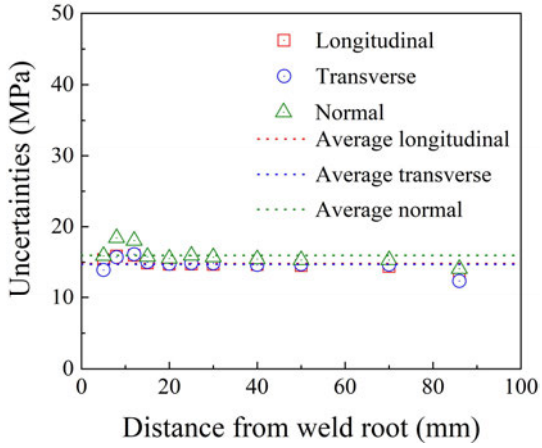

(a) F8-1

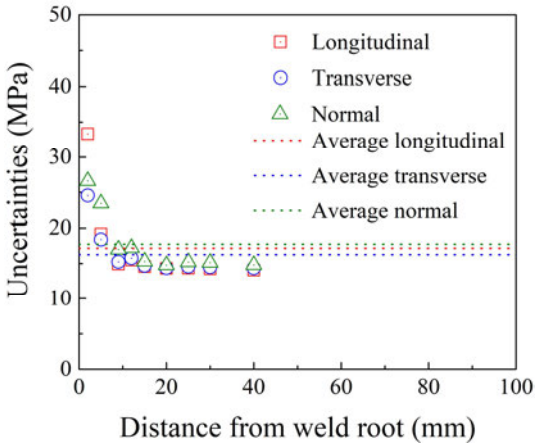

(b) F8-2

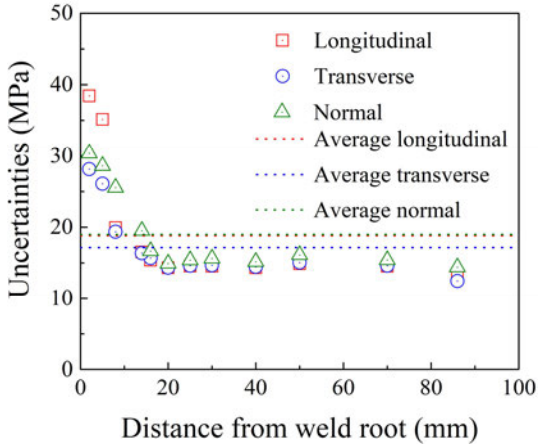

(c) F12-1

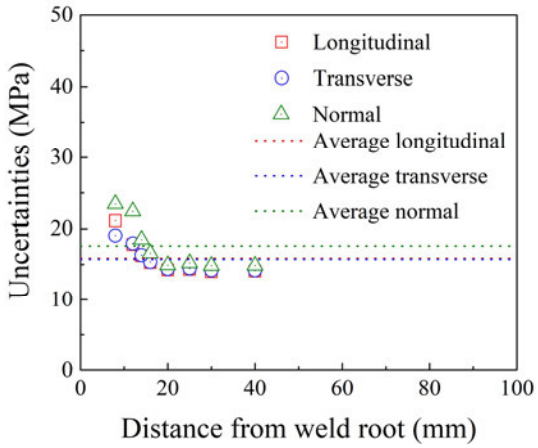

(d) F12-2

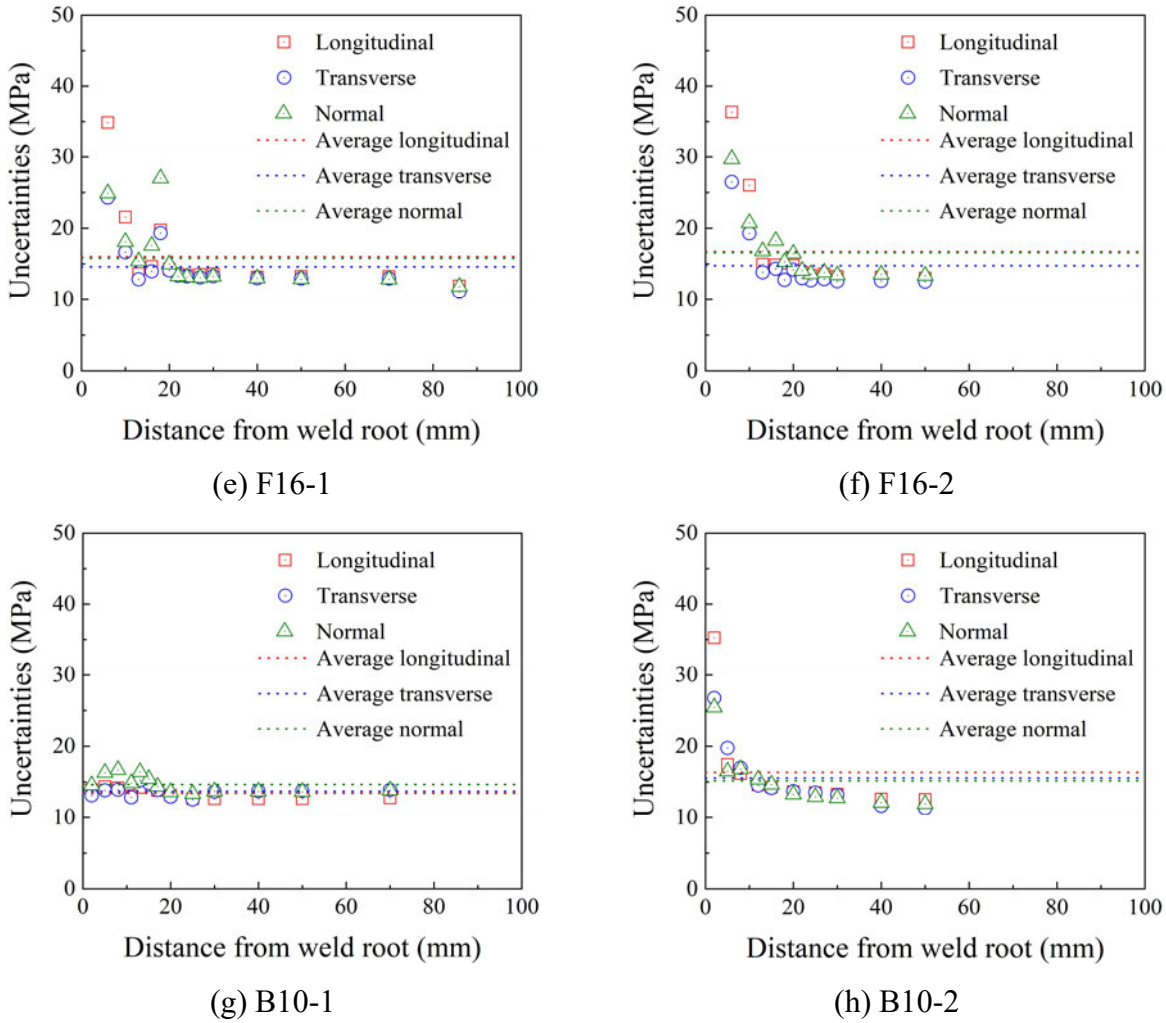

(e) F16-1 (f) F16-2

(g) B10-1 (h) B10-2

Figure 6-12. Experimental uncertainties of calculated residual stresses of points at various distances from weld root.

The average distribution curves for the residual stresses measured from the fillet-welded cruciform specimens are plotted in Fig. 6-13. The solid part of the curve was obtained by averaging the residual stresses measured along the two weld legs, while the dash part was taken from results measured from the supported or supporting plate when only one result was available. The distributions of the residual stresses are similar among the three specimens, where the longitudinal stresses are the highest among the residual stresses in the three directions, and the values of the residual stresses decrease with increasing distance from the weld root. The comparison of the residual stress magnitudes of the fillet-welded cruciform specimens shows that the residual stresses of the F16 specimen are the highest among the three specimen types in the three directions, while the difference in the stress magnitudes between the F12 and F8 specimens is less distinct. Therefore, it is concluded that the larger the weld size, the higher the residual stresses in all three directions. The distance between the point where the longitudinal stresses transform from tensile to compressive, and the weld root is

termed the longitudinal peak distribution range, and Fig. 6-12(a) shows that the longitudinal peak distribution range increases with increasing weld size. It is concluded that the larger the weld size, the wider the longitudinal peak distribution range. Among the three specimens discussed in this section, it is observed that the effect of the weld length was not significant in this study.

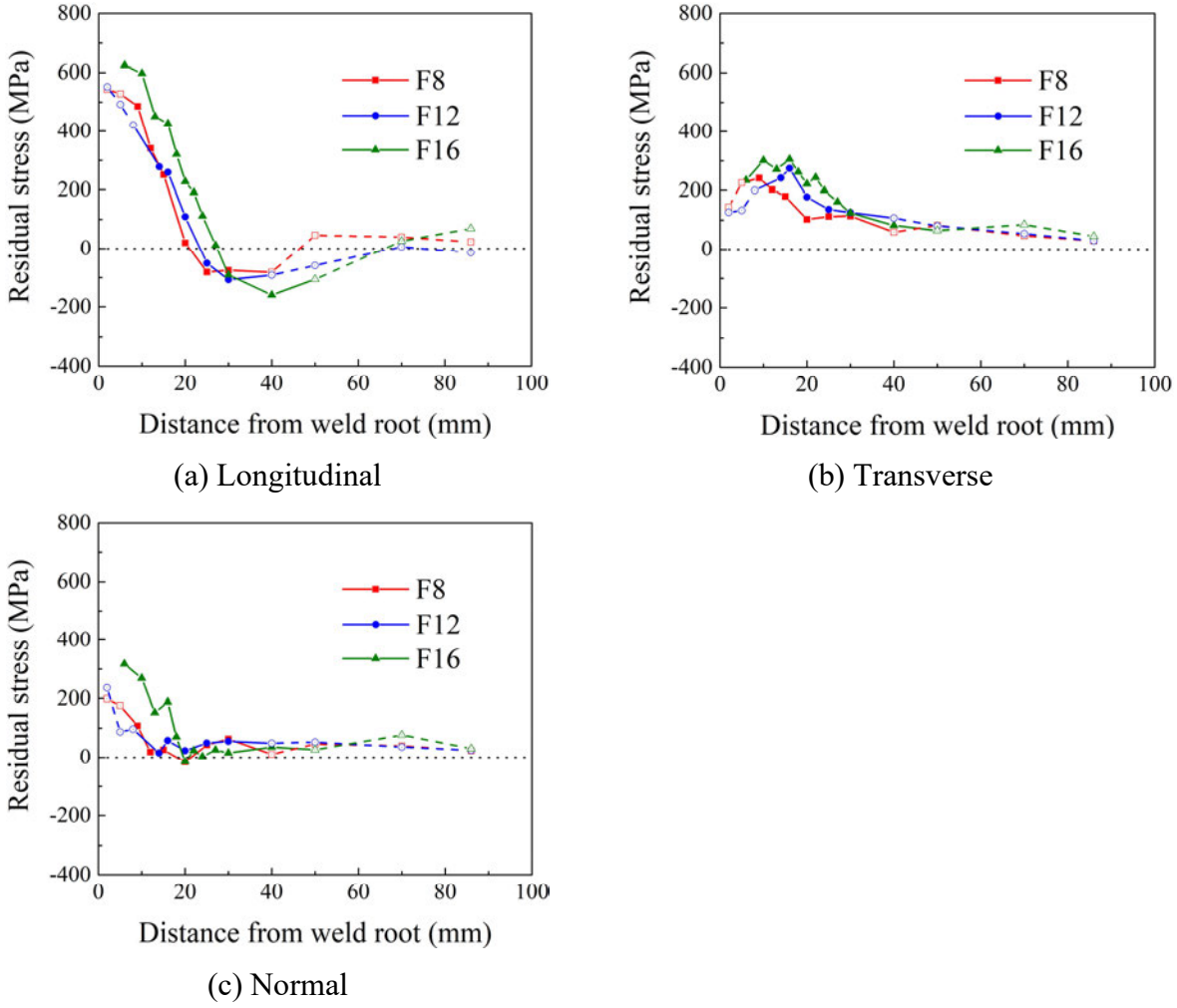

(a) Longitudinal

(b) Transverse

(c) Normal

Figure 6-13. Comparison of residual stresses of fillet-welded cruciform specimens.

6.4 Residual stresses in a welded end-plate connection

6.4.1 Specimen design

A welded end-plate connection was designed and fabricated to investigate the magnitude and distribution of residual stresses in a complex practical connection, as shown in Fig. 6-14. For the residual stress measurement purpose, a 205 mm long I beam was made by welding together three plates through 8 mm double-sided fillet welds and a butt weld. The end plate was then welded to the I beam through 12 mm fillet welds and butt welds. All plates forming the end-plate connection were extracted from the 20 mm thick steel plate, except the 10 mm thick web

in the I beam. Considering the welds in the end-plate connection were made along various directions, two sets of coordinate systems were defined in Fig. 6-14(b), where the letters "L-I", "T-I", and "N-I" refer to the longitudinal, transverse and normal directions for the welds in the I beam, while letters "L-E", "T-E", and "N-E" refer to the three directions for the welds connecting the I beam and the end plate.

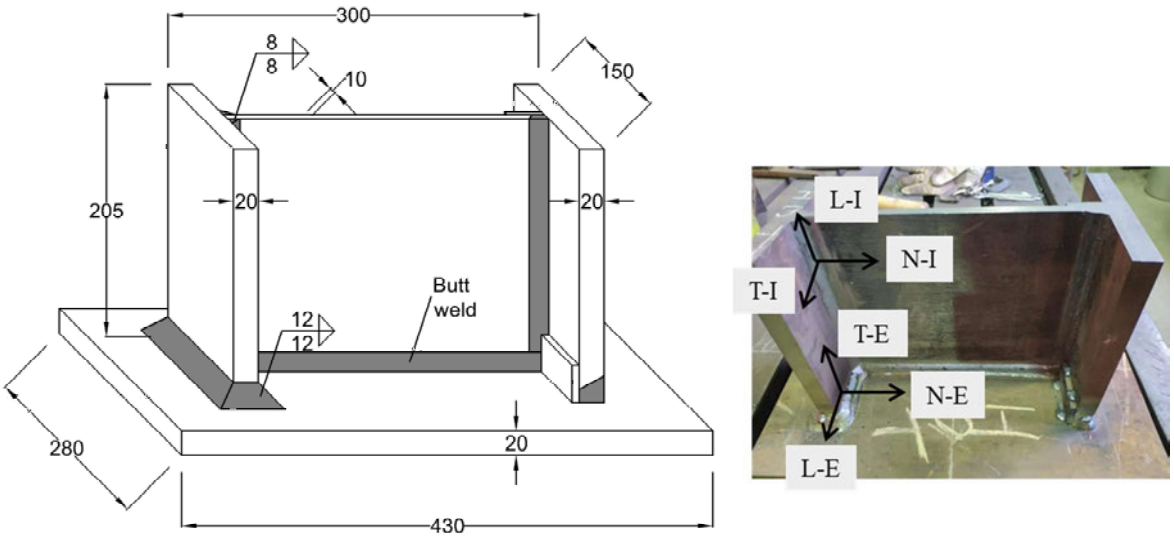

(a) Geometry of end-plate connection (b) Photo of end-plate connection

Figure 6-14. Design of welded end-plate connection.

6.4.2 Test setup

For the end-plate connection, residual stresses were measured at four cross-sections on the fillet-welded side of the specimen, as shown in Fig. 6-15. The magnitude and distribution of residual stresses in the I beam were measured at section A, which is 150 mm from the end plate, as shown in Fig. 6-15(a). The residual stresses were measured at points on the flange with different distances from the web centreline, as shown in Fig. 6-15(b), and the measurements were conducted in the three directions as defined as "L/T/N-I" in Fig. 6-14(b). The residual stresses of the welds connecting the I beam and the end plate were measured at sections B, C and D, as shown in Fig. 6-15(c). The measured points were on the flange of the I beam with different distances from the weld root, as shown in Fig. 6-15(d), and the measurements were conducted in the three directions as defined as "L/T/N-E" in Fig. 6-14(b). At these sections, the interval of points near the welds was set to be 2 mm, while the measurements were carried out at larger intervals in low stress gradient range. All the points were measured at a depth of 2.5 mm from the surface of the plates, and different scanning times were set for the points at different positions, following the same strategy as for the measurements of cruciform specimens. The end-plate connection was fixed on the translational table at various positions

and directions to measure the longitudinal, transverse and normal strains for each section, as shown in Fig. 6-16. For the neutron diffraction measurement of the welds in the end-plate connection, the gauge volume was set as 3×3×3 mm^3 for the longitudinal direction and 3×3×20 mm^3 for the normal and transverse directions to speed up the data acquisition.

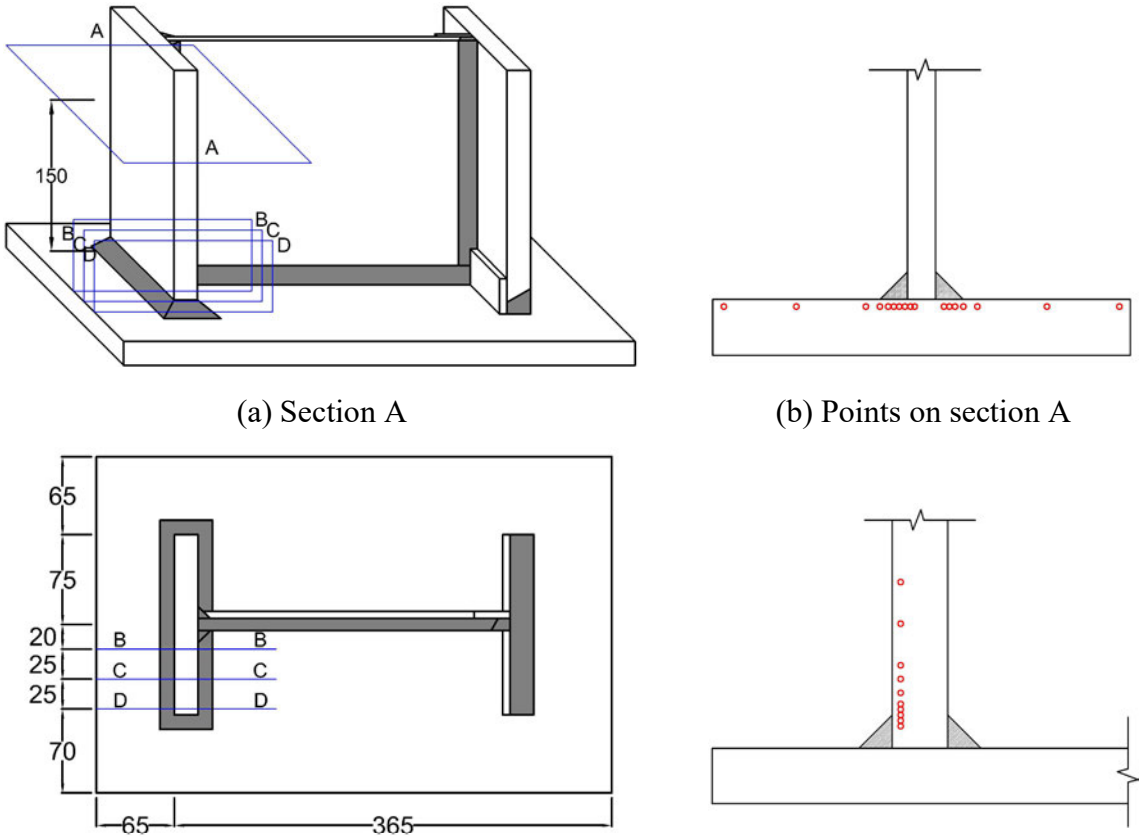

(a) Section A (b) Points on section A

(c) Sections B/C/D (d) Points on sections B/C/D

Figure 6-15. Point positions of each specimen.

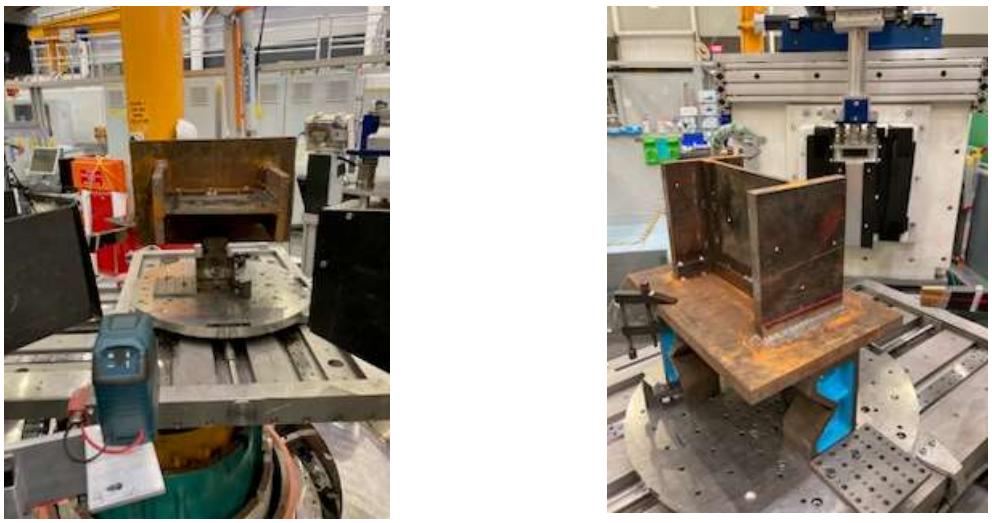

(a) Longitudinal-A (b) Longitudinal-B/C/D

Figure 6-16. Test setup for welded end-plate connection.

6.4.3 Experimental results and discussion

The residual stresses in section A were calculated based on the measured strains using Eqs. (6-3) to (6-5) and plotted in Fig. 6-17. It is shown that the residual stresses are higher for the points near the welds, and the longitudinal stress is the highest among the residual stresses in the three directions, which is consistent with the results of the cruciform specimens. The stress peak is observed near the middle of the flange, and it is slightly unsymmetric with respect to the web centreline, which can be explained by the welding sequence. The blue curves named F8 in Fig. 6-17 are the residual stresses of the 8 mm fillet weld measured from the welded cruciform specimen in Section 6.2 and were plotted symmetrically according to the distance from the weld root. The comparison of residual stresses of the 8 mm fillet welds measured from the I beam and the cruciform specimen shows that the distributions of the residual stresses of the two specimen types are similar. The magnitudes of longitudinal and normal stresses of the F8 specimen are higher than those of section A, while the magnitudes of their transverse stresses are similar. Considering that the web thickness of the I beam is 10 mm and thinner than the supported plate in the cruciform specimens, the difference in the stress magnitude can likely be explained by the different support conditions of the welds in the two specimen types and the effect of the welding sequence. A more rigid support condition will result in more constrained thermal contraction and lead to higher weld residual stresses. It is concluded that generally, the welded specimen types using the same materials and the same welding process will produce residual stresses with similar magnitudes and distributions.

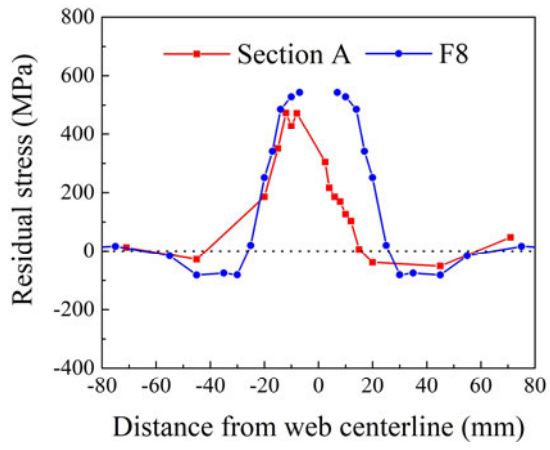

(a) Longitudinal

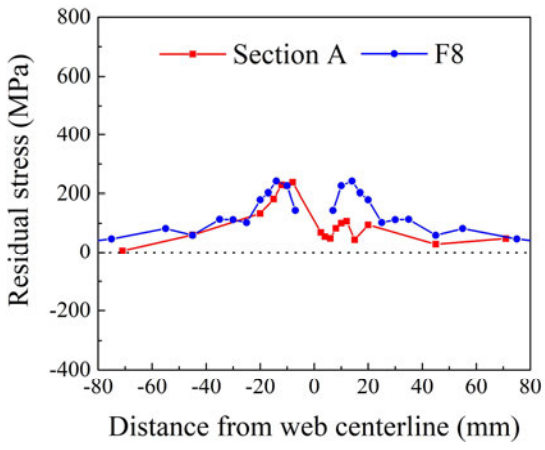

(b) Transverse

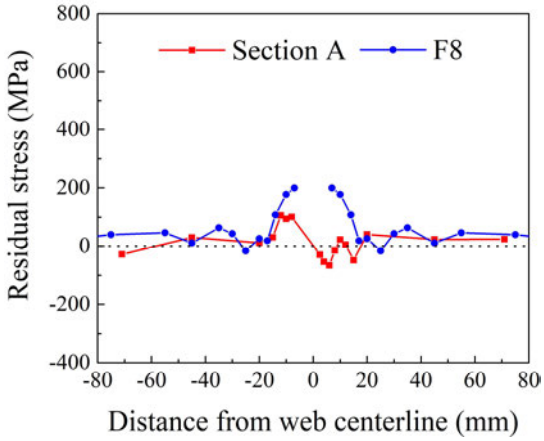

(c) Normal

Figure 6-17. Comparison of residual stresses of fillet welds being 8 mm.

The residual stresses at sections B, C and D were calculated and plotted in Fig. 6-18. It is observed that for the three sections, the residual stresses in three directions decrease with increasing distance from the weld root, and the highest residual stress is in the longitudinal direction, which is consistent with the results of the cruciform specimens. Sections B and C present similar magnitudes and distributions of residual stresses, while the results in section D are different. It is because section D is near the end of the flange where the weld changes its direction around the flange, and its constraints are different from those of sections B and C. The orange curves named F12 in Fig. 6-18 are the residual stresses of the 12 mm fillet weld measured from the cruciform specimen in Section 6.2 and were plotted according to the distance from the weld root. The comparison of residual stresses of the 12 mm fillet welds measured from the end-plate connection and the cruciform specimen shows that the distributions of the residual stresses of the two specimen types are similar. The magnitudes of longitudinal and normal stresses of F12 are slightly lower than those of sections B and C, because in the end-plate connection, the flange of the I beam was welded to the end plate instead of to a single supported plate in the welded cruciform specimen and the more rigid support conditions of the welds in the end-plate connection most likely led to higher deformation constraints and higher residual stresses. The comparison of the results of sections B and C and the cruciform specimen further verifies the conclusion that under the same welding process, similar residual stresses will be generated by different specimen types made of the same materials.

The uncertainties of the residual stresses measured from the end-plate connection were calculated and plotted in Fig. 6-19. The average measurement errors of the end-plate

connection ranged from 11.39 MPa to 16.35 MPa, which were lower than 6% of the yield stress of the base metal. Therefore, it is verified that the measured results were reliable.

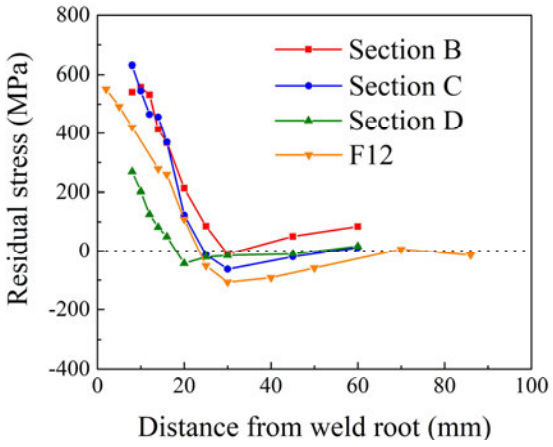

(a) Longitudinal

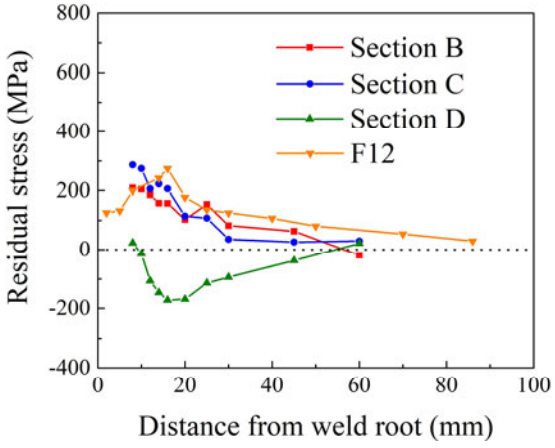

(b) Transverse

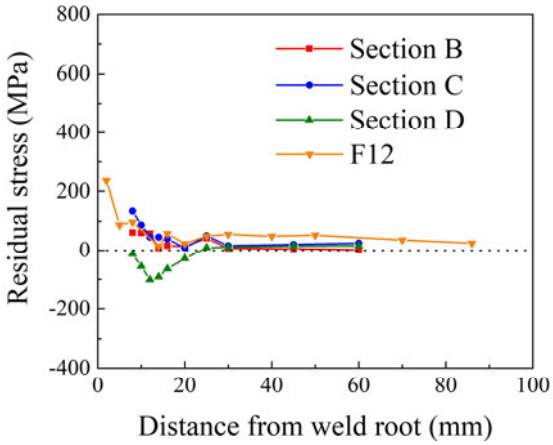

(c) Normal

Figure 6-18. Comparison of residual stresses of fillet welds being 12 mm.

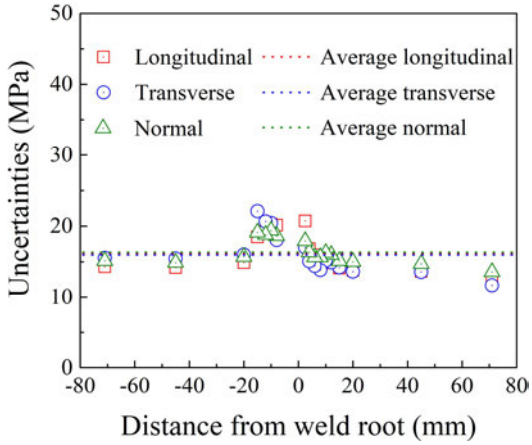

(a) Section A

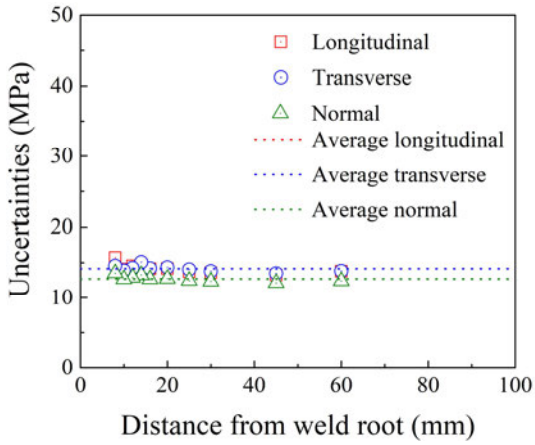

(b) Section B

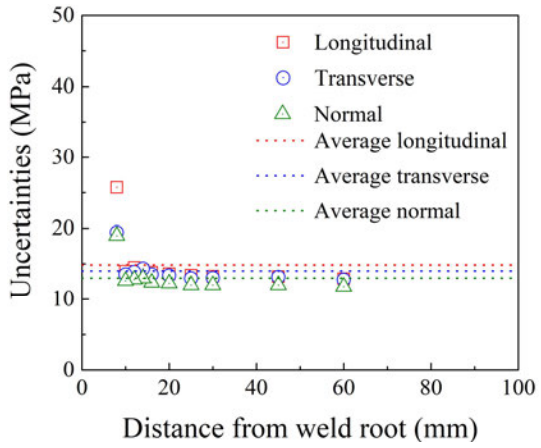

(c) Section C

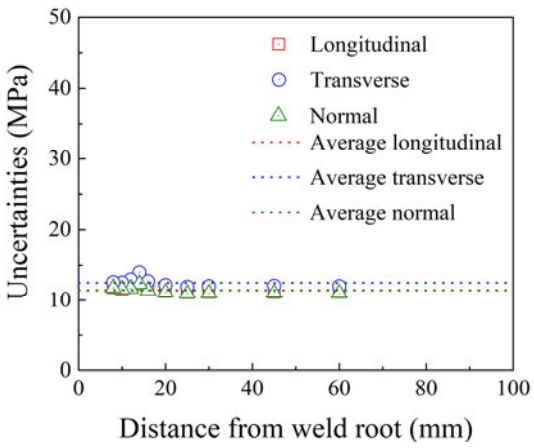

(d) Section D

Figure 6-19. Comparison of residual stresses of fillet welds being 8 mm.

6.5 Summary

In this chapter, the magnitude and distribution of residual stresses in four welded cruciform specimens and an end-plate connection were measured using the neutron diffraction method. The lattice spacing d_0 of the stress-free reference sample was first measured along one weld leg, and it was observed that the values of d_0 for points in the weld and HAZ range were generally higher than those in the base metal. Therefore, the results of d_0 were divided into two groups, where the average d_0 for weld and HAZ was 1.1469 Å, and the average d_0 for base metal was 1.1468 Å. The uncertainties of the residual stresses measured from the welded cruciform specimens and the end-plate connection were calculated, and the average measurement errors were lower than 6% of the yield stress of the base metal, which verified the reliability of the test results measured by the neutron diffraction method.

The four cruciform specimens were fabricated using 16 mm fillet welds, 12 mm fillet welds, 8 mm fillet welds, or butt welds. The residual stresses were measured for one weld along two weld legs in each cruciform specimen at points with different distances from the weld root, and it was shown that among all the cruciform specimens, the longitudinal residual stresses were the highest among stresses in the three directions. The residual stresses of the fillet-welded specimens with different weld sizes presented similar distributions, which were different from those of the butt-welded specimens, especially in the transverse and normal directions. The comparison of the measurement results of the welded cruciform specimens with different fillet weld sizes showed that the larger the weld size, the higher the residual stresses and the wider the peak distribution range.

The welded end-plate connection was fabricated by welding an end plate to an I beam using 12 mm fillet welds and butt welds, where the I beam was fabricated by welding together three plates using 8 mm double-sided fillet welds and a butt weld. The residual stresses in the I beam were measured at a cross-section 150 mm from the end plate, while the residual stresses of the welds connecting the I beam and the end plate were measured at three sections with different distances from the web centreline. It was observed that the residual stresses were higher near the welds, and the longitudinal stress was the highest among the three directions, which is consistent with the results of the cruciform specimens. Generally, the residual strain results of fillet welds measured from the end-plate connection agreed well with those of the cruciform specimens, and it was concluded that under the same welding process, similar residual stresses will be generated for the fillet welds with the same weld size by different specimen types made by the same materials.

Chapter 7 Fracture investigation of welded connections

7.1 Introduction

As one of the main failure modes of steel structures, fracture in welded connections has widely been discussed based on experimental investigations and numerical simulations, as introduced in Section 2.4. However, the weld-zone mechanical properties, such as stress-strain relationships and fracture strains of the weld and HAZ, have rarely been considered in these analyses. Therefore, in this chapter, the fracture process of a series of welded cruciform specimens is discussed to investigate the effects of the inhomogeneity of mechanical properties in the weld zone.

Section 7.2 describes the tensile tests carried out on the welded cruciform specimens fabricated using 8 mm or 12 mm fillet welds. To match the capacity of the testing machine, the cruciform specimens studied in this chapter were cut from the long specimens described in Chapter 6, and the thickness of these specimens was 10 mm. Considering the thickness of these specimens was only a few millimetres thicker than the stress-free reference samples used in Chapter 6, the effect of the weld residual stresses is ignored in this study. The macroetching and hardness tests were performed on the cross-sections of the welded cruciform specimens. Based on the macroetching results, the weld, HAZ and base metal areas in the weld zone were identified, and the width of HAZ was measured and compared with those of the butt-welded plates in Chapter 4. The values of the Vickers hardness were then measured for the three material areas in the weld zone and compared with those measured from the butt-welded plates. Considering that the hardness of the material is related to its mechanical properties, if the hardness of the three material areas measured from the cruciform specimens is consistent with that measured from the butt-welded plates, it is indicated that the mechanical properties of the three material areas measured from the butt-welded plates can be used in the simulation of the cruciform specimens. After conducting the tensile tests on the welded cruciform specimens, the experimental results, including load-deformation curves and fracture deformation, are discussed and compared between the two specimen types.

In Section 7.3, finite element models are developed for the welded cruciform specimens, and the simulation results are compared with the experimental results to discuss the effects of the material inhomogeneity in the weld zone. Based on the measurement results of the mechanical properties of the weld, HAZ and base metal in Chapter 4, the test process was simulated using

the FE models by ignoring or considering the inhomogeneous mechanical properties of the three material areas. Using the free parameters calibrated by the fracture strains of the three material areas in Chapter 5, the fracture process of the welded cruciform specimens was simulated using the fracture model LMVGM, and the comparison shows that the mechanical properties of the weld and HAZ should be included in the investigation of fracture in welded connections to obtain reliable simulation results. Section 7.4 summarizes the whole chapter.

7.2 Tests on fracture in welded cruciform specimens

7.2.1 Welded cruciform specimens

As described in Section 6.3, 230 mm or 150 mm long cruciform specimens were made by perpendicularly welding the supported plates to the supporting plate using fillet welds with various weld sizes. In this chapter, slices were cut from the long specimens, as shown in Fig. 7-1(a). The 40 mm long part from the edges was first removed to eliminate the run-on and run-out effects, and then four 10 mm thick slices were cut from the long specimens, which were made through 8 mm fillet welds by one weld pass or 12 mm fillet welds by three weld passes. In the following sub-sections of this chapter, these cruciform slices are named "cruciform specimens", whose geometries are shown in Fig. 7-1(b). The letters "F8" and "F12" refer to the two specimen types cut from the long specimens with weld sizes of 8 mm or 12 mm, respectively.

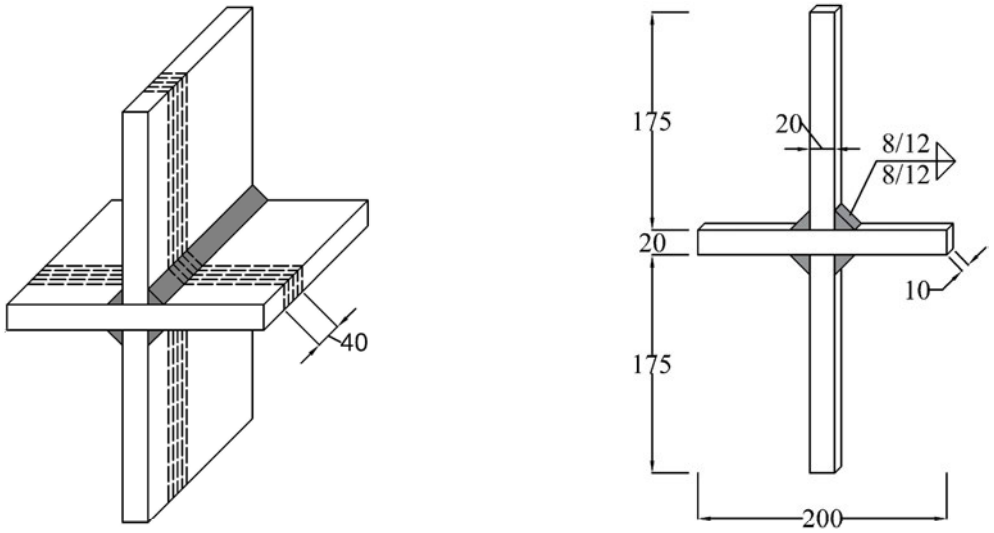

(a) Slices cut from long specimens (b) Geometry of F8 and F12 specimens

Figure 7-1. Welded cruciform specimens (Dimensions in mm).

As introduced in Section 6.3.3, in order to obtain the weld residual stresses using the neutron diffraction method, a 5 mm thick sample was cut perpendicular to the weld from a specimen

which was the same as the tested specimen and was termed as the stress-free reference sample. Since the residual stresses were assumed to be released for the stress-free sample, its lattice spacing was measured and used as the reference value for the residual stress calculation of the tested specimen. Since the thickness of these cruciform specimens was 10 mm, which was only a few millimetres thicker than those of the stress-free reference samples, they were assumed to be free from weld residual stresses. Therefore, the effect of the weld residual stresses was not considered in the fracture investigation of the welded cruciform specimens in this study.

The surface of each cruciform specimen was macroetched, after which the dividing lines were determined, and the distribution of weld and HAZ could be distinguished. It is observed from the photo of the macroetched surface of an F12 specimen in Fig. 7-2 that the three weld passes in the 12 mm fillet welds formed curved dividing lines, and the width of HAZ was larger near the weld toe than the weld root. The weld area was always larger than the theoretical size since the high temperature during the welding process melted the base metal near the edge allowing the weld area to blend into the supported and supporting plates. The length of the two weld legs of each weld in the cruciform specimens was measured from four replicated specimens, producing 48 results as summarized for the F8 and F12 specimens in Fig. 7-3. It is shown that the weld legs of the F8 specimens ranged from 7.53 mm to 10.35 mm, and those of the F12 specimens ranged from 11.64 mm to 15.00 mm. The average lengths of the weld legs were 9.21 mm and 13.42 mm for the F8 and F12 specimens, respectively.

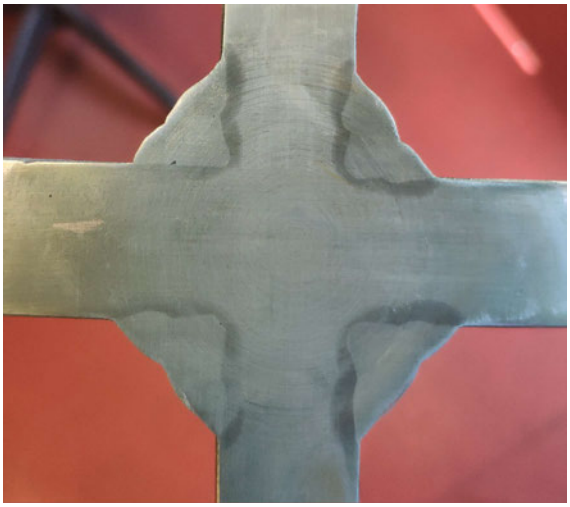

Figure 7-2. Photo of the macroetched surface of a F12 specimen.

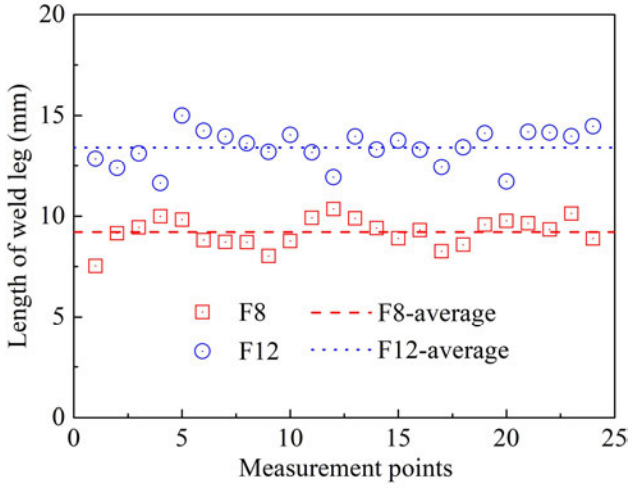

Figure 7-3. Lengths of weld legs of F8 and F12 specimens.

Two welds were chosen from each specimen type, and the width of HAZ and hardness of the three materials were then measured for these two welds. The widths of HAZ were measured as the horizontal distances between the two dividing lines on the supported plates and as the vertical distances on the supporting plates. For each weld, the HAZ widths were measured from four points at different distances from the weld root along the weld legs on the supported and supporting plates, resulting in a total of 32 measurements for both the F8 and F12 specimens, as shown in Fig. 7-4. The results of most measurement ranged from 1.5 mm to 3.0 mm, and the average width of the HAZ area was 2.28 mm, which was close to the average horizontal HAZ width measured from the butt-welded plates in Chapter 4. Therefore, it is concluded that under the same welding process, the widths of HAZ measured from different specimen types made using the same materials will be similar.

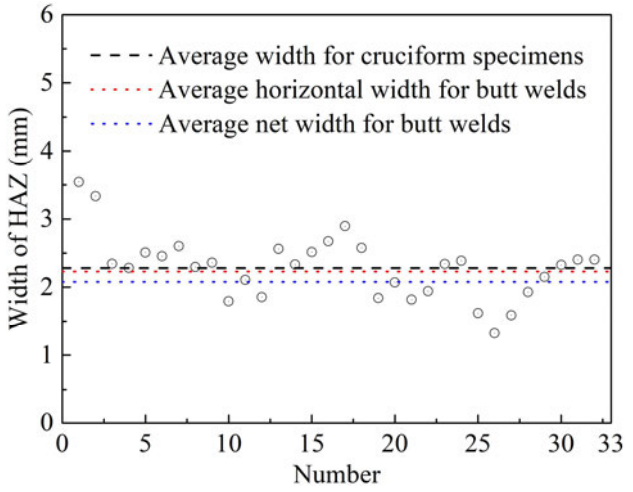

Figure 7-4. Width of HAZ in the welded cruciform specimens.

The Vickers hardness was measured for these two welds for each specimen type using the Dura Scan machine at 15 locations, three in the weld area, six in the HAZ and six in the base metal area. The three locations in each material area from each piece were randomly selected, and the distance between each location was large enough that they did not interact with each other. Under the load of 4.9 N (0.5 kg), the average indentation sizes were 78.07 μm, 70.78 μm and 65.25 μm, and the average HV0.5 values were computed as 152.16, 185.41 and 217.83, for the base metal, HAZ and weld, respectively. The test results show that the weld had the highest hardness while the base metal was the softest. The hardness of the three material areas was plotted in Fig. 7-5 and compared with those measured from the butt-welded plates in Chapter 4, where letters "BW", "FW-8", and "FW-12" refer to butt welds, 8 mm fillet welds, and 12 mm fillet welds. The comparison shows that the values of hardness of the three material areas in the weld zone measured from the cruciform specimens are consistent with those of the butt-welded plates. Considering the hardness of steel is related to its mechanical properties, it is indicated that the mechanical properties of the three material areas in the cruciform specimens were similar to those in the butt-welded plates. Therefore, the results of the stress-strain relationships and fracture strains of the weld, HAZ and base metal measured in Chapters 4 and 5 were then used in the simulation of welded cruciform specimens in the following sections.

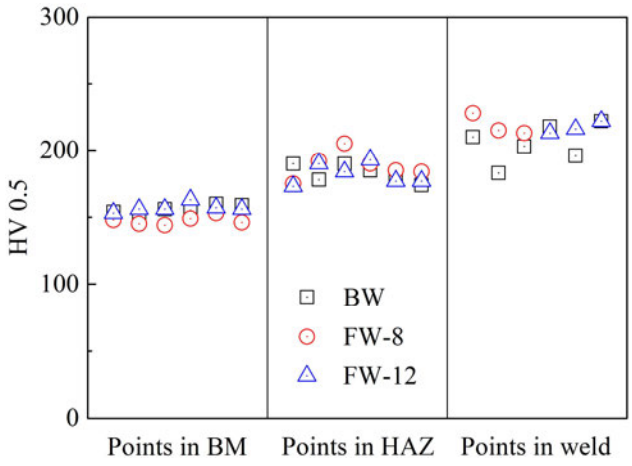

Figure 7-5. Hardness results of cruciform specimens.

7.2.2 Test setup and experimental results

Tensile tests were conducted on the welded cruciform specimens to investigate their fracture process. The tests were performed in a 300 kN MTS Sintech testing machine, and four replicated tests were carried out for each specimen type. The photos of the test setup of the F8 and F12 specimens are shown in Fig. 7-6. To measure the deformation during the loading process, a pair of special clamps were fixed on the supported branches, and two displacement

meters were fixed on the clamps. The deformation of the specimen was then obtained by averaging the measured results of the two displacement meters. The distance between the two clamps was 90 mm, which was termed the gauge length for the cruciform specimens. To obtain the static load-deformation curves, the loading was controlled at a low speed of 2 mm/min and paused three times for 100s to allow stress relaxation. The static load-deformation curves were then converted from the original quasi-static curves following the same method adopted in Chapter 3.

(a) Unloaded F8 specimen

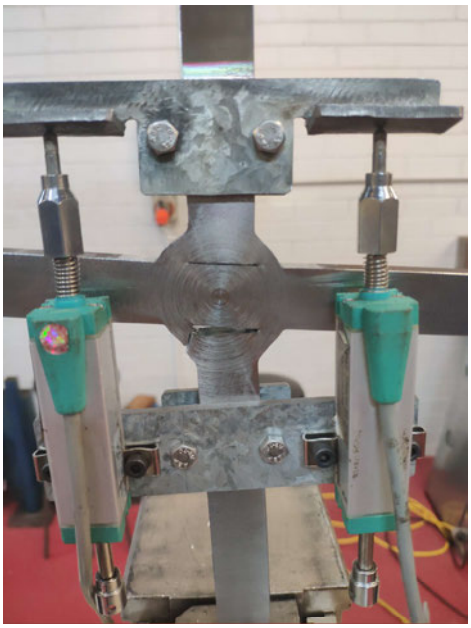

(b) Fractured F8 specimen

(c) Unloaded F12 specimen

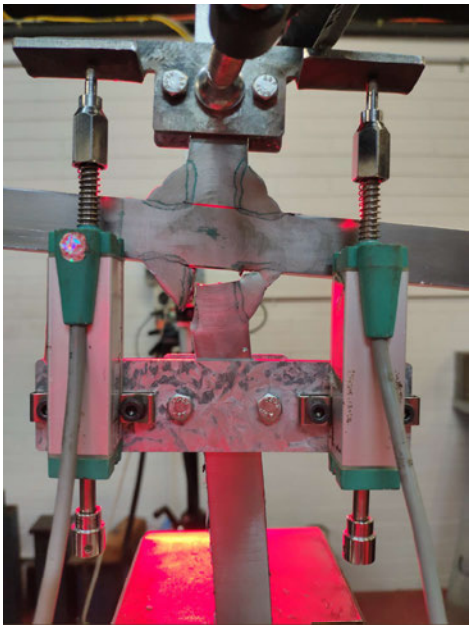

(d) Fractured F12 specimen

Figure 7-6. Test setup for cruciform specimens.

The photos of the fractured F8 and F12 specimens are shown in Figs. 7-7 and 7-8, where the first crack was noted in the black circle. It is observed that a plastic deformation developed and localized in the weld zone during the loading process, and the first crack initiated from one weld root before a decrease in the loading capacity occurred. The crack propagated horizontally for a small distance, and a vertical crack was then formed, leading to the final fracture of the weld. The exceptions are the F8-1 specimen, whose first crack propagated horizontally along the fusion line, and the F12-2 specimen, whose first crack propagated to the middle of the weld leg and then propagated vertically in the weld area. After the weld totally fractured due to the first crack, another crack occurred in the other weld on the same supported branch leading to the final failure of the cruciform specimen. It is shown that generally, the first crack of the cruciform specimens formed vertically in the weld zone, while the second crack formed in the weld zone horizontally or at an angle of about 45°. Compared to F8 specimens, the first crack in F12 specimens occurs closer to the HAZ in the weld zone. The difference in the crack location may be caused by the different weld sizes, and the fact that a crack will appear closer to the HAZ in the weld zone with a larger weld size.

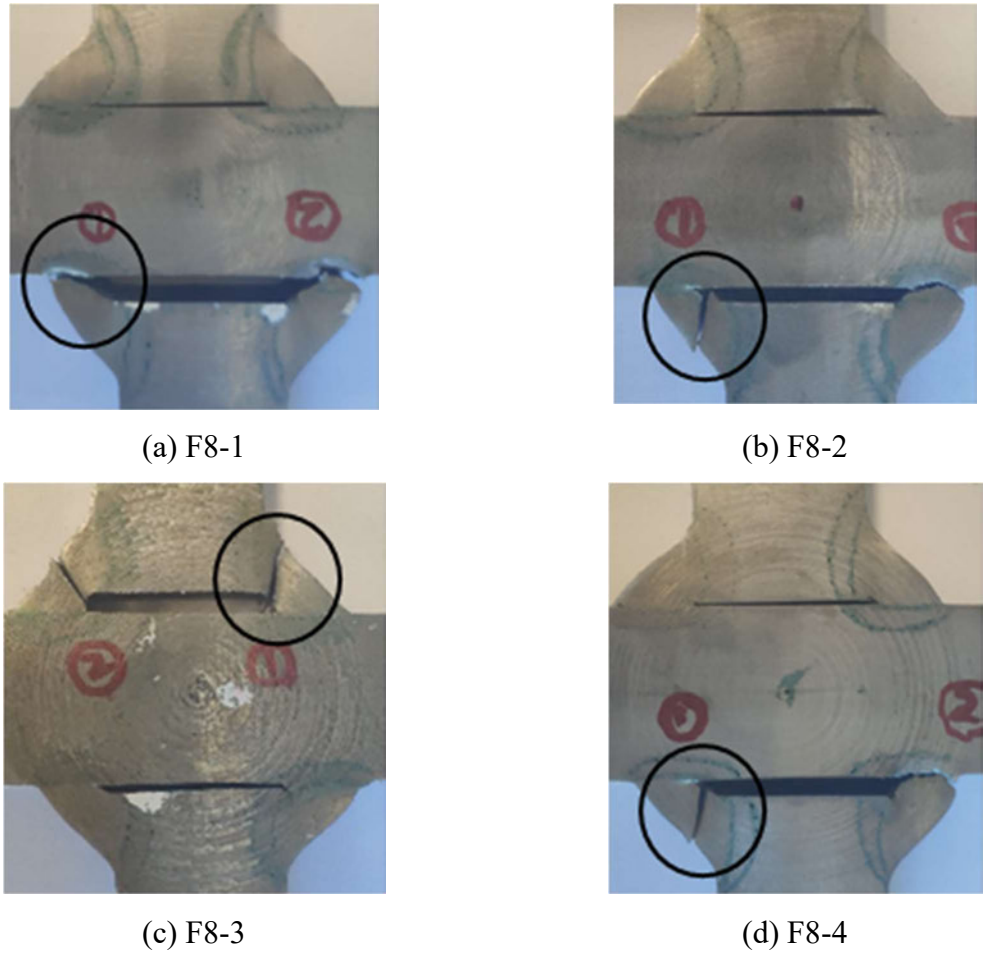

(a) F8-1 (b) F8-2

(c) F8-3 (d) F8-4

Figure 7-7. Photos of fractured F8 specimens.

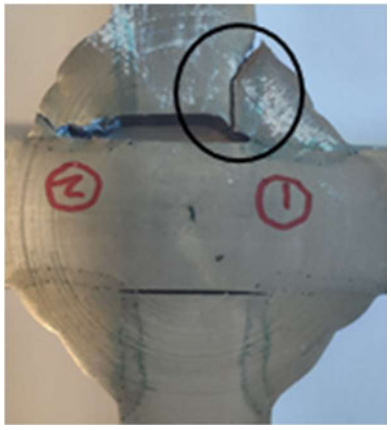

(a) F12-1

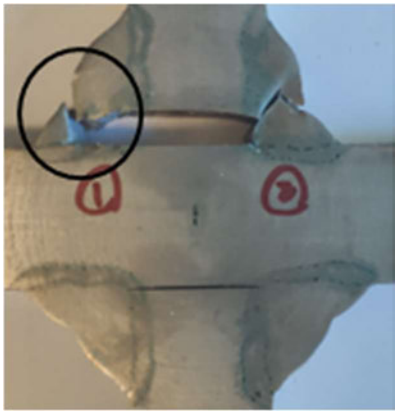

(b) F12-2

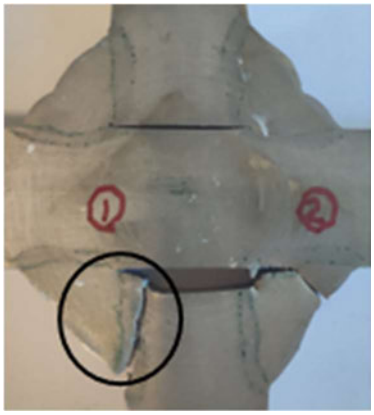

(c) F12-3

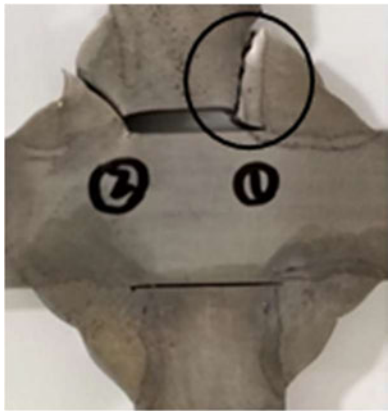

(d) F12-4

Figure 7-8. Photos of fractured F12 specimens.

The load-deformation curves of the specimens are plotted in Fig. 7-9. It is observed that the results of the replicated tests for the F8 and F12 specimens were consistent with each other. The curves of the F8 specimens consistently increased to the maximum load after the elastic range and then decreased gradually to final failure, while the F12 specimens experienced a yield plateau stage before the increase, and the post-ultimate curves dropped more sharply. The maximum load, P_{max}, and the fracture deformation (the deformation under which first crack formed), D_f, are summarized in Table 7-1. The average maximum load and average fracture deformation of the F12 specimens were 84.44 kN and 5.54 mm, and were much larger than those of the F8 specimens, which were 51.39 kN and 2.17 mm. Considering that the thickness of the supporting and supported plates was the same in the two specimen types, the difference in their strength and ductility was caused by the different weld sizes.

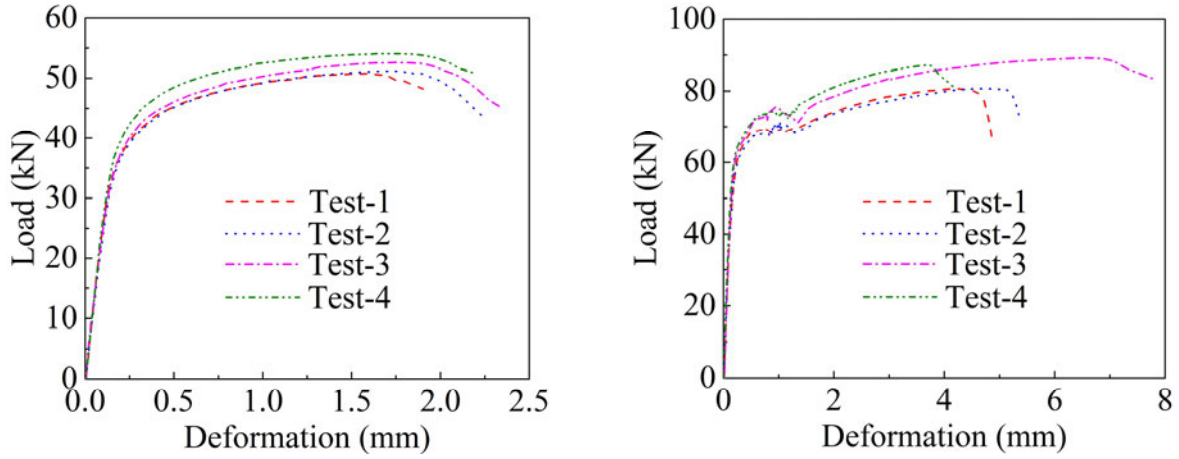

(a) F8 (b) F12

Figure 7-9. Load-deformation curves of cruciform specimens.

Table 7-1. Maximum loads and fracture deformations of cruciform specimens.

	P_{max} (kN)	D_f (mm)		P_{max} (kN)	D_f (mm)
F8-1	47.75	1.92	F12-1	80.68	4.88
F8-2	51.16	2.24	F12-2	80.71	5.36
F8-3	52.59	2.35	F12-3	89.16	7.77
F8-4	54.06	2.18	F12-4	87.19	4.16
F8-avg	51.39	2.17	F12-avg	84.44	5.54

7.3 Numerical simulation of fracture in welded cruciform specimens

7.3.1 Simulation considering the mechanical properties of weld and HAZ

In order to simulate the test process, three-dimensional FE models were developed for the F8 and F12 specimens using ABAQUS, as shown in Fig. 7-10. Since the geometry of the specimen was symmetric, one-eighth of the specimen was modelled using eight-node linear solid elements with reduced integration (C3D8R). Considering the fracture occurred within the weld zone, the mesh size in the critical area was set to be 0.2 mm, while the element size of other parts of the specimen was 2 mm. As discussed in Chapter 4, the mechanical properties within the weld zone were not homogenous, and the stress-strain relationships were measured for the base metal, weld and HAZ of the butt-welded plates, as plotted in Fig. 4-19. The hardness results measured in Section 7.2.1 showed that the values of the hardness of the three material areas in the weld zone measured from the cruciform specimens were consistent with those measured from the butt-welded plates, indicating that the mechanical properties of the weld,

HAZ and base metal in the cruciform specimens were similar to those in the butt-welded plates. Therefore, the stress-strain relationships of the three material areas measured from the butt-welded plates in Chapter 4 were used in the simulation of the welded cruciform specimens in this chapter.

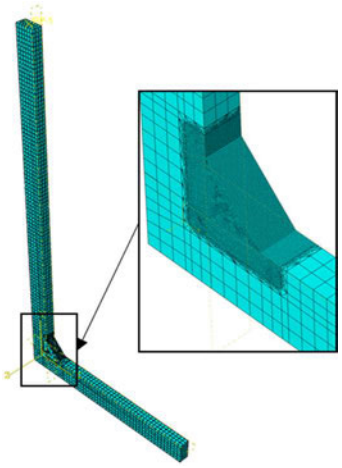

Figure 7-10. Numerical model for cruciform specimens.

Three FE models were established for each specimen type to investigate the effect of the material heterogeneity within the weld zone, as shown in Fig. 7-11. In the first model, FEM-B, the mechanical properties within the weld zone were assumed to be homogenous, and the stress-strain relationship of the base metal was used for the whole FE model, as shown in Fig. 7-11(a). In the second model, FEM-BW, the mechanical properties of the weld were used in the weld area, while other parts adopted the properties of the base metal, as shown in Fig. 7-11(b). In the third model, FEM-BWH, in addition to adopting the properties of the weld, the mechanical properties of the HAZ were used for the HAZ area near the weld, and the width of the HAZ was assumed to be the same as the horizontal width measured from the butt-welded plates, which was 2.23 mm, as shown in Fig. 7-11(c).

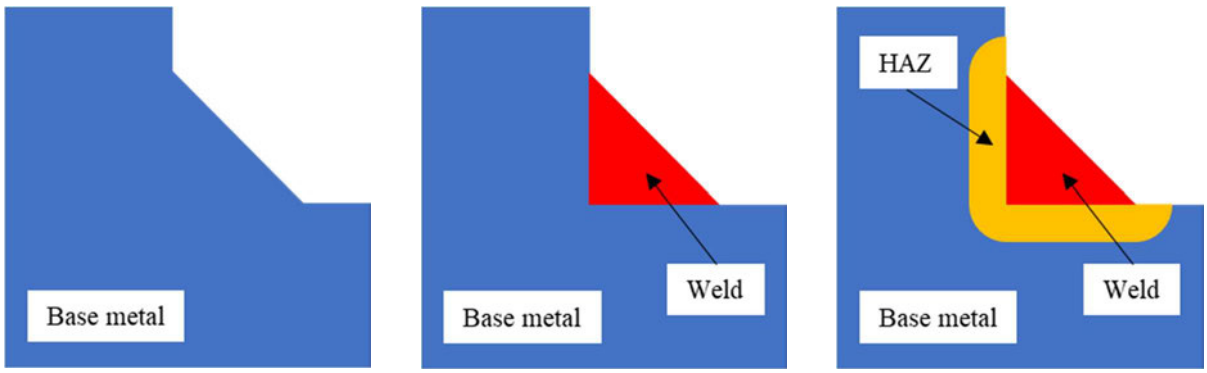

(a) FEM-B (b) FEM-BW (c) FEM-BWH

Figure 7-11. Material areas in the weld zone.

The load-deformation curves simulated using the three FE models for the F8 and F12 specimens are plotted in Fig. 7-12. It is observed that without defining fracture models in the FE models, the FE curves do not drop due to the onset of fracture and continue to develop into a very large deformation. The simulated curves of the FEM-B models were always lower than the test results, showing that assuming the stress-strain relationships of the weld and HAZ were the same as those of the base metal would underestimate the strength of the welded cruciform specimens. The simulated curves of the FEM-BW models were higher than the results of the FEM-B models but were still slightly lower than the test curves, showing that considering the mechanical properties of the weld area would increase the accuracy of the simulation results. The simulated curves of the FEM-BWH models were higher than the results of both the FEM-B and FEM-BW models, and it is observed that the difference between the results of the FEM-BWH models and the FEM-BW models decreased with increasing deformation. The FEM-BWH models provided the simulation results with the best agreement with the test results. Therefore, it is concluded that the material heterogeneity within the weld zone has a significant effect on the simulation results of the welded cruciform specimens and using the different stress-strain relationships of the three material areas in the FE models will increase the accuracy of the simulation results.

The von Mises stress contours of the FEM-BWH models corresponding to the deformation of the gauge length equal to the fracture deformation are plotted for the two specimen types in Figs. 7-13. A non-uniform distribution of the von Mises stresses with large plastic deformation in the weld zone is observed with the stresses concentrating near the weld root and weld toe of the vertical fusion line.

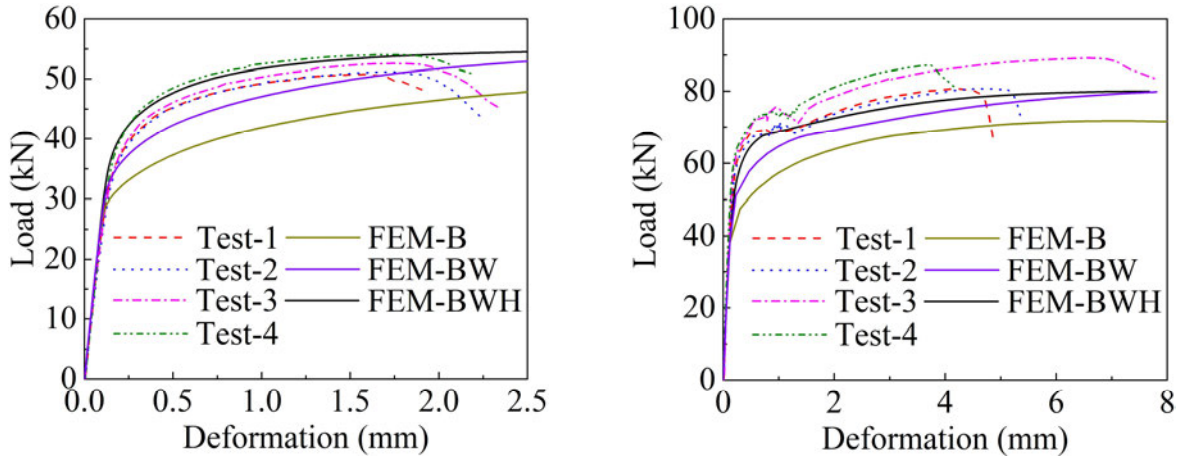

(a) F8 (b) F12

Figure 7-12. Load-deformation curves considering material properties of three material areas.

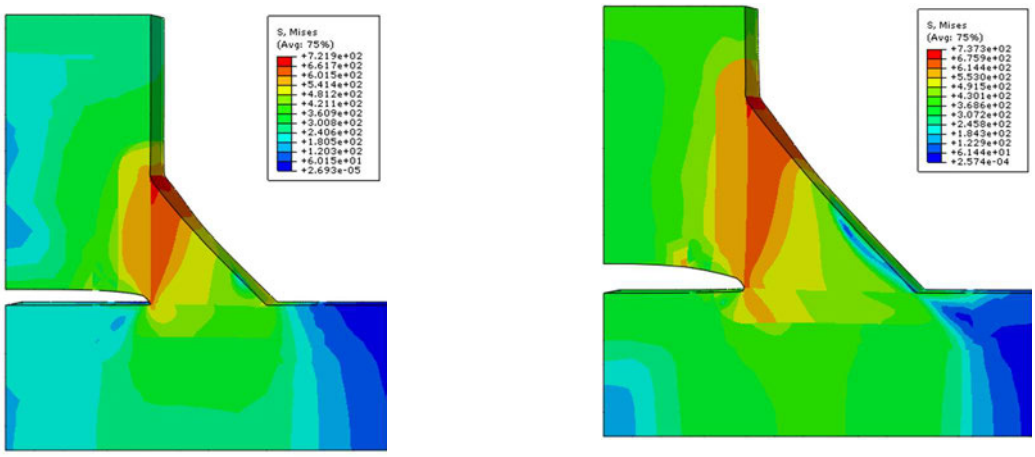

(a) F8 (b) F12

Figure 7-13. Von Mises stress distribution of FEM-BWH models.

7.3.2 Simulation considering the fracture strains of weld and HAZ

After discussing the effect of the material heterogeneity in the simulation of the welded cruciform specimens, the fracture model LMVGM was used to simulate the fracture process of the F8 and F12 specimens in the FE models by employing the user subroutine VUSDFLD in ABAQUS. The fracture strains of the three material areas in the weld zone under various stress states, including the axisymmetric tension states with high or medium stress triaxiality and the plane strain tension states, were obtained from the tensile tests on the miniature FPs, NRBs and GPs extracted from the butt-welded plates in Chapter 5. As discussed in Section 7.3.1, the mechanical properties of the base metal, weld and HAZ of the welded cruciform specimens were assumed to be the same as those of the butt-welded plates, because they were fabricated using the same materials under the same welding process and the values of their hardness were consistent with each other. Therefore, the fracture strains measured from the butt-welded plates were used in the simulation of the welded cruciform specimens in this chapter.

The stress triaxiality T, the Lode angle parameter ξ, and the fracture strain ε_f are summarized in Tables 5-4 to 5-7, which were used to calibrate the free parameters of the fracture model LMVGM, as shown in Table 5-8. Based on the different fracture strains of the three material areas in the weld zone, the FEM-BWH models shown in Fig. 7-11(c) were developed for the F8 and F12 specimens using the calibrated LMVGM to predict the fracture initiation and propagation. During the simulated loading process, the LMVGM was implemented in the VUSDFLD subroutine. In each step increment, the stress and strain tensors were first obtained and used to calculate the stress triaxiality and the Lode angle parameter. The value of the damage index D was then calculated using Eq. (3-14), and when D reached unity, the fracture was predicted to initiate. Finally, the elements that reached the fracture criterion were deleted

to simulate the propagation of the fracture. It is noted that in the fracture simulation of a full-scale connection, the mesh size of the elements in the critical area should be close to the characteristic length of the material since the fracture model is mesh size dependent. Accordingly, the mesh size in the weld zone of the welded cruciform specimens was set to 0.2 mm, as shown in Fig. 7-10.

The von Mises stress contours of the F8 and F12 specimens were plotted at various stages during the simulated loading process in Figs. 7-14 and 7-15. It is shown that the fracture initiation, propagation, and final failure of the weld zone were captured by the FEM-BWH models. Before the fracture initiation, the stress concentrated in the weld zone near the vertical fusion line, as shown in Figs. 7-14(a) and 7-15(a). The fracture then initiated from the weld root, which was consistent with the experimental observation, as shown in Figs. 7-14(b) and 7-15(b). After that, the fracture propagated in the weld zone, as shown in Figs. 7-14(c) and 7-15(c), which led to the final failure of the specimen, as shown in Figs. 7-14(d) and 7-15(d). The simulated fracture initiation and propagation process of the F8 and F12 specimens agreed well with the photos of the fractured specimens in Figs. 7-7(c) and 7-8(b). The simulated load-deformation curves were compared with the test curves in Fig. 7-16, and it is shown that the simulated curves for both the F8 and F12 specimens agreed well with the test results. Therefore, it is concluded that the fracture process can be captured by adopting the mechanical properties of the base metal, weld and HAZ in the weld zone using the fracture model LMVGM.

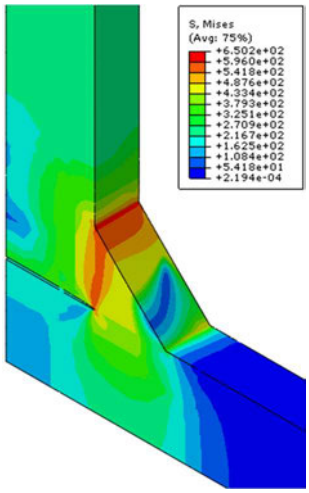

(a) Unfractured specimen

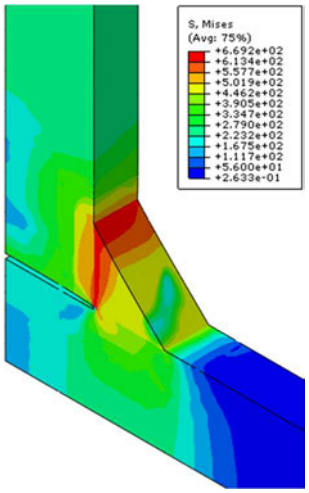

(b) Fracture initiation

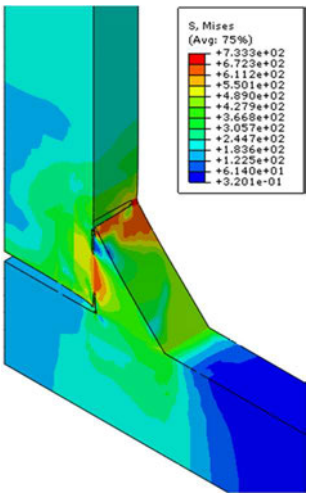

(c) Fracture propagation

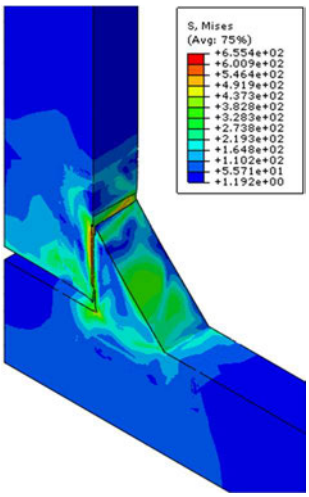

(d) Complete fracture

Figure 7-14. Simulated fracture process of the F8 specimen (Von Mises stress).

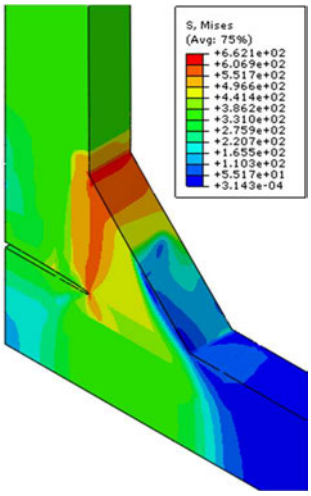

(a) Unfractured specimen

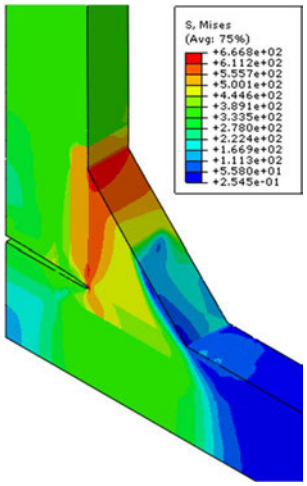

(b) Fracture initiation

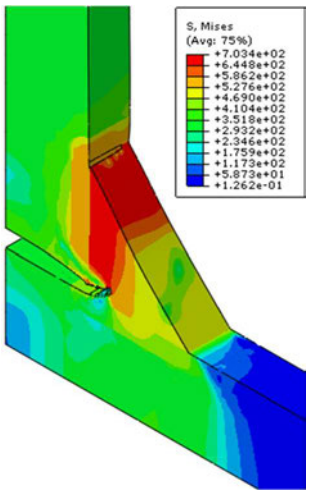

(c) Fracture propagation

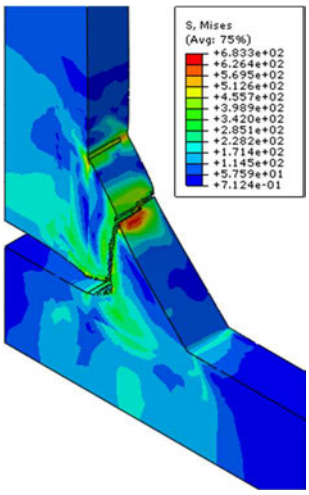

(d) Complete fracture

Figure 7-15. Simulated fracture process of the F12 specimen (Von Mises stress).

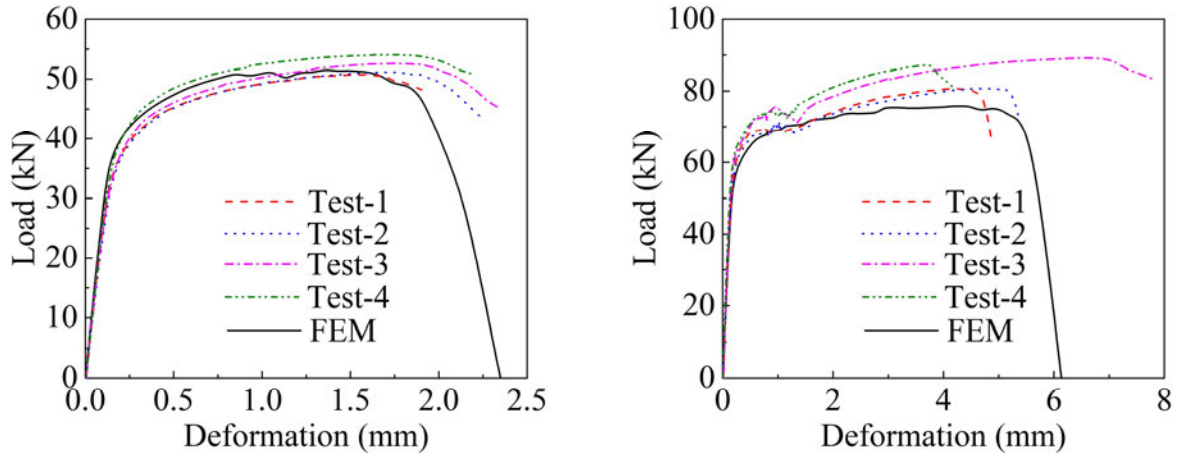

(a) F8 (b) F12

Figure 7-16. Load-deformation curves considering fracture process.

7.4 Summary

In this chapter, the fracture process of the cruciform specimens with 8 mm fillet welds (F8) or 12 mm fillet welds (F12) was experimentally investigated, and the fracture process was simulated using the fracture model LMVGM through the user subroutine VUSDFLD in ABAQUS. Four 10 mm thick replicated cruciform specimens were cut perpendicular to the welds from the long specimens described in Chapter 6.

The width of the HAZ was measured from the macroetched cruciform specimens, the average value of which was similar to the average value of the HAZ horizontal width measured from the butt-welded plates in Chapter 4. The Vickers hardness of the base metal, weld and HAZ measured from the welded cruciform specimens was also consistent with those measured from the butt-welded plates. Therefore, it is concluded that the properties within the weld zone were similar among different specimen types made using the same materials under the same welding process and heat input. Tensile tests were conducted on the F8 and F12 specimens, and the test results showed that the plastic deformation developed and localized in the weld zone, and the fracture initiated from one weld root and generally propagated near the vertical fusion line. The average maximum load and fracture deformation of the F12 specimens were higher than those of the F8 specimens.

The loading process of the cruciform specimens was simulated to investigate the effect of material heterogeneity within the weld zone. The mechanical properties of the base metal, weld and HAZ measured from the butt-welded plates in Chapters 4 and 5 were used in the simulation of welded cruciform specimens considering the values of their hardness were consistent with each other. Three FE models were developed by assuming the stress-strain relationships of the

weld and HAZ were the same as the base metal (FEM-B), adopting the properties of the weld (FEM-BW) or the properties of both the weld and HAZ (FEM-BWH).

The FEM-BWH models provided results that agreed well with the test results, while the simulated curves of the FEM-B and FEM-BW models were lower than the test curves. It is shown that using the mechanical properties of the three material areas in the weld zone will increase the accuracy of the simulation results. Therefore, the material heterogeneity within the weld zone has a significant effect on the simulation results of the welded cruciform specimens, and the assumption of homogenous properties within the weld zone using the properties of the base metal will underestimate the strength of the welded cruciform specimens. The fracture process of the F8 and F12 specimens was simulated using the fracture model LMVGM with the free parameters calibrated using the fracture strains under various stress states measured for the weld, HAZ and base metal. The fracture initiation and propagation were simulated by deleting the elements that reached the fracture criterion using the user subroutine VUSDFLD in ABAQUS. The simulated load-deformation curves agreed well with the test results, and it is concluded that the fracture process of the welded connections can be simulated by considering the mechanical properties of the base metal, weld and HAZ in the weld zone using the fracture model LMVGM.

Chapter 8 Conclusion

8.1 Summary of developments and findings

The thesis consists of eight chapters. After introducing the research topic and current understanding of the mechanical properties and fracture of welded steel connections in Chapters 1 and 2, the effects of the key factors, the stress triaxiality and the Lode angle, on the fracture strains of steels were discussed, and a new fracture model was proposed in Chapter 3. The mechanical properties of the weld and HAZ, including their stress-strain relationships and fracture strains under various stress states, and the weld residual stresses were measured in Chapters 4, 5 and 6. Note that the conclusions are limited to the tested AS350 grade steel and accompanying weld, laid using grade B-G49 welding wire using the documented welding process. The fracture process of welded cruciform specimens was investigated by considering these weld-zone mechanical properties using the proposed fracture model in Chapter 7. The following developments and findings were summarized from the core chapters:

In Chapter 3, the effects of the stress triaxiality and the Lode angle on the fracture of structural steels under a wide range of stress states were investigated based on a large amount of experimental data was collected from the literature, and additional series of newly designed plane strain specimens and rectangular notched specimens. First, the validity of the void growth-based exponential function over the full range of stress triaxialities was assessed, and it was concluded that generally, the VGEF can be adopted to accurately describe the effect of stress triaxiality over the full range of stress triaxialities. Second, a thorough understanding of the Lode angle effect was discussed, and it was observed from the data sets that the effect of the Lode angle increased with a decreasing value of the stress triaxiality and was more pronounced for high strength steels, such as Q690 grade, than lower strength steels, such as A572, AISI 1045 and Q460 grades. It was concluded that its dependence can be captured by an exponential function, which implied an asymmetric fracture locus with respect to the central Lode angle parameter line, $\xi = 0$. Finally, a new fracture model LMVGM was proposed, which combined the effect of stress triaxiality T, through the VGEF, and the effect of the Lode angle parameter ξ, using an exponential function.

In Chapter 4, the stress-strain relationships of the weld and HAZ were measured for both longitudinal and transverse directions and compared with those of the base metal, by conducting tensile tests on the miniature coupons extracted from the butt-welded plates. First, the three material areas in the weld zone were distinguished by macroetching, and the hardness

tests showed that the weld was the hardest, and the base metal was the softest. Second, a series of miniature flat plate coupons were extracted from the base metal, weld and HAZ along both the longitudinal and transverse directions. The stress-strain relationships were then obtained by tensile tests on these miniature coupons. It was observed that for the base metal and HAZ, the yield stresses in the longitudinal direction were higher than their transverse counterparts, while the strength of the weld was observed to be nearly independent of the direction. Consistent with the hardness tests' results, the maximum load and yield stress of the HAZ were higher than those of the base metal but lower than those of the weld in both directions. Finally, the accuracy of the miniature testing scheme was verified by comparing the test results obtained from the normal-size specimens and the miniature coupons.

In Chapter 5, the fracture strains of the weld and HAZ were measured for both longitudinal and transverse directions, and their values were compared with those of the base metal. Tensile tests were conducted on a series of miniature notched round bars and grooved plates extracted from the three material areas along both the longitudinal and transverse directions. It was shown that generally, the maximum loads of the HAZ were higher than those of the base metal but lower than those of the weld, and the maximum loads of the three material areas were higher in the longitudinal direction than the transverse direction. The average stress triaxiality, average Lode angle parameter and fracture strain of miniature coupons were obtained and used to calibrate the free parameters of the fracture model LMVGM, which was used to predict the fracture loci for the whole stress state regime. It was observed that the fracture initiation more easily occurred under stress states with high T and low ξ. Generally, the fracture locus of the HAZ was lower than that of the base metal but higher than that of the weld, and the three material areas had higher longitudinal ductility under low stress triaxialities, but higher transverse ductility under high stress triaxialities.

In Chapter 6, the magnitude and distribution of residual stresses of fillet welds and butt welds were measured from four welded cruciform specimens and an end-plate connection using the neutron diffraction method. First, after determining the lattice spacing d_0 of the stress-free reference sample, the residual stresses were measured for one weld in each cruciform specimen along two weld legs at points with different distances from the weld root. The residual stresses generated by the fillet welds with different weld sizes present similar distributions, which were different from butt welds, especially in the transverse and normal directions. The comparison of results showed that the larger the weld size, the higher the residual stresses and the broader the peak distribution range. Then, a welded end-plate connection was made of the same

materials under the same welding process as those of the cruciform specimens. The residual stresses in the I beam were measured at a cross-section which was 150 mm from the end plate, while the residual stresses of the welds connecting the I beam and the end plate were measured at three sections which were at different distances from the web centreline. Generally, the results of fillet welds measured from the end-plate connection agreed well with those of the cruciform specimens, and it was concluded that under the same welding process, similar residual stresses will be generated for the fillet welds with the same weld size by different specimen types made by the same materials.

In Chapter 7, the fracture process of welded cruciform specimens welded was experimentally investigated, and their fracture process was simulated using the fracture model LMVGM through the user subroutine VUSDFLD in ABAQUS. The cruciform specimens were made using the same materials under the same welding process as those of the butt-welded plates in Chapter 4. The comparison of the macroetching and hardness results measured from the cruciform specimens and the butt-welded plates showed that their width of HAZ and Vickers hardness were similar, and it was concluded that the mechanical properties within the weld zone were similar among different specimen types made using the same materials under the same welding process and heat input. The mechanical properties of the base metal, weld and HAZ measured from the butt-welded plates in Chapters 4 and 5 were used in the simulation of welded cruciform specimens. Three FE models were developed for each specimen type by considering or ignoring the material inhomogeneity in the weld zone and the comparison of the simulation results showed that the material heterogeneity within the weld zone has a significant effect on the simulation results of the welded cruciform specimens and the assumption of homogenous properties within the weld zone using the properties of the base metal will underestimate the strength of the welded cruciform specimens. The fracture process of the cruciform specimens was simulated using the fracture model LMVGM with the calibrated free parameters for the three material areas and the simulated load-deformation curves agreed well with the test results. It was concluded that the fracture process of the welded steel connections can be simulated by considering the mechanical properties of the base metal, weld and HAZ in the weld zone.

8.2 Future research

The following subjects might be highlighted for future research work:

1) Further investigation for stress states with negative stress triaxiality or negative Lode angle parameter can be conducted to provide more experimental data for the second, third and fourth quadrants in the space of the stress triaxiality and the Lode angle parameter. The applicability of the proposed fracture model LMVGM should be further verified using different data sets of various steel grades and its accuracy in simulating the fracture process of welded connections can be further discussed by comparing predicted results with other existing fracture models.
2) The properties in the subareas of the weld and HAZ can be further investigated using the miniature testing method. The mechanical properties at the points with different distances from the fusion line in the HAZ area and at the points in different runs of the weld area can be further discussed.
3) The distribution of the weld residual stresses through the thickness of the plates can be further discussed. Using the results of weld residual stresses, a thermo-mechanical FE simulation and lifetime prediction of welded connections can be conducted. The effect of the weld residual stresses on the fracture in welded connections should be further studied by conducting experiments and numerical simulations on long cruciform specimens and end-plate connection specimens.
4) The discussion of the effect of the mechanical properties can be conducted on other welded connections with various specimen geometries made from various materials under various welding conditions to obtain a more comprehensive understanding. Parametric studies can be conducted on welded cruciform specimens to further discuss the fracture performance of welded connections. The results of F12 specimens showed a relatively large deviation, which may be related to the manufacturing process. The discretization of the results of welded cruciform specimens can be further discussed in future research.

References

[1] Anderson, T.L., 2017. *Fracture mechanics: fundamentals and applications*. CRC press.

[2] Rice, J.R. and Tracey, D.M., 1969. On the ductile enlargement of voids in triaxial stress fields∗. *Journal of the Mechanics and Physics of Solids*, *17*(3), pp.201-217.

[3] Hancock, J.W. and Mackenzie, A.C., 1976. On the mechanisms of ductile failure in high-strength steels subjected to multi-axial stress-states. *Journal of the Mechanics and Physics of Solids*, *24*(2-3), pp.147-160.

[4] Johnson, G.R. and Cook, W.H., 1985. Fracture characteristics of three metals subjected to various strains, strain rates, temperatures and pressures. *Engineering fracture mechanics*, *21*(1), pp.31-48.

[5] Kanvinde, A.M. and Deierlein, G.G., 2006. The void growth model and the stress modified critical strain model to predict ductile fracture in structural steels. *Journal of Structural Engineering*, *132*(12), pp.1907-1918.

[6] Zhang, K.S., Bai, J.B. and Francois, D., 2001. Numerical analysis of the influence of the Lode parameter on void growth. *International Journal of Solids and Structures*, *38*(32-33), pp.5847-5856.

[7] Barsoum, I. and Faleskog, J., 2007. Rupture mechanisms in combined tension and shear—Experiments. *International journal of solids and structures*, *44*(6), pp.1768-1786.

[8] Wierzbicki, T., Bao, Y., Lee, Y.W. and Bai, Y., 2005. Calibration and evaluation of seven fracture models. *International Journal of Mechanical Sciences*, *47*(4-5), pp.719-743.

[9] Bai, Y. and Wierzbicki, T., 2008. A new model of metal plasticity and fracture with pressure and Lode dependence. *International journal of plasticity*, *24*(6), pp.1071-1096.

[10] Yan, S. and Zhao, X., 2018. A fracture criterion for fracture simulation of ductile metals based on micro-mechanisms. *Theoretical and Applied Fracture Mechanics*, *95*, pp.127-142.

[11] Zhu, Y. and Engelhardt, M.D., 2018. Prediction of ductile fracture for metal alloys using a shear modified void growth model. *Engineering Fracture Mechanics*, *190*, pp.491-513.

[12] Wang, Y.Z., Li, G.Q., Wang, Y.B., Lyu, Y.F. and Li, H., 2020. Ductile fracture of high strength steel under multi-axial loading. *Engineering Structures*, *210*, p.110401.

[13] Huang, X., Ge, J., Zhao, J. and Zhao, W., 2020. A continuous damage model of Q690D steel considering the influence of Lode parameter and its application. *Construction and Building Materials*, *262*, p.120067.

[14] Smith, C.M., Deierlein, G.G. and Kanvinde, A.M., 2014. A stress-weighted damage model for ductile fracture initiation in structural steel under cyclic loading and generalized stress states. *Technical Rep*, *187*.

[15] Smith, C., Ziccarelli, A., Terashima, M., Kanvinde, A. and Deierlein, G., 2021. A stress-weighted ductile fracture model for steel subjected to Ultra Low Cycle Fatigue. *Engineering Structures*, *245*, p.112964.

[16] Lou, Y., Huh, H., Lim, S. and Pack, K., 2012. New ductile fracture criterion for prediction of fracture forming limit diagrams of sheet metals. *International Journal of Solids and Structures*, *49*(25), pp.3605-3615.

[17] Lou, Y. and Huh, H., 2013. Extension of a shear-controlled ductile fracture model considering the stress triaxiality and the Lode parameter. *International Journal of Solids and Structures*, *50*(2), pp.447-455.

[18] Ganjiani, M., 2020. A damage model for predicting ductile fracture with considering the dependency on stress triaxiality and Lode angle. *European Journal of Mechanics-A/Solids*, *84*, p.104048.

[19] Quach, H., Kim, J.J., Nguyen, D.T. and Kim, Y.S., 2020. Uncoupled ductile fracture criterion considering secondary void band behaviors for failure prediction in sheet metal forming. *International Journal of Mechanical Sciences*, *169*, p.105297.

[20] Peng, Z., Zhao, H. and Li, X., 2021. New ductile fracture model for fracture prediction ranging from negative to high stress triaxiality. *International Journal of Plasticity*, *145*, p.103057.

[21] Hooputra, H., Gese, H., Dell, H. and Werner, H., 2004. A comprehensive failure model for crashworthiness simulation of aluminium extrusions. *International Journal of Crashworthiness*, *9*(5), pp.449-464.

[22] Bao, Y., 2003. *Prediction of ductile crack formation in uncracked bodies* (Doctoral dissertation, Massachusetts Institute of Technology).

[23] Wierzbicki, T., Bao, Y. and Bai, Y., 2005, June. A new experimental technique for constructing a fracture envelope of metals under multi-axial loading. In *Proceedings of the 2005 SEM annual conference and exposition on experimental and applied mechanics* (Vol. 1, pp. 1295-1303). Portland USA.

[24] Bridgman, P.W., 2013. Studies in large plastic flow and fracture. In *Studies in Large Plastic Flow and Fracture*. Harvard University Press.

[25] Bai, Y., Teng, X. and Wierzbicki, T., 2009. On the application of stress triaxiality formula for plane strain fracture testing. *Journal of Engineering Materials and technology*, *131*(2).

[26] Abushawashi, Y., Xiao, X. and Astakhov, V., 2013. A novel approach for determining material constitutive parameters for a wide range of triaxiality under plane strain loading conditions. *International Journal of Mechanical Sciences*, *74*, pp.133-142.

[27] Bao, Y. and Wierzbicki, T., 2004. On fracture locus in the equivalent strain and stress triaxiality space. *International Journal of Mechanical Sciences*, *46*(1), pp.81-98.

[28] Bai, Y. and Wierzbicki, T., 2010. Application of extended Mohr–Coulomb criterion to ductile fracture. *International Journal of Fracture*, *161*(1), pp.1-20.

[29] Qin, S. and Beese, A.M., 2020. Multiaxial fracture of DP600: Experiments and finite element modeling. *Materials Science and Engineering: A*, *785*, p.139386.

[30] Gu, B., He, J., Li, S. and Lin, Z., 2020. Anisotropic fracture modeling of sheet metals: From in-plane to out-of-plane. *International Journal of Solids and Structures*, *182*, pp.112-140.

[31] Zerbst, U., Ainsworth, R.A., Beier, H.T., Pisarski, H., Zhang, Z.L., Nikbin, K., Nitschke-Pagel, T., Münstermann, S., Kucharczyk, P. and Klingbeil, D., 2014. Review on fracture and crack propagation in weldments–A fracture mechanics perspective. *Engineering fracture mechanics*, *132*, pp.200-276.

[32] Jia, Q., Guo, W., Li, W., Peng, P., Zhu, Y., Zou, G., Peng, Y. and Tian, Z., 2017. Experimental and numerical study on local mechanical properties and failure analysis of laser welded DP980 steels. *Materials Science and Engineering: A*, *680*, pp.378-387.

[33] Ma, Y., Takikawa, A., Nakanishi, J., Doira, K., Shimizu, T., Lu, Y. and Ma, N., 2021. Measurement of local material properties and failure analysis of resistance spot welds of advanced high-strength steel sheets. *Materials & Design*, *201*, p.109505.

[34] Yan, R., El Bamby, H., Veljkovic, M., Xin, H. and Yang, F., 2021. A method for identifying the boundary of regions in welded coupon specimens using digital image correlation. *Materials & Design*, *210*, p.110073.

[35] Ronevich, J.A., D'Elia, C.R. and Hill, M.R., 2018. Fatigue crack growth rates of X100 steel welds in high pressure hydrogen gas considering residual stress effects. *Engineering Fracture Mechanics*, *194*, pp.42-51.

[36] Eller, T.K., Greve, L., Andres, M., Medricky, M., Geijselaers, H.J., Meinders, V.T. and van den Boogaard, A.H., 2016. Plasticity and fracture modeling of the heat-affected zone in resistance spot welded tailor hardened boron steel. *Journal of materials processing technology*, *234*, pp.309-322.

[37] Bally, J., De Waele, W., Verleysen, P., Gubeljak, N. and Hertelé, S., 2015. Characterisation of weld heterogeneity through hardness mapping and miniature tensile testing. *International Journal of Sustainable Construction and Design*, *6*(3).

[38] Kanvinde, A.M., Fell, B.V., Gomez, I.R. and Roberts, M., 2008. Predicting fracture in structural fillet welds using traditional and micromechanical fracture models. *Engineering Structures*, *30*(11), pp.3325-3335.

[39] Liao, F., Wang, W. and Chen, Y., 2012. Parameter calibrations and application of micromechanical fracture models of structural steels. *Structural Engineering and Mechanics*, *42*(2), pp.153-174.

[40] Pavlina, E.J. and Van Tyne, C.J., 2008. Correlation of yield strength and tensile strength with hardness for steels. *Journal of materials engineering and performance*, *17*, pp.888-893.

[41] Khalfallah, A., 2014. Experimental and numerical assessment of mechanical properties of welded tubes for hydroforming. *Materials & Design (1980-2015)*, *56*, pp.782-790.

[42] Pham, T.H. and Kim, S.E., 2015. Determination of mechanical properties in SM490 steel weld zone using nanoindentation and FE analysis. *Journal of Constructional Steel Research*, *114*, pp.314-324.

[43] Peng, Y., Wu, C., Gan, J. and Dong, J., 2019. Characterization of heterogeneous constitutive relationship of the welded joint based on the stress-hardness relationship using micro-hardness tests. *Construction and Building Materials*, *202*, pp.37-45.

[44] LaVan, D.A. and Sharpe, W.N., 2001. Local properties of undermatched steel weld metal. *Metallurgical and Materials Transactions A*, *32*, pp.913-922.

[45] Tao, H., Tong, W., Hector Jr, L.G. and Zavattieri, P.D., 2008. Uniaxial tensile and simple shear behavior of resistance spot-welded dual-phase steel joints. *Journal of Materials Engineering and Performance*, *17*(4), pp.517-534.

[46] Molak, R.M., Paradowski, K., Brynk, T., Ciupinski, L., Pakiela, Z. and Kurzydlowski, K.J., 2009. Measurement of mechanical properties in a 316L stainless steel welded joint. *International Journal of Pressure Vessels and Piping*, *86*(1), pp.43-47.

[47] Ma, J., Kong, F., Liu, W., Carlson, B. and Kovacevic, R., 2014. Study on the strength and failure modes of laser welded galvanized DP980 steel lap joints. *Journal of Materials Processing Technology*, *214*(8), pp.1696-1709.

[48] Wudtke, I., Talebi, H., Silani, M. and Werner, F., 2015. A hierarchical multi-scale approach to mechanical characterization of heat affected zone in welded connections. *Computational Materials Science*, *96*, pp.396-402.

[49] Yang, B., Xuan, F.Z. and Chen, J.K., 2018. Evaluation of the microstructure related strength of CrMoV weldment by using the in-situ tensile test of miniature specimen. *Materials Science and Engineering: A*, *736*, pp.193-201.

[50] Reynolds, A.P. and Duvall, F., 1999. Digital image correlation for determination of weld and base metal constitutive behavior. *WELDING JOURNAL-NEW YORK-*, *78*, pp.355-s.

[51] Sutton, M.A., Yan, J.H., Avril, S., Pierron, F. and Adeeb, S.M., 2008. Identification of heterogeneous constitutive parameters in a welded specimen: uniform stress and virtual fields methods for material property estimation. *Experimental Mechanics*, *48*, pp.451-464.

[52] Leitão, C., Galvão, I., Leal, R.M. and Rodrigues, D.M., 2012. Determination of local constitutive properties of aluminium friction stir welds using digital image correlation. *Materials & Design*, *33*, pp.69-74.

[53] Lee, H., Kim, C. and Song, J.H., 2015. An evaluation of global and local tensile properties of friction-stir welded DP980 dual-phase steel joints using a digital image correlation method. *Materials*, *8*(12), pp.8424-8436.

[54] Peng, Y., Wu, C., Gan, J. and Dong, J., 2018. Determination of the local constitutive properties of the welded steel joints using digital image correlation method. *Construction and Building Materials*, *171*, pp.485-492.

[55] Ran, M.M., Sun, F.F., Li, G.Q., Kanvinde, A., Wang, Y.B. and Xiao, R.Y., 2019. Experimental study on the behavior of mismatched butt welded joints of high strength steel. *Journal of Constructional Steel Research*, *153*, pp.196-208.

[56] Myers, A.T., 2009. *Testing and probabilistic simulation of ductile fracture initiation in structural steel components and weldments*. Stanford University.

[57] Cai, W.Y., Wang, Y.B. and Li, G.Q., 2022. Experimental and numerical study on strength of high-strength steel double-V butt-welded joint. *Journal of Constructional Steel Research*, *196*, p.107397.

[58] Mae, H., Teng, X., Bai, Y. and Wierzbicki, T., 2007. Calibration of ductile fracture properties of a cast aluminum alloy. *Materials Science and Engineering: A*, *459*(1-2), pp.156-166.

[59] Gorji, M.B. and Mohr, D., 2017. Micro-tension and micro-shear experiments to characterize stress-state dependent ductile fracture. *Acta Materialia*, *131*, pp.65-76.

[60] Pandya, K.S., Grolleau, V., Roth, C.C. and Mohr, D., 2020. Fracture response of resistance spot welded dual phase steel sheets: Experiments and modeling. *International Journal of Mechanical Sciences*, *187*, p.105869.

[61] Withers, P.J. and Bhadeshia, H.K.D.H., 2001. Residual stress. Part 1–measurement techniques. *Materials science and Technology*, *17*(4), pp.355-365.

[62] Withers, P.J. and Bhadeshia, H.K.D.H., 2001. Residual stress. Part 2–Nature and origins. *Materials science and technology*, *17*(4), pp.366-375.

[63] Ziara-Paradowska, A.M., 2007. *Investigation of residual stress in steel welds using neutron and synchrotron diffraction* (Doctoral dissertation, Monash University).

[64] Bailey, N., 1994. *Weldability of ferritic steels*. Elsevier.

[65] Rossini, N.S., Dassisti, M., Benyounis, K.Y. and Olabi, A.G., 2012. Methods of measuring residual stresses in components. *Materials & Design*, *35*, pp.572-588.

[66] Cheng, W. and Finnie, I., 1985. A method for measurement of axisymmetric axial residual stresses in circumferentially welded thin-walled cylinders.

[67] Hill, M.R., 2013. The slitting method. *Practical residual stress measurement methods*, pp.89-108.

[68] Yaowu, X.U. and Rui, B.A.O., 2017. Residual stress determination in friction stir butt welded joints using a digital image correlation-aided slitting technique. *Chinese Journal of Aeronautics*, *30*(3), pp.1258-1269.

[69] Mathar, J., 1934. Determination of initial stresses by measuring the deformations around drilled holes. *Transactions of the American Society of Mechanical Engineers*, *56*(3), pp.249-254.

[70] Olabi, A.G. and Hashmi, M.S.J., 1996. Stress relief procedures for low carbon steel (1020) welded components. *Journal of materials processing technology*, *56*(1-4), pp.552-562.

[71] Roy, G., Braid, M. and Shen, G., 2003. Application of ADINA and hole drilling method to residual stress determination in weldments. *Computers & structures*, *81*(8-11), pp.929-935.

[72] Nasim, K., Arif, A.F.M., Al-Nassar, Y.N. and Anis, M., 2015. Investigation of residual stress development in spiral welded pipe. *Journal of Materials Processing Technology*, *215*, pp.225-238.

[73] Li, Y., Wu, J., Qiang, B., Zhou, S., Liu, W. and Yao, C., 2021. Measurements of residual stresses in a welded orthotropic steel deck by the hole-drilling method considering stress biaxiality. *Engineering Structures*, *230*, p.111690.

[74] Li, D., Paradowska, A., Uy, B., Wang, J., Proust, G., Azad, S.K. and Huang, Y., 2021. Residual stress measurements of lean duplex stainless steel welded sections. *Journal of Constructional Steel Research*, *186*, p.106883.

[75] Gou, R., Zhang, Y., Xu, X., Sun, L. and Yang, Y., 2011. Residual stress measurement of new and in-service X70 pipelines by X-ray diffraction method. *Ndt & E International*, *44*(5), pp.387-393.

[76] Ahmed, I.I., Adebisi, J.A., Abdulkareem, S. and Sherry, A.H., 2018. Investigation of surface residual stress profile on martensitic stainless steel weldment with X-ray diffraction. *Journal of King Saud University-Engineering Sciences*, *30*(2), pp.183-187.

[77] Ao, S., Li, C., Huang, Y. and Luo, Z., 2020. Determination of residual stress in resistance spot-welded joint by a novel X-ray diffraction. *Measurement*, *161*, p.107892.

[78] Alipooramirabad, H., Paradowska, A., Ghomashchi, R. and Reid, M., 2017. Investigating the effects of welding process on residual stresses, microstructure and mechanical properties in HSLA steel welds. *Journal of Manufacturing Processes*, *28*, pp.70-81.

[79] Le, T., Paradowska, A., Bradford, M.A., Liu, X. and Valipour, H.R., 2020. Residual stresses in welded high-strength steel I-Beams. *Journal of Constructional Steel Research*, *167*, p.105849.

[80] Li, D., Paradowska, A., Uy, B., Wang, J., Proust, G., Azad, S.K. and Huang, Y., 2021. Residual stress measurements of lean duplex stainless steel welded sections. *Journal of Constructional Steel Research*, *186*, p.106883.

[81] Shen, C., Ma, Y., Reid, M., Pan, Z., Hua, X., Cuiuri, D., Paradowska, A., Wang, L. and Li, H., 2022. Neutron diffraction residual stress determinations in titanium aluminide component fabricated using the twin wire-arc additive manufacturing. *Journal of Manufacturing Processes*, *74*, pp.141-150.

[82] Coelho, A.M.G., Bijlaard, F.S., Gresnigt, N. and da Silva, L.S., 2004. Experimental assessment of the behaviour of bolted T-stub connections made up of welded plates. *Journal of constructional Steel research*, *60*(2), pp.269-311.

[83] Liang, G., Guo, H., Liu, Y., Yang, D. and Li, S., 2019. A comparative study on tensile behavior of welded T-stub joints using Q345 normal steel and Q690 high strength steel under bolt preloading cases. *Thin-Walled Structures*, *137*, pp.271-283.

[84] Wang, Y., Zhou, H., Shi, Y. and Xiong, J., 2011. Fracture prediction of welded steel connections using traditional fracture mechanics and calibrated micromechanics based models. *International Journal of Steel Structures*, *11*, pp.351-366.

[85] Shi, G. and Chen, Y., 2018. Investigation of ductile fracture behavior of lap-welded joints with 460 MPa steel. *Advances in Structural Engineering*, *21*(9), pp.1376-1387.

[86] Kanvinde, A.M., Gomez, I.R., Roberts, M., Fell, B.V. and Grondin, G.Y., 2009. Strength and ductility of fillet welds with transverse root notch. *Journal of Constructional Steel Research*, *65*(4), pp.948-958.

[87] Ran, M.M., Sun, F.F., Li, G.Q. and Wang, Y.B., 2021. Mechanical behaviour of longitudinal lap-welded joints of high strength steel: Experimental and numerical analysis. *Thin-Walled Structures*, *159*, p.107286.

[88] Ghaderi-Garekani, M. and Maleki, S., 2022, November. An investigation of shear failure in welded channel and angle brace members. In *Structures* (Vol. 45, pp. 1287-1306). Elsevier.

[89] Ran, M.M., Zhong, Y.C., Wang, Y.Z., Li, G.Q., Xiong, F. and Ge, Q., 2022. Fracture prediction in transverse fillet welded joints of high strength structural steel. *Journal of Constructional Steel Research*, *189*, p.107101.

[90] Ma, X., Wang, W., Chen, Y. and Qian, X., 2015. Simulation of ductile fracture in welded tubular connections using a simplified damage plasticity model considering the effect of stress triaxiality and Lode angle. *Journal of Constructional Steel Research*, *114*, pp.217-236.

[91] Liao, F., Wang, W. and Chen, Y., 2015. Ductile fracture prediction for welded steel connections under monotonic loading based on micromechanical fracture criteria. *Engineering Structures*, *94*, pp.16-28.

[92] Yaghoubshahi, M., Sun, M. and Tousignant, K., 2019. Design of fillet welds in RHS-to-RHS moment T-connections under branch in-plane bending. *Journal of Constructional Steel Research*, *159*, pp.122-133.

[93] Zhu, C., Rasmussen, K.J., Yan, S. and Zhang, H., 2019. Experimental full-range behavior assessment of bolted moment end-plate connections. American Society of Civil Engineers.

[94] Yelek, İ., Ardalı, R. and Yılmaz, İ., 2021. Fracture investigation of different welded steel beam-column connections under three-point bending test. *Journal of Constructional Steel Research*, *187*, p.106945.

[95] Qu, X., Qin, C., Sun, G. and Xie, Y., 2022, September. Research on fracture of steel structure welded joint based on micro-mechanism. In *Structures* (Vol. 43, pp. 434-448). Elsevier.

[96] Chen, H., Shi, Y.J. and Wang, Y.Q., 2004. Fracture toughness properties of moment resistant column-beam connections Part II: inelastic analysis. *International Journal of Steel Structures*, *4*(1), pp.9-14.

[97] Song, Q.Y., Heidarpour, A., Zhao, X.L. and Han, L.H., 2018. Experimental and numerical investigation of ductile fracture of carbon steel structural components. *Journal of Constructional Steel Research*, *145*, pp.425-437.

[98] Chi, W.M., Deierlein, G.G. and Ingraffea, A., 2000. Fracture toughness demands in welded beam-column moment connections. *Journal of structural engineering*, *126*(1), pp.88-97.

[99] Chi, W.M., Kanvinde, A.M. and Deierlein, G.G., 2006. Prediction of ductile fracture in steel connections using SMCS criterion. *Journal of structural engineering*, *132*(2), pp.171-181.

[100] AS/NZS 3678. Structural Steel–Hot-rolled plates, floor plates and slabs. Standards Australia, Sydney; 2011.

[101] AS 1391. Metallic Materials – Tensile Testing at Ambient Temperature. Standards Australia, Sydney; 2020.

[102] Huang, Y. and Young, B., 2014. The art of coupon tests. *Journal of Constructional Steel Research*, *96*, pp.159-175.

[103] Yan, S., Jiang, L., Rasmussen, K. and Zhang, H., 2021. Full-range behavior of top-and-seat angle connections. *Journal of Structural Engineering*, *147*(1), p.04020308.

[104] Wang, Y.Z., Li, G.Q., Wang, Y.B., Lyu, Y.F. and Li, H., 2020. Ductile fracture of high strength steel under multi-axial loading. *Engineering Structures*, *210*, p.110401.

[105] Li, W., Liao, F., Zhou, T. and Askes, H., 2016. Ductile fracture of Q460 steel: Effects of stress triaxiality and Lode angle. *Journal of Constructional Steel Research*, *123*, pp.1-17.

[106] Kubík, P., Šebek, F., Hůlka, J. and Petruška, J., 2016. Calibration of ductile fracture criteria at negative stress triaxiality. *International Journal of Mechanical Sciences*, *108*, pp.90-103.

[107] Šebek, F., Kubík, P., Hůlka, J. and Petruška, J., 2016. Strain hardening exponent role in phenomenological ductile fracture criteria. *European Journal of Mechanics-A/Solids*, *57*, pp.149-164.

[108] Tang, B., Wu, F., Wang, Q., Liu, J., Guo, N., Ge, H., Wang, Q. and Liu, P., 2020. Damage prediction of hot stamped boron steel 22MnB5 with a microscopic motivated ductile fracture criterion: Experiment and simulation. *International Journal of Mechanical Sciences*, *169*, p.105302.

[109] Barsoum, I. and Faleskog, J., 2011. Micromechanical analysis on the influence of the Lode parameter on void growth and coalescence. *International Journal of Solids and Structures*, *48*(6), pp.925-938.

[110] Khan, A.S. and Liu, H., 2012. A new approach for ductile fracture prediction on Al 2024-T351 alloy. *International Journal of Plasticity*, *35*, pp.1-12.

[111] AS/NZS 1554. Structural steel welding. Standards Australia, Sydney, 2014.

[112] Li, D., Paradowska, A., Uy, B., Wang, J. and Khan, M., 2020. Residual stresses of box and I-shaped columns fabricated from S960 ultra-high-strength steel. *Journal of Constructional Steel Research*, *166*, p.105904.

[113] Khan, M., Paradowska, A., Uy, B., Mashiri, F. and Tao, Z., 2016. Residual stresses in high strength steel welded box sections. *Journal of Constructional Steel Research*, *116*, pp.55-64.